THE EFFECT OF PROCESSING CONDITIONS AND CHEMISTRY ON THE ELECTROCHEMISTRY OF GRAPHITE AND ALUMINUM METAL MATRIX COMPOSITES

by

MARK ANTHONY BUONANNO

B. Eng. Metallurgical Engineering
Polytechnic University
(1985)

S.M. Metallurgy
Massachusetts Institute of Technology
(1987)

Submitted to the Department of
Materials Science and Engineering in
Partial Fulfillment of the Requirements for the Degree of

DOCTOR OF PHILOSOPHY
in
MATERIALS SCIENCE AND ENGINEERING
at the
MASSACHUSETTS INSTITUTE OF TECHNOLOGY
June 1992

Signature of the Author ____________________
Department of Materials Science and Engineering
May 1, 1992

Certified by ____________________
Ronald M. Latanision
Professor, Materials Science and Engineering
Thesis Supervisor

Accepted by ____________________
Linn W. Hobbs
Professor of Materials Science
Chairman, Departmental Committee on Graduate Students

THE EFFECT OF PROCESSING CONDITIONS AND CHEMISTRY ON THE ELECTROCHEMISTRY OF GRAPHITE AND ALUMINUM METAL MATRIX COMPOSITES

by

MARK ANTHONY BUONANNO

Submitted to the Department of Materials Science and Engineering
on 1 May, 1992, in partial fulfillment of the requirements for the
Degree of Doctor of Philosophy in Materials Science and Engineering

Abstract

This work examines the interplay between processing and chemistry in continuous fiber G/Al MMCs with particular attention to subsequent effects on electrochemical behavior.

The scanning potential microprobe (SPM) was used to identify cathodic and anodic sites *in-situ* in NaCl solutions above model G/Al composites and commercial 0-90° interlaminar G/6061 Al MMCs. SPM testing of model G/Al MMCs was carried out to examine the possibility of reducing corrosion by two different methods: 1) electrical insulation of graphite and 2) cathodic inhibition of oxygen reduction on graphite.

Electrical insulation of graphite by coating with Al_2O_3 in model G/Al MMCs was unsuccessful in reducing galvanic corrosion due to crevice formation. However, Zn ion implantion reduced corrosion by a factor of 20 after 48 hours in aerated NaCl solution by cathodic inhibition of oxygen reduction on graphite.

Anodic polarization of continuous graphite fiber/Al MMCs containing Si, Mg, Cu and Zn alloy additions compared well with those predicted by the mixed-electrode model. Deviations attained were associated with commercial fiber type and interfacial intermetallics. At high anodic overpotentials, graphite fiber oxidation and subsequent crevice formation resulted in larger deviations from that predicted by mixed-electrode theory. Although Al_4C_3 was quantified for commercial G/Al MMCS, Al_4C_3 hydrolysis was not detectable on the time scale of the polarization studies performed.

The rate limiting step for the corrosion of commercial G/Al MMCs was determined to be the cathodic diffusion-limited oxygen reduction reaction occurring on the graphite fibers.

DC anodic and cyclic polarization studies in deaerated and aerated NaCl indicate that little protection was gained with Zn additions in the Al matrix. Auger electron and X-ray photoelectron spectroscopy of a G/Al-5 wt.% Zn MMC exposed to aerated 3.15 wt.% NaCl showed that only patches of an Al-Zn oxygenated film had formed on the surface of graphite fibers and that cathodic protection from this film was negligible.

Galvanic corrosion occurring in 0-90° interlaminar G/6061 Al MMCs was related to the local fiber distribution between interlaminar layers. The corrosion current densities for interlaminar composites determined by the SPM were an order of magnitude greater as compared to similar continuous fiber composites.

Thesis Supervisor: Professor Ronald M. Latanision
Title: Professor of Materials Science and Engineering

TABLE OF CONTENTS PAGE

LIST OF FIGURES

LIST OF TABLES

It has been my experience that any success that I was able to make was primarily attainable by effort or hard work, rather than serendipitously... what my Father had been telling me all along.

Therefore, I would like to dedicate this work to my Father, who, besides working hard all his life to financially support my education, has had the unenviable job of trying to push his children to their intellectual limits, for which I am grateful - at last.

I would also like to dedicate this work to my wife Nobuko who has helped me through the entire production of this dissertation with much love and encouragement.

ACKNOWLEDGEMENTS

Under the guidance of Professor Latanision, I enjoyed doing research not only at MIT, but in Japan and in Austria as well. Besides allowing for my travel, Professor Latanision was both knowledgeable and instructive, guiding me to areas that were pertinent to our goals in this research. He was able to correct mistakes without destroying confidence-a skill which I hope I can emulate. I would like to heartily thank him.

Sincere appreciation is extended to Professor Lloyd Hihara of the University of Hawaii, for his help and recommendations.

To Andreas who helped guide my career while at MIT. His advice and friendship were sincerely appreciated. As Professor Mortensen, he was a superb committee member and added much to the technical content of this thesis and to my learning experience while at MIT.

Professor Russell, a committee member for his technical contribution to the content of this thesis. His door was always open for me to come and make a visit.

I would also like to thank the following people:

Ms. Connie Beal, the Administrative Assistant for the H.H. Uhlig Corrosion Laboratory, for her help and friendship.

Dr. Pradnya Nagarkar for her helpful advice and introduction to XPS surface analysis.

Professor Francesco Bellucci for his help in the lab and his friendship.

The members of the H.H Uhlig Corrosion Laboratory who have helped me in countless ways, notably: Omar Abdul-Hamid, Steven Attanasio, Dr. Marius Kloppers, and Dr. Bryce Mitton.

The technical staff at Aluminium Ranshofen; those especially worthy of note: Dr. Helmut Kaufmann who arranged my travels, Dr. Theo Schmitt, Dr. Jackie Isaacs, Herr Georg Priewasser and Herr Ekon Neuwirth. I would like to heartily thank these people for teaching me about the processing of composites and for enriching my life while in Austria.

Special mention should be given to Dr. Peter Degischer of Aluminium Ranshofen, for allowing me to come and investigate composites, and for allowing me to explore the beautiful city of Salzburg.

Al Shipley of the Marine Biological Laboratory, Woods Hole, MA for his expertise concerning the SPM. Al was always willing to lend a hand. The SPM work could not have been accomplished without his help and his generosity.

Mark Gore and Gary Carinci who helped me overcome my early years at MIT, I thank you both.

Pat Kearny for technical laboratory assistance and photographic reproduction.

Libby Shaw and John Martin for analytical surface microscopy.

John Kang and Valerie Jordan, UROP students, for their assistance in laboratory experiments.

Ilda Moura for administration assistance.

Julia Duncan for syntactical editing and for her long support and friendship during my years at MIT.

Bruce Pint for his friendship and support.

Tom Fitzgerald for his friendship and technical discussion related to the processing of composites. His help in polishing and etching of the composites was much appreciated.

Robert Schmidt, my close friend, who helped me upon my return to MIT in 1987.

Roseann Brogna for her support and academic counseling.

To my family, both in Japan and America, who during the time this dissertation was undertaken, supported my marriage and education with financial support and much encouragement. Throughout my life they have helped me in so many ways.

I would like to thank my dear wife Nobuko, my friend. She helped me with the long struggle and with technical editing. In many respects this work reflects her efforts and time as well as mine.

1. INTRODUCTION

Currently, fibrous graphite aluminum (G/Al) metal matrix composites (MMCs) are being considered for structural components in aircraft and other applications where superior specific strength and weight savings are important parameters [Meyers, et al., 1984; Mortensen, 1988a; Taya, et al., 1989]. However, in part because they are susceptible to galvanic corrosion [Hack and Amateau, 1983; Aylor, et al., 1983; Czyrklis, 1985], their application has been limited. It has long been known that there is a synergistic corrosion effect due to the galvanic electrical contact at the fiber-matrix interface in G/Al MMCs. Therefore, G/Al MMC parts are usually fabricated with a protective coating (e.g., covering exposed areas with aluminum foil) to avoid such galvanic problems; however, it has been shown that such structures can be compromised during fabrication, structural assembly, usage, or by the chemical environment [Payer and Sullivan, 1976; Aylor, et al. 1983, 1984; Mansfeld, et al., 1988, 1990].

Chemical passivation of Al-foil linings on G/Al MMCs and, more recently the composite itself, has been used to increase corrosion resistance [Mansfeld, et al., 1988, 1990]. Although these techniques improve the corrosion resistance of MMCs, it is desirable to further improve the corrosion characteristics of the inherent composite fiber-matrix couple to ensure the integrity of the components in the event the surface foils should be compromised during service. It is also necessary that remedies to reduce corrosion (e.g., insulating coatings, matrix modification, processing conditions, etc.) do not degrade the mechanical properties of G/Al MMCs in such a way as to preclude their use.

The corrosion of G/Al MMCs has been studied extensively [Hihara, 1989; Dull, et al. 1977; Aylor, et al., 1984, 1985], and the galvanic effect in MMCs was modelled with the mixed-electrode theory [Hihara, 1989]. In the past, commercial G/Al MMCs studied were produced by a process known as diffusion-bonding. This process left behind trace microstructural chlorides, which increased the corrosion rate of the composite significantly [Hihara and Latanision, 1989, 1990, 1991]. Hihara [1989] determined that the anodic potentiodynamic behavior of diffusion-bonded commercial G/Al MMCs deviated significantly from that which was predicted by the mixed-electrode theory. The present study compares the anodic potentiodynamic behavior of several new commercial G/Al MMCs, produced without microstructural chlorides, in deaerated 0.5M Na_2SO_4 and 3.15 wt.% NaCl solutions.

Since the galvanic corrosion behavior of G/Al MMCs has been well established, it was decided that the problem of controlling corrosion should be addressed. Hihara [1989] considered cathodic protection, electronic insulation of fibers, and ion implantation of graphite with cathodic inhibitors as corrosion-control schemes for G/Al MMCs. This study will address electronic insulation of fibers and ion implantation of graphite with Zn as methods to reduce the corrosion rate of G/Al MMCs.

Previous work on G/Al MMCs suggested that the corrosion behavior of these composites may have been strongly related to the processing conditions employed during fabrication [Hihara, 1987, 1988b]. In order to derive the benefit of these advanced high specific strength materials, it is necessary to be able to control the parameters which govern the chemical stability of a material. It is well known that the formation of aluminum carbide (Al_4C_3) takes place when molten Al is in contact with graphite fibers [Amateau, 1976]. Subsequently, in the presence of an aqueous solution, hydrolysis of Al_4C_3 with methane evolution occurs. This reaction degrades the mechanical strength and structural integrity of G/Al MMCs by destroying the interface where Al_4C_3 forms. Therefore, the present work attempts to determine the relationship between Al_4C_3 content and the chemical stability of G/Al MMCs. In order to accomplish this, composites were produced with careful control and monitoring of processing conditions and tested in DC potentiodynamic polarization.

The development of a "self-protecting" composite was attempted. Zn of varying concentrations was alloyed with Al and used to fabricate commercial G/Al-Zn MMCs, which were subsequently tested for their electrochemical response.

2. LITERATURE SURVEY

2.1 THE ELECTROCHEMISTRY OF ALUMINUM

2.1.1 Introduction

The electrochemistry of Al has been extensively reviewed [Uhlig and Revie, 1985; Hihara, 1989]. It will be reviewed briefly so that the current text can be understood in its entirety.

Uhlig and Revie [1985] begin their discussion of Al with a description of the protective film which spontaneously forms in oxygen-containing environments. It is known that at very low pH values (~<4) and at very high pH values (~>8) the stability of this film breaks down, and underlying Al begins to corrode in the presence of an electrolyte.

Hihara [1989] gives a review of the nature of the protective film on Al. In his review, he points out that the film that forms on Al generally consists of two parts: 1) a thin inner amorphous 'barrier' film (~10Å) and 2) a thicker porous outer layer. It is possible to form only the barrier layer in specific non-aggressive environments, but the porous layer cannot be formed without the inner barrier film also being present [Keller and Edwards, 1948]. The inner barrier film was found to remain at the near steady state value of 10Å regardless of porous layer thickness. The barrier film was determined to be a function of applied voltage and temperature [Hass, 1949; Walkenhorst, 1947; Taylor and Edwards,1939]. Recently, Moshier, et al. [1987] determined that the barrier film has a composition which is most nearly a hydrated alumina. In films where alumina has been found to be soluble, duplex films will grow under anodic polarization [Keller et al., 1953].

The protective film that forms on Al can be alumina (Al_2O_3), böhmite ($Al_2O_3{\cdot}H_2O$), or hydrargillite, ($Al_2O_3{\cdot}3H_2O$) a more completely hydrated film. (In aqueous environments the alumina film will hydrate to hydrargrillite, the most thermodynamically stable form [Deltombe, et al., 1974]). The Pourbaix diagram for Al with a hydrated hydragrillite film is given in Appendix A.

The electrochemical reactions that take place on Al have been taken directly from Hihara's work [1989] and are shown below. The reaction potentials are given with reference to a saturated calomel reference electrode. All reactions in this text will be written in the reduction sense.

In acidic solutions, the Al dissolution reaction is

$$Al^{3+} + 3e^- = Al \qquad E° = -1.904\ V_{SCE} \qquad (2.1.1),$$

and in basic solutions, the overall dissolution reaction is

$$AlO_2^- + 4H^+ + 3e^- = Al + 2H_2O \qquad E° = -1.503\ V_{SCE} \qquad (2.1.2).$$

Films form on Al in acidic and basic solutions [Hihara, 1989; Moshier, et al., 1987], but their formation is an intermediate step in the overall dissolution process. In near neutral solutions, Al is passive and the reaction is

$$Al_2O_3 + 6H^+ + 6e^- = 2Al + 3H_2O \qquad (2.1.3).$$

$$E°_{hydrargillite} = -1.791\ V_{SCE}$$
$$E°_{böhmite} = -1.746\ V_{SCE}$$

At least one of the following cathodic reduction reactions must occur, in accordance with mixed potential theory. In deaerated media, the cathodic hydrogen reaction is

$$2H^+ + 2e^- = H_2 \qquad E° = -0.241\ V_{SCE} \qquad (2.1.4),$$

and in aerated media, the cathodic oxygen reduction reaction may occur as

$$O_2 + 4H^+ + 4e^- = 2H_2O \qquad E° = 0.988\ V_{SCE} \qquad (2.1.5).$$

In acidic media this can be written as

$$O_2 + 2H_2O + 4e^- = 4OH^- \qquad E°=0.160\ V_{SCE} \qquad (2.1.6).$$

It is important that the general features of active-passive behavior on an Evans diagram [1937] be introduced in order to aid subsequent discussion. Figure 2.1.1 shows the general behavior of an active-passive material [Jones, 1991]. Jones states that materials which have the ability to passivate (e.g., Al, Fe and Ni) at low potentials in deaerated acidic solutions will exhibit high anodic corrosion current densities which increase until the primary passive potential, Epp, is reached. At potentials above this, a passive film may form with a corresponding drop in current density. Since the drop may be as great as six orders of magnitude, the polarization behavior is plotted on a semi-log scale. At higher potentials, passive films will break down, and corrosion will greatly increase. For some alloys, this process is accompanied by oxygen evolution above the oxygen evolution potential.

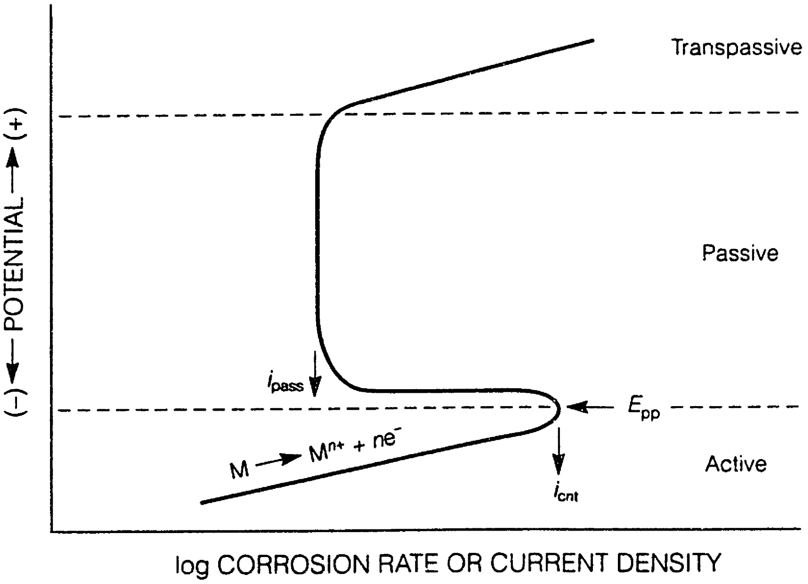

Figure 2.1.1: Schematic active-passive polarization.
[Jones, D.A., 1991, p.118]

Kloppers [1991], who studied the passivation of Fe-Cr alloys, summarized the importance of the cathodic reactions in relation to a material's ability to passivate. Figure 2.1.2 shows schematically the importance of the cathodic reaction for passivating materials in aqueous environments. He points out that in the absence of external oxidants, one of the aforementioned cathodic reactions must occur to raise the corrosion potential (Ecorr) of the material into the passive regime. Kloppers describes the three case scenarios shown in Figure 2.1.2. For case i, in deaerated solution, the cathodic hydrogen reaction takes the corrosion potential above the nose of the anodic polarization curve and directly into the passive regime. The cathodic current density, sustained on the surface of the material, is great enough in magnitude to sustain a current density greater than the critical passivation current density of the material. In aerated aqueous solutions, where cathodic reactions 2.1.5 and 2.1.6 may occur, the cathodic current density may be supplied by: the cathodic hydrogen reaction (case i), the cathodic oxygen reduction reaction (case ii) or the cathodic oxygen reduction reaction in the diffusion-limited regime (case iii). The cathodic hydrogen reaction may occur simultaneously with either the cathodic reduction reaction or the cathodic diffusion-limited oxygen reduction reaction. The pH, solution characteristics, temperature, partial pressure of a gas in the environment, and material will determine both the anodic and cathodic reaction rates.

Hihara [1989] studied the electrochemistry of high purity Al (99.999 wt.%Al) and 6061-T6 Al in near neutral pH aerated and deaerated 0.5M Na_2SO_4 and 3.15 wt.% NaCl solutions. Hihara found that the exchange current densities for both materials are at least four orders of magnitude greater in the NaCl solution as compared with the same material in the Na_2SO_4 solution.

Figure 2.1.3 shows that high purity Al was able to passivate in aggressive deaerated and aerated NaCl solutions. The critical pitting potential (Ecrit) was determined to be -0.750 and -0.725 V_{SCE} in deaerated and aerated NaCl solutions, respectively.

Figure 2.1.4 shows that 6061-T6 Al passivates in aerated and deaerated 0.5M Na_2SO_4 solutions during anodic polarization in virtually the same manner as that of high purity Al (see Figure 2.1.3). In 3.15 wt.% NaCl solution, however, 6061-T6 Al pits spontaneously at -0.650 V_{SCE} in aerated solutions. In deaerated 3.15 wt.% NaCl solution, Ecrit is -0.725 V_{SCE}. Hihara attributes the spontaneous pitting of 6061-T6 Al in aerated NaCl solutions to the abundance of intermetallics (Mg_2Si and Fe_3Al_{12}) and 'un-filmed' Al spots produced from the interaction of the film with chloride ions. Once pitting initiates, oxygen reduction and additional hydrogen evolution within newly formed pits will occur [Wood, et al., 1974; Hubner and Wranglin, 1964].

It is also clear from Figure 2.1.4 that the oxygen reduction overpotential was large enough to polarize the 6061-T6 Al so that it pitted spontaneously in aerated 3.15 wt.% NaCl solution.

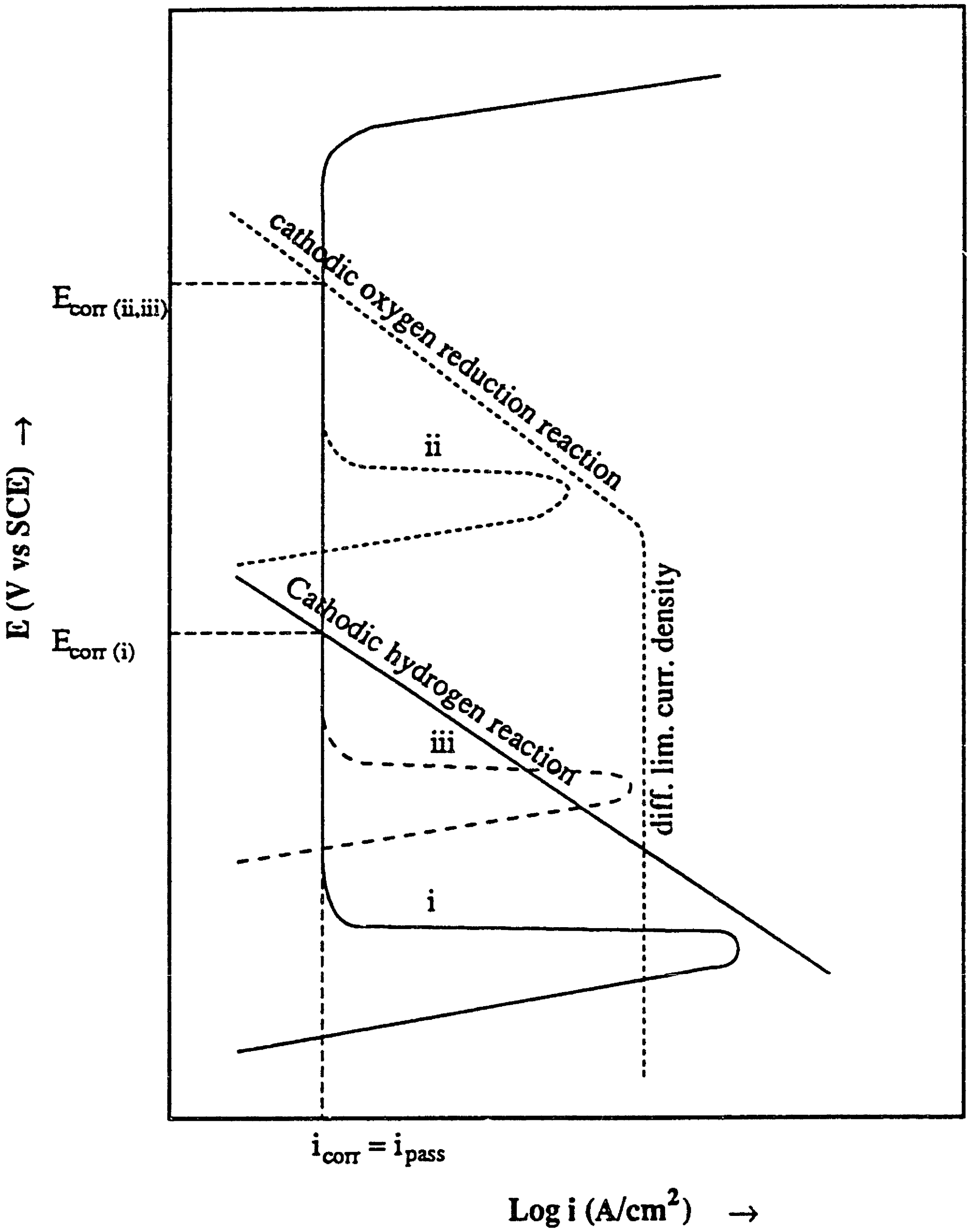

Figure 2.1.2: Schematic showing: a) hydrogen, b) non-diffusion-limited, and 3) the cathodic diffusion-limited oxygen reduction reactions.
[Kloppers, M.J., 1991, p.39]

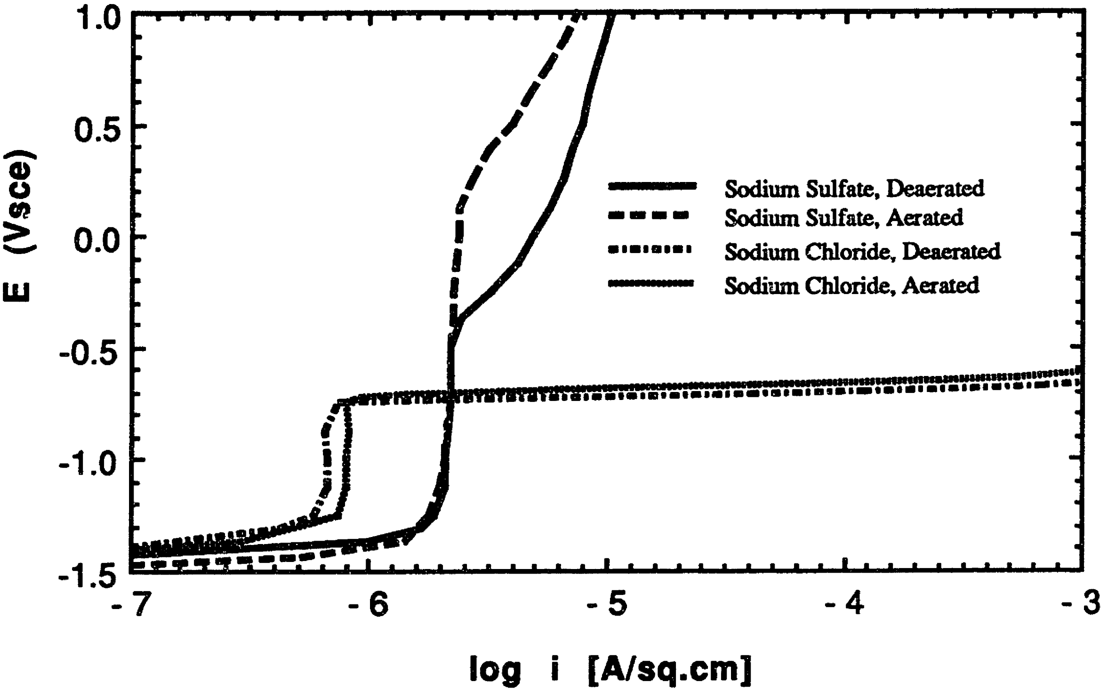

Figure 2.1.3: Anodic polarization diagrams of ultra pure Al (99.999 wt.%) in 0.5M Na_2SO_4 and 3.15 wt.% sodium chloride solutions of pH 7 at 30°C. Scan rate = 0.1 mV/s. [Hihara, 1989, p.61]

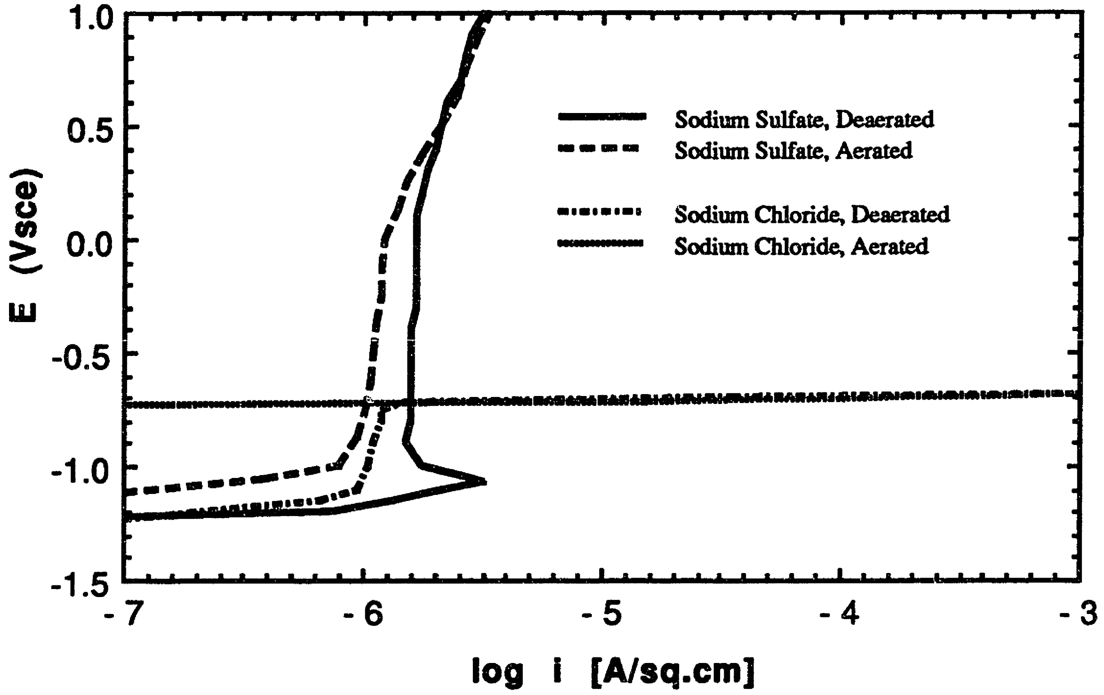

Figure 2.1.4: Anodic polarization diagrams of 6061-T6 Al in 0.5 M Na_2SO_4 and 3.15 wt.% NaCl solutions of pH 7 at 30°C. Scan rate = 0.1 mV/s. [Hihara, 1989, p.67]

2.2 ELECTROCHEMISTRY OF GRAPHITE

2.2.1 Introduction

The basic development of carbon fiber has progressed from cellulose-based threads and rayon fibers to technologically useful polyacrylonitrile (PAN) and pitch-based graphite fibers. Production of graphite fibers, in most cases, requires extrusion of an organic precursor (e.g., benzene or PAN) into a polymeric fiber, followed by heat treatment (stabilization), subsequent carbonization (heat treatment above ~1000°C) and then further heat treatment up to ~3000°C (graphitization) in an inert atmosphere [Dresselhaus et al., 1988].

Graphite fibers derive their high specific strength from the covalent C-C bond alignment of the graphite basal planes along the fibers' longitudinal axis. The two-dimensional planar arrays of carbon atoms are sometimes referred to as 'graphene' planes. A stack of graphene planes is referred to as a 'ribbon.' While PAN-based fibers often have a circumferential arrangement of ribbons in the sheath region and a random core, pitch-based fibers often show a radial arrangement of aligned graphite fiber ribbons and sometimes display a "PAC-man" section (see Figure 2.2.1). There are other orientations that the graphene planes can take, since orientation is primarily controlled by the spinning nozzle used during fiber processing. Today, commercially available graphite fibers have an approximate diameter of 6 to 12 μm.

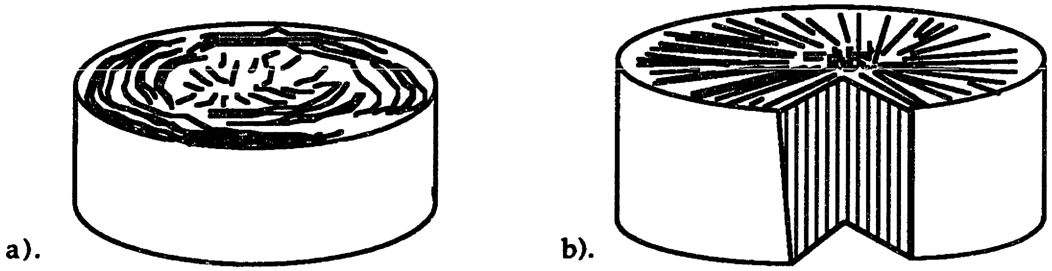

Figure 2.2.1: Illustration of observed polymer fiber cross-sectional macroscopic morphology: a) partially graphitic PAN-based fibers, with a circumferential arrangement of ribbons in the sheath region, and random in the core; b) pitch-based (mesophase pitch), "PAC-man" section showing a radial arrangement of the ribbons. [Dresselhaus et al., 1988, p.4]

Hihara [1989] reviewed the three possible electrochemical processes associated with graphite in an electrolytic solution. In his review, he points out that graphite can: 1) act as an inert electrode, 2) be consumed in the electrochemical reaction to form compounds of carbon, and 3) be intercalated with ions to form carbon compounds. The specific cathodic and anodic behavior of graphite will be discussed in the following sections.

2.2.2 Cathodic Behavior of Graphite Fibers

Hihara's work [1989] confirmed that during cathodic polarization of pitch-based graphite fiber, no appreciable methane could be detected in Na_2SO_4 and NaCl solutions. The major reaction in similar aerated solutions was oxygen reduction (see Figure 2.2.2). If the solution were sufficiently deaerated, hydrogen evolution was the major cathodic reaction. However, as shown in Figure 2.2.2, some oxygen reduction still occurred in deaerated solutions. Hihara attributes this to a small amount of oxygen still present in the solution. He determined that only 3.0 ppb of oxygen can result in an oxygen diffusion-limited current density of 0.5 $\mu A/cm^2$. Since the hydrogen used to purge the solution contained up to but not more than 5 ppm oxygen, this behavior seems plausible for the deaerated case.

Graphite fibers were determined to be inert during cathodic polarization. It was found that the electrochemical nature of the fibers was altered by cathodic polarization. Subsequent anodic polarization of previously cathodically polarized fibers showed a marked difference when compared to anodic polarization of 'virgin' graphite fibers (see Figure 2.2.3). This was attributed to some form of intercalation of cations in graphite fibers which were released during the early stages of subsequent anodic polarization. The specific intercalated ions have not been identified. Kinoshita [1988] reviews the specific ions that have been successfully intercalated in graphite.

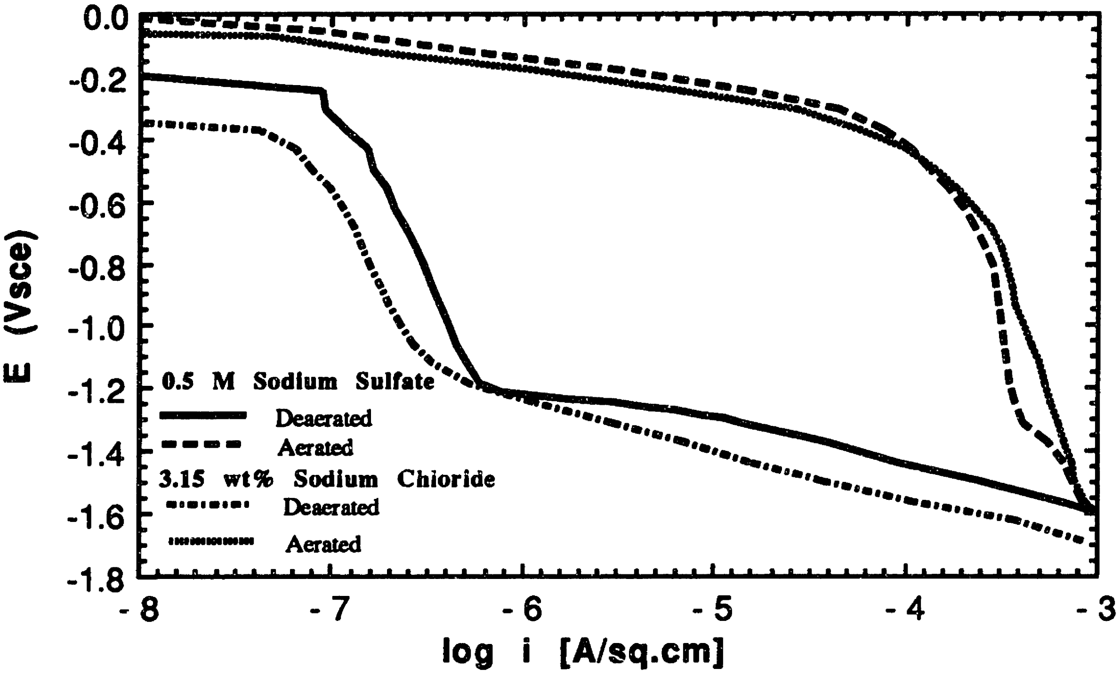

Figure 2.2.2: Comparison of cathodic polarization diagrams of pitch-based (P100) graphite fibers in various neutral solutions at 30°C. Scan rate = 0.1 mV/s.
[Hihara, 1989, p.90]

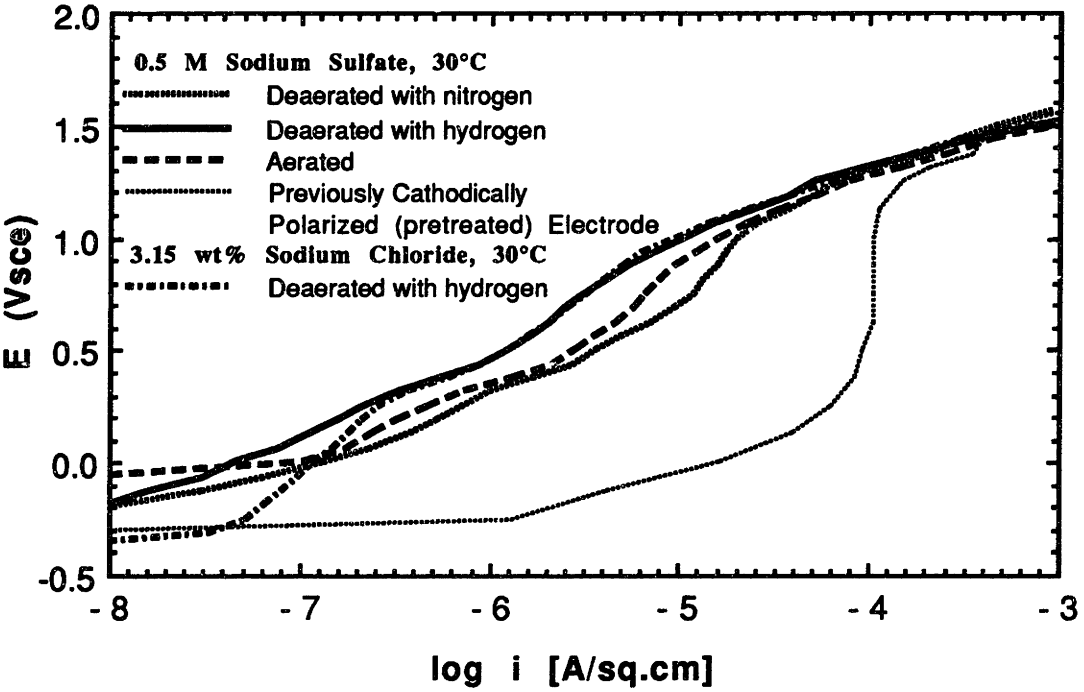

Figure 2.2.3: Comparison of anodic polarization diagrams of pitch-based (P100) graphite fiber electrodes in various neutral solutions at 30°C. A previously cathodically polarized graphite fiber electrode was held galvanostatically at 0.255 A/cm^2 for 4 hrs. in neutral 0.5M Na_2SO_4 at 30°C, followed by baking at 75°C for 12 hrs.
[Hihara, 1989, p.92]

2.2.3 Anodic Behavior of Graphite Fibers

Hihara [1989] determined that pitch-based graphite fibers were partially consumed during anodic polarization. Some researchers have determined that various carbon compounds may form during graphite oxidation [Van Muylder and Pourbaix, 1974]. However, Hihara [1989], Kinoshita [1988], Kokhanov and Milova [1969] have established that the formation of CO_2 and CO are the dominant reactions. The formation of CO_2 was found to be the primary reaction resulting in the consumption and, hence, the degradation of the graphite fibers. The equilibrium reactions [Hihara, 1989] are

$$CO_2 + 4H^+ + 4e^- = C + 2H_2O, \qquad E^\circ = -0.034\ V_{SCE} \qquad (2.2.1)$$

and

$$CO + 2H^+ + 2e^- = C + H_2O, \qquad E^\circ = 0.277\ V_{SCE} \qquad (2.2.2).$$

CO, being thermodynamically unstable with respect to CO_2, reacts to form CO_2 based on the equilibrium reaction

$$CO_2 + 2H^+ + 2e^- = CO + H_2O, \qquad E^\circ = -0.344\ V_{SCE} \qquad (2.2.3).$$

Evolution of oxygen and chlorine gas on graphite fibers in Na_2SO_4 and NaCl solutions were ruled out by Hihara [1989]. Figure 2.2.3, shows that at potentials which approach and exceed the oxygen evolution potential (0.556 SCE, @ pH = ~7), there were no abrupt changes in the anodic polarization curves. Therefore oxygen evolution was deemed insignificant compared to CO_2 production. Chlorine evolution was also ruled out, since there was little difference in the anodic behavior of graphite fibers in NaCl solutions as compared to Na_2SO_4 solutions (see Figure 2.2.3). The latter finding was in agreement with the results of Kokhanov and Milova [1969].

2.2.4 Oxide Formation on Graphite

In 1928, Brown and Storey determined that a film of non-conducting oxide can form on graphite in acidic or neutral electrolytes with oxygen-containing anions such as H_2SO_4, HNO_3, and $NaClO_3$. The stoichiometry of the oxide is still unknown. Thirty-three years later, Ksenzhek and Chaikovskaya [1962] examined the anodic oxidation of graphite in 1N H_2SO_4 and found that, during anodic galvanostatic polarization, the potential versus time curve showed a maximum. They concluded that the rise in potential was a result of the gradual oxidation of the graphite surface. They attributed the activation energy needed to form the oxide at 20°C to have been supplied by electrical energy with a potential maximum at the boundary between unformed and completely formed surface oxide. The surface oxide layer was believed to be an adsorbed layer formed by the partial ionization of oxygen. Hihara [1989] performed similar studies with pitch-based graphite fibers in near neutral deaerated 0.5M Na_2SO_4 solution, and observed a similar maximum at the onset of his tests. He also observed that the fibers formed a 'cavern' or 'split' during anodic polarization on the exposed transverse cross-sectional surfaces of the fibers. Hihara modelled the potential behavior as a function of time for a graphite fiber anodically polarized in solution, taking into account the growth of a nonconductive oxide film and simultaneous cavern formation.

2.3 GALVANIC COUPLING OF GRAPHITE AND ALUMINUM

When two electrochemically dissimilar conductive materials such as graphite and Al are connected while being immersed in solution, a galvanic cell will form. The anode (Al) will be seen to corrode at a higher rate than the uncoupled material in the same condition. Galvanic corrosion has been explained by the mixed electrode theory. In this theory, the sum of cathodic and anodic currents are equal and opposite in magnitude. For monolithic materials that are not clearly anodic or cathodic, local anodic and cathodic sites form on the surface of the material. As mentioned before, intermetallics can act as sites for facilitating cathodic reduction on the surface of monolithic Al in the absence of graphite fibers.

Hihara [1989] has considered galvanic coupling of graphite and Al as well as coupling of Al with other noble materials such as SiC and TiB_2 in aerated and deaerated neutral Na_2SO_4 and NaCl solutions. The rate of oxygen reduction was highest on graphite fiber-Al couples [Hihara, 1989]. SiC/Al and TiB_2/Al galvanic couples had much lower corrosion rates than G/Al MMCs (e.g., 1/30th the corrosion rate of G/Al couple in aerated 3.15 wt.% NaCl solution).

Hihara [1989] found that for aerated 3.15 wt.% NaCl solutions, DC polarization diagrams predicted that galvanic corrosion would be controlled by the diffusion-limited oxygen reduction reaction occurring at noble constituents (see Figure 2.3.1). Current is relatively independent of potential in the region of transport control of oxygen. Hihara's polarization results suggest that in the aerated solutions there was little advantage to be gained over using high purity Al as compared with 6061-T6 Al (see Figure 2.3.1) as a matrix constituent in G/Al MMCs.

Results from zero resistance ammeter (ZRA) tests on electrodes of equal cross-sectional area of pitched-based graphite fiber and 6061-T6 Al couples were in excellent agreement with galvanic currents measured from the intersection of anodic and cathodic polarization curves [Hihara, 1989]. His polarization diagrams predicted that galvanic corrosion would be controlled by Al passivation in aerated Na_2SO_4 solution, but at higher currents than predicted from ZRA galvanic tests for the same solution. He attributed this to edge effects on his sample.

Interestingly, Hihara [1989] was able to manipulate separate anodic and cathodic polarization results based on the mixed-electrode theory to derive an expression for the galvanic current (anodic current) as a function of noble constituent volume fraction (X_N) and noble cathodic current (i_N) as shown below:

$$i_{galv} = i_N \cdot (X_N/1-X_N) \qquad (2.3.1).$$

From the intersection of cathodic (graphite) and anodic (Al) current in Figure 2.3.1, he was able to determine the value of the cathodic current (i_{galv}). From expression (2.3.1), he was able to determine that only a small fraction of graphite (vol.% fiber = 1.0) could be added before the corrosion rate exceeded the uncoupled corrosion rate for monolithic 6061-T6 Al. Graphite fiber coupled to an equal amount of 6061-T6 Al was predicted to have a corrosion rate of about 80 times the uncoupled corrosion rate of monolithic 6061-T6 Al.

Turnbull [1990] has reviewed the galvanic effects that may occur in MMCs. He considers reports in the literature by Trzaskoma [1983, 1986, 1990], and Aylor and Moran [1985] which draw conclusions based upon long term measurements of the corrosion potential.

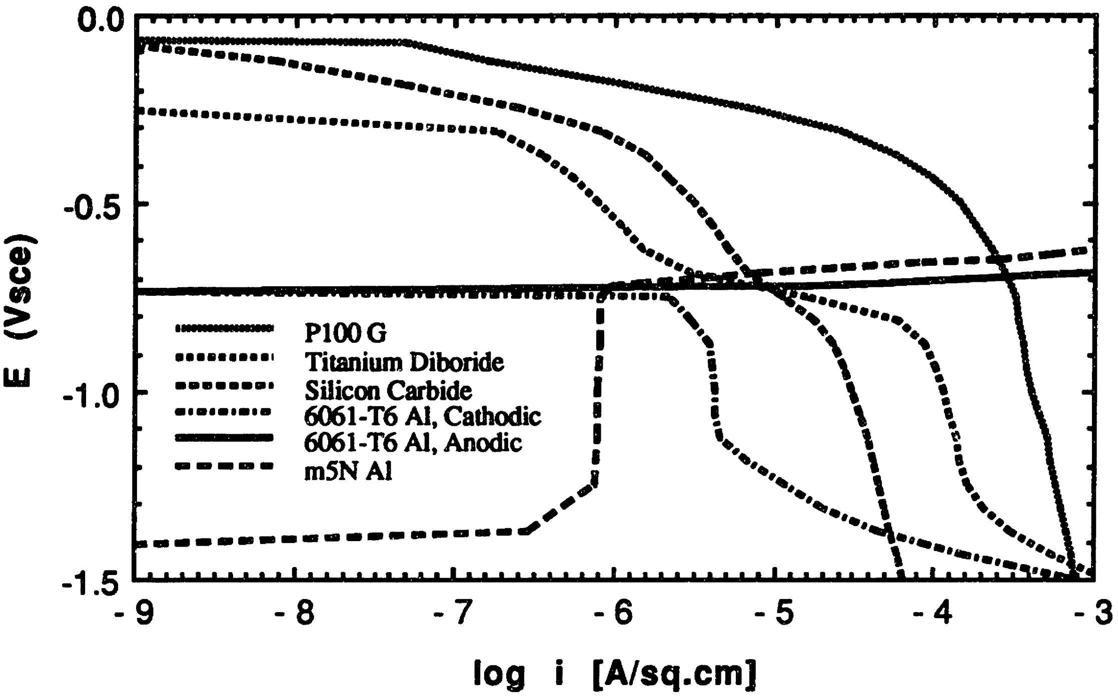

Figure 2.3.1: Polarization diagrams generated in aerated 3.15 wt.% NaCl of pH 7 at 30°C. Galvanic corrosion rates can be predicted with these diagrams using the mixed electrode theory. Intersection of anodic and cathodic curves gives predicted corrosion rates of couples with a 0.5 area fraction.
[Hihara, 1989, p.180]

As time proceeds, the area fraction of noble constituent has been shown to increase in SiC/Al MMCs immersed in NaCl solution [Trzaskoma, 1990], which is followed by an increase in the corrosion current. Turnbull [1990] suggests that as many pits initiate, there will be an increased activity of the surface which will act to decrease the corrosion potential. If the corrosion potential becomes increasingly negative the electrochemical driving force for dissolution will be decreased.

2.4 MATRIX PRECIPITATES IN MMCs AND CORROSION PHENOMENA

The role that matrix alloy precipitates play in facilitating cathodic reaction processes has already been mentioned. Hihara [1989] points to Pryor and Keir [1955] who have shown that Cu will deposit on ultra pure Al in localized regions providing preferred cathodic sites, as opposed to Cu uniformly plating on Cu, Fe, Sn, Pb, and Zn under similar conditions. Hihara [1989] has summarized the electrochemical potential of precipitates; the results are shown in Table 2.4.1.

Table 2.4.1: Electrochemical Potential of Al Intermetallics

Precipitate	Solution	E (V_{SCE})
Al_3Mn	3% NaCl	-0.44 to -0.90
Al_3Fe		-0.39 to -0.59
Al_3Ni		-0.72
Al_2Cu		-0.61
Mg_2Si		-1.52
		-0.67 after 25 hrs.

[Akimow and Oleschko, 1934, p.134]

With regard to precipitates, it is well known that their presence acts to increase corrosion by allowing additional cathodic oxygen reduction to occur by either destroying the protective alumina film (see Section 2.1) and/or actually acting as sites for oxygen reduction and subsequent pit formation in chloride-containing environments. For instance, Mg_2Si and $(Fe,Cr)_3SiAl_{12}$ intermetallics are present in 6061 Al.

These intermetallics have often been found to surround graphite fibers (see Figure 2.4.1) after solidification through solute rejection, which occurs if a MMC has been processed by pressure infiltration or by squeeze casting [Mortensen, 1986]. Trzaskoma [1991] has found that for SiC/Al MMCs the intermetallic precipitates tended to be ubiquitous and of a smaller size. This accounted for facilitated pit formation, as intermetallics were cited as the primary location for incipient pit formation. SiC/Al MMC pits were more shallow compared to the monolithic Al matrix in the same heat-treated condition and electrolytic solution. She indicated that the morphology of the pits varied from smooth in SiC/Al MMCs to (100) faceted pits in the monolithic Al alloys studied (i.e., 6061, 2024, and 5456 Al). Trzaskoma [1991] also compared the amount of corrosion due to galvanic corrosion with weight-loss measurements. For tungsten-reinforced depleted uranium MMC in 3.5 wt.% NaCl solution, corrosion rates determined by weight-loss measurements were nearly the same as those determined by separate galvanic coupling between the reinforcement and matrix.

Figure 2.4.1: Secondary electron SEM micrograph of graphite fiber in 6061 Al matrix. Note the Mg_2Si "script-like" eutectic intermetallic surrounding fiber and extending into matrix. Composite was produced by D.W.A. Composite Specialties Inc., Chatsworth, CA.

Galvanic corrosion was therefore the principal mechanism of corrosion for the composite. However, for TiB_2-coated graphite fibers within a matrix of Mg, only 10% of the corrosion in immersion tests could be attributed to galvanic coupling of graphite fibers to the Mg matrix. Trzaskoma attributed the remaining corrosion to additional cathodic reactions occurring on intermetallics in the Mg matrix.

Thus, matrix precipitates play an integral role in oxygen reduction, and, the amount of oxygen reduction occurring on precipitates can out-weigh the amount of corrosion that is attributable to the galvanic corrosion between the reinforcement and the matrix.

As a minor point, Hihara and Latanision [1990] have found that TiB_2-coated specimens often have residual microstructural chlorides left behind from the reactant $TiCl_4$ and BCl_3 gases used in diffusion bonding processing; these chlorides result in increased corrosion by creating crevices. This was not mentioned as having played a role in the results that Trzaskoma found for G/Mg MMCs; the fibers used in her study were TiB_2-coated. Residual microstructural chlorides have been shown to cause a significant deviation from the corrosion behavior predicted by mixed-electrode theory [Hihara, 1989].

Careful consideration should therefore be given to other corrosion mechanisms which may be responsible for corrosion rates higher than those measured in galvanic ZRA testing.

2.5 INTERFACIAL PHENOMENA IN G/AL MMCs

2.5.1 Introduction

It is well known that the interface between fiber and matrix plays a critical role in the behavior of MMCs. Many researchers have concentrated on the role of the interface and the resulting physical and mechanical properties from alteration of the interface. Still, there are many parameters relating to the nature of interfacial bonding that have not been resolved. Interfacial reactions in MMCs and bonding are affected by: processing conditions, the nature of the reinforcement phase, and chemical additions to the matrix alloy. This section will review the parameters which will later be examined in this study, namely: the effects on the interface as a result of compositional differences in the matrix alloy, the infiltration processing conditions which give rise to Al_4C_3 formation, quantification of Al_4C_3 content and any results which shed light on the chemical stability of G/Al MMCs as related to the interface. Finally, some mention must be made of changes in mechanical properties as a response to modifications of the interface.

2.5.2 Physico-Chemical Properties of the Interface in G/Al MMCs

Simensen [1989] has compared his results with antecedent research on the solubility of carbon in Al and confirmed that at temperatures as high as 1000°C, only ~50 ppm of carbon are dissolved in Al, and furthermore, at 950°C the concentration of dissolved carbon was only 5 ppm. At temperatures used in the processing of G/Al MMCs, it is expected that little carbon is dissolved in Al, and that the predominant reaction is the formation of stoichiometric Al_4C_3 by the reaction:

$$4Al(l) + 3C(s) \rightarrow Al_4C_3(s) \qquad (2.5.1).$$

Al_4C_3 has a theoretical density of 2.36 gm/cm^3, lattice parameters of a = 3.33 nm and c = 2.499 nm, and a melting point of 2704°C [Iseki et al., 1983]. In the presence of an aqueous solution, hydrolysis of Al_4C_3 with methane evolution occurs by the following reaction:

$$Al_4C_3(s) + 12H_2O(l) \rightarrow 3CH_4(g) + 4Al(OH)_3(s) \qquad (2.5.2).$$

The latter reaction will degrade the mechanical strength and structural integrity of a G/Al MMC by destroying the interface where Al_4C_3 forms. Subsequent hydrolyzation will develop fissures in sites where Al_4C_3 had once existed. Continual Al_4C_3 hydrolysis along the interface of the fiber or crevice corrosion may form a pipeline for an electrolytic solution, which will destroy the interface between graphite and Al.

Hihara [1989] studied the hydrolysis of Al_4C_3 by taking commercially available stoichiometric hot-pressed Al_4C_3 and immersing it in pure water. Thereafter, the volume of water displaced due to evolved methane was measured. The hot-pressed Al_4C_3 hydrolyzed at a rate of 1 vol.%/hour. Therefore, Al_4C_3 hydrolysis will present a problem in the presence of an aqueous environment, and consequently, Al_4C_3 formation should be minimized to maintain the mechanical strength and chemical stability of the interface. Mortensen [1986] provides an assortment of micrographs displaying Al_4C_3 platelets at the interface of a continuous fiber SiC/Al MMC, and has unequivocally identified the Auger Al and C energy transitions associated with Al_4C_3.

2.5.3 The Effect of Alloying Elements at the Fiber-Matrix Interface

Mortensen [1991, 1992a] has reviewed the infiltration process and requirements for complete wetting. It is well known that molten Al does not wet graphite well; moreover, alloy additions to the Al matrix in MMCs often improve wetting by increasing the reactivity between the molten Al and the substrate and by modifying the oxide layer on the surface of the molten Al (e.g., Mg in Al for most reinforcements and Li in Al for alumina fibers). Modification is not limited to alloy additions to the matrix, as metallic and oxide fiber-coatings act to alter the oxide layer in much the same way.

As described in Section 2.4, TiB_2 coatings have been used to decrease the wetting angle between graphite and Al. Hihara and Latanision [1990] have found that residual chlorides left behind by process gases have resulted in increased corrosion rates between fibers and at the location of diffusion-bonded tows. Recently, Wu [1988] has suggested that chlorides may in fact be the main chemical at the interface that results in the wetting improvement between graphite and Al for TiB_2-coated fibers. He points out that other researchers have found that the wetting angle between TiB_2 and molten Al was greater than 90° [Rkee, 1970]. Wu noted the strong signal for chloride found by ion analysis, and side-by-side wetting angle determination was approximately 35°. When no chloride was found the wetting angle was greater than 90°.

Xiu-Qin and Geng-Xiang [1988] performed TEM studies on G/Al MMCs which contained a higher concentration of Cu (~4 wt.%), which resulted in the formation of lump-shaped interfacial $CuAl_2$ as well as rod-like Al_4C_3 at the G/Al interface. The tensile strength of the MMC with the Cu-enriched Al matrix was disproportionately weaker than MMCs with little or no $CuAl_2$ found at the interface. The interfacial bond between the matrix and the fiber was found to be too strong for the G/Al MMC with 4 wt.% Cu. This phenomenon was also observed for G/5056 Al MMCs [Motoki and Okura, 1982] which contain Mg as an alloy addition; however, no TEM studies were performed on the interfacial products of these composites.

Wu [1988] determined that additions of Ti to the Al matrix in G/Al MMCs provided the maximum increase in tensile strength and impact toughness compared to similar composites with varying copper contents and other alloy variations. He attributes this to the free energy of formation of TiC (-41 kcal/mole @ 727°C) as compared to that for Al_4C_3 (-12 kcal/mole). The TiC preferentially forms at the G/Al interface and prevents subsequent Al_4C_3 formation. Cornie, et al. [1990] have noted the grain refinement (~1 μm diameter grains) in the G/Al-0.34 wt.% Ti MMC system that occurred due to both the presence of fibers and the addition of Ti.

Cornie, et al. [1990] have shown that additions of ~7 wt.% Si successfully decrease the solubility of carbon in Al by decreasing the activity of Al and allowed for lower infiltration temperatures to be used, decreasing Al_4C_3 formation. However, the resultant strength of their composites was relatively poor due to embrittlement of Si rich intermetallic phases at the interface. Other researchers [Chernysyshova and Kobeleva, 1985; Portnoi, et al., 1981; Towata, et al., 1985; Wu, 1988; Li, et al., 1985; Kohara and Muto, 1985] have outlined similar effects for Mg, Ca, Ti and Si additions to G/Al MMCs.

2.5.4 The Effect of Processing Parameters on Al_4C_3 Content

Chernysyshova and Kobeleva [1985] have studied the effect of processing of a carbon fiber tape/Al-12 wt.% Si MMC and determined the effect of pressure and temperature on the Al_4C_3 content. Increasing processing temperature had the greatest effect on the carbide content, while increasing processing pressure also caused significant increases in Al_4C_3 content when applied at higher temperature. They argue that higher pressures increase contact between the melt and fiber. They also found a maximum in tensile strength at an intermediate carbide content level (13.8 mg Al_4C_3/gm graphite fiber), while the shear strength of the MMCs they studied increased with increasing carbide content. Li et al. [1985] and Wu [1988] obtained similar results for Al_4C_3 content when varying pressure and temperature. Wu found that a slight increase in tensile strength occurred at the onset of Al_4C_3 formation but a rapid degradation of tensile strength occurred after treating the composites thermally at ~500°C.

2.5.5 Fiber Type

Different types of carbon and graphite fiber exhibit differences in reactivity with molten Al. In carbon fibers the orientation of the graphene planes is random and therefore these fibers are only partially graphitic.

Many researchers [Amateau, 1976; Kohara and Muto, 1985] find that in general, fully graphitized PAN-based fibers have a higher reactivity than pitch-based graphite fibers in molten Al. High modulus (HM) PAN-based graphite fibers are degraded less by molten Al than the high-strength (HS) PAN-based graphite fibers [Baker and Bonfield, 1978]. These differences have been attributed to the orientation of the graphite basal planes at the surface of the fiber. The basal planes have a much lower surface energy per unit area (0.14 J/m^2) than do the perpendicular covalently-bonded carbon planes (14 to 55 J/m^2).

Baker and Bonfield [1978] have determined that for HM and HS graphite fibers ultimate tensile strength (UTS) degradation occurred above 550°C and 475°C, respectively. The specific surface energies, determined by assuming the Griffiths theory for brittle fracture was applicable, for HM and HS PAN-based graphite fiber were 0.7 J/m^2 and 2.33 J/m^2, respectively. Therefore, the type of fiber used will also play a role in the amount of carbide formed at the interface due to its reactivity with the melt. HM pitch-based fibers should be less-prone to carbide formation, as compared to HS pitch-based fibers.

Wu [1988] has determined that partially graphitized fibers, or carbon fibers, have a decreased tendency to form Al_4C_3. Also, the hygrothermal nature of carbon and graphite revealed that after thermal exposure, the water absorption of graphite fibers in an Al matrix was almost an order of magnitude greater than absorption of carbon fibers in a similar matrix. The difference was attributed to the amount of Al_4C_3 available to react with water after thermal treatment.

2.6 CORROSION OF G/Al MMCs

2.6.1 History

Evans and Braddick [1971] found that continuous fiber Al-foil covered G/Al MMC suffered from subcutaneous corrosion in oxygen saturated 3 wt.% NaCl. The corrosion was believed to have progressed below the surface because of the longitudinal nature of the conductive fibers. They also commented that chopped graphite fiber/Al MMC should suffer less than the equivalent continuous graphite fiber MMC in similar weight-loss tests. This was later confirmed by Saxena, et al. [1987].

Dull, et al. [1977] studied the effect of matrix and fiber composition on the mechanical strength and corrosion behavior of G/Al MMCs. In their experiments, they examined the effects of various Al matrix compositions given in Table 2.6.1. When comparing 5154 and 6061 Al under cathodic polarization, they found that Al film formation occurred for both alloys in 3.5 wt.% NaCl deaerated solutions.

Table 2.6.1: Chemical Composition of Matrix Al Alloys by wt.%

Alloy	Mg	Si	Cr	Mn	Cu
2024	1.2-1.8	0.50 max	0.0 max	0.3-0.9	3.8-4.9
5052	2.2-2.8	0.25 max	0.15-0.35		
5154	3.1-3.9	0.20 max	0.15-0.35		
5456	4.7-5.5	0.25 max	0.05-0.20	0.5-1.0	
6061	0.8-1.2	0.4-0.8	0.15-0.35		0.15-0.40

[Dull, et al., 1977, p.5]

The film formation during cathodic polarization acted to reduce the amount of hydrogen that could be evolved. In similar graphite fiber/Al composites, with Ti + B additions, no such films formed, and hydrogen evolved readily. In oxygenated environments, G/5154 and 6061 Al (Ti +B) MMCs corroded with similar diffusion-limited current density's of 40 μA/cm^2 during cathodic polarization It was noted that as time progressed, a film formed on the Al for the 5154 MMC, while no film formed for the G/6061 Al MMC (i.e, the diffusion-limited current density remained constant).

Anodic polarization of the same composites showed that the composites had higher passive current densities as compared to their monolithic matrix alloy in deaerated 3.5 wt.% NaCl solution (see Table 2.6.2).

Table 2.6.2: Pitting Potential and Onset of Pitting Current Density of 6061 and 5154 Alloys and Composites in Deaerated 3.5 wt.% NaCl Solution

Alloy	Pitting Potential mVsce	Onset Pitting Current (μA/cm^2)
6061	-712	1.3
5154	-744	0.87
Composite		
T50/6061	-753	1.4
T50/5154	-726	20

[Dull, et al., 1977, p.5]

Dull, et al. [1977] also studied the effect of oxygen partial pressure. They found that corrosion rates increased with P_{O_2}. Interestingly, the addition of Ti and B did not affect the corrosion rates of similar composites that did not have these additions. They found that hydrogen evolution that took place in deaerated solution on G/5154 Al (Ti + B) MMCs was highest when pitch-based graphite-fibers were used. However, in aerated solutions the type of fiber used in the MMC was not as significant.

Czyrklis [1985] concluded that G/Al 6061 MMCs had a greater corrosion rate than its monolithic alloy. He also found that a shift in the corrosion potential for G/Al 6061 MMCs in the noble (more positive) direction as compared to the corrosion potential of monolithic alloy MMC gave evidence that galvanic action between fibers and matrix had occurred. It was also noted that Mg_2Si in G/Al 6061 MMCs showed little or no effect on the corrosion behavior of the composite. The predominant mode of corrosion was found to be pitting parallel to the fiber direction. Exposure to a chloride-containing solution severely compromised the fracture strength of the G/6061 Al MMCs studied.

Bhagat, et al. [1989] studied high pressure squeeze casting of G/Al MMCs. They produced composites that were essentially free from porosity and gas defects which result from low pressure squeeze casting. The high rate of cooling resulted in less interfacial Al_4C_3. However, the amount of Al_4C_3 was not quantified. They produced composites with vol.% graphite fiber varying from 5 to 55%, and studied them in tensile, fatigue, damping and corrosion tests. Their results in aerated 3.5 wt.% NaCl solution maintained at pH = 6.6 are summarized as follows: 1) at a fixed voltage, the mass loss of the composites was, in general, proportional to the time of corrosion, 2) the mass loss increased with increasing volume fraction of graphite fiber, 3) the corrosion rate was greater for composites produced without prior coating of graphite with Ni, and 4) increased temperature caused a concomitant increase in corrosion rate for all composites studied. They also determined that the Ni coating stayed in place during high pressure infiltration, and hence, no Al_4C_3 was able to form. They found that no galvanic coupling between graphite fiber and active Al took place for the Ni-coated fibers.

Coleman, et al. [1990] suggest that the corrosion of MMCs with noble constituents which were poor conductors (e.g., alumina and SiC fibers) was primarily due to increased reactions occurring at intermetallic phases in the matrix. They found that for continuous fiber G/Al MMCs, corrosion occurs at the interface, since graphite fibers are good conductors. However, they could not determine whether or not Al_4C_3 played a role in the corrosion observed at the interface. After monitoring open circuit potentials for Saffil alumina fiber and SiC reinforced composites in deaerated 3.5 wt.% NaCl, they found the composites stabilized at their pitting potential (Ecrit) and after prolonged time re-stabilized at their protection potential (Eprot). A schematic showing the location of these values in an open circuit potential test is shown in Figure 2.6.1. Ecrit values determined by open circuit measurements (Figure 2.6.1) were compared with those determined by polarization testing; they were within 20 mV_{SCE} of each other.

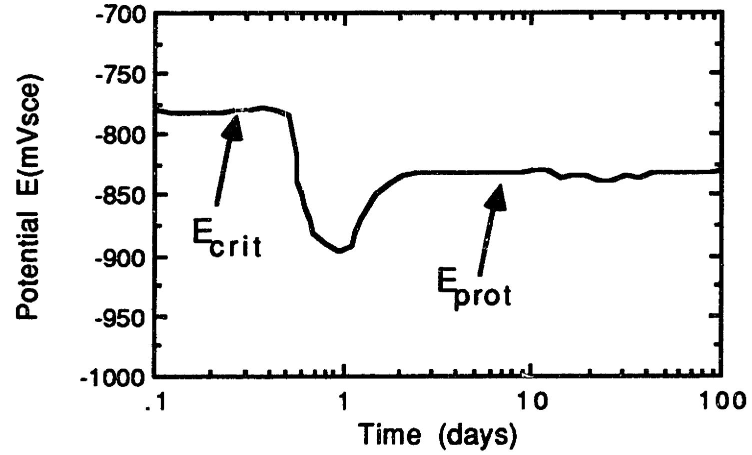

Figure 2.6.1: Open circuit potential curve; Saffil alumina fiber reinforced Al-7 Si [Coleman, et al., 1990, p.292]

Friend, et al. [1990] studied the corrosion behavior of G/1100 Al MMCs in aerated and deaerated 3 wt.% NaCl solutions. They found that the MMC with HM fiber exhibited the best corrosion resistance. HS fiber G/Al MMC showed the highest corrosion rate. These findings were confirmed by low frequency AC impedance and cyclic polarization tests. Unfortunately, neither an explanation for this behavior nor any experimental statistics were offered.

Faciej and Agarwala [1988] studied the influence of processing variables on the corrosion susceptibility of particulate SiC/Al MMCs. Although these composites are not of direct interest to this study, their results can be extended to G/Al MMCs. For instance, they were able to determine that there was a significant deviation in corrosion resistance due to the solution treatment and aging conditions employed on their material. In fact, solution heat treatment of the as-processed MMCs caused an increase in the void content which was responsible for a decrease in corrosion resistance (exfoliation and general corrosion). Differential expansion and contraction of SiC particulates from heat treating and water quenching resulted in an increase in the local dislocation density near the SiC-matrix interface. Due to the increase in the prismatic loop dislocation density [Taya and Mori 1987; Li, et al., 1989; Kim, et al., 1990; Dunand and Mortensen, 1991] surrounding particulates, there may also be a concomitant increase in the amount of active phase precipitating during subsequent aging [England and Hall, 1986]. Paciej and Agarwala [1988] also noted that the pH of the 3.5 wt.% NaCl test solutions increased by several tenths after several days of exposure to the MMCs. The change in pH correlated well with the corrosion rate determined by weight-loss measurements.

Galvele [1978] has determined that the pitting potential is linearly dependent on the logarithm of the halogen anion concentration. In order for Al to pit in the open circuit condition, a cathodic reaction must polarize Al to potentials noble to its pitting potential. Bruun and Nielsen [1991] were able to fit the pitting potential with the Cl^- ion concentration in the well-known relationship

$$\mathrm{Ecrit} = \mathrm{Ecrit}^\circ + n \cdot R \cdot T / [(3F) \cdot \ln[Cl^-]] \qquad (2.6.1)$$

where:

Ecrit = the actual pitting potential
Ecrit° = the pitting potential at $[Cl^-] = 1M$
n = a stoichiometric factor
R, T, F = gas constant, temperature in degrees Kelvin, and Faraday's constant, respectively.

They found values for n between 4-6 for solutions containing 50 ppm, 0.1%, and 3.5 wt.% NaCl. They successfully fitted the pitting potential behavior for the FP® [Dupont, MI] alumina fiber composites that they studied with regression factors between 0.873-0.995. A similar relationship may exist for G/Al MMCs.

Bruun and Nielsen [1991] studies demonstrated that Ecrit in chloride-containing environments could be divided into two values: 1) the pit-initiation potential and 2) the pit-growth potential using multipotentiostatic measurements. The majority of their composites showed a 10-30 mV_{SCE} difference between pit initiation and growth potentials. This difference was greatest for the alumina fiber/2024 Al MMC, indicating that it had a strong tendency for film formation. No crevice formation was found between the alpha alumina fiber and 2024 Al matrix; however, noble $CuAl_2$ was determined to be important for oxygen reduction. Al_8Mg_5 and Mg_2Si provided tunnel-like corrosion paths in FP® alumina fiber/5052 and 6201 Al MMCs in the extrusion direction.

2.6.2 Protection Methods

Payer and Sullivan [1976] investigated various coatings to protect exposed G/Al MMC surfaces. Metallic coatings such as electroplated Ni, chemical vapor deposited (CVD) Ni and chromium carbide, and physically deposited coatings were investigated. The most protective coating was determined to be electroplated Ni. All other coatings showed flaws that led to subsequent corrosion in chloride environments.

Later, Aylor, et al. [1984] discovered that electroless Ni coatings on G/Al MMCs suffered from severe galvanic corrosion on the G/Al substrate because of the highly unfavorable Ni to Al ratio at flaw sites in the Ni coating. Anodized Al coatings, 13-25 μm in thickness, were not protective against corrosion in chloride environments due to the underlying G/Al MMCs. The foregoing results of Payer and Sullivan [1976] indicate that coatings may not be the best means to protect G/Al MMCs.

Mansfeld, et al. [1988] used $CeCl_3$ as an inhibitor for protection of G/Al MMCs with 6061 and 7075 Al-foil coatings as additional protection. The G/Al MMCs were soaked in the inhibitor, and then removed and placed in an aggressive environment. Their work demonstrates that AC impedance is useful for the determination of the onset of pitting. Later, similar work [Mansfeld, et al., 1990] was conducted on non-protected G/Al and SiC/Al MMCs. They found that the $CeCl_3$ inhibitor greatly reduced corrosion on the MMCs studied without a protective Al-foil coating.

Hihara [1989] considered electrical insulation of fibers, cathodic protection, and cathodic inhibition as methods of protection for G/Al and SiC/Al MMCs. Electrically insulating or coating the fibers could theoretically restrict the flow of electrons across the fiber-matrix interface; however, Hihara calculates that a material must have a resistivity of 1.26×10^{17} Ω·cm if a galvanic current is to be limited to 0.1 $\mu A/cm^2$. Not many materials with this resistivity exist. It is also very difficult to produce a flawless coating on the surface of the fibers to limit electron flow; moreover, in the presence of a defect in the coating, electronic leakage will render the coating useless as an electric insulator.

TiO_2 has a resistivity of between 10^{13} and 10^{18} Ω·cm depending on the temperature, and could provide the adequate resistance [CRC Handbook of Chemistry and Physics, 1991]. Clement, et al. [1990] have produced crack-free TiO_2 coatings from sol-gel processing, but these have not been produced on a commercial scale.

Alternatively, SiO_2 has a resistivity of between 10^6 and 10^{15} Ω·cm, and may theoretically afford a certain degree of protection; no experiments have been performed to date to confirm this, however, many researchers have produced crack-free coatings of SiO_2 by the sol-gel or alkoxide process [Katzman, 1986; Mohallem and Aegerter, 1988].

Isaikin, et al. [1981] have found that SiC (resistivity = 10^0 Ω·cm) coatings on carbon fibers reduced the corrosion rate of the composite by a factor of 3. Although, this does not seem possible from theoretical calculations [Hihara, 1989], there may be other factors which influence corrosion processes for the SiC-coated carbon fiber/Al MMCs that have not been determined.

Hihara and Latanision [1988a] found that overprotection of G/Al MMCs resulted in a localized increase in the pH (alkanization) due to cathodic processes occurring on G/Al MMCs which required greater cathodic currents to suppress anodic reactions. This led to an increase in the corrosion of the composite studied. Therefore, cathodic protection was ruled out as a viable means of protecting G/Al MMCs.

Finally, cathodic inhibitors (i.e., $ZnCl_2$ and Na_2CrO_4) were added to galvanic couples of graphite fiber and 6061-T6 Al to determine if the galvanic current could be reduced. These inhibitors affect the cathodic reaction by acting as a source of ions (e.g., Zn^{2+} and CrO_4^{2-}) which can form a protective film (e.g., $Zn(OH)_2$) over graphite [Boffardi, 1987]. Low levels of chromates (~10 ppm) have been shown to inhibit cathodic reactions [Hatch, 1964]. $ZnCl_2$ and Na_2CrO_4 inhibitors were successful in reducing the galvanic current by a factor of 10 to 100. With such low concentration levels (~10 ppm) it seems that these inhibitors would be useful for corrosion reduction. However, since MMC materials are commonly used for structural support, inhibitors will have to be incorporated into the microstructure or applied to exposed surfaces (e.g., $CeCl_3$) in order to derive the potential benefit of cathodic inhibition.

2.7 MODIFICATION OF GRAPHITE FIBERS TO REDUCE CORROSION

2.7.1 Intercalation of Graphite Fibers

The possibility of using intercalation to alter oxygen reduction characteristics on fibers has already been pointed out by Hihara [1989]. In the past, intercalation has been considered as a means to modify graphite to produce a lightweight conductor or superconductor rather than as a method to alter the electrochemistry of graphite fibers in a way that could reduce oxygen reduction.

Intercalation is readily accomplished with many forms of graphitic carbon including highly ordered graphite fibers. Dresselhaus, et al. [1988] have extensively reviewed the intercalation process. In general, atoms and simple molecules are usually intercalated from a vapor, but larger and more complex organic molecules are intercalated from a liquid solution.

The importance of the intercalation of ions to the electrochemistry of G/Al MMCs has been noted [Besenhard et al., 1982; Hihara, 1989]. In the past, cyclic voltammograms of carbon fiber bundles have provided information quantifying the amount of energy (the integral of the voltage peak) associated with the irreversible threshold observed during the initial intercalation of a fiber.

Meschi, et al. [1986] and Endo, et al. [1981] have determined that degradation of the tensile strength and Young's modulus occur in intercalated graphite fibers intercalated with alkali metals. There was a larger decrease in the tensile strength as compared to the change in the Young's modulus.

When heating graphite containing an intercalation compound, a relatively large (~3.5 x 10^{-5}/°C) expansion occurs along the c-axis of the graphene planes, while the in-plane lattice constant remains almost unchanged [Dresselhaus, et al., 1988]. Martin and Brocklehurst [1964] describe this phenomenon as an 'exfoliation' process by assuming the intercalant undergoes a phase change to the vapor phase, forming disc-shaped bubbles in the interlayer region between the graphene planes. Unfortunately, the critical temperature at which exfoliation occurs is as low as 100°C.

Due to the degradation of the mechanical strength of the graphite fibers and exfoliation, which results from subsequent heating of intercalated graphite, intercalation of graphite of MMCs was not considered as a practical means of modifying oxygen reduction on graphite fibers in G/Al MMCs.

2.7.2 Ion Implantation of Graphite Fibers

Ion implantation offers a convenient route to implant Zn^{2+} atoms into the surface of graphite fibers. In order to attain cathodic inhibition of G/Al MMCs, Zn ion implantation of model G/Al MMCs was attempted. Therefore, a brief synopsis of ion implantation in graphite is provided below.

During the ion implantation process, ions are accelerated by a certain voltage and are allowed to impinge the surface of a material and become imbedded in the matrix with a characteristic depth, R_p, and Gaussian distribution of half width at a half maximum, ΔR_p (see Figure 2.7.1). Since ion implantation is a near surface phenomenon, the 'fluence,' or the number of incident atoms per surface area, can influence the concentration of thin fibers in a significant way. Therefore, the depth profile is controlled by the ion beam energy and the substrate to ion mass ratio. The concentration is controlled by the fluence. Since ion implantation is a non-equilibrium process, it is possible to achieve high concentrations of dopant as a metastable system. However, because ion implantation is a surface process, implantation depths are only on the order of 1000Å. Ion implantation, a versatile, low temperature process can be controlled by masking, which does not produce an accompanying oxide or interfacial barrier.

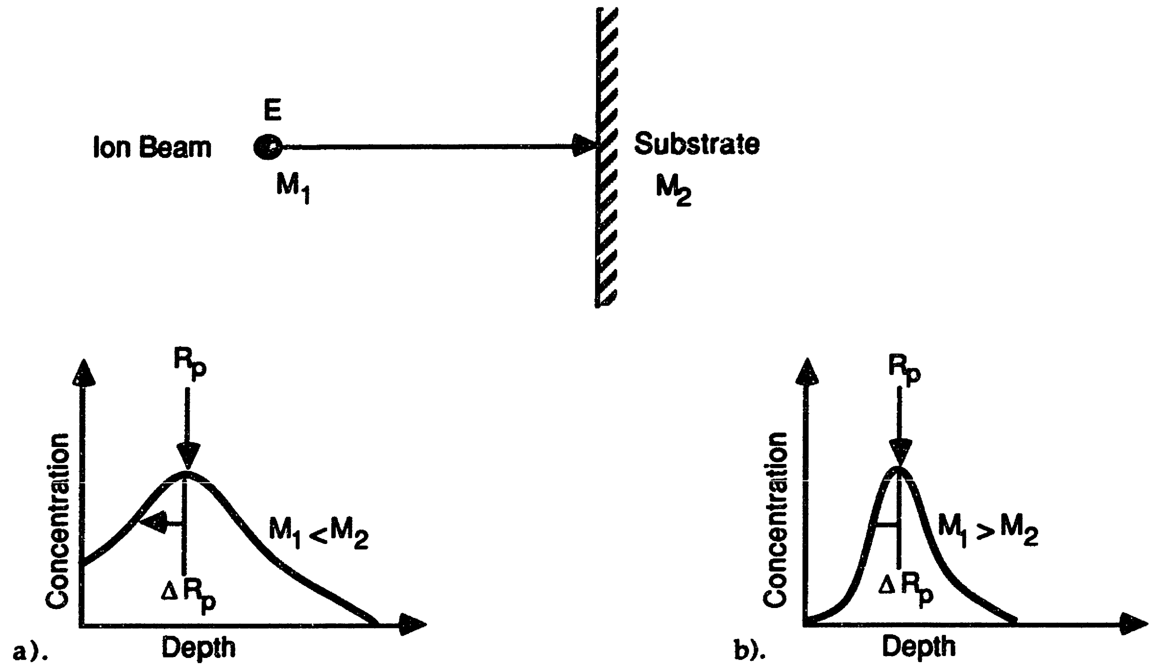

Figure 2.7.1: Depth distribution of implanted atoms in an amorphous target for the case in which the ion mass is less than (case a) or greater than (case b) the mass of the substrate atoms. To a first approximation, the mean depth Rp depends on ion mass M_1 and incident ion energy E, whereas the relative width $\Delta Rp/Rp$ of the distribution depends primarily on the ratio between the masses of the ions and the substrate carbon atoms M_2. In almost all practical cases for the implantation of carbon fibers $M_1 >> M_2$.
[Dresselhaus et al., 1988, p. 292]

However, undesirable radiation damage accompanies the process, and either high temperature implanting or post-annealing is necessary in order to restore order to the deformed graphite and to recrystallize the surface. Fortunately, an extremely high post-annealing temperature (~1500-2300°C) is necessary to cause evaporation of the implanted material in graphite [Salmanaca-Riba, et al., 1985; Elman et al., 1985]. Therefore, unlike intercalated graphite which suffers from exfoliaton at moderately low temperatures (~100°C) [Martin and Brocklehurst, 1964], ion-implanted graphite fibers provide doped materials which are stable at relatively high temperatures.

It should be noted that ion implantation of a cylindrical graphite fiber will be a problem for commercial development. In the experiments which were performed in the present study, the transverse cross-sectional area of a model G/Al MMC (Chapter 6) was ion-implanted producing a geometrically uneven distribution of ions at a depths of ~1000Å.

2.8 THE SCANNING POTENTIAL MICROPROBE/ SCANNING VIBRATING ELECTRODE TECHNIQUE (SVET)

The scanning potential microprobe (SPM) was developed by Agar [1940] to observe currents flowing from and to macroscopic sites in partially immersed metals in an aqueous solution. A Luggin probe connected to a Calomel electrode was used to determine the equipotential field above the surface of immersed Zn. Well-aerated regions (i.e., regions 1 cm below the water line) were cathodic to the rest of the sample which acted as an anode. A comparison of the corrosion rate estimated by measured currents versus corrosion rate determined by the weight-loss techniques agree to within 10%, giving validity to the technique. Since then, much has been done to improve the spatial resolution of the probe. When Jaffe and Nuticelli [1974] developed the vibrating probe technique for examining biological cells and tissue, the resolution of the probe had progressed from macroscopic to microscopic. The use of the SPM linked with a mechanically movable vibrating probe is known as the scanning vibrating electrode technique (SVET).

At the most basic level, the SVET consists of a very fine electrode that vibrates at a fixed frequency over the surface of a specimen immersed in an electrolyte. The SVET enables the researcher to measure net ionic currents associated with corrosion microcells with spatial and current resolution on the order of 15 to 20 μm and 5 nA/cm^2, respectively [Scheffey, 1988]. The electrode reflects the difference between the electric field potential at the surface of the specimen and a point further away from the surface. By moving the probe at a given height across the equipotential field (see Figure 2.8.1) in solution, which is related to the flow of ionic current emanating from anodic regions and moving to cathodic regions, it is possible to determine where anodic and cathodic current sources and drains exist, respectively.

Figure 2.8.2 shows a schematic of the vibrating electrode probe. The probe is vibrated vertically and horizontally by a piezoelectric vibrating reed made of lead zirconium titanate. By applying two different sinusoidal voltages with a peak to peak amplitude of 2 volts at 445Hz to three coupled bimorphs, the probe tip deflects approximately 20 μm peak to peak in the vertical and

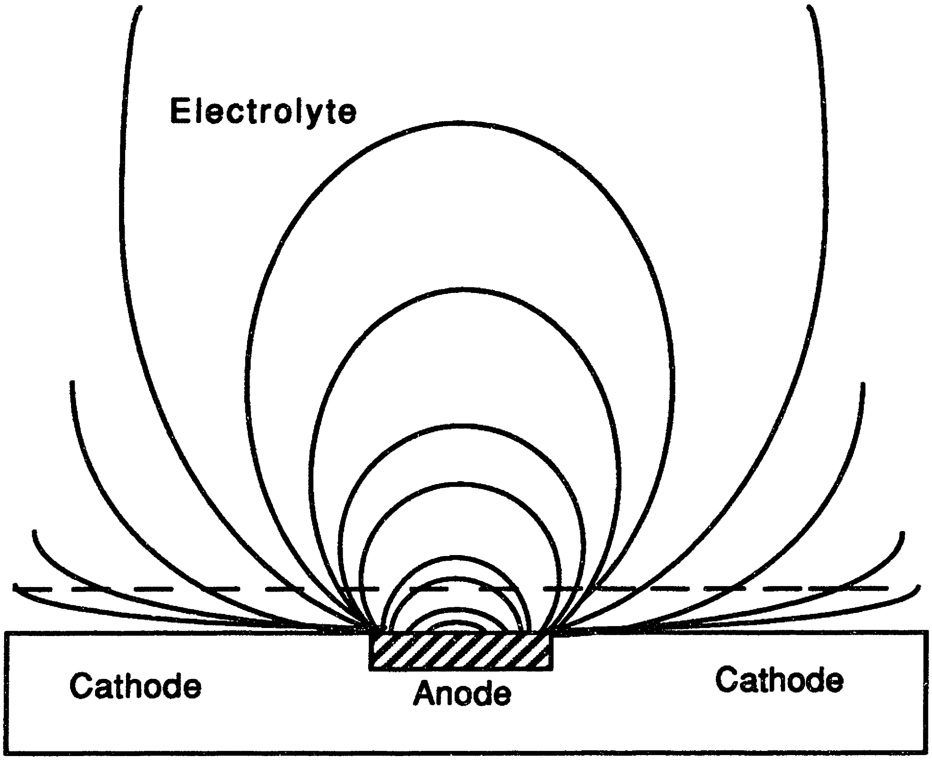

Figure 2.8.1: Schematic of a local corrosion cell showing calculated equipotential lines. [Isaacs, 1986, p.37]

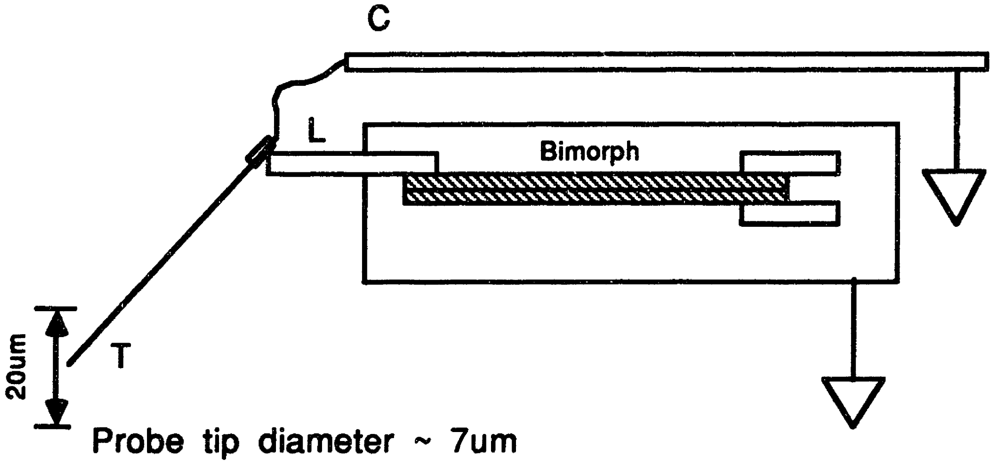

Figure 2.8.2: Bimorph holder for vertical vibration. C: the grounded metal tube containing the coax cable to the preamplifier. L: a lucite beam mounted to the bimorph. The bimorph itself is a cantilever. T: the tip of the vibrating probe. [Scheffey, 1988, p.788]

horizontal direction. The high capacitance surface of the probe tip senses the difference in voltage potential, which is sent to the input of the capacitively coupled preamplifier shown in Figure 2.8.3.

The voltage measured during vibration is measured relative to a distant Pt reference electrode, and the current density component of the medium at the center point of vibration tangential to the direction of vibration is calculated according to the following expression [Crowe, 1985]:

$$i\ (\mathrm{A/cm^2}) = \sigma\ (\Omega\cdot\mathrm{cm})^{-1}\ \Delta V\ (\mathrm{volts})/\Delta r\ (\mathrm{cm}) \qquad (2.8.1),$$

where i is the current density component parallel to probe vibration, σ is the conductivity of the solution, ΔV is the voltage difference between the two extremes of vibration, and Δr is the vibration stroke. For example, a current density of 50 $\mu A/cm^2$ would correspond to a voltage difference of 100 μV which is a very small potential difference. The same frequency signal is then fed to the reference input of a precision lock-in amplifier which also reads the voltage signal from the vibrating probe (see Figure 2.8.3).

Scheffey [1988] reports that the SPM located at the National Vibrating Probe Facility, Marine Biological Laboratory (MBL), Woods Hole, MA, has a resolution on the order of 5-40 μm. One of the advantages of the instrument at the MBL is the *in-situ* observation by the probe over the surface of the specimen (see Figure 2.8.3). With a normal metallographic objective (25X) and binocular (10X) lens, it is relatively simple to resolve carbon fibers with a diameter of 10 μm at 250X magnification. Another advantage of their instrument is that the computer can step automatically to a new location with a precision of approximately 2 μm in either the x or y direction. One is able to move and scan the surface of a specimen at regular calibrated steps. The final data can be overlaid on the video image other specimen in solution.

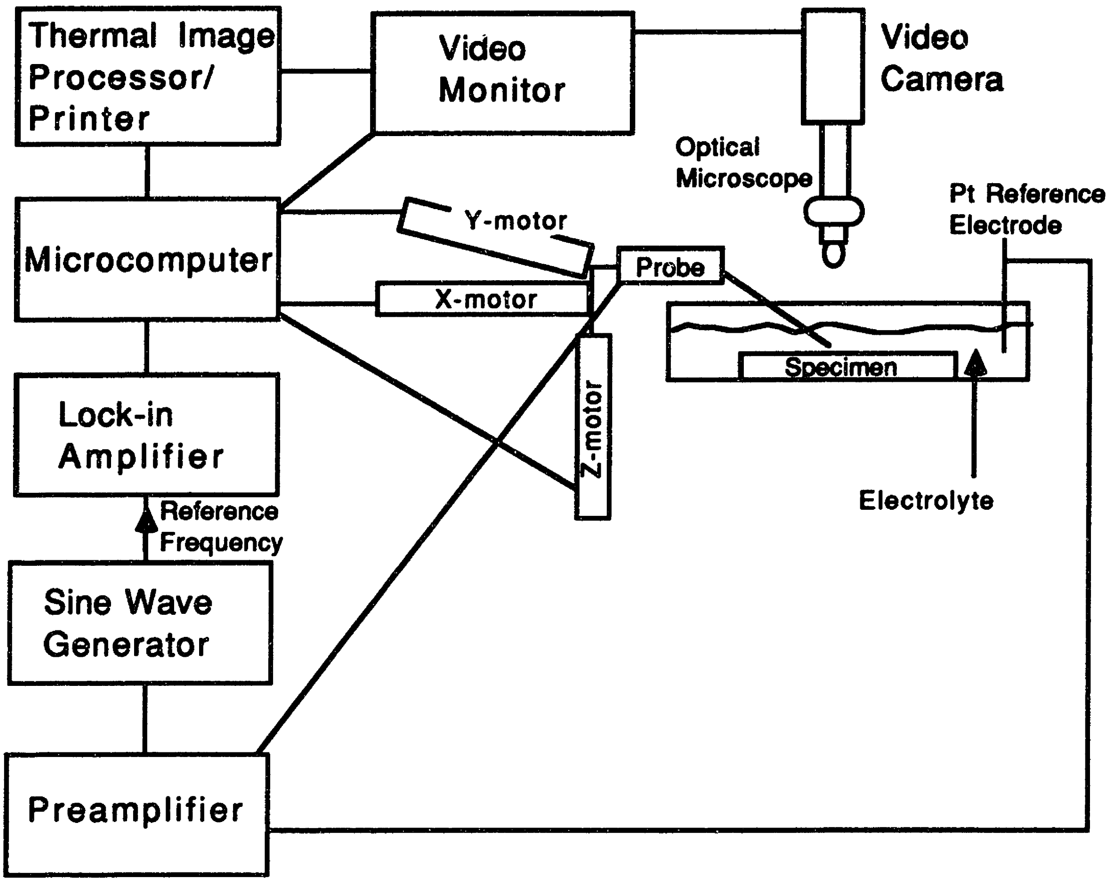

Figure 2.8.3: Complete schematic for SVET assembly.

The solution employed for the SVET must have a high resistivity to allow for good spatial resolution of local potential differences. The measured resistivity of the 0.01 M NaCl solution which was used in this study was 920 Ω·cm. The relationship for rms current noise attained during SVET is:

$$i\ (\mathrm{A/cm^2}) = 3 \times 10^{-11} / [d\ (\mathrm{cm})^{3/2}\ r\ (\Omega\cdot\mathrm{cm})^{1/2}] \qquad (2.8.2),$$

where d is the electrode tip diameter, and ρ is the electrolyte resistivity [Scheffey, 1988]. Thus, the minimum rms current noise for each measurement of each component of the field vector was ± 0.02 $\mu A/cm^2$ (i.e., assuming a probe diameter of 15 μm and that current noise was due only to the thermal noise of resistance in the electrolyte between the electrode surface and distant ground).

The movement of specific ionic species in the solution is not possible to determine from the type of probe used in this study, which only senses the net ionic current flowing in the presence of a potential field created by the galvanic G/Al couple. In this case, species such as Al^{+3}, OH^-, H^+ and $Al(OH)^{+3}$ are flowing from the surface through the solution.

Crowe [1985] examined localized ionic currents on welded G/Al and SiC/Al composites. The spatial resolution of his probe was on the order of 20 µm, which proved useful for determining the nature of the weld region, but was not useful in determining localized corrosion at the fiber/matrix or particle/matrix interface.

Isaacs [1988] has examined localized breakdown and repair of passive surfaces during pitting. The SVET was used to investigate active pit growth and repassivation. The study served to reveal passivation, localized corrosion, and repassivation of iron and a stainless steel in chloride environments. A Ni alloy was also examined with this technique for a longer period of time. Active pit formation and repassivation events in Ni were clearly discernable for pits on the order of 6-9 µm in size over longer periods of time (~30 hrs.).

The SPM has been shown to be a useful instrument in determining the corrosion characteristics of many galvanically coupled materials. It should be pointed out that there are very few articles concerning the use of the SVET in the literature, and even fewer in connection with MMCs. However, given recent advances in technology such as the improvement in spatial resolution of the probe, model G/Al MMCs were examined in order to determine valuable electrochemical characteristics and to monitor changes due to intentional modification of graphite in Al (see Chapter 6).

3. FABRICATION AND CHARACTERIZATION OF G/Al MMCs

3.1 INTRODUCTION

This chapter concentrates on the processing of commercial G/Al MMCs with particular attention to the amount of Al_4C_3 produced by the fiber-matrix reaction. Composite processing and matrix alloy chemistry play an important role in determining the nature of the interface and are therefore paramount to this investigation. Therefore after composites were produced, gas chromatography was performed to quantify the amount of Al_4C_3 at fiber interfaces before examining the electrochemical behavior of specimens with varying known Al_4C_3 contents.

3.2 EXPERIMENTAL

3.2.1 Processing of Composites (Pressure Infiltration)

The pressure infiltration casting apparatus used by PCAST Equipment Co., Pittsburgh, PA, for preparing G/6061 MMCs is shown in Figure 3.2.1. A mold containing a graphite fiber preform was held in the same pressure vessel as the melt. The 6061 Al ingot was put into the crucible and the graphite fiber-wrapped preform enclosed in a steel tube was also placed in the vessel. The vessel was sealed and evacuated to a pressure range of approximately 10.34 Pa (7.8×10^{-2} torr) to 17.23 Pa (1.29×10^{-1} torr). The melt was superheated 80 to 100°C, and the mold heated 10 to 30°C above the liquidus temperature of the Al alloy. The crucible was raised to meet the steel tube containing the preform, and nitrogen gas at a pressure of 8.96 MPa (1300 psi) was applied to the surface of the melt to force the melt to penetrate the graphite preforms completely.

The pressure was maintained during the solidification period, since premature release would result in shrinkage cavities and hot-tears in the composite. When the temperature was approximately 50°C below the Al melt solidus, and hence, the composite had solidified completely, the outlet valve was opened to release the inert gas. When the specimen's temperature was below 300°C, the pressure vessel was opened and the composite was taken out of the mold.

Other samples processed at Aluminium Ranshofen, Ges.m.b.H., Ranshofen, Austria were produced in a similar pressure vessel; however, for proprietary reasons the exact geometry was not disclosed.

The procedure used to fabricate the specimen made at MIT (Specimen 1) is described elsewhere [Cornie, et al., 1990].

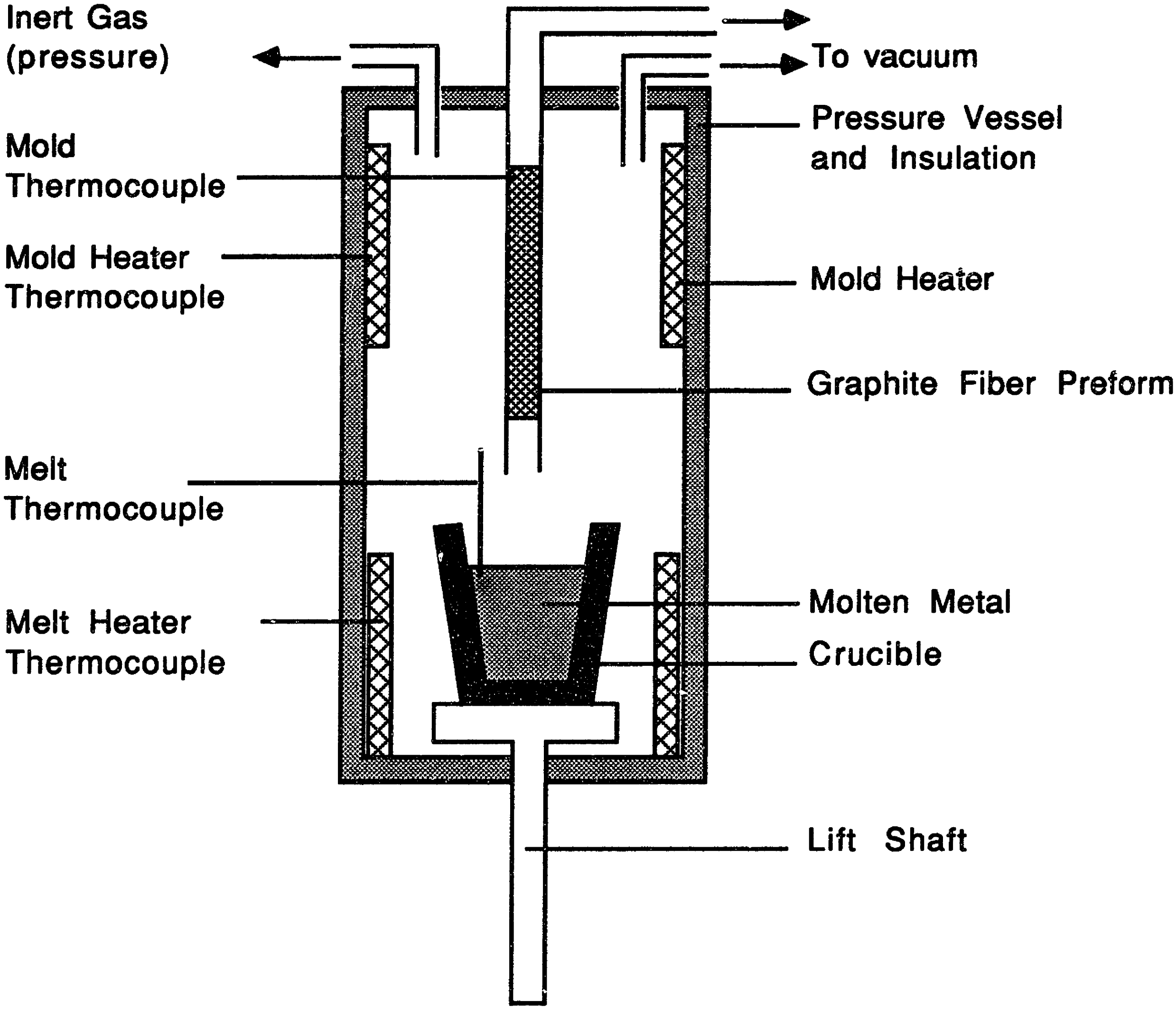

Figure 3.2.1: Schematic of infiltration vessel used to fabricate G/6061 MMCs.

The commercial continuous fiber G/Al MMCs processed are shown in Table 3.2.1. Specimen 1 was fabricated at MIT, Cambridge, MA. Specimens 2-5 and 10-13 were fabricated at Aluminium Ranshofen, Ranshofen, Austria, while Specimens 6-8 were fabricated at PCAST Equipment Co., Pittsburgh, PA.

Table 3.2.1: G/Al MMC Material with 1100, 6061 and Al-Zn Matrices

Spec. #	Matrix	Vol.% Fiber	Fiber Type	Fiber E mod.	Fiber UTS	Lab. Code
1	1100 Al	55%	* Pitch-based Thornel P55s diam. = 11μm.	399.5 GPa 57.9 Msi	1.84 GPa 266.8 ksi	120
2	1100 Al	65%	PAN-based * *Courtaulds EHMS 10k 0.7E diam. = 7.8μm.	340 GPa 49.3 Msi	2.5 GPa 363 ksi	130
3	1100 Al	67%				181
4	1100 Al	69%				182
5	6061 Al	64%	PAN-based †Torayca M40 3k diam. = 6.5 μm.	392 GPa 56.8 Msi	2.74 GPa 397.3 ksi	254
6	6061 Al	70%	Pitch-based Thornel P55s diam. = 11μm.	399.5 GPa 57.9 Msi	1.84 GPa 266.8 ksi	255
7	6061 Al	68%				256
8	6061 Al	62%				257
9	6061 Al	74%				258
10	0.1wt.% Zn in Al	69%	PAN-based Courtaulds EHMS 10k 0.7E diam. = 7.8μm	340 GPa 49.3 Msi	2.5 GPa 363 ksi	247
11	0.5 wt.% Zn	69%				248
12	1.0 wt.% Zn	70%				249
13	5.0 wt.% Zn	73%				250

*Union Carbide Corp., NJ **Courtaulds Inc, U.K. †Toray Inc, Japan

1100 Al is 99.99 wt.% pure Al, while 6061 Al contains 0.6 and 1.0 wt.% Si and Mg, respectively. The alloying elements are added to give the wrought alloy additional strength through precipitation hardening which is achieved through heat treatment. G/6061 Al MMCs were later tested to confirm the electrochemical results found by Hihara [1989] and Hihara and Latanision [1990] (Section 2.1.1). The selection of G/Al MMCs in Table 3.2.1 also allowed comparison of the electrochemical behavior of chemically similar continuous MMCs that had been processed by diffusion-bonding (see Chapter 6) and by pressure infiltration; the former process was shown to leave microstructural chlorides in the composite [Hihara, 1989]. G/6061 Al MMCs were not heat treated to the commercial 'T6' solutionized and aged condition for the following reasons: 1) additional heat treatments would have resulted in further Al_4C_3 formation, degrading the strength of the fiber and thwarting comparison with as-processed G/1100 Al MMCs which were not precipitation hardenable, 2) other researchers have shown over-aging occurs with MMCs when using a typical heat treating sequence [Trzaskoma, 1991], and 3) the supply of the material studied was very limited as well as expensive.

During processing, a problem with production of the G/Al-Zn MMCs occurred. The partial pressure of Zn in rough vacuum at 700°C is higher than that of Al and therefore evaporates out of the molten alloy, to find its way to the cooler parts of the pressure infiltration vessel during infiltration. Zn alloyed with monolithic Al evaporated during infiltration of the G/Al-5%Zn MMC, leading to a decrease (~0.5 wt.%) in the nominal Zn concentration in the composite.

Specimens containing Zn in their Al matrices (see Table 3.2.1) were produced to determine if some reduction in galvanic corrosion could be gained from the dissolution of Zn in matrix. Although it is well known that Zn additions to Al alloys result in a reduction in the corrosion resistance of the alloy (e.g., 7075 Al), we wished to explore whether galvanic corrosion between the fiber and the matrix could be reduced at the expense of minute corrosion of the matrix. The addition of $ZnCl_2$ in aqueous solutions [Hihara, 1989], and Zn ion implantation into model G/Al MMCs [Buonanno et al., 1991] showed favorable results and led to the belief that this might be feasible. More specifically, since the galvanic couple between the fiber and the matrix produces the strongest electrochemical driving force for corrosion in G/Al MMCs, it may be possible to take advantage of the fact that only 10 ppm of Zn^{2+} cations in solution results in a reduction of the corrosion rate by a factor of 10 to 100 (see Section 2.3.4). As the matrix begins to corrode, minute quantities of Zn^{2+} cations in the solution should be free to migrate to exposed graphite fiber surfaces. Thereafter, a $Zn(OH)_2$ film could form over the surface of exposed fibers and inhibit oxygen reduction.

3.2.2 Cooling Rate and Time for Solidification

The Al-rich portion of the Al-Mg silicide psuedo-binary system can be found in Appendix B. For 6061 Al, eutectic Mg_2Si formation occurs during equilibrium cooling. For Al-Zn binary alloys used to produce G/Al-Zn MMCs, the applicable phase diagram can be found in Appendix C. The solubility of Zn in Al at 100°C is approximately 4 wt.%.

Specimens with a 1100 (99.99%) pure Al matrix solidified with a single composition from the liquid into the solid region. Figure 3.2.2 shows the schematic of the general cooling sequence for G/6061 MMCs (Specimens 5-9); other specimens had similar cooling curves. The schematic shows: the initial melt temperature (Ti), the liquidus (TL), the solidus or in some cases the eutectic temperature (Ts), and 350°C. It has been determined that below 350°C, Al_4C_3 formation does not occur [Wu, 1988]. The contact time of molten Al with the fibers governs Al_4C_3 formation [Wu, 1988; Chernyshova and Kobeleva, 1985]. Lower cooling rates used to process G/Al MMCs resulted in significant Al_4C_3 contents due to longer contact time.

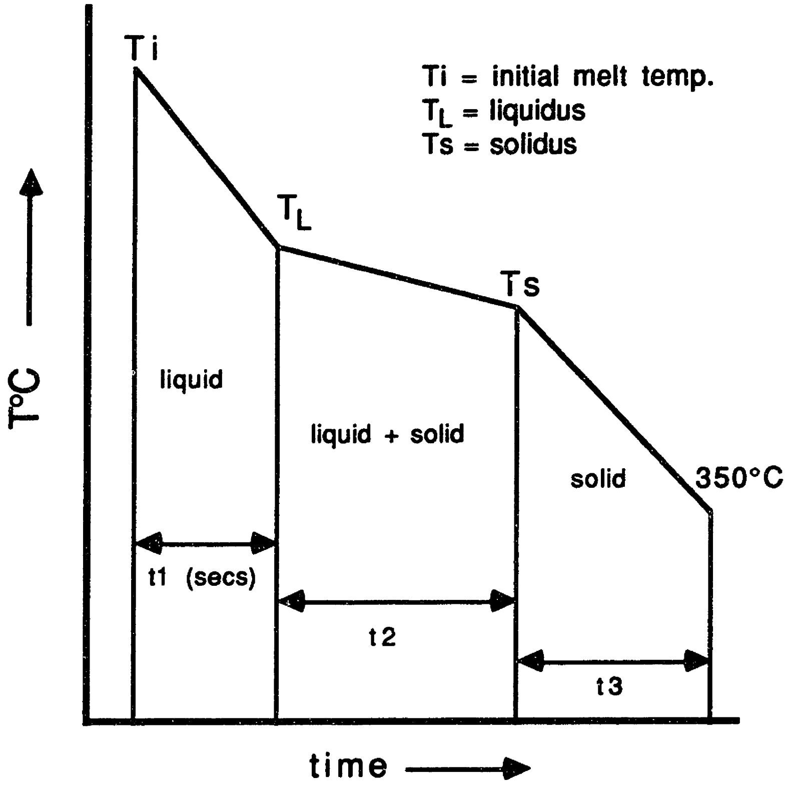

Figure 3.2.2: Cooling curve schematic for G/6061 Al MMCs.

The final solute distribution in the matrix is governed by the fiber interstice spacing, and the cooling rate [Mortensen, 1986; Mortensen et al., 1988b]. The cooling temperature and time data are shown in Table 3.2.2. These data are from thermocouples placed within the pressure vessel, and are thereby only approximations of the actual solidification process.

Table 3.2.2: Cooling Rate Data

Spec. #	Ti	TL	Ts	350°C	t1	t2	t1+t2	t3
	(°C)	(°C)	(°C)		(sec.)	(sec.)	(sec.)	(sec.)
Specimens below have a 1100 pure Al matrix.								
2	694	658	656	400	36	50	86	261
3	699	658	656	350	22	40.5	62.5	184
4	693	658	656	350	20.4	47.7	68.1	156
Specimens below have a 6061 Al matrix.								
6	700	650	630	350	200	118	318	1230
7	700	650	630	350	265	90	355	1278
8	695	650	630	350	13	18	31	1530
9	660	650	630	350	2.4	5.5	7.9	1344
Specimens below have an Al-Zn matrix.								
10	698	658	653	350	27	69	96	300
11	710	658	653	350	40	68	108	318
12	702	657	648	350	34	71	105	324
13	699	657	643	350	35	76	111	318

3.3 ALUMINUM CARBIDE ANALYSIS (Al_4C_3)

In an attempt to correlate the solidification rate with the kinetics of Al_4C_3 formation, gas chromatography was performed on resulting composite specimens[1]. The technique requires the removal of the Al matrix with aqueous 5% NaOH solution. Upon addition of the solution the following reactions occur:

$$Al_4C_3 + 4NaOH + 12H_2O \rightarrow 4NaAl(OH)_4 + 3CH_4(g) \qquad (3.3.1)$$

---

[1] Performed by Dr. H. Danninger at the Technische Universitat Wein, Vienna, Austria

and

$$\mathrm{Al} + \mathrm{NaOH} + 3\mathrm{H_2O} \rightarrow \mathrm{NaAl(OH)_4} + \frac{3}{2}\mathrm{H_2}\,(g) \qquad (3.3.2).$$

Standard analysis was performed on known Al_4C_3 samples. From the above relations and from the results on known standards, it is possible to determine the ratio of the mass of Al_4C_3 to mass of Al in composite samples. The relation used to determine the wt.% Al_4C_3 is:

$$\mathrm{wt\%\ Al_4C_3} = \frac{m_o^{Al}}{m_o^{Al} + m_o^{fiber} + m_o^{Al_4C_3}} \times \frac{m_f^{Al_4C_3}}{m_f^{Al}} \qquad (3.3.3),$$

where $m_o{}^x$ is the initial mass of Al, fiber, and Al_4C_3 in the composite, respectively; the second term containing $m_f{}^{Al_4C_3}$ and $m_f{}^{Al}$ is determined by the ratio of methane and hydrogen evolved in equations 3.3.1 and 3.3.2. The amount of Al_4C_3 can be expressed in milligrams per square meter of fiber by the relation,

$$\mathrm{Al_4C_3}\left(\frac{mg}{m^2}\right) = 590 \times d \times \frac{\mathrm{vol.\%\ Al_4C_3}}{\mathrm{vol.\%\ fiber}} \qquad (3.3.4),$$

where d is the average fiber diameter in microns [Schmitt, 1991]. The vol.% Al_4C_3 is obtained from equation (3.3.3) by converting wt.% Al_4C_3 to vol.% assuming that the density of Al_4C_3 is 2.36 g/cm^3. The vol.% fiber is best determined with traditional metallurgical statistical point counting techniques [Annual Book of ASTM Standards, 1991a]. A sixteen point grid was used for counting.

Tables 3.3.1, 3.3.2, and 3.3.3 present the results of Al_4C_3 analysis for G/1100 (Specimens 2-4), G/6061 Al (Specimens 6-9), and G/Al-Zn (Specimens 10-13) MMCs, respectively. Also shown in the tables are the vol.% fiber determined by point counting techniques. The values obtained for the Al_4C_3 content are subject to differences that are a direct consequence of the temperature and cooling profile within the pressure infiltration vessel, and more importantly, the location of a specimen in relation to the heating elements.

Table 3.3.1: Aluminum Carbide Analysis of G/1100 Al MMCs

Spec.#	Lab Code	$\frac{m_f^{Al}}{m_f^{Al_4C_3}}$	wt%C	wt%Al	wt%Al_4C_3	vol%C	vol%Al	vol%Al_4C_3	Al_4C_3 $\frac{mg}{m^2}$
2	130	35.00	54.15	44.51	1.345	63.95	34.84	1.209	76.66
3	181	44.85	56.22	42.77	1.019	65.84	33.25	0.909	56.27
4	182	75.81	59.45	39.98	0.573	68.75	30.75	0.505	30.11

Table 3.3.2: Aluminum Carbide Analysis of G/6061 Al MMCs

Spec.#	Lab Code	$\frac{m_f^{Al}}{m_f^{Al_4C_3}}$	wt%C	wt%Al	wt%Al_4C_3	vol%C	vol%Al	vol%Al_4C_3	Al_4C_3 $\frac{mg}{m^2}$
6a	255 I	55.27	62.66	36.65	0.689	69.35	30	0.646	54.45
6b	255 II	63.09	62.74	36.65	0.604	69.43	30	0.566	47.72
7a	256 I	12.34	57.98	38.85	3.167	65	32	3.001	260.35
7b	256 II	18.85	59.06	38.85	2.096	66.02	32	1.982	171.99
8a	257 I	68.80	54.06	45.28	0.666	61.36	38	0.640	60.92
8b	257 II	259.34	54.54	45.28	0.178	61.83	38	0.170	16.27
9a	258 I	231.57	67.68	32.17	0.147	73.86	26	0.136	10.84
9b	258 II	487.42	67.76	32.17	0.070	73.94	26	0.065	5.16

Table 3.3.3: Aluminum Carbide Analysis of G/Al-Zn MMCs

Spec.#	Lab Code	$\frac{m_f^{Al}}{m_f^{Al_4C_3}}$	wt%C	wt%Al	wt%Al_4C_3	vol%C	vol%Al	vol%Al_4C_3	$Al_4C_3 \frac{mg}{m^2}$
10	247 -0.1wt.% Zn	79.39	58.91	40.54	0.554	68.26	31.25	0.489	29.37
11	248 -0.5wt.% Zn	39.80	58.36	40.54	1.098	67.78	31.25	0.971	58.36
12	249 -1.0wt.% Zn	49.33	60.30	38.85	0.857	69.50	29.75	0.753	44.25
13	250 -5.0wt.% Zn	39.80	62.74	36.26	1.001	71.63	27.50	0.871	49.61

Studies were performed at Aluminium Ranshofen to assess the Al_4C_3 difference along the length of several 6cm long G/Al MMC bars. Al_4C_3 contents at four equidistant points along the length of the bars had a standard deviation from the mean Al_4C_3 content of ±14 mg/m^2 in the worst case, and an average standard deviation in Al_4C_3 content from the mean measurement of ±8 mg/m^2. Therefore, the Al_4C_3 analyses performed on specimens in this study were obtained from similar regions in a specimen with respect to their position inside the pressure infiltration vessel. For composites produced at the PCAST Equipment Company, the Al_4C_3 content varied by a factor of 1.5 (compare Specimens 7a and 7b in Table 3.3.2) from one end of a composite bar to the other. The PCAST composite bar was much greater in length (30cm) compared to the composite bar fabricated at Aluminum Ranshofen (6cm); therefore, the contact time of fibers with molten Al was longer for portions of the composite which were last to undergo directional solidification. Error in the measured Al_4C_3 contents arises from the temperature data, which are strongly dependent on the location of the thermocouples in the pressure vessel. Despite this, a good correlation between the measured Al_4C_3 content and ultimate fracture strength (UFS) was determined from mechanical three-point bend testing of composite materials (see Appendix D).

When plotting the final Al_4C_3 content against the time to cool molten Al from the initial melt temperature to the solidus (i.e. $Ti - T_L$) and the time to cool to the solidus (i.e., $Ti - Ts$), the difference was relatively small, since the time to cool from the liquidus to the solidus is relatively small. Therefore, Figure 3.3.1, which plots the time to cool molten Al from the initial melt temperature to the liquidus (i.e. $Ti - T_L$) versus the final Al_4C_3 content measured, best represents the contact time and growth of Al_4C_3 determined.

Figure 3.3.1 shows that increasing the time of contact of molten Al with graphite fibers results in greater Al_4C_3 contents for the G/6061 Al and G/1100 Al MMCs. For the G/6061 Al MMCs, the growth rate of Al_4C_3 at the interface decreased at longer times, perhaps because of the addition of silicon, which is known to decrease the activity of molten Al. The G/Al-Zn MMCs, which were intentionally solidified with nearly the same cooling rate, had comparable Al_4C_3 contents, within experimental error of each other.

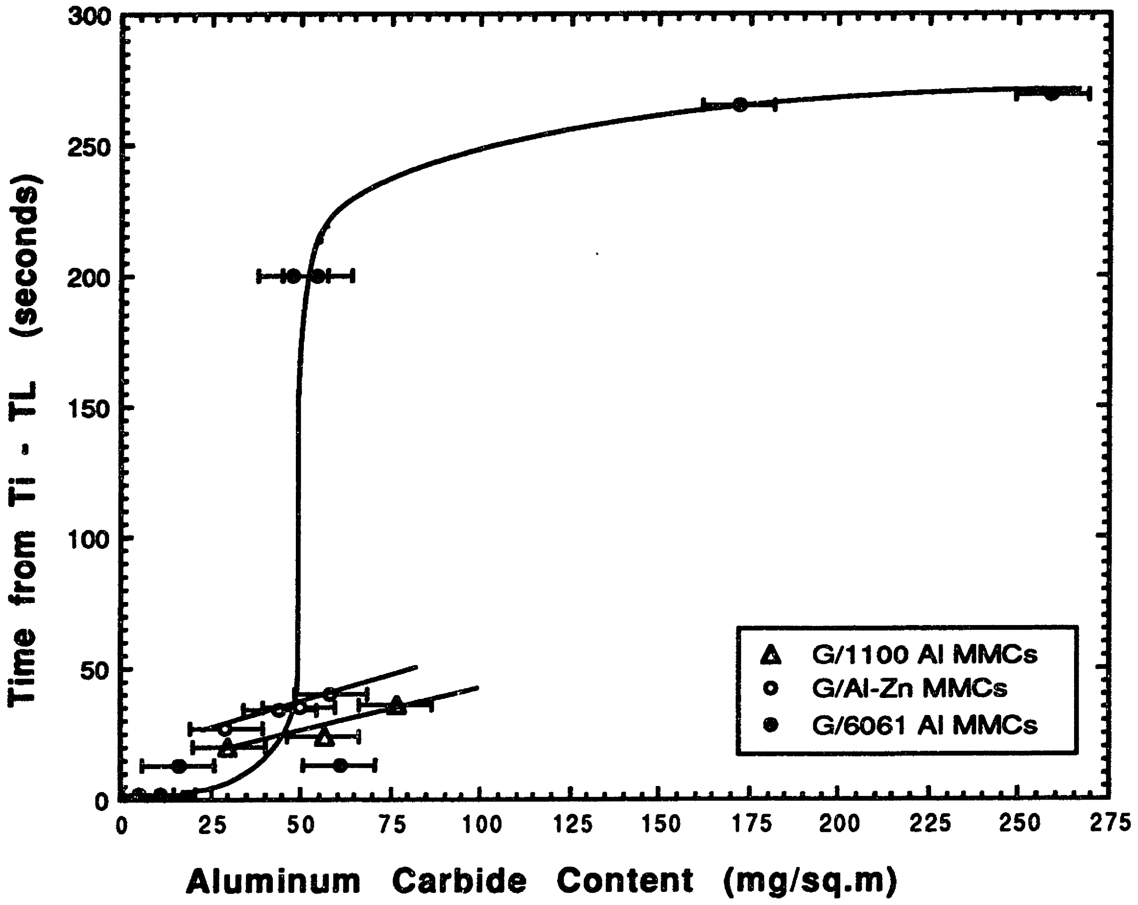

Figure 3.3.1: Time to reach liquidus from the initial melt temperature vs. the final Al_4C_3 content measured for G/1100 Al MMCs.

3.4 OPTICAL METALLOGRAPHY

Optical metallography was performed on all specimens to assess the microstructural features before and after exposure to a mild acid etch. The samples were also viewed by SEM in both secondary and backscattered electron imaging modes. The latter imaging technique has often proved useful for determining elemental segregation in MMCs [Mortensen, 1986].

3.4.1 PREPARATION FOR METALLOGRAPHY

Specimens were encapsulated in Epon® 828 Resin [Shell Chemical Company, TX] with a slow cure rate (~7 days) to reduce the amount of separation between specimen and mount due to shrinkage. Thereafter, G/Al MMCs were polished with 240, 400, and, 600 grit silicon carbide grinding paper, respectively. All mounted specimens were polished from 1µm to a 0.25µm finish with Diamond Paste® using Polishing Oil ® [Buehler, Ltd., OH] as a lubricant to reduce the amount of corrosion which would have occurred if water had been used for polishing G/Al MMCs. "Dix-Keller's" reagent [Petzow, 1976] was used in the following concentration: 190ml distilled water, 5 ml nitric acid, 3ml hydrochloric acid, and 2ml hydrofluoric acid (40% by volume). The specimens were successively etched for intervals of 15 seconds, until the appropriate etch was attained. Optical micrographs were taken before and after metallographic etching, while SEM was performed on etched samples. EDAX analysis was performed on etched samples with the Cambridge 600 SEM.

3.4.2 RESULTS

Figure 3.4.1 shows the G/Al MMCs which had a 6061 Al matrix. These specimens had been produced by pressure infiltration by the PCAST Equipment Co., Pittsburgh, PA. It is clear that the specimens in Figure 3.4.1 have significant amounts of Al_4C_3 platelets at the matrix/fiber interface. This is corroborated by the gas chromatography performed on the samples (see Table 3.3.2). Figure 3.4.1a and b (Specimen 6: 51 mg/m^2 and Specimen 7: 216 mg/m^2) show that the large difference in average Al_4C_3 content measured for the G/6061 Al MMCs was observable by optical micrography. In Figure 3.4.1c and d, interfacial Al_4C_3 platelets were not easily discernible in the transverse cross-sectional micrographs for Specimens 8 (39 mg/m^2) and 9 (8 mg/m^2), due to the decreased average Al_4C_3 contents of the samples.

The Al_4C_3 distribution at fiber interfaces can be seen more clearly in Figures 3.4.2a and b. These figures show the longitudinal cross-sectional areas for two G/6061 Al MMCs (Specimens 6 and 7). Al_4C_3 platelets have formed along the the fiber-matrix interface, respectively, and are observable approximately every 5µm; rarely do these precipitates extend into the matrix beyond the interface. In Figure 3.4.2b, gross formation of Al_4C_3 in a G/6061 Al MMC can be seen. It appears as though some Al_4C_3 is adrift in fiber interstices; however, this is probably due to Al_4C_3 precipitation from sub-fiber surfaces.

A macrograph of one G/6061 Al MMC (Specimen 8) reveals that large Al channels formed during pressure infiltration (see Figure 3.4.3). The small interstitial spacing between fibers resulted in eutectic segregation at the fiber-matrix interface. Interfacial segregation of Mg_2Si and Fe_xAl_x intermetallics was found in all samples which were infiltrated with a 6061 Al matrix. Backscattered electron images were less effective in identifying eutectic, since the average atomic number of the Mg_2Si segregant was nearly the same as that of Al (i.e., 13). Several examples of intermetallic segregants in narrow fiber interstices of G/6061 Al MMCs are shown in Figures 3.4.4 and 3.4.5. These intermetallic segregants were primarily rich in Fe and Cu, although other segregants were found to be rich in Mg and Si eutectic. Eutectic and intermetallic bridging between fibers was observed for the G/6061 Al MMCs (see Figure 3.4.6). Bridge formation or fiber bonding, a result of solute segregation, has been shown to drastically reduce the strength of fibers in composites [Cornie, et al. 1991].

Figure 3.4.7 shows crevice formation occurring in a G/6061 Al MMCs after etching. Later, similar crevices were found to occur during anodic polarization testing of the same composite specimens. When comparing unetched photos of the same samples, Figures 3.4.1c and d, it is apparent that the crevices were of the same frequency and size as the observed Al_4C_3, suggesting that the dissolution of Al_4C_3 acts as a pipeline for crevice corrosion in G/6061 Al MMCs. In Figure 3.4.8, an Al_4C_3 platelet was apparently in the process of dissolving at the fiber interface (i.e., it was found to contain only Al from EDAX analysis). In the matrix, small ($<0.5\mu m$) black pits are prevalent as a result of the acid etch.

After exposure to the etch, crevice corrosion around PAN-based graphite fibers in a G/Al-4wt.% Cu MMC (see Figure 3.4.9) was not as significant as it was for the specimens with the 6061 Al matrix. It seems that the edges of the fibers after etching were serrated, and indicate that the fiber may have reacted in a different manner as that of the pitch-based G/6061 Al MMCs. The backscattered electron image (see Figure 3.4.9) shows white interfacial eutectic $CuAl_2$, in a recessed rough matrix. It was difficult to find islands or pools of segregated alloy in middle of interstices; however, eutectic segregation of Cu-rich Al can be seen around the serrated fiber edges. This was also found in the backscattered electron image for the G/Al-2% Cu MMC with Mg and Mn additions (see Figure 3.4.10). The matrix alloying elements Mg and Mn were not detected at the interface in the analysis, possibly because they were below the sensitivity of the instrument. Figure 3.4.11 shows how the G/Al-2% Cu MMC with Mg and Mn additions was far more susceptible to pitting when etched than specimens with a 6061 Al matrix. The pits were on the order of ~2μm in diameter and were ubiquitous between fiber interstices. The pits were most likely formed in regions where greater concentrations of Cu were present; SEM EDAX analysis is not able to discern the composition difference on such a fine scale. The solubility of Cu in Al is approximately 0.3 wt.% at room temperature (see Appendix E).

Porosity occurred in a particularly large Al channel for the G/Al-5% Zn MMC (see Figure 3.4.12). No increase in Zn concentration was detected near the void. This particular Al channel was later observed to be the site for increased oxide formation after exposure to NaCl solution, which will be discussed in Chapter 5.

Hihara [1989] found that upon anodic polarization of monolithic fibers mounted in epoxy, caverns often resulted on the surface of graphite fibers. This was attributed to the evolution of CO_2 and CO gases from oxidized graphite fibers surfaces. A similar phenomenon was observed with PAN-based G/Al MMCs upon etching and exposure to aerated NaCl solution. A cavern or fissure formed as a result of etching is shown in Figure 3.4.13.

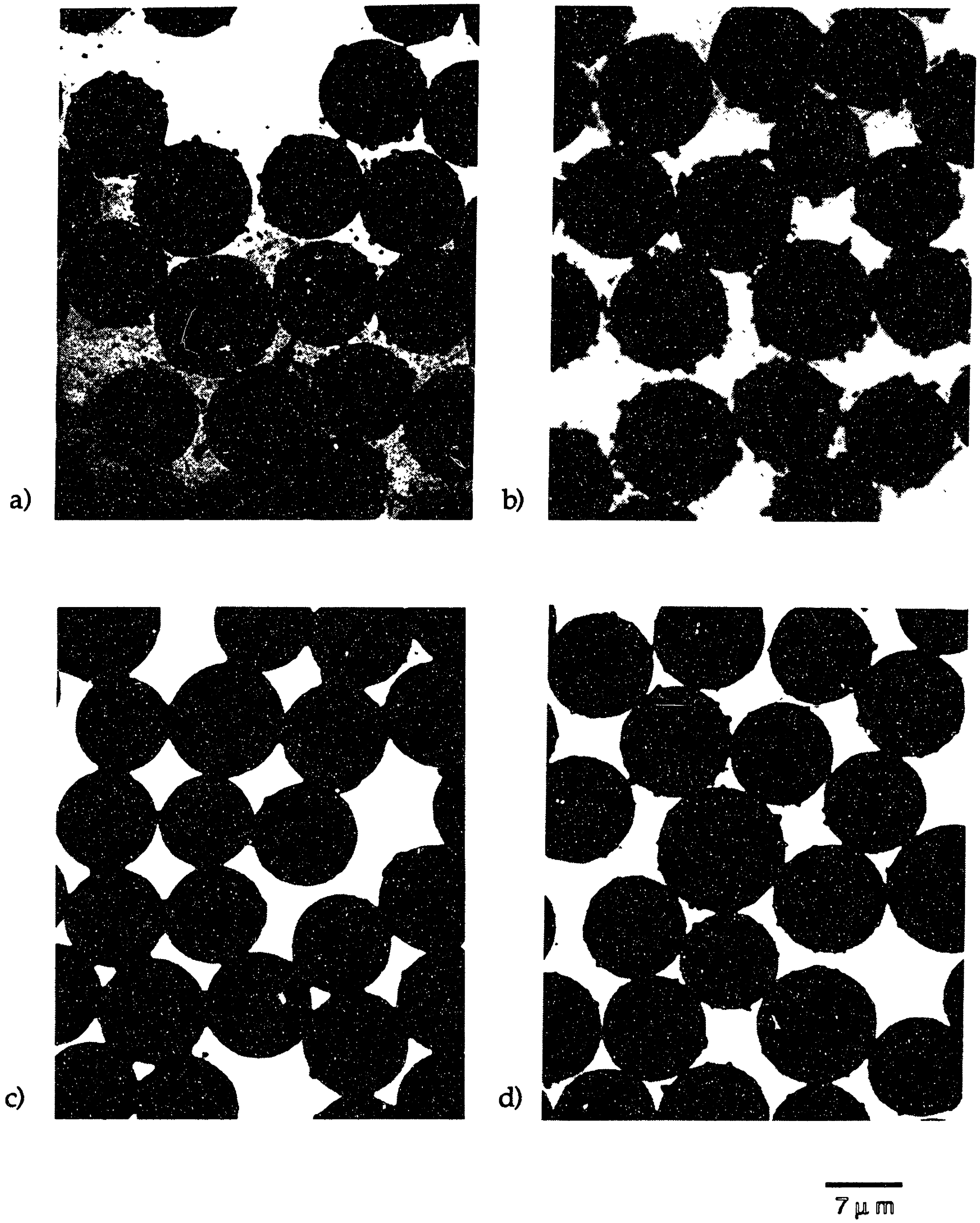

Figure 3.4.1: Transverse cross-sectional optical micrographs of G/6061 Al MMC specimens: a) 6, b) 7, c) 8, and d) 9, before metallographic etching. Notice aluminum carbide platelet at graphite fiber interfaces.

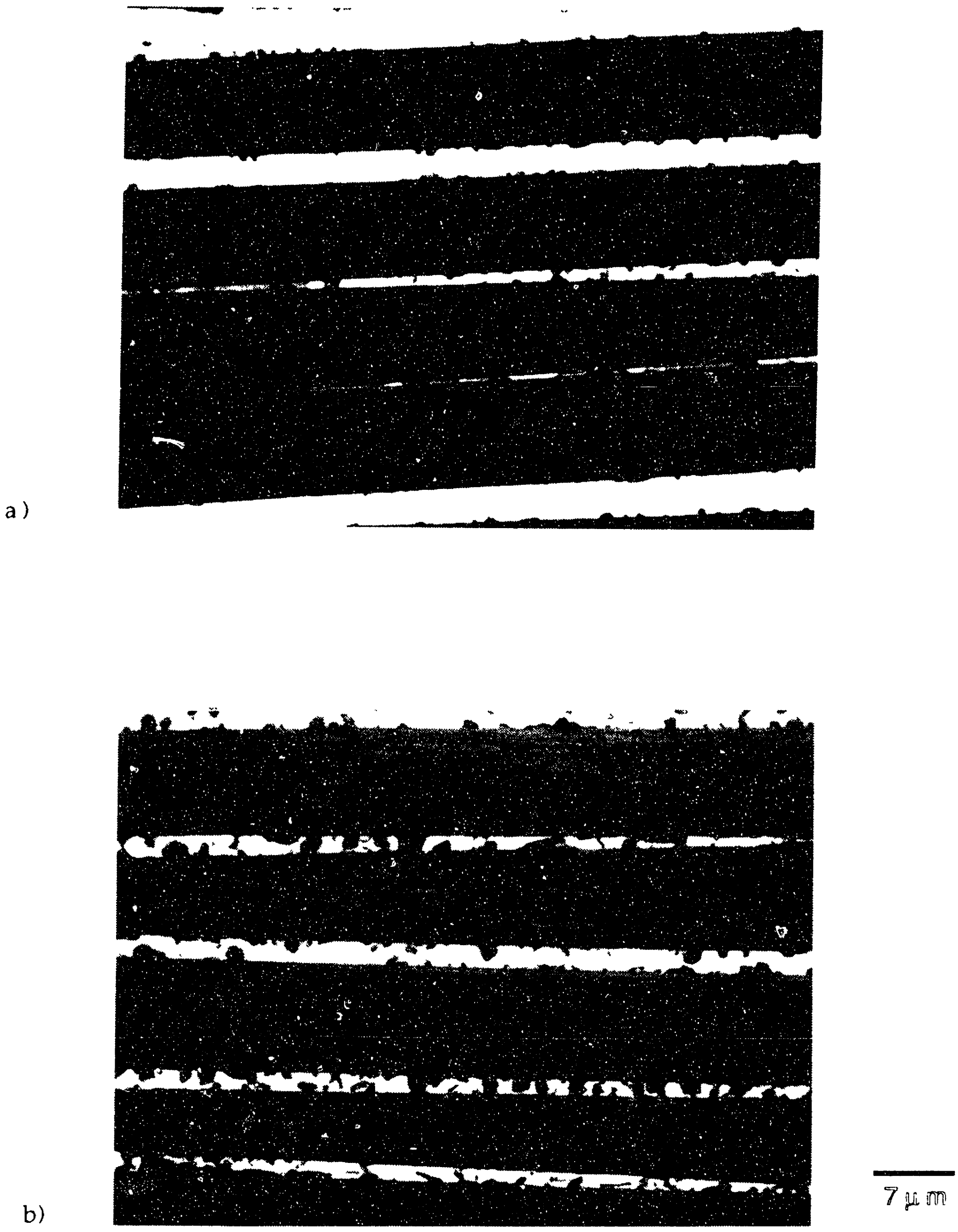

Figure 3.4.2: Longitudinal cross-sectional optical micrographs of G/6061 Al MMC specimens before etching: a) Specimen 6 and b) Specimen 7.

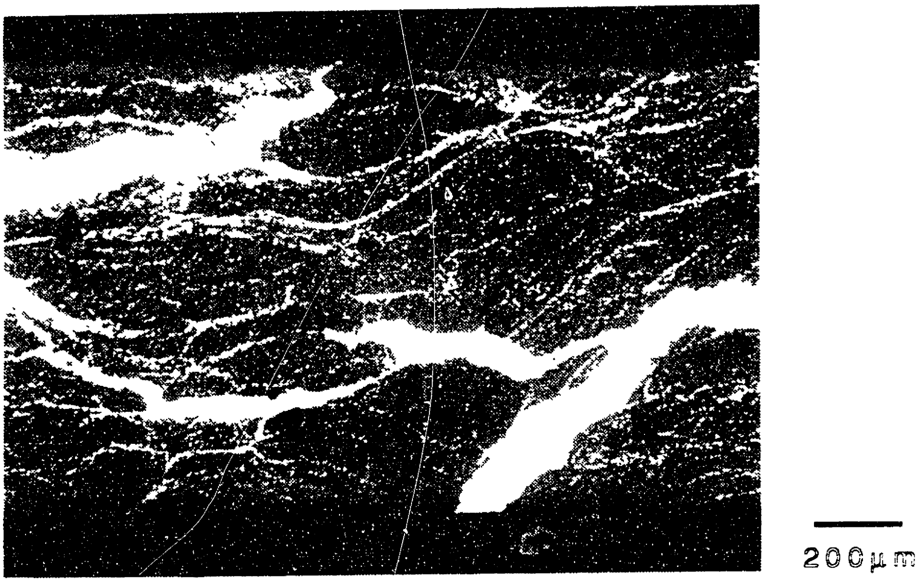

Figure 3.4.3: Transverse cross-sectional optical macrograph of the G/6061 Al MMC before etching (Specimen 8), showing Al matrix channelling.

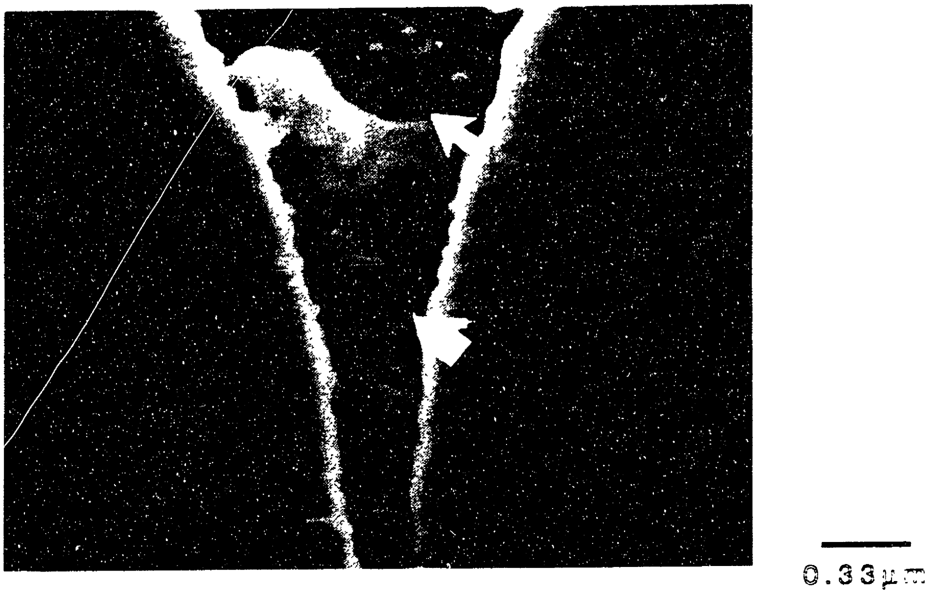

Figure 3.4.4: Secondary electron SEM micrograph showing Fe and Cu-rich intermetallic in narrow interstice of a G/6061 Al MMC after etching (Specimen 8).

Figure 3.4.5: Secondary electron SEM micrograph showing Fe-rich intermetallic in narrow interstice of a G/6061 Al MMC after etching (Specimen 9).

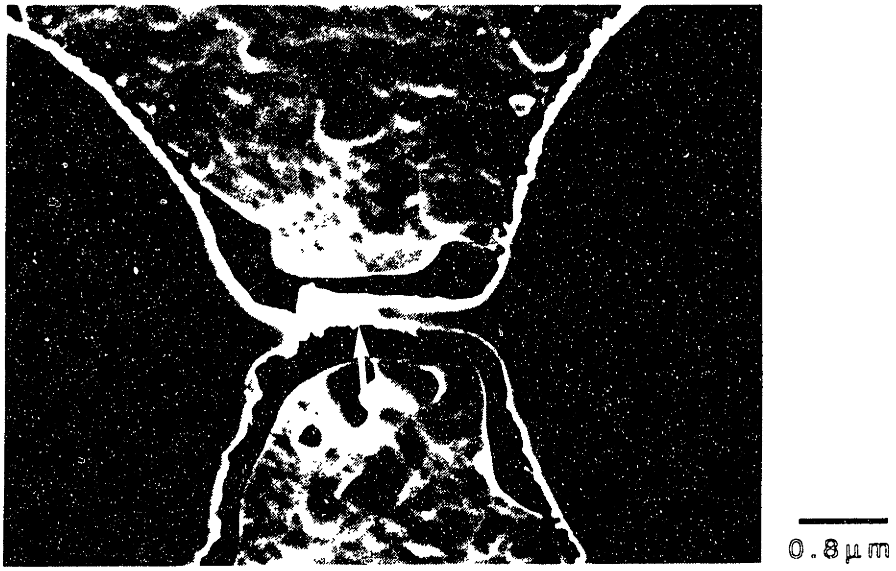

Figure 3.4.6: Secondary electron SEM micrograph showing Fe-rich intermetallic bridge between fibers in an interstice of a G/6061 Al MMC after etching (Specimen 9).

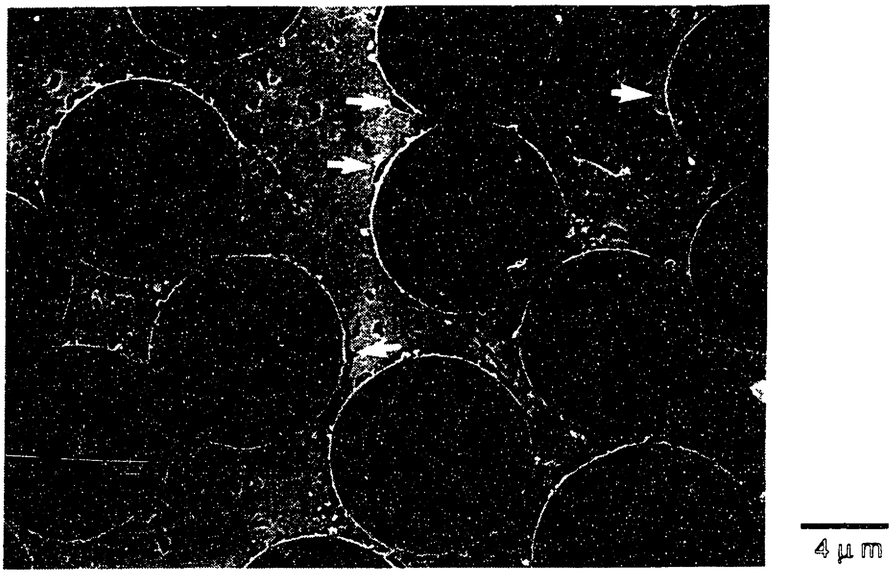

Figure 3.4.7: Secondary electron SEM micrograph showing crevice formation (black) at fiber-matrix interface for a G/6061 Al MMC after etching (Specimen 9).

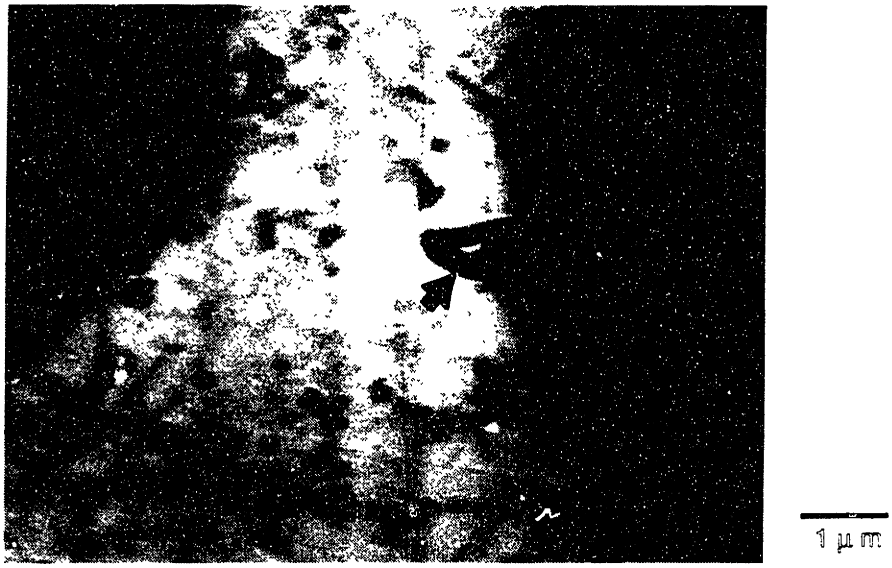

Figure 3.4.8: Backscattered electron SEM micrograph showing crevice formation (black) initiating at Al_4C_3 platelet at the fiber-matrix interface for G/6061 Al MMC after etching (Specimen 8).

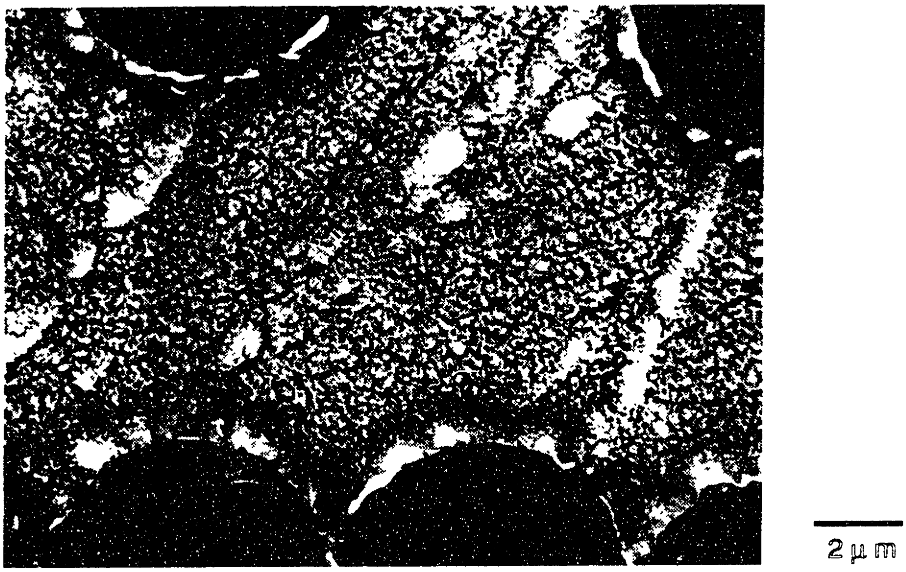

Figure 3.4.9: Backscattered electron SEM micrograph showing interfacial $CuAl_2$ (white) for the G/Al-4% Cu MMC after etching (Specimen 21).

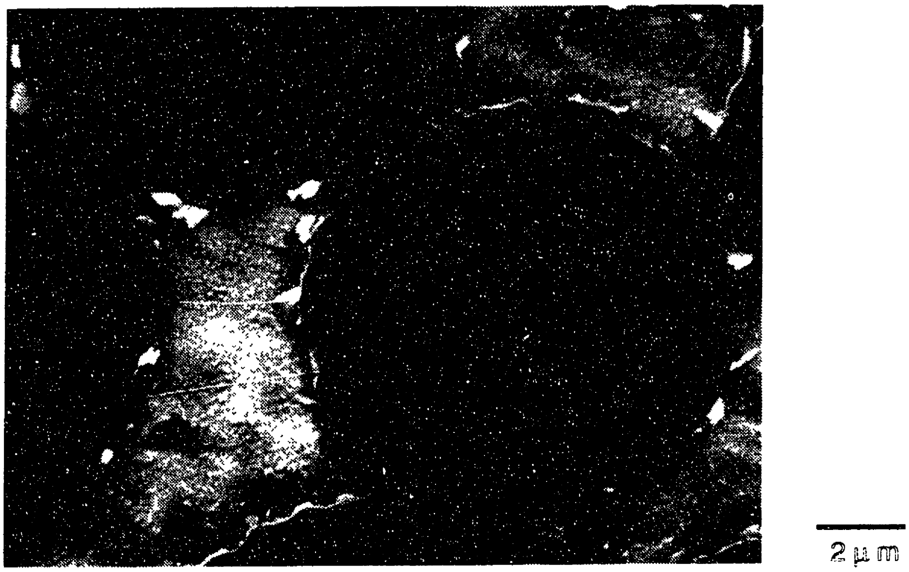

Figure 3.4.10: Backscattered electron SEM micrograph showing interfacial $CuAl_2$ (white) for a G/Al-2% Cu MMC with Mg and Mn additions after etching (Specimen 22).

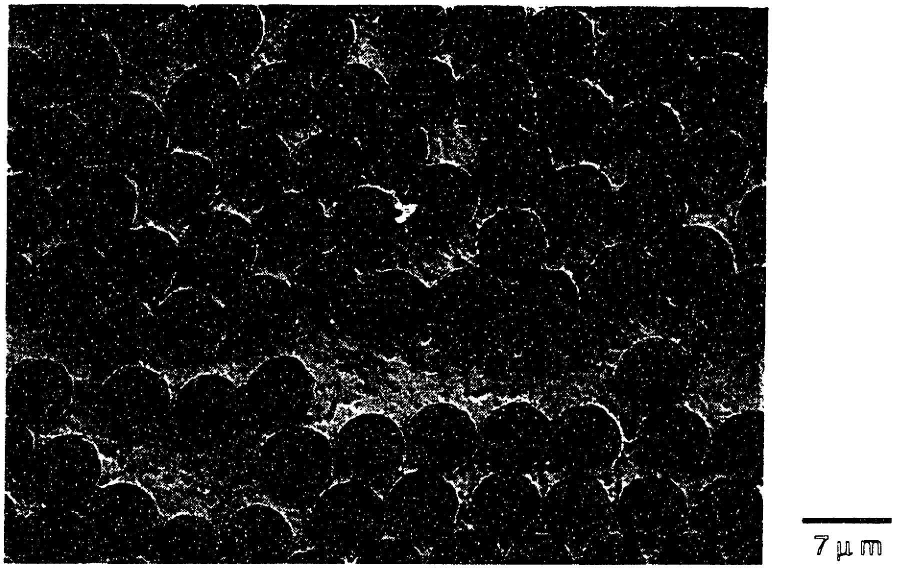

Figure 3.4.11: Secondary electron SEM micrograph showing finely-dispersed pitting phenomenon for a G/Al-2% Cu MMC with Mg and Mn additions after etching (Specimen 22).

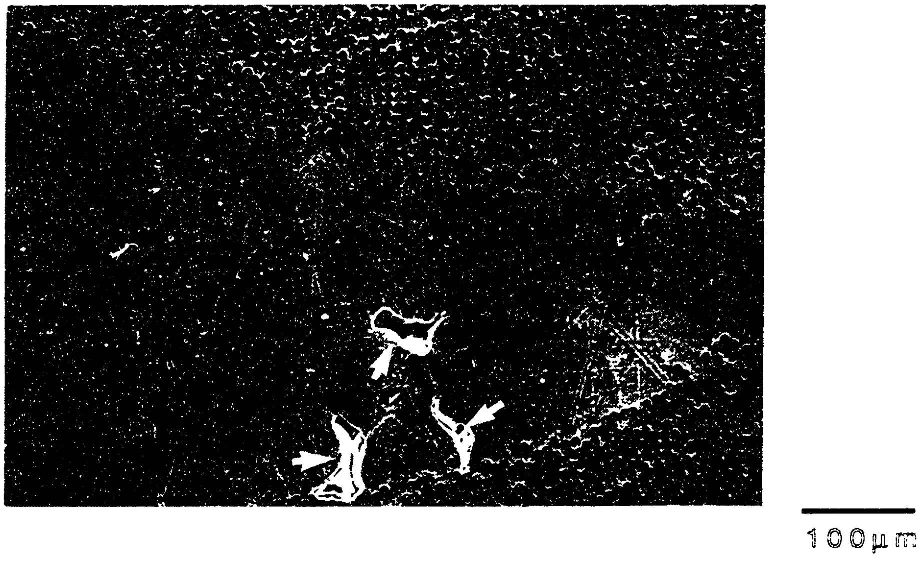

Figure 3.4.12: Secondary electron SEM micrograph showing Al channel with void formation in a G/Al-5% Zn MMC after etching (Specimen 13).

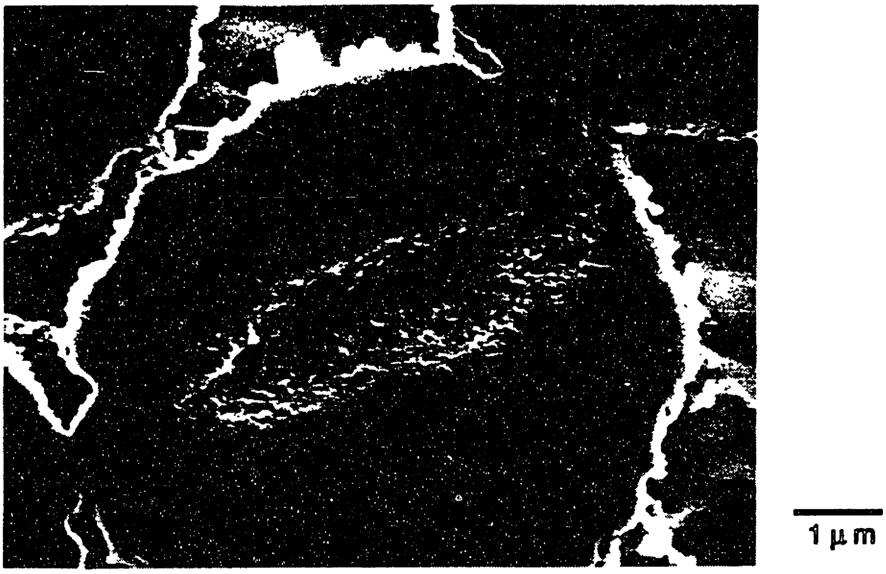

Figure 3.4.13: Cavern formation on fibers as result of acid etch in a G/Al-5% Zn MMC (Specimen 13). A similar phenomenon was observed by Hihara [1989] for anodically polarized fibers.

4. DC ELECTROCHEMISTRY OF G/Al MMCS

4.1 INTRODUCTION

The major emphasis for this work was to establish the validity of the mixed-electrode theory for predicting the anodic polarization behavior for continuous fiber composites. This section attempts to determine which processing and material parameters effect the electrochemistry of the G/Al MMCs. One of the questions that this chapter seeks to answer is, "How strongly does Al_4C_3 content effect the dissolution characteristics in G/Al MMCs?"; while another goal was to uncover processing and materials selection parameters which could help designers produce chemically stable composites in simulated fresh and salt water environments.

In order to accomplish these goals, direct current (DC) potentiostatic tests at near equilibrium conditions were conducted on the several variations of commercial G/Al MMCs including: anodic polarization testing in deaerated Na_2SO_4 and NaCl solutions, and cathodic polarization in aerated NaCl solution.

4.2 EXPERIMENTAL

4.2.1 Electrodes

G/Al MMCs specimens were pre-polished with 600 grit Carbimet® [Buehler Ltd., OH] silicon carbide grinding paper to remove any Al foil or 'skin' which may have been a result of infiltration processing or subsequently added to protect composites against corrosion. The cross-sectional area of the composites studied had a transverse cross-sectional area equal to or greater than ~$0.15 cm^2$ in order to reduce edge effects during polarization. The electrical contact to composite specimens was made by attaching a 24 gauge copper wire to the back of a specimen by means of silver paint; thereafter, the contact was covered with a dab of 5 Minute Epoxy® [Devcon Corp., MA] to insure the mechanical strength of the contact. The specimen was then painted with two coats of Amercoat® 90 [Ameron Inc., CA], an oxide paint that protects against crevice formation on the sides of specimens in contact with the mounting medium, a result of mounting resin shrinkage. Thereafter, the specimens were encapsulated in Epon® 828 Resin [Shell

Chemical Co., TX] with a slow cure rate (~7 days). The encapsulated specimen was mounted to a 7mm outer diameter Pyrex® [Corning Glass Works Inc., NY] glass tube which contains and protects the extended copper wire from interfering with electrochemical measurements (see Figure 4.2.1). The glass tube was mounted with water-insoluble clear Epoxy-Patch® [Dexter Corp., NH]. Since Hihara [1989] has shown that intercalation of G/Al MMCs can effect subsequent polarization tests (Figure 2.2.3), care was given to remove at least 3mm of each specimen after having been polarized. In order to accomplish this, a permanent ink marker was used to mark the side of the electrode on the Epon® 828 Resin mount, 3mm from the composite surface by means of a caliper, thereafter, polishing was carried out to remove the mark completely [Hihara, 1990]. Since the fibers in the composites had approximately 10μm in diameter, it was necessary to polish the specimens to 0.3μm with gamma Al_2O_3 powder in distilled water. Specimens were rinsed before polarization testing.

All electrodes were prepared by the aforementioned process, which has been used extensively in the H. H. Uhlig Corrosion Laboratory at MIT. The reason for using the elaborate and often time consuming process was to alleviate problems associated with crevice formation and to gain control of polishing by having a mounted specimen. However, there are also drawbacks in using these electrodes: the inability to take micrographs after polarization without cutting the sample from the fabricated electrode, the production of scratches during fine-polishing that result from the abrasion of the oxide Amercoat® 90 surrounding the specimens, and the inability to control the angle of the polishing surface with relation to the encapsulated specimen, that is, the specimen, with a connected glass rod, must be polished by hand.

4.2.2 DC Polarization Apparatuses

The two electrochemical cells employed were based on a modifyed Pyrex® glass Florence flask. A schematic of the modified cell is given (see Figure 4.2.2). The reference potential was monitored approximately 2mm from the surface of the specimen by means of a Luggin probe electrolytically connected to a Cole-Parmer ceramic junction saturated calomel electrode (SCE). This reference electrode was used for all electrochemical experiments conducted.

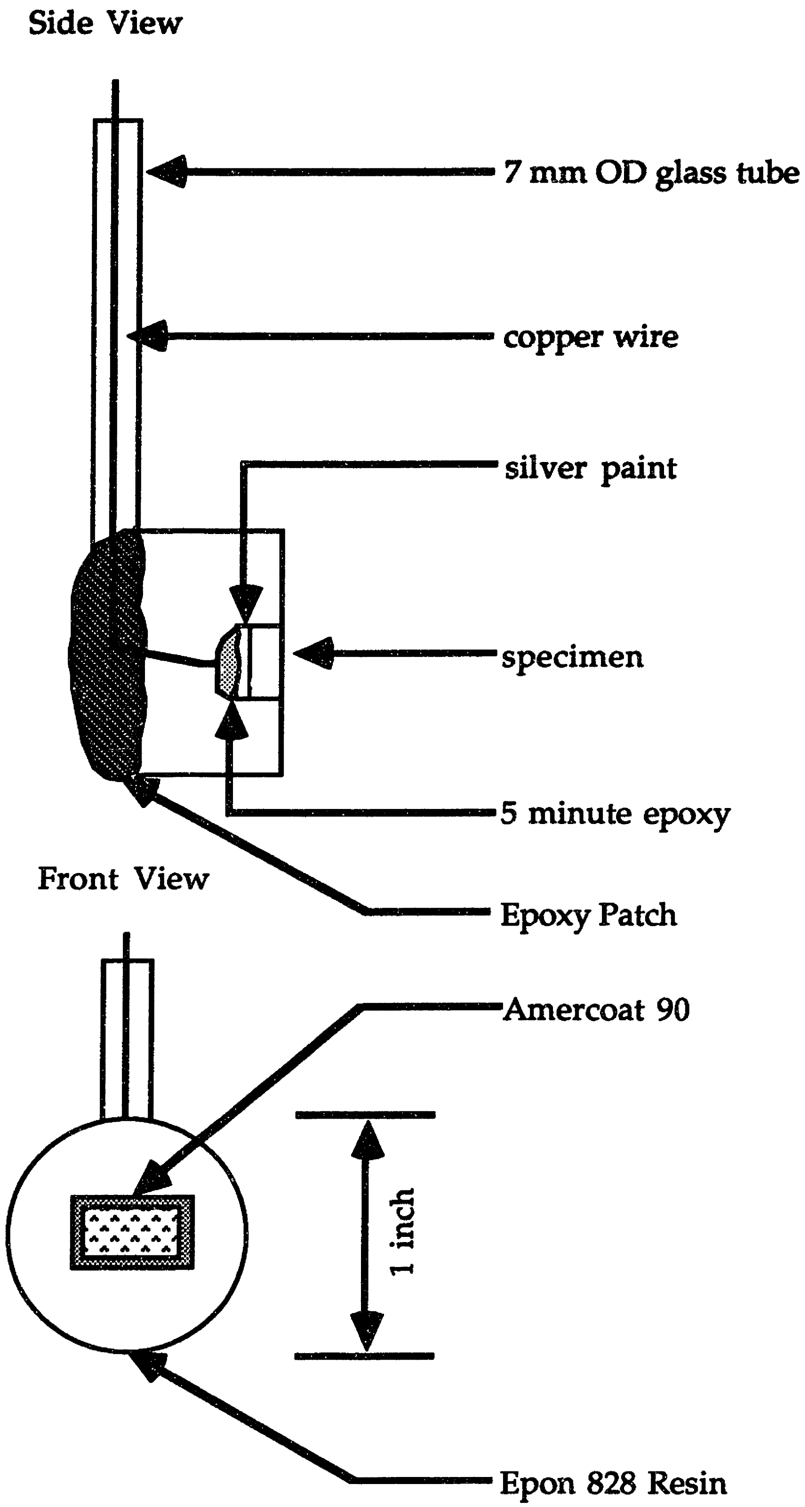

Figure: 4.2.1: Electrode designed to hold composite without crevice formation. [Kloppers, 1991, p.101]

Therefore, all reference potential values are given relative to the saturated calomel reference electrode. For Na_2SO_4 solutions, a K_2SO_4 salt bridge was employed in order to ensure that no chlorides from the KCl reference electrode would enter the electrochemical cell (see Figure 4.2.3). The salt bridge medium was a mixture of 8gm of agar, 6gm of K_2SO_4 mixed and 200ml of 18 MΩ·cm water. A platinum 'screen' counterelectrode was employed, since it offered a greater surface area than compared to "thin-foil" type counterelectrodes.

The cell temperature was maintained at 30±0.2°C by a Cole-Parmer Lab Monitor® III thermoregulator, connected to a nichrome wire heating coil located in the electrochemical cell (see Figure 4.2.2). Power was supplied by a Staco Energy Products type 3P1010 variable auto transformer set at 10-15 V AC. The Lab Monitor ® III was modified to switch the power output from the auto transformer to minimize electrical noise.

Polarization of commercial G/Al MMCs was accomplished with a Model 273 EG&G Princeton Applied Research (PAR) potentiostat, which had a built-in logarithmic converter. The accuracy of the current measuring capability and output were measured, by means of a series of standard resistors. Metered currents were accurate to 3% from the true theoretical currents. The smallest currents measurable were on the order of 1×10^{-9} A (1 nA).

Open circuit potentials (Ecorr) were monitored and recorded with a Fischer x-time plotter for approximately 30 minutes or until an equilibrium value was attained. The potential-current output for electrochemical tests was recorded with a Hewlett Packard 7044 B X-Y chart recorder. The results were not corrected for IR drop, since the conductivity of the electrolytes employed was relatively high.

4.2.3 Electrolytes

In order to compare results on G/Al MMCs studied by Hihara [1989], it was decided that the same electrolytes should be used for polarization studies; these were neutral (~pH= 7) 0.5 M Na_2SO_4 and 3.15 wt.% NaCl solution; these solutions are often used to simulate fresh water and sea water solutions, respectively. Solutions were prepared with purified water with a minimum resistivity of 18 MΩ·cm, and deaerated for a minimum of 30 minutes before test initiation by sparging with pre-purified hydrogen containing less than 5ppm oxygen.

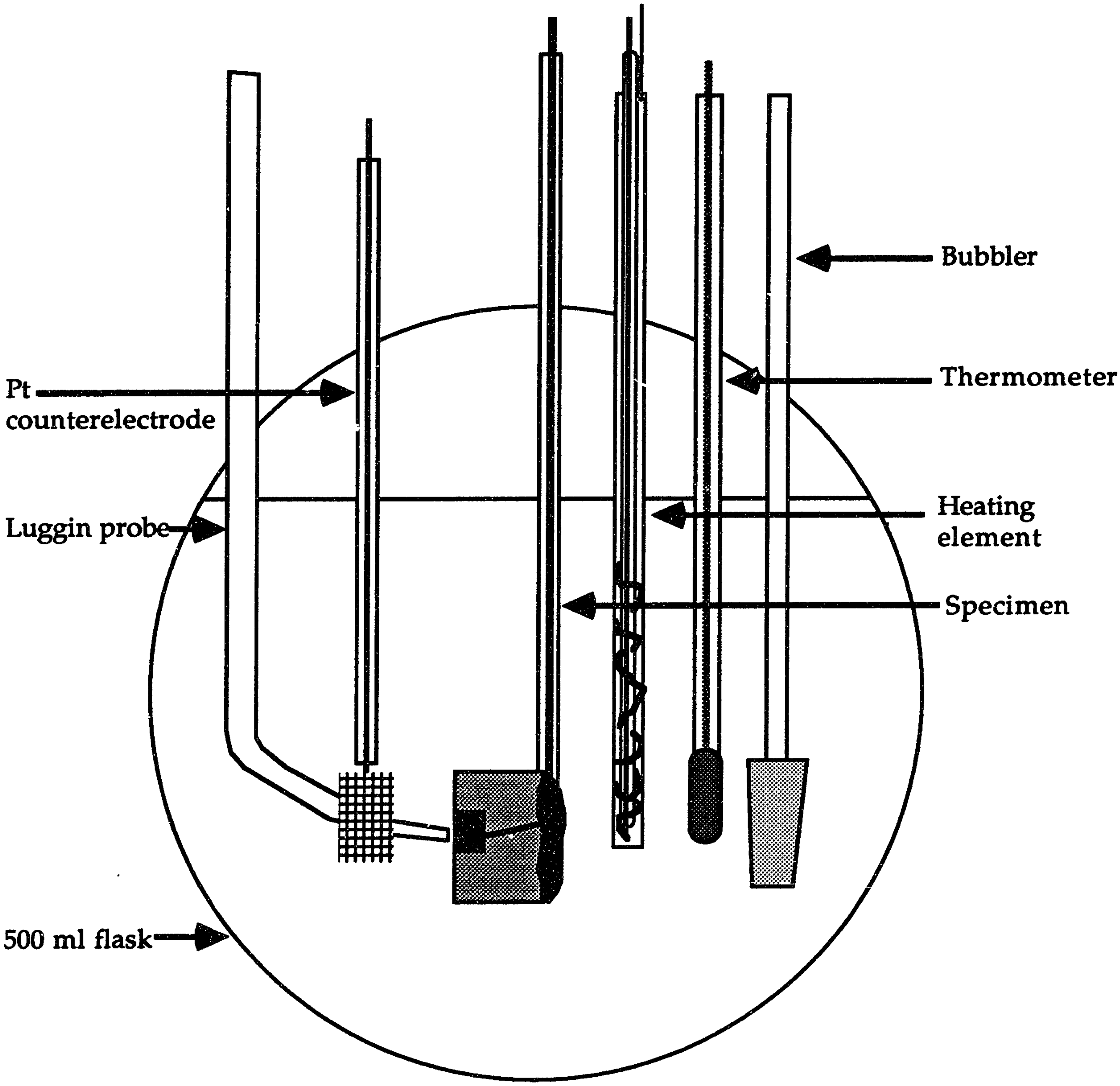

Figure: 4.2.2: Schematic of electrochemical cell used for DC polarization. [Kloppers, 1991, p.102]

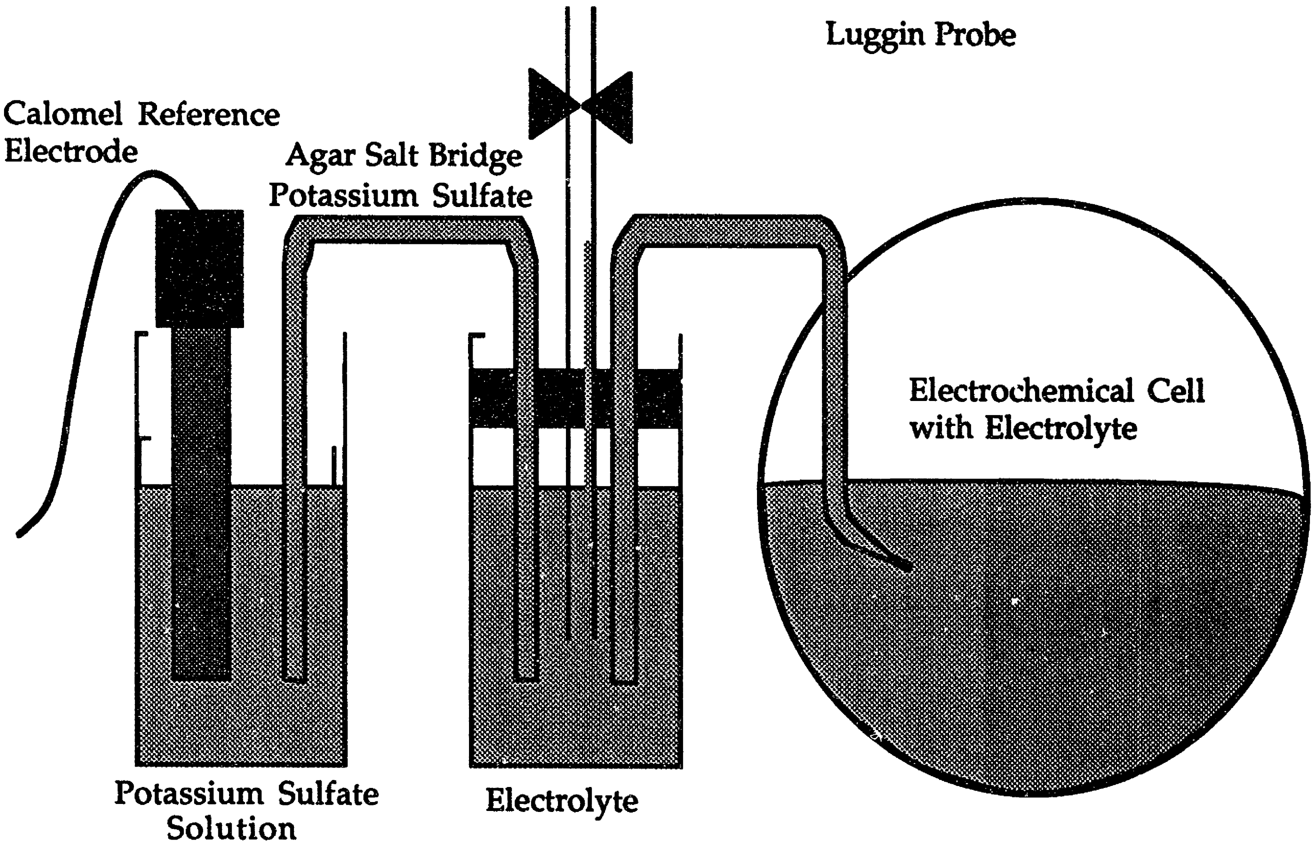

Figure 4.2.3: Schematic diagram of the salt bridge arrangement used to prevent the intrusion of chloride into the electrochemical cell.

[Kloppers, 1981, p.156]

4.2.4 Polarization Procedures

Anodic polarization of 430 stainless steel in deaerated 1N H_2SO_4 was performed to determine the apparatus reliability [Annual Book of ASTM Standards, 1991b]. The results were reproducible and gave the accepted current potential relationship. All electrodes were allowed to stabilize at their corrosion potentials (Ecorr) and were subsequently polarized at a rate less than 0.167±5% mV/sec, in accordance with the aforementioned standard. At least three individual tests were performed for each commercial MMC studied in anodic polarization with deaerated 0.5M Na_2SO_4 solution. The individual polarization graphs also show the peak-to-peak width of the standard deviation as error bars, equal to two times the standard deviation in the log i values, and can be found in Appendix F. Ecorr values are given in the caption with standard deviation for individual polarization scans. Standard deviation bars for comparison diagrams were omitted to avoid confusion. Only two tests were performed for deaerated NaCl polarization tests, and the average of the two is given with no error bars. Because Al is amphoteric, there was an unusually large standard deviation in the open circuit potential, even with the removal of several millimeters of material. The presence of fibers, alloy constituents in Al, and the nature of the alumina film formation on the surface affected the open circuit potential.

Cathodic polarization scans in aerated 3.15 NaCl solution (see Section 4.5) showed deflection in the width to width current density measurements on the order of one to two current decades. This is related to the breakdown and repassivation of the alumina film over Al in the pressure of chlorides. Therefore, the plotted log i current densities were taken from the center of the recorded curve.

Cyclic polarization studies were carried out on select specimens to determine the ability of G/Al MMCs to repassivate. Standard cyclic polarization requires polarization reversal at 5 mA/cm^2 [Annual Book of ASTM Standards, 1991c].

Table 3.2.1 in Chapter 3 gives the characteristics of most of the composites which were electrochemically studied; in addition, G/Al-Cu MMCs with different graphite fibers and various Cu additions in the Al matrix (see Table 4.2.1) were also electrochemically studied. Al_4C_3 was not quantified for the samples in Table 4.2.1. Graphite fibers used for Specimens 14-17 were higher in modulus and strength than those used for Specimens 19-22. Fibers for Specimens 14-17 came in fiber tows of 12,000 fibers each, and with an epoxy sizing of 1% the fiber diameter (see Table 4.2.1). Commercial suppliers will not disclose the composition of the sizing. Because graphite fibers are heated above 600°C before infiltration, it is believed that the sizing is completely removed by volatilization. This may not strictly be true, since some elements may be trapped in the basal planes of the graphite because of the relative ease of intercalation of graphite fibers.

Table 4.2.1: G/Al MMCs with Cu Alloy Additions

Spec. #	Al Matrix and alloy in wt.%	Vol.% Fiber	Fiber Type	Fiber E mod.	Fiber UTS	% e to failure	Lab. Code
14	0.5 Cu	~63%	PAN-based *Courtaulds EHMS 12k 1E diam.= 6.8 µm.	390 GPa 56.6 Msi	3.2 GPa 464 ksi	0.8	213A
15	1.0 Cu						214A
16	4.0 Cu						215A
17	2.0 Cu 0.7 Mg 0.3 Mn						216A
18	2.0 Cu 1.0 Mg 0.5 Mn	~62%	PAN-based †Torayca M40 3k diam.= 6.5µm.	392 GPa 56.8 Msi	2.74 GPa 397.3 ksi	0.7	217
19	0.5 Cu	~63%	PAN-based Courtaulds EHMS 10k 0.7E diam.= 7.8µm.	340 GPa 49.3 Msi	2.5 GPa 363 ksi	0.73	213D
20	1.0 Cu						214D
21	4.0 Cu						215D
22	2.0 Cu 0.7 Mg 0.3 Mn						216D

*Courtaulds Inc., U.K. †Toray Inc., Japan
Composites were fabricated at Alumiinium Ranshofen,Ges. m. b.H., Ranshofen, Austria

Previous work on G/Al MMCs [Hihara, 1989; Buonanno, et al., 1991] suggests that the corrosion behavior of the composites is strongly related to the processing conditions employed during fabrication. The processing parameters used for the production of G/1100 and 6061 Al MMCs, determined in Chapter 3, will be compared with the electrochemical behavior of the composites.

4.2.5 Anodic Polarization and Mixed-Electrode Theory

The mixed-electrode theory states that the absolute value of the total sum of cathodic current must equal the total sum of the anodic current. In the case of a G/6061-T6 Al MMC of 50 vol.% fiber (see Figure 4.2.4), predicted behavior is achieved mathematically by adding 50% of the anodic current density values of graphite fiber to 50% of the anodic current density values of 6061-T6 Al, attained from separate anodic polarization experiments performed on graphite fibers and monolithic 6061-T6 Al in deaerated 0.5M Na_2SO_4 [Hihara, 1989]. Prediction can also be made for differing vol.% fiber of material by multiplying and dividing by the appropriate fractions.

It is important to note that at low overpotentials above Ecorr, Al is predicted to contribute more to the passive current density than graphite fibers, until about 700 mVsce (see Figure 4.2.4), where the contribution from fiber oxidation, evolving CO_2 and CO gases, begins to predominate. Therefore the contribution to the current density from Al to the predicted current density, will be greater at low anodic overpotentials.

The log i current measurements taken have been normalized with respect to the cross-sectional areas of the specimens. This is the standard method of reporting current densities: with composites there is an additional problem, the vol.% of fiber constituents can alter the relative magnitude of the passivation and dissolution current densities.

In polarization measurements, the vol.% fiber of the composites must be considered. When producing G/Al MMCs by pressure infiltration, it is difficult to control the vol.% fiber of constituent due to fiber displacement during infiltration. While comparing the anodic polarization behavior, attention will be given to specimens which significantly deviated from other specimens in vol.% fiber.

Figure 4.2.5 shows the predicted anodic polarization behavior from mixed electrode theory for 50, 55, 60, 65, and 70 vol.% fiber G/6061-T6 Al MMCs obtained from modification of the data determined by Hihara [1989].

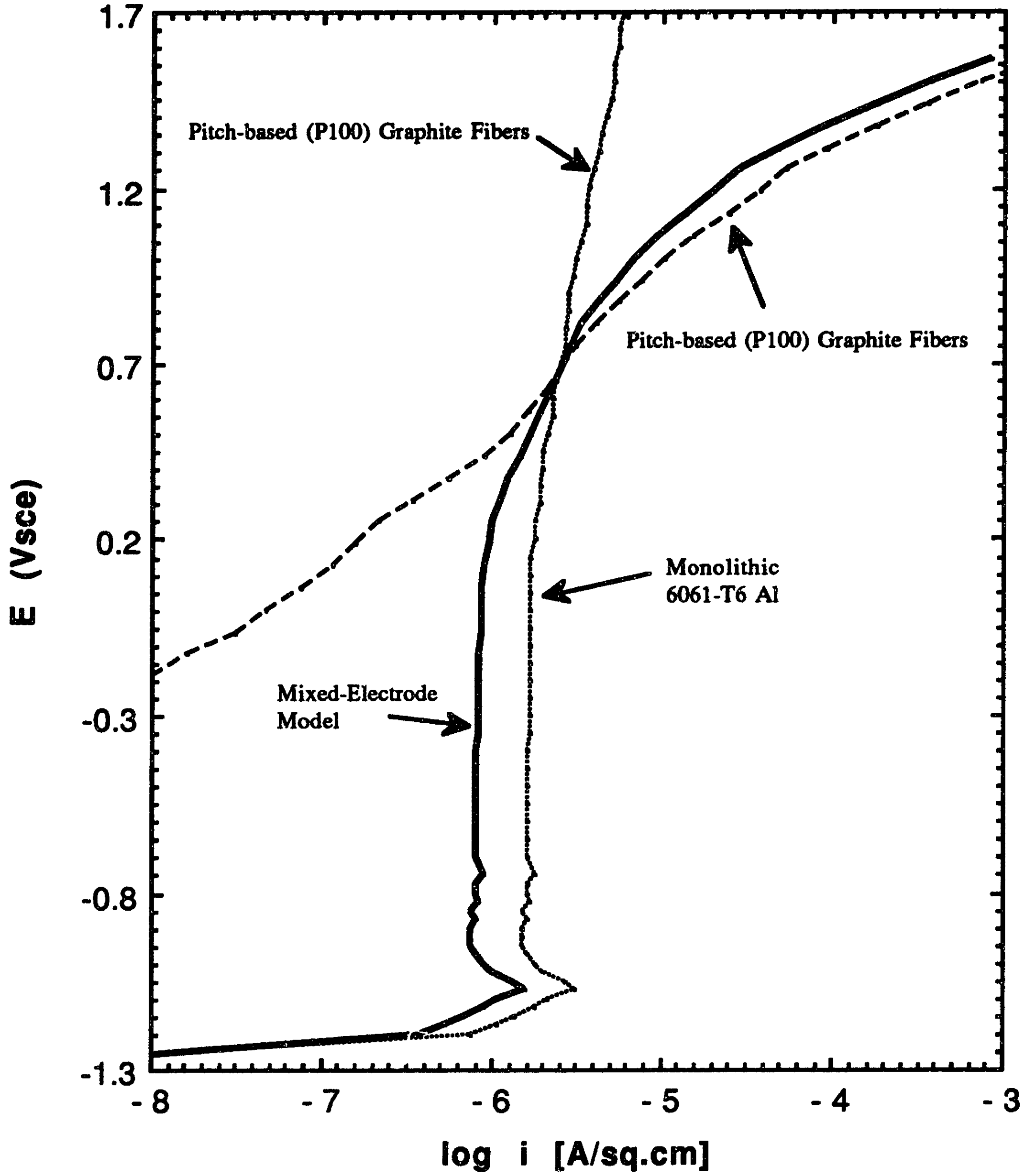

Figure 4.2.4: Generation of an anodic polarization diagram of a 50% pitch-based (P100) graphite fiber/6061-T6 Al composite based on the mixed-electrode model in deaerated 0.5M Na_2SO_4 solution of pH 7 at 30°C. Scan rate = 0.1 mV/s. [Hihara, 1989, p.152]

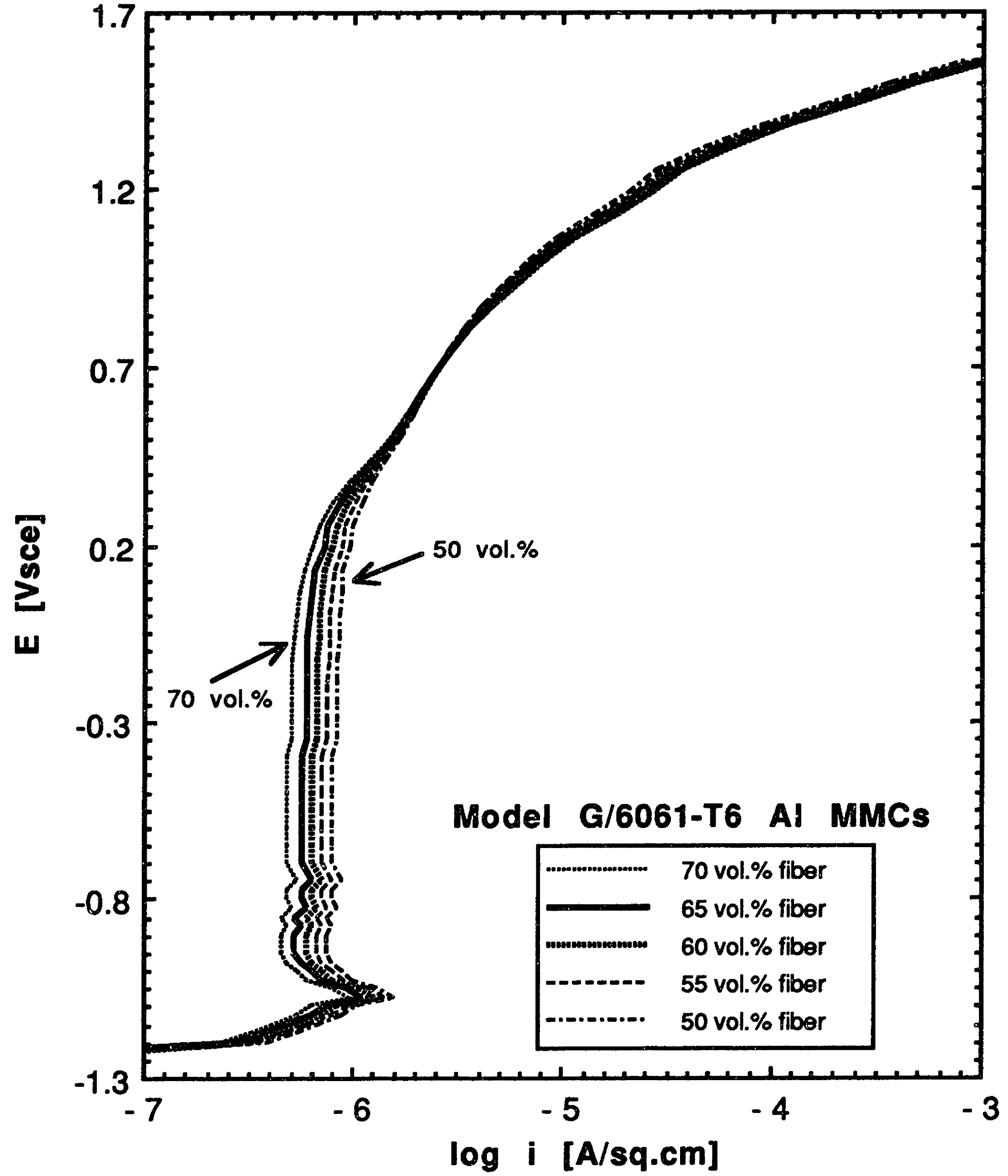

Figure 4.2.5: Generation of an anodic polarization diagram of a pitch-based (P100) graphite fiber/6061-T6 Al composite varying in volume fraction fiber as shown, based on the mixed-electrode model in deaerated 0.5 M Na_2SO_4 of pH 7 at 30°C. Scan rate = 0.1 mV/s.

The difference between using monolithic 1100 Al and 6061-T6 Al alloys in G/Al MMCs is negligible on the predicted anodic polarization behavior in deaerated 0.5 M Na_2SO_4 solution. The passive current densities of the two monolithic alloys were nearly identical (i.e., 2μA/cm^2 for 1100 Al and 1.6μA/cm^2 for monolithic 6061-T6 Al; the 6061-T6 Al actually had a smaller passive current density [Hihara, 1989]) in deaerated 0.5 M Na_2SO_4 solution. Using 1100 Al as opposed to 6061-T6 Al in G/Al MMCs would result in transposition of the predicted behavior curve by +0.1 log i A/cm^2 at low anodic overpotentials. In more aggressive environments (e.g., NaCl solution), the corrosion behavior of these alloy matrices is markedly different. In the case of more aggressive environments, one must obtain separate results from the individual matrix alloy and graphite fibers, plot them additively and then discern any appreciable differences in the commercial composites behavior from that predicted by mixed-electrode theory.

4.3 RESULTS OF ANODIC POLARIZATION IN DEAERATED 0.5M Na_2SO_4

4.3.1 G/1100 Al MMCs

The individual anodic polarization diagrams with standard deviation bars for G/1100 Al MMCs (Specimens 1-4: Table 3.2.1) appear in Appendix F. A comparison among these materials is shown in Figure 4.3.1. The vol.% fiber of Specimens 1, 2, 3 and 4 were 55, 65, 66.7, and 69.2, respectively. Examination of Figure 4.3.1 reveals that all of the composites passivated spontaneously upon polarization in deaerated 0.5M Na_2SO_4 solution and were under activation control. The G/1100 Al MMCs (Specimens 3 and 4) passivated and maintained a nearly constant passive current density between -1100 to 400 mVsce of 2.5 μA/cm^2. Specimen 2 also readily passivated in the range of -1000 to -300 mVsce, but subsequently, began to shift to higher current densities at potentials above -300 mVsce.

Since the G/1100 Al MMC (Specimen 2) with the highest Al_4C_3 content (89.97 mg/m^2: Table 3.3.1) did not have reduced corrosion resistance, it must be concluded that the corrosion resistance of the G/1100 MMCs was only slightly modified by the presence of Al_4C_3 at the fiber-matrix interface in deaerated 0.5M Na_2SO_4 solutions.

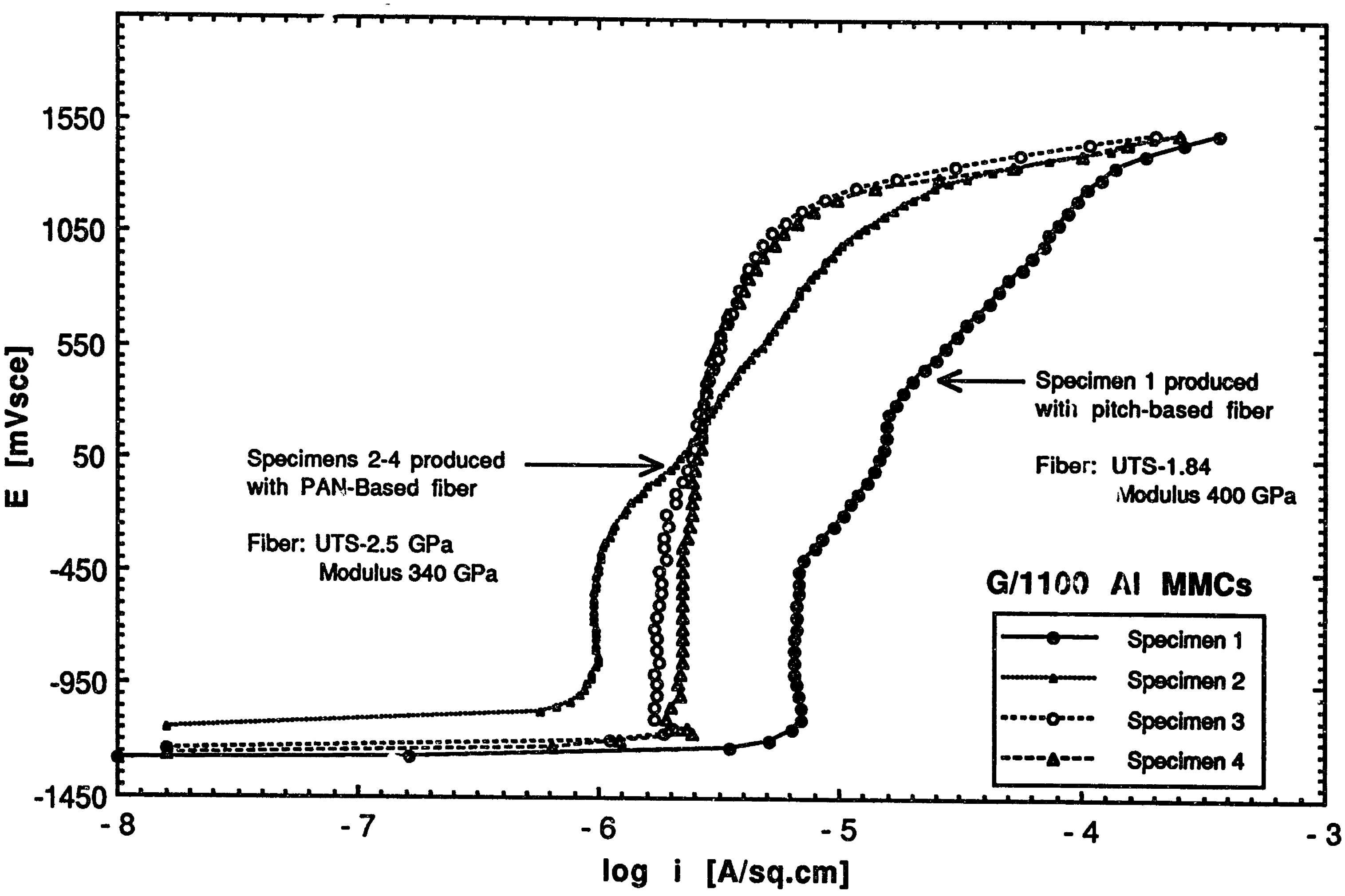

Figure 4.3.1: Comparison of anodic polarization results from G/1100 Al MMCs in deaerated 0.5M Na_2SO_4 solution of pH 7 at 30°C. Scan rate = 0.167 mV/s.

Comparing the anodic polarization curve for the G/1100 Al MMC fabricated with pitch-based fiber (Specimen 1) alongside those fabricated with PAN-based fiber (Specimen 2-4) shows that the curves are of the same general shape; however, the composite with pitch-based fibers had notably higher current densities throughout the anodic polarization scan. It was expected that the pitch-based composite with only 55 vol.% fiber (Specimen 1) would show an increase in passive current density relative to the G/1100 Al MMCs with 65 vol.% fiber. However, the large increase in the magnitude of the passive current density for Specimen 1 in Figure 4.3.1 is not accounted for by the difference in vol.% fiber from the mixed-electrode theory.

Figure 4.3.2 shows the results of anodic polarization at +1200 mVsce for a period of 30 minutes. Anodic potentiostatic polarization of the specimens resulted in little crevice formation, while the radial graphene planes of the fibers were found to preferentially oxidize (see Figure 4.3.3).

4.3.2 G/6061 Al MMCs

The individual anodic polarization diagrams with standard deviation bars for G/6061 Al MMCs (Specimens 5-9: Table 3.2.1) appear in Appendix F. The vol.% fiber of Specimens 5, 6, 7, 8, and 9 were 64, 70, 68, 62, and 74, respectively. Figure 4.3.4 compares the average values for the G/6061 MMCs tested by anodic polarization in deaerated 0.5M Na_2SO_4 solution.

Some G/6061 Al MMCs with pitch-based graphite fibers (Specimens 6, 7 and 9) passivated spontaneously and were under activation control. These specimens had passive current densities which were on the order of 100 $\mu A/cm^2$. In an earlier study performed on a commercial G/6061 Al MMC (Specimens 23: Chapter 6; Table 6.2.1) by Hihara [1989], it was not possible to attain passivation in the same non-aggressive environment under similar conditions due to the presence of residual microstructural chlorides in the microstructure.

Due to poor processing, large Al channels occurred in one G/6061 Al MMC (Specimen 8: see Figure 3.4.3). The inhomogeneity of the composite surface is believed to be responsible for the unusually high current densities attained during anodic polarization of this specimen. Specimen 5 did not have gross

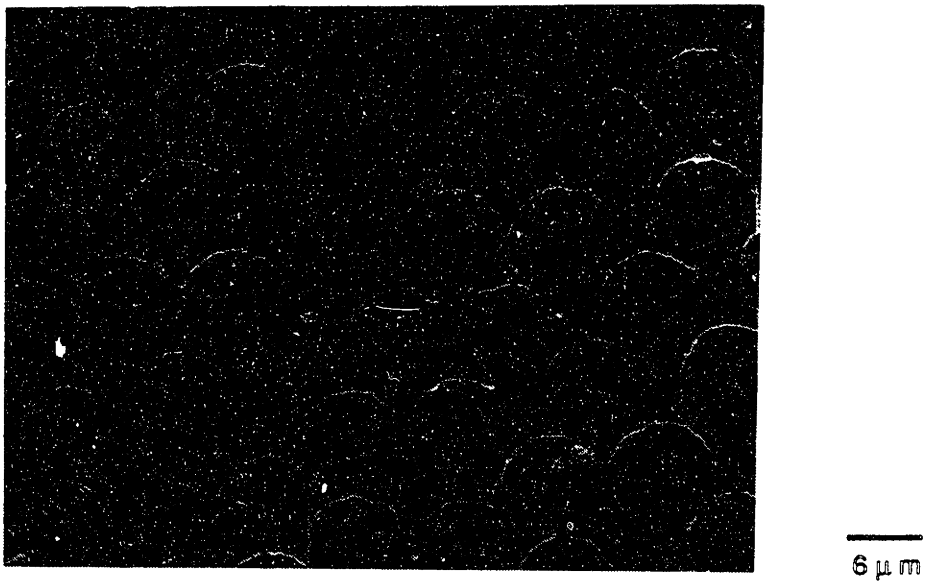

Figure 4.3.2: Secondary electron SEM micrograph of a G/1100 Al MMC (Specimen 4) after potentiostatic polarization. Specimen was maintained at +1200mVsce in deaerated 0.5M Na_2SO_4 solution of pH~7 for a period of 30 minutes.

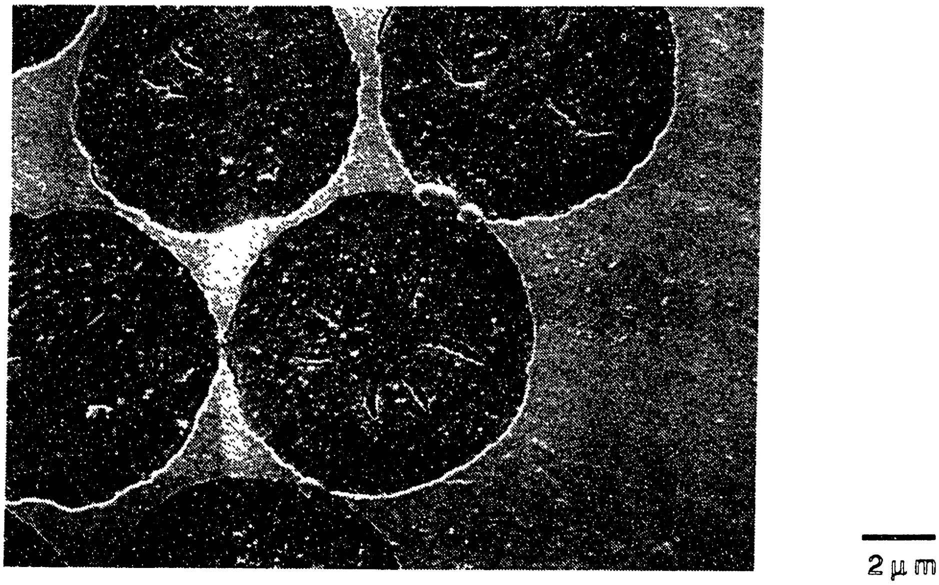

Figure 4.3.3: Secondary electron SEM micrograph at higher magnification of the G/1100 Al MMC in Figure 4.3.2 above. Note the preferential oxidation of the radial graphene planes which occurred.

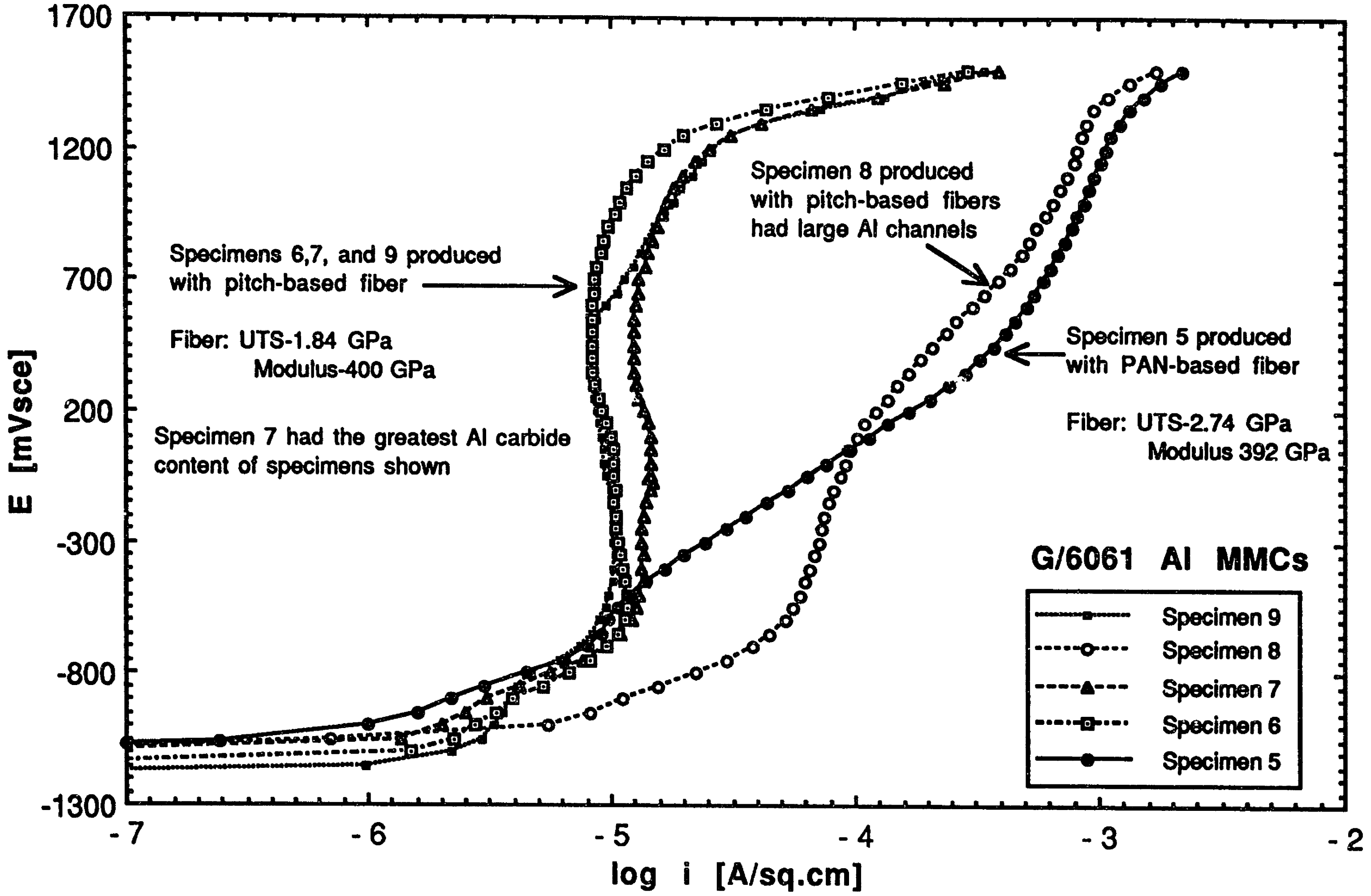

Specimens 6,7, and 9 produced with pitch-based fiber

Fiber: UTS-1.84 GPa
Modulus-400 GPa

Specimen 7 had the greatest Al carbide content of specimens shown

Specimen 8 produced with pitch-based fibers had large Al channels

Specimen 5 produced with PAN-based fiber

Fiber: UTS-2.74 GPa
Modulus 392 GPa

Figure 4.3.4: Comparison of anodic polarization results from G/6061 Al MMCs in deaerated 0.5M Na_2SO_4 solution of pH 7 at 30°C. Scan rate = 0.167 mV/s.

Al channeling, but was fabricated with Torayca PAN-based fibers which had a significantly higher ultimate tensile strength than the pitch-based fibers shown in Figure 4.3.4.

G/6061 MMCs with similar Al_4C_3 contents (Specimens 8 and 9) exhibited significant deviation in anodic current densities in Figure 4.3.4. Importantly, the G/6061 Al MMC (Specimen 7) which had the greatest average Al_4C_3 content (215 mg/m^2) of the specimens tested in this study (see Table 3.3.2), did not deviate significantly from the anodic behavior of the other G/6061 Al MMCs (Specimens 6 and 9). This was unexpected, since it is well known that Al_4C_3 will hydrolyze to $Al(OH)_3$ (equation 2.5.2) at a rate of 1 vol.% per hour [Hihara, 1989], evolving methane gas. Crevice corrosion similar to that observed for the etched samples in Figures 3.4.7 and 3.4.8 was observed after anodic potentiostatic polarization of G/6061 MMCs specimens at +1200 mVsce for 30 minutes in deaerated 0.5M Na_2SO_4 solution. In Figure 4.3.5, the resultant crevice corrosion is shown to 'percolate' through the microstructure via the fiber-matrix interface connected by intermetallic bridges (see Figures 3.4.5 and 3.4.6). The increase in passive current densities measured for G/6061 Al MMCs is attributed to the formation of crevices at the fiber-matrix interface, which can be seen more clearly in Figure 4.3.6. The magnitude of the passive current densities measured for G/6061 Al MMCs were at least one order of magnitude (one log decade) greater than those determined for G/1100 Al MMCs.

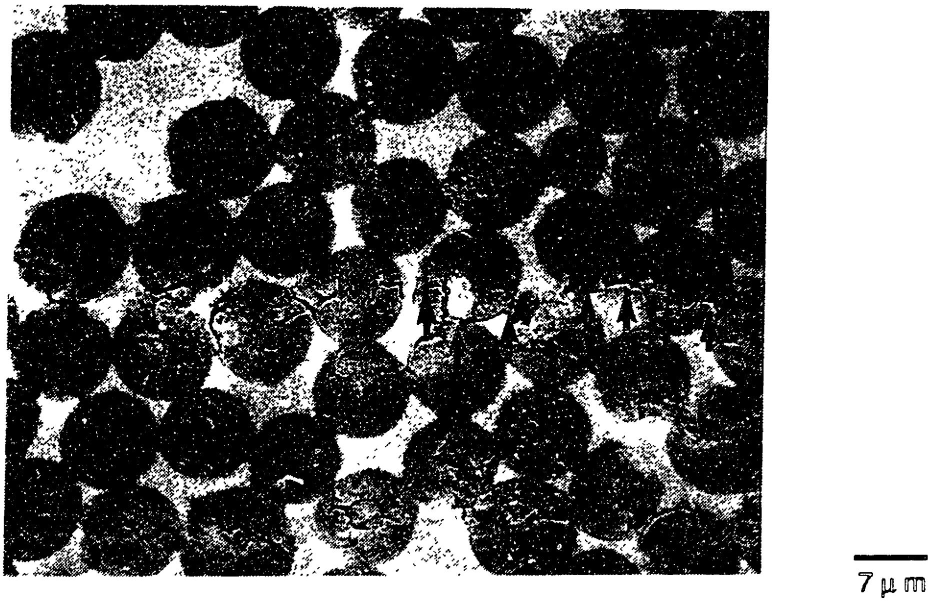

Figure 4.3.5: Secondary electron SEM micrograph of a G/6061 Al MMC (Specimen 7) after potentiostatic polarization. Specimen was maintained at +1200 mVsce in deaerated 0.5M Na_2SO_4 solution of pH~7 for a period of 30 minutes. A corrosion path formed along the fiber-matrix interface.

Figure 4.3.6: Secondary electron SEM micrograph at higher magnification of the G/6061 Al MMC in Figure 4.3.5 above. Note the preferential crevice formation at the fiber-matrix interface.

4.3.3 G/Al-Cu MMCs

The individual anodic polarization diagrams with standard deviation bars for G/Al-Cu MMCs (Specimens 14-22) appear in Appendix F. All specimens had approximately 63 vol.% fiber. Figure 4.3.7 shows the effects of alloy additions of Cu. The G/Al-Cu MMC with 4% Cu addition to the Al matrix had a slightly higher passive current density than similar composites with only 0.5 and 1% Cu additions; however, the G/Al-2% Cu MMC with Mg and Mn alloy additions had the highest passive current density (5 $\mu A/cm^2$).

Observation of anodically polarized composites revealed that little crevice corrosion had occurred at the fiber-matrix interface. The distribution of matrix alloying elements, other then the segregation of Cu to the G/Al interface, could not be determined with EDAX analysis; fine sub-micron precipitates were not easy to chemically identify. However, metallographic observation of the etched matrix structure shows that the general matrix of the composite containing 2% Cu (Specimen 22) was different from that containing 4% Cu addition to the Al matrix (see Figures 3.4.9 and 3.4.10).

G/Al-Cu specimens produced with the same matrix composition (see Table 4.2.1) as those specimens shown in Figure 4.3.7 were produced with a PAN-based graphite fiber with a higher Young's modulus (Specimens 14-18). The individual anodic polarization diagrams with standard deviation bars for G/Al-Cu MMCs fabricated with these fibers (Specimens 14-18) are shown in Appendix F. All specimens were also approximately 63 vol.% fiber.

It is known that fibers of higher strength have a higher surface energy (0.7 J/m^2 (HM) and 2.33 J/m^2 (HS), respectively [Baker and Bonfield, 1978]). The internal covalent C-C bonding is also in a higher energy state. Therefore, it is likely that during anodic polarization the higher modulus fibers more readily oxidized into CO_2 and CO gases.

Figure 4.3.8 shows the anodic polarization results for G/Al-Cu MMCs fabricated with the stiffer and stronger graphite PAN-based fibers. Evidently, the effects of increased Cu additions are not observable, due to increased current densities attained through anodic dissolution of the higher strength graphite fibers. The composite which was produced with Torayca PAN-based

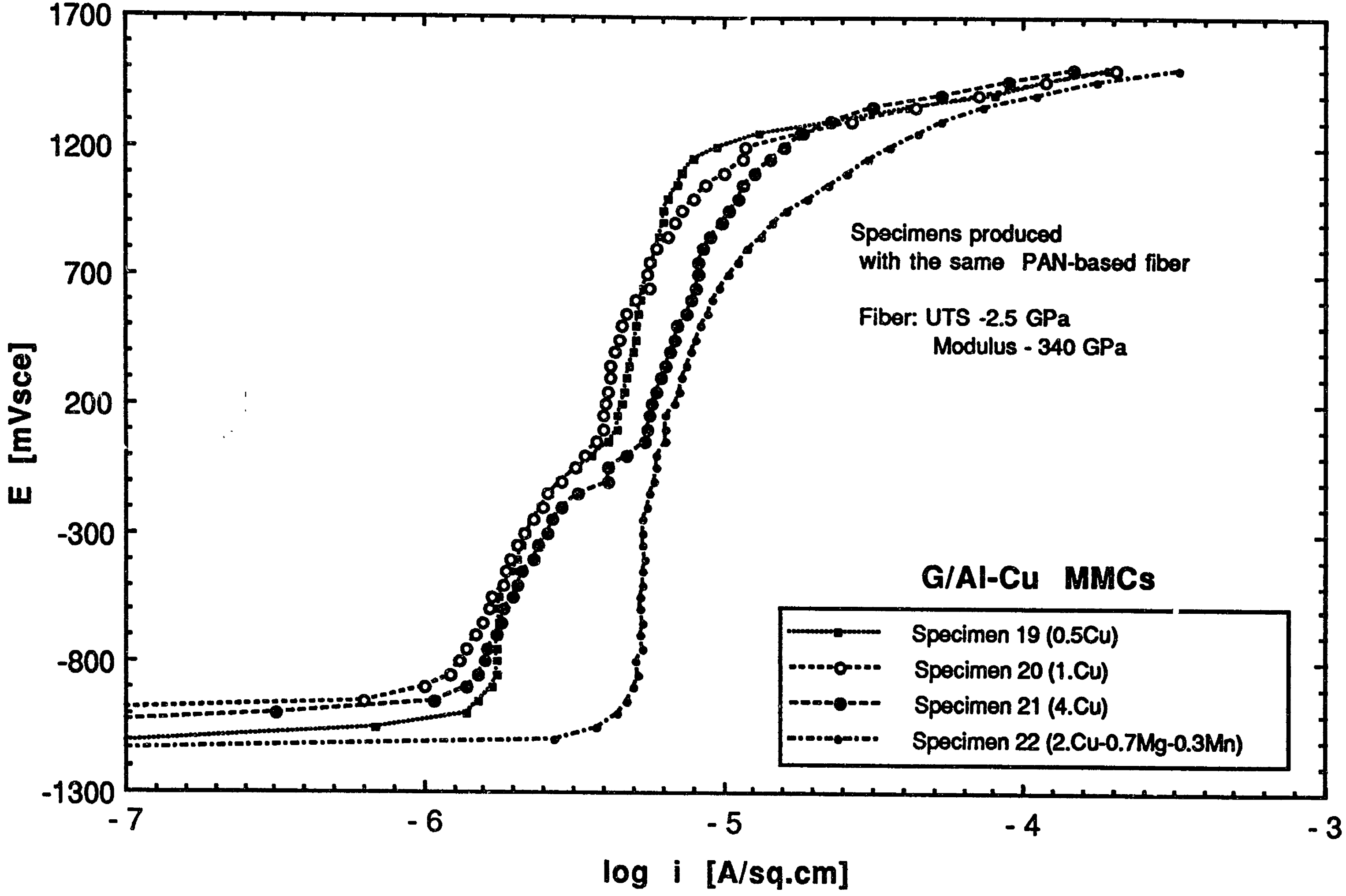

Figure 4.3.7: Comparison of anodic polarization results from G/Al-Cu MMCs in deaerated 0.5M Na_2SO_4 solution of pH 7 at 30°C. Scan rate = 0.167 mV/s.

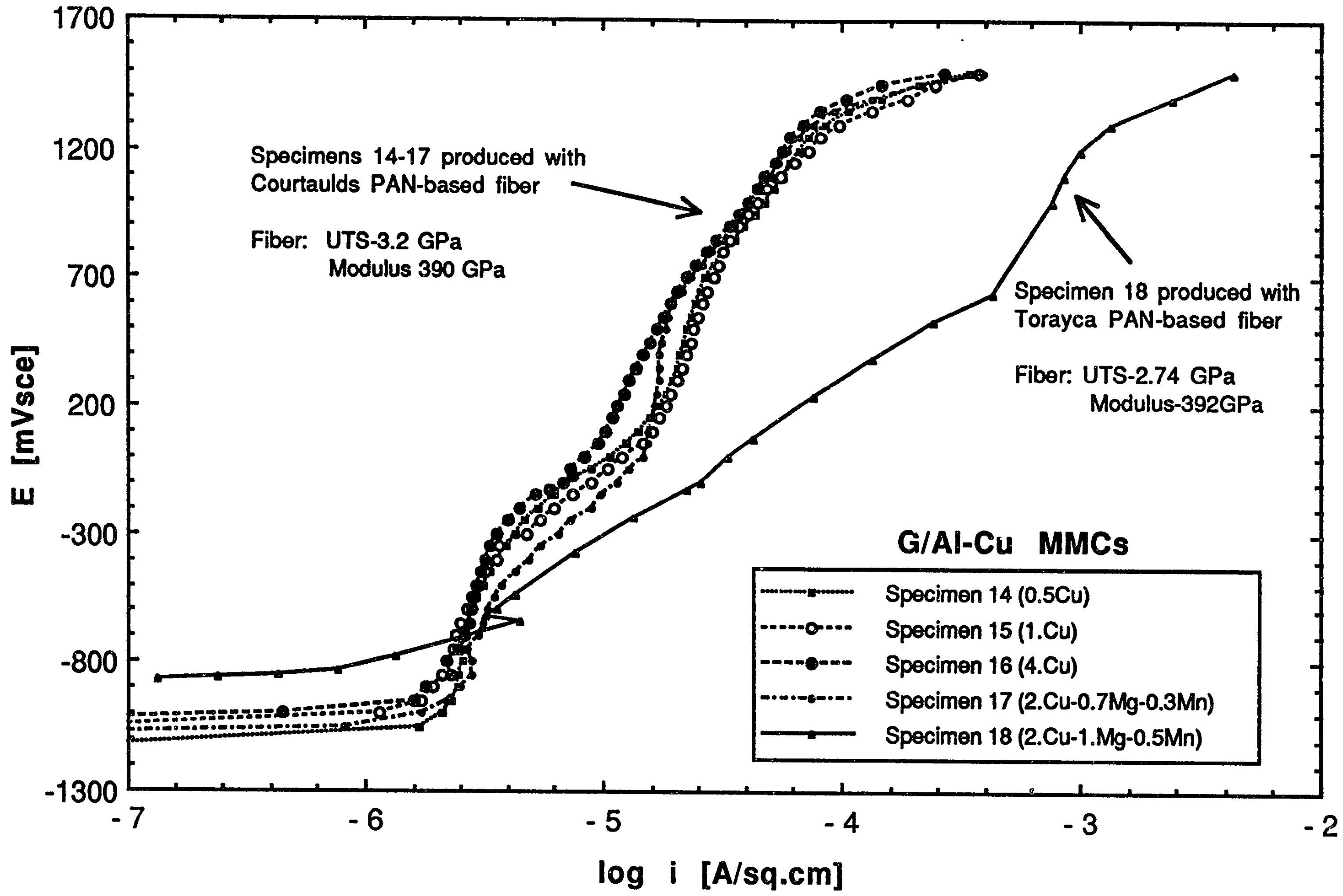

Figure 4.3.8: Comparison of anodic polarization results from G/Al-Cu MMCs with relatively higher modulus fibers than for those composites in Figure 4.3.7 in deaerated 0.5M Na_2SO_4 solution of pH 7 at 30°C. Scan rate = 0.167 mV/s.

fiber had unusually high corrosion current densities during anodic polarization. This will be explained in the discussion (see Section 7.1.2).

Figure 4.3.9 compares the results for two sets of G/Al-Cu MMCs produced with similar alloy additions. It is clear that the difference in modulus played the most significant role in determining the magnitude of the anodic current density at potentials above ~ -200 mVsce, as the data are spread between two distinct regions.

4.3.4 G/Al-Zn MMCs

The individual anodic polarization diagrams with standard deviation bars for G/Al-Zn MMCs (Specimens 5-9: Table 3.2.1) appear in Appendix F. The vol.% fiber of Specimens 10, 11, 12, and 13 were 69, 69, 70, and 73, respectively. Figure 4.3.10 compares the average values for G/Al-Zn MMCs tested by anodic polarization in deaerated 0.5M Na_2SO_4 solution. All G/Al-Zn MMCs with PAN-based graphite fibers passivated spontaneously and were under activation control.

The passive current density of the G/Al-5% Zn MMC (Specimen 13) was on the order of 2 $\mu A/cm^2$, and was similar to that determined for G/1100 Al MMCs. Superposition of standard deviation bars, shown in Appendix F, confirms that the addition of 5% Zn (Specimen 13) resulted in lower passive current densities at low anodic overpotentials. Specimens which contained less than 5% Zn in Al had twice the anodic passivation corrosion current density (4 $\mu A/cm^2$). Relatively small alloy additions of Zn in the matrix seem to increase the passive current density in deaerated 0.5M Na_2SO_4 solution (Specimens 10 and 11).

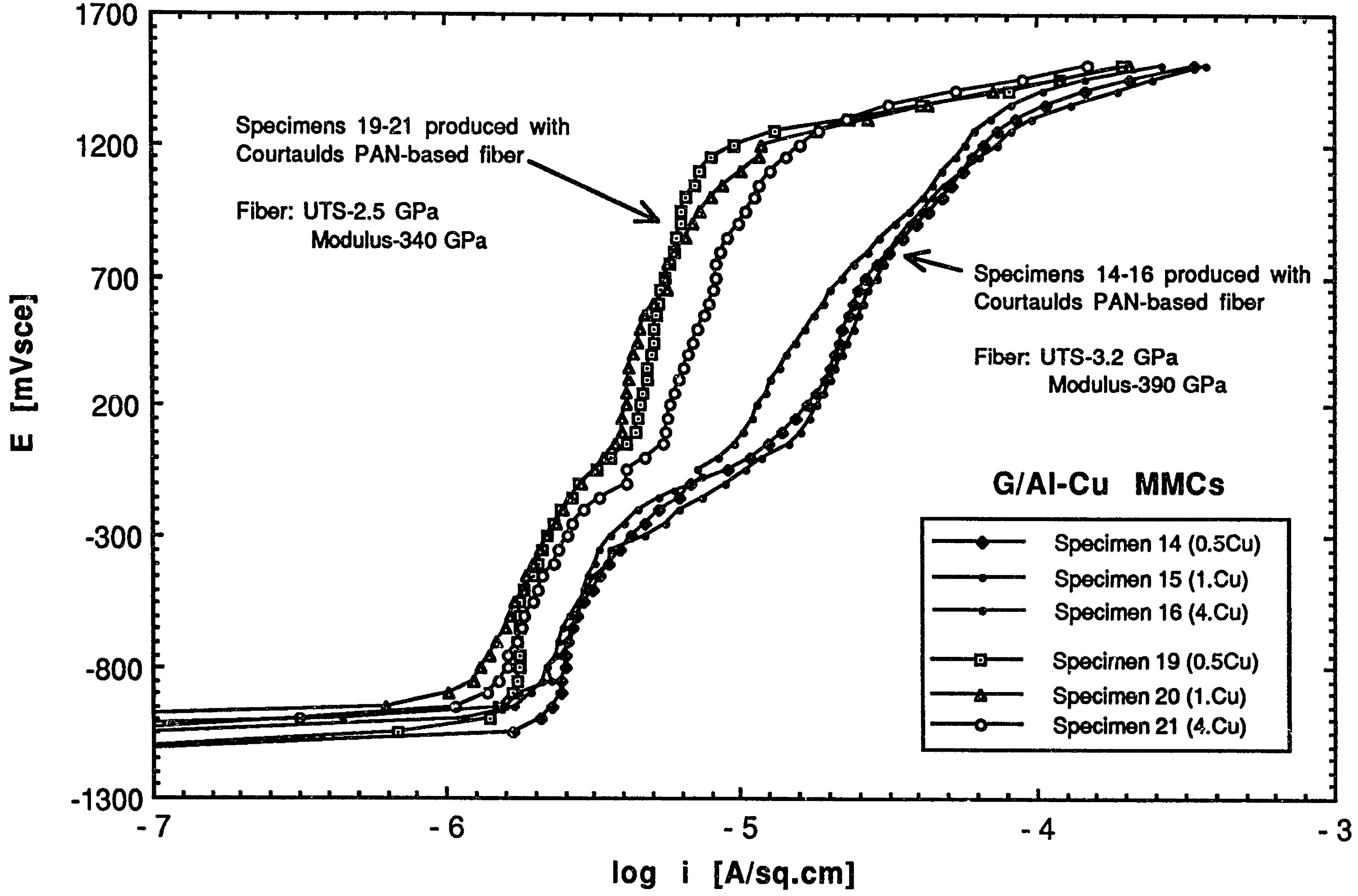

Figure 4.3.9: Comparison of anodic polarization results from G/Al-Cu MMCs with two different graphite fiber types in deaerated 0.5M Na_2SO_4 solution of pH 7 at 30°C. Scan rate = 0.167 mV/s.

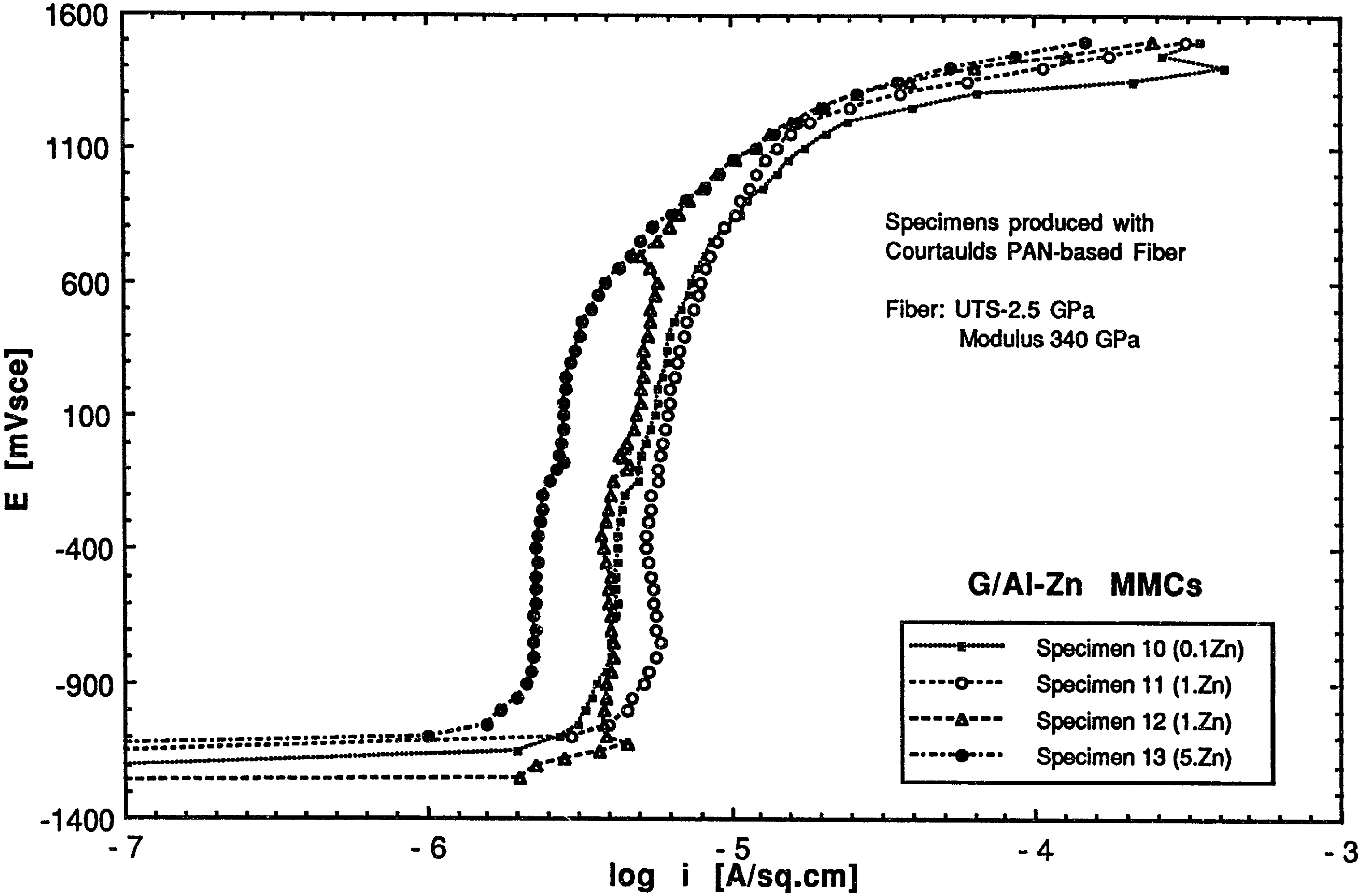

Figure 4.3.10: Comparison of anodic polarization results from G/Al-Zn MMCs in deaerated 0.5M Na_2SO_4 solution of pH 7 at 30°C. Scan rate = 0.167 mV/s.

4.4 RESULTS OF ANODIC POLARIZATION IN DEAERATED 3.15 wt.% NaCl SOLUTION

4.4.1 G/1100 Al MMCs

At the onset of anodic polarization all G/1100 Al MMCs spontaneously passivated and were under activation control. Thereafter, pitting ensued marked by a substantial increase in the corrosion current density. The values for the pitting potentials were nearly the same (-757 to -780 mVsce: see Table 4.4.1) as that obtained for pure Al (-750 mVsce) under the same conditions obtained by Hihara [1989]. This result verifies the fact that the presence of the fibers in the matrix does not significantly alter the nature of the film on the Al matrix.

The values for Ecrit, Eprot, and the passive current densities for all three G/1100 Al MMC specimens appear in Table 4.4.1. The value of Eprot ranged between -953 and -1000 mVsce, indicating that repassivation for G/Al MMCs was not very rapid (i.e., there was a large hysteresis (not shown) associated with the reverse polarization scan). Below the protection potential (Eprot) propagating pits cease to propagate. The differences in Al_4C_3 content for the G/Al MMCs did not correlate with Ecrit values.

4.4.2 G/6061 Al MMCs

In Figure 4.4.1, the effect of alloy additions to the Al matrix can be seen for the G/6061 Al MMCs tested. It is clear that the G/6061 MMCs had a modified passivation regime with no true pitting potential. Three separate tests were performed on each specimen to confirm these results. Hihara has determined that monolithic 6061-T6 Al had a true pitting potential of -725 mVsce in deaerated NaCl solution (see Table 4.4.1); therefore, the absence of a pitting potential is explained by the occurrence of crevice corrosion in the G/6061 Al MMCs at the fiber-matrix interface as was observed (see Figure 4.4.2).

Interfacial segregation of modified eutectic Mg_2Si and Al_4C_3 precipitation played a significant role in the anodic polarization of the G/6061 Al MMC tested in 0.5M Na_2SO_4 solution by acting as sites for crevice formation at the interface. Current densities were increased in the G/6061 Al MMCs due to the formation of crevices at the fiber-matrix interface (see Figure 4.4.2). Although pitting was observed at

Table 4.4.1: Corrosion Parameters Determined for G/Al MMCs in Deaerated 3.15 wt.% NaCl Solution

Specimen Number	Specimen Matrix	Ecorr mVsce	Ecrit mVsce	Eprot mVsce	i_p $\mu A/cm^2$
	pure Al (99.999%)	-1400	-750	N/A	0.63
	6061-T6 Al	-1220	-725	N/A	1
G Fiber	Composite				
	1100 Al				
2	"	-1155	-760	-950	1.8
3	"	-1240	-780	-960	5
4	"	-1140	-757	-1000	1.8
	6061 Al				
6	"	-1055	~-850	none	none
7	"	-1100	~-850	none	none
8	"	-1090	~-850	-978	10
9	"	-1080	~-850	N/A	1.8
	Al-Cu				
14	0.5% Cu	-1020	-700	N/A	6.3
15	1.% Cu	-1020	-710	N/A	10
16	4.% Cu	-1010	-790	N/A	6.3
17	2.% Cu	-990	-700	N/A	5.6
	0.7% Mg				
	0.3% Mn				
	Al-Cu				
19	0.5% Cu	-1037	-700	-920	5.6
20	1.% Cu	-1060	-710	-840	3.2
21	4.% Cu	-1030	-825	none	3
22	2.% Cu	-1025	-700	N/A	1.9
	0.7% Mg				
	0.3% Mn				
	Al-Zn				
10	0.1% Zn	-1060	-780	N/A	3.2
11	0.5% Zn	-1000	-770	-940	3.2
12	1.% Zn	-975	-975	none	none
13	5.% Zn	-980	-980	none	none

N/A = not available

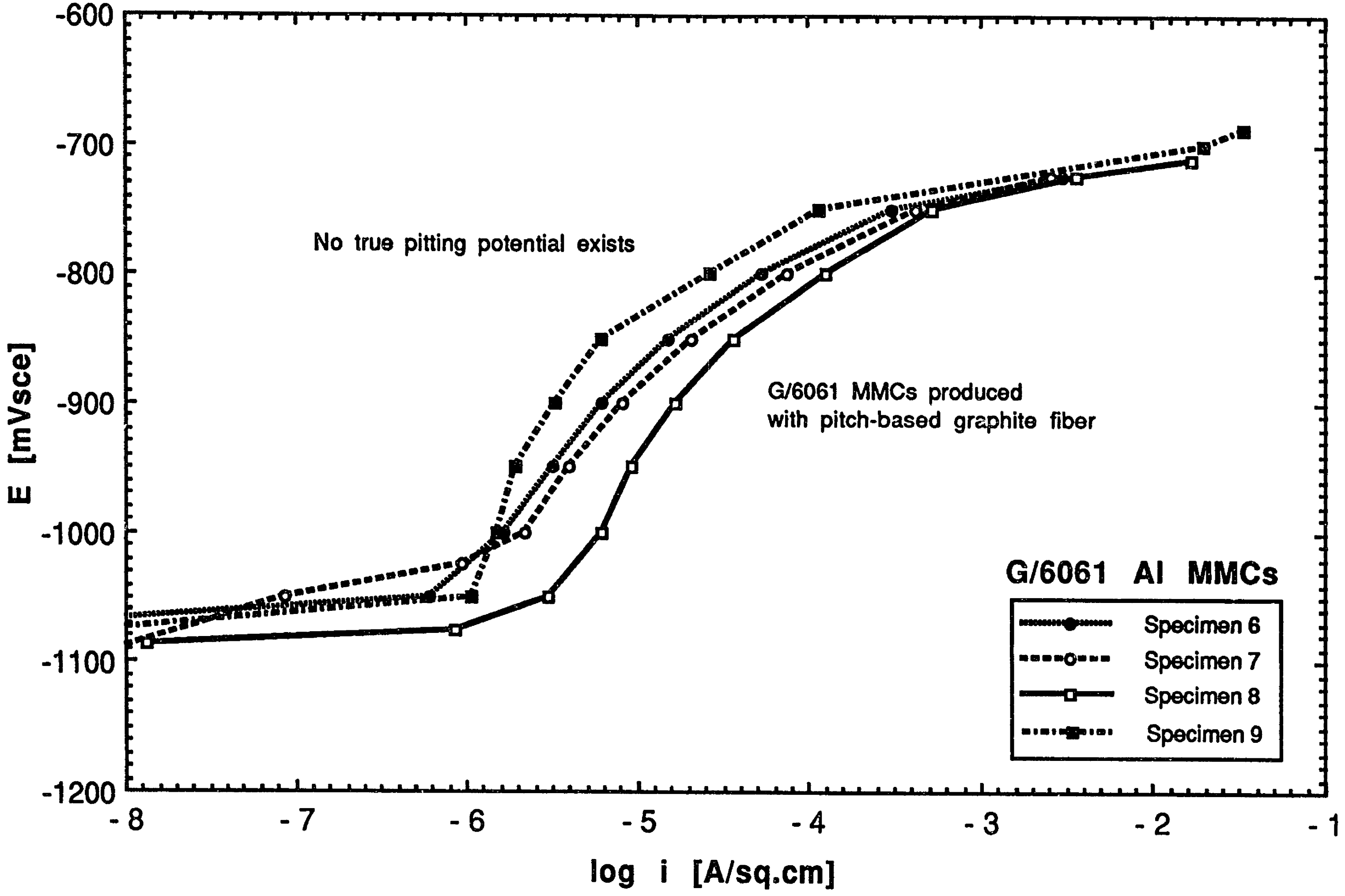

Figure 4.4.1: Comparison of anodic polarization results from G/6061 Al MMCs in deaerated 3.15 wt.% NaCl solution of pH 7 at 30°C. Scan rate = 0.167 mV/s.

potentials noble to ~ -850 mVsce, the formation of crevices did not allow for an accurate measurement of the pitting potential since *in-situ* observation of pitting was not performed.

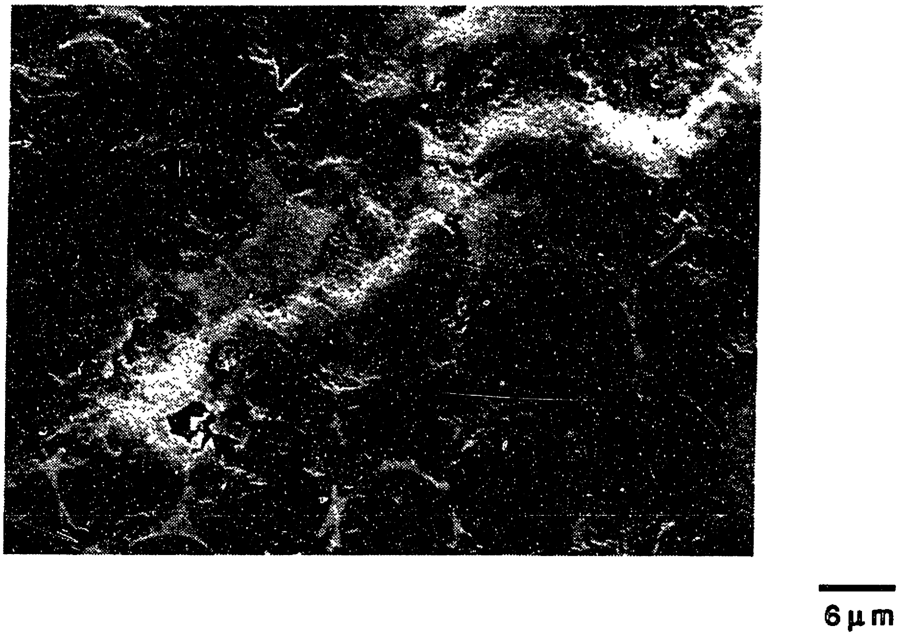

Figure 4.4.2: Secondary electron SEM micrograph of a G/6061 Al MMC (Specimen 7) after potentiostatic polarization. The specimen was maintained at 30 mVsce noble to the pitting potential in deaerated 3.15 wt.% NaCl solution of pH~7 for a period of 30 minutes. Points marked A are crevices, a result of corrosion, while points marked B are areas rich in intermetallic.

4.4.3 G/Al-Cu MMCs

All G/Al-Cu MMCs spontaneously passivated and were under activation control during anodic polarization in deaerated 3.15 wt.% NaCl solution. The addition of 0.5 wt.% Cu in (Specimens 14 and 19: see Table 4.4.1) resulted in an Ecrit value (-700 mVsce) which was more noble than that obtained for G/1100 Al MMC and of high purity Al. The specimens with 2 wt.% Cu, 0.7 wt.% Mg, and 0.3 Mn alloy additions also exhibited similar pitting behavior.

Additions of Cu to the Al matrix above 0.5 wt.% without Mg resulted in a decrease in Ecrit values as shown graphically in Figure 4.4.3. In the figure the

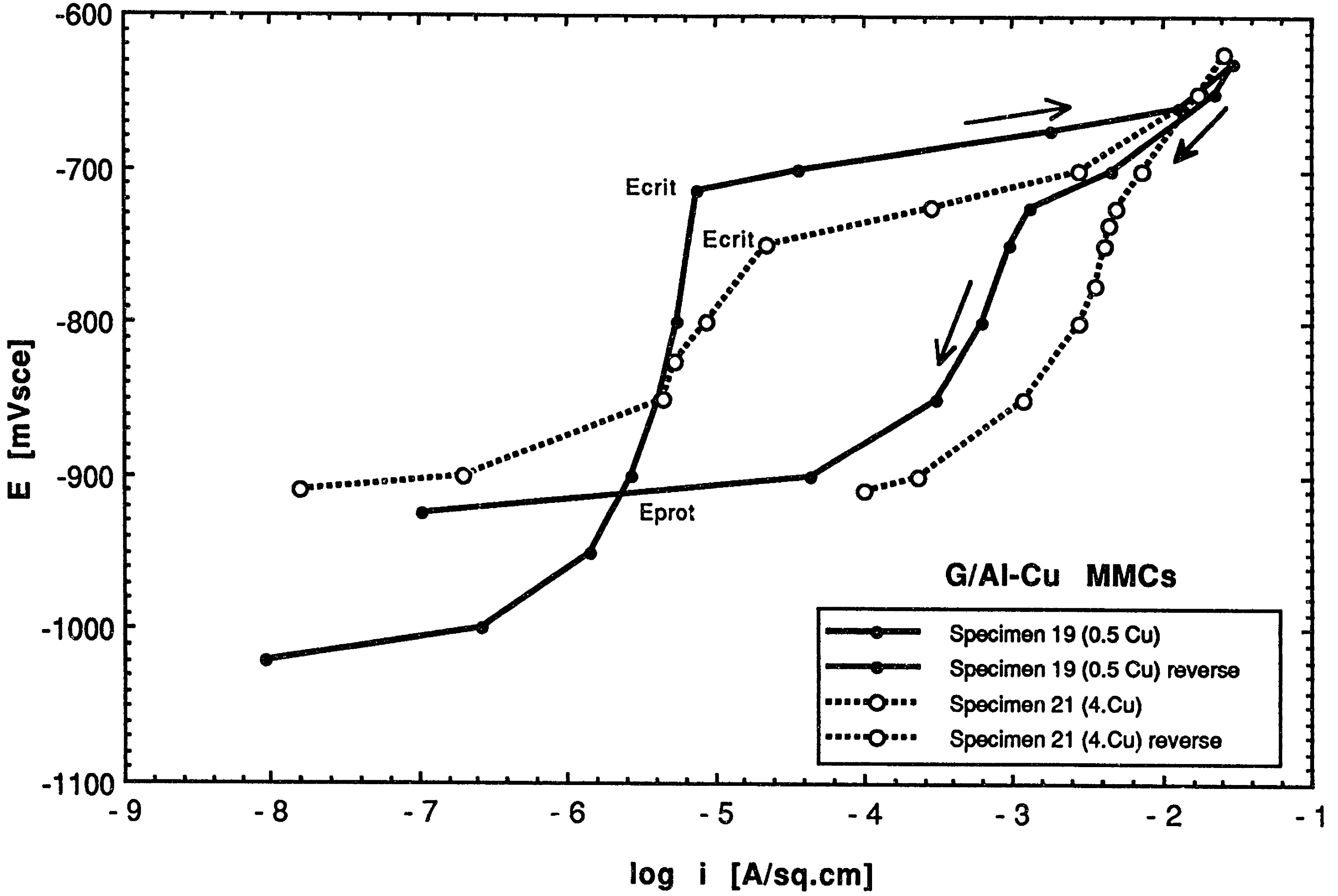

Figure 4.4.3: Comparison of cyclic anodic polarization results for two G/Al-Cu MMCs in deaerated 3.15 wt.% NaCl solution of pH 7 at 30°C. Scan rate = 0.167 mV/s.

repassivation ability of G/Al-0.5 % Cu MMC (Specimen 19) is relatively poor; however, the hysteresis was even larger for the G/Al-4% Cu MMC (Specimen 21).

Figure 4.4.4 reveals the fairly linear relationship of the Ecrit values determined for additions of Cu to the Al matrix of the G/Al-Cu MMCs. The difference in fiber types did not effect the Ecrit, since the pitting phenomenon is associated with chloride attack of the alumina film on Al. However, G/Al-Cu MMCs fabricated with higher strength fibers (Specimens 14-17) sustained greater passive current density's during anodic polarization. This is shown graphically in Figure 4.4.5 This phenomenon repeated itself for all G/Al-Cu MMCs studied (see i_p in Table 4.4.1). Also, the Ecorr values for the G/Al-Cu MMCs fabricated with higher modulus fibers (Specimens 14-17) were more noble than those of similar matrices but with different fibers (Specimens 19-22), suggesting a greater galvanic effect as a result of commercial fiber type.

Figure 4.4.6 shows the result of potentiostatic polarization at a value 30 mVsce noble to the experimentally determined pitting potential (see Table 4.4.1) for a G/Al-2% Cu MMC (Specimen 22). Sub-micron pitting was well-distributed throughout the matrix. Crevice formation was absent, as expected, at the low anodic overpotential relative to the equilibrium potential for graphite oxidation (see equations 2.2.1 to 2.2.3).

Figure 4.4.7 shows that for a G/Al-4% Cu MMC (see Specimen 16) under similar conditions, crevice or deep pits formed between the copper-rich eutectic (see Figure 3.4.9) and Al matrix. The crevices did not form at the fiber-matrix interface. This phenomenon has been observed to occur near intergranular regions in Al-4% Cu alloys in the absence of graphite fibers [Galvele and DeMicheli, 1970].

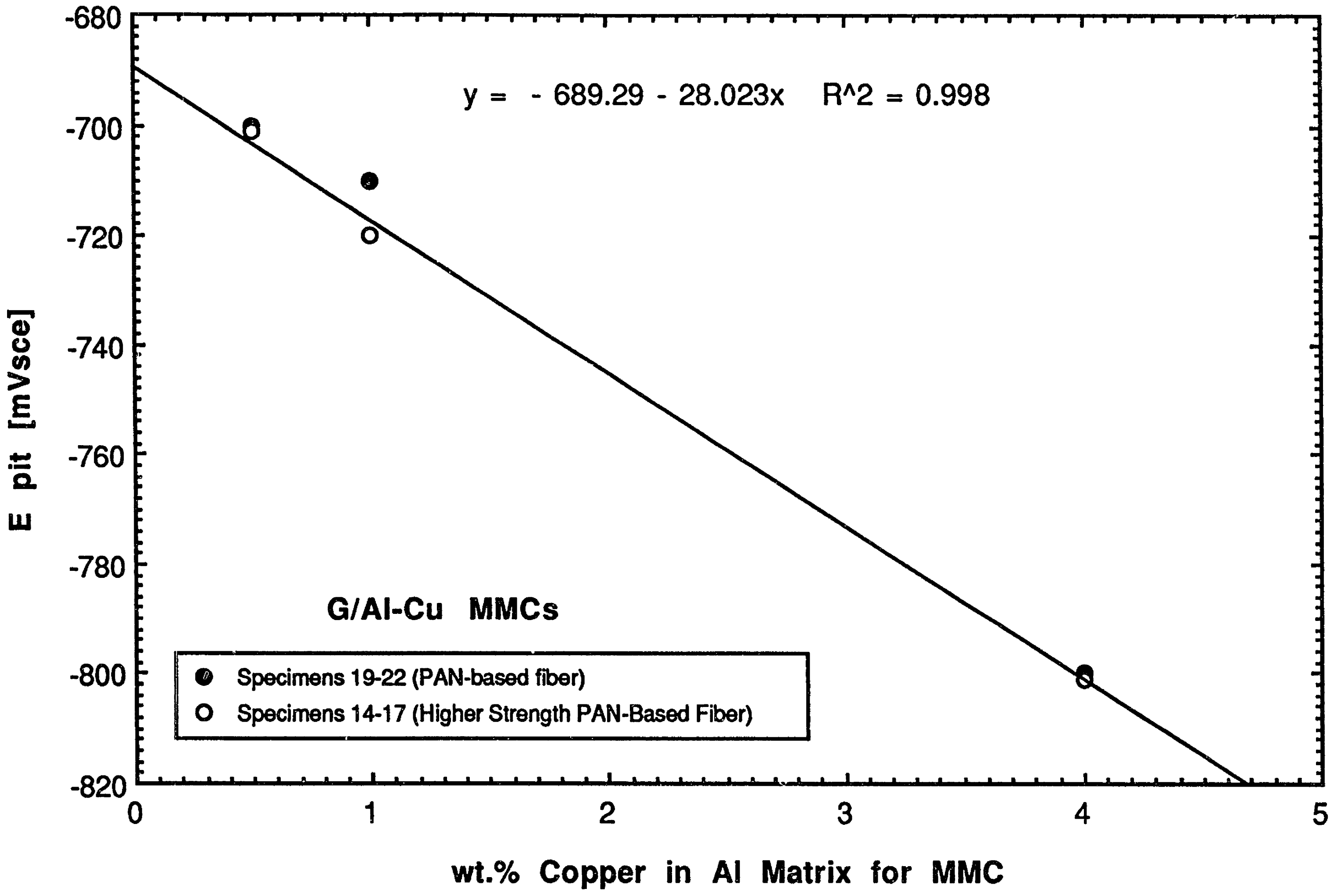

Figure 4.4.4: Plot of pitting potential vs. wt.% Cu in an Al matrix for G/Al-Cu MMCs in deaerated 3.15 wt.% NaCl solution of pH 7 at 30°C.

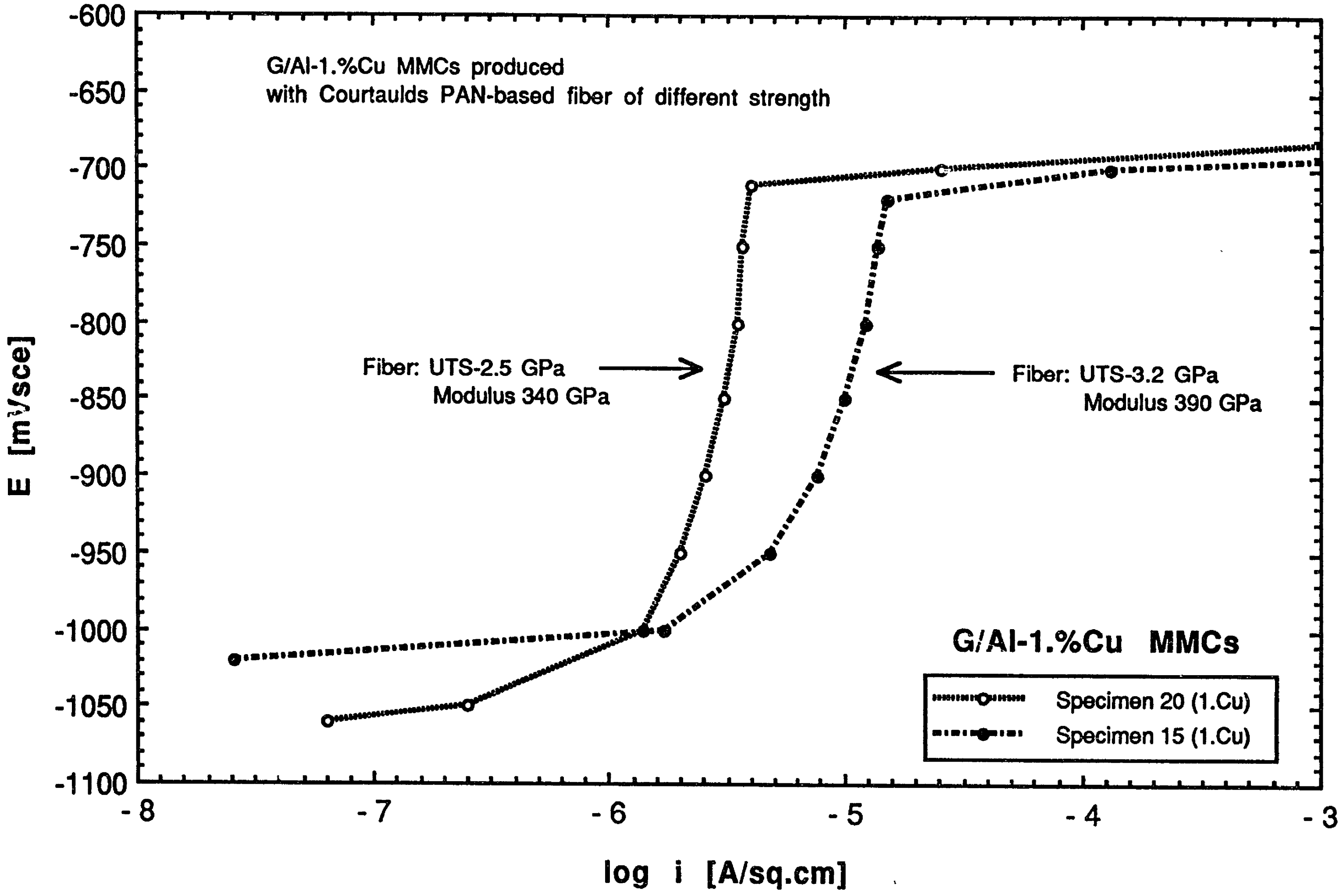

Figure 4.4.5: Comparison of anodic polarization results for G/Al-1%Cu MMCs in deaerated 3.15 wt.% NaCl solution of pH 7 at 30°C. Scan rate = 0.167 mV/s.

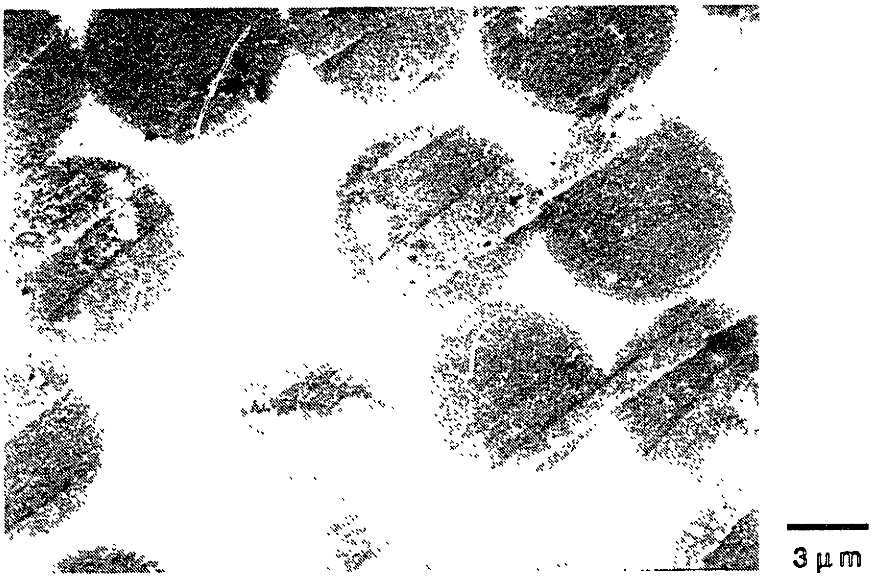

Figure 4.4.6: Secondary electron SEM micrograph of a G/Al-2% Cu MMC (Specimen 16) maintained at 30 mVsce noble to the pitting potential in deaerated 3.15 wt.% NaCl solution of pH~7 for a period of 30 minutes. Pits in the matrix were sub-micron and well-distributed, no crevice formation was found.

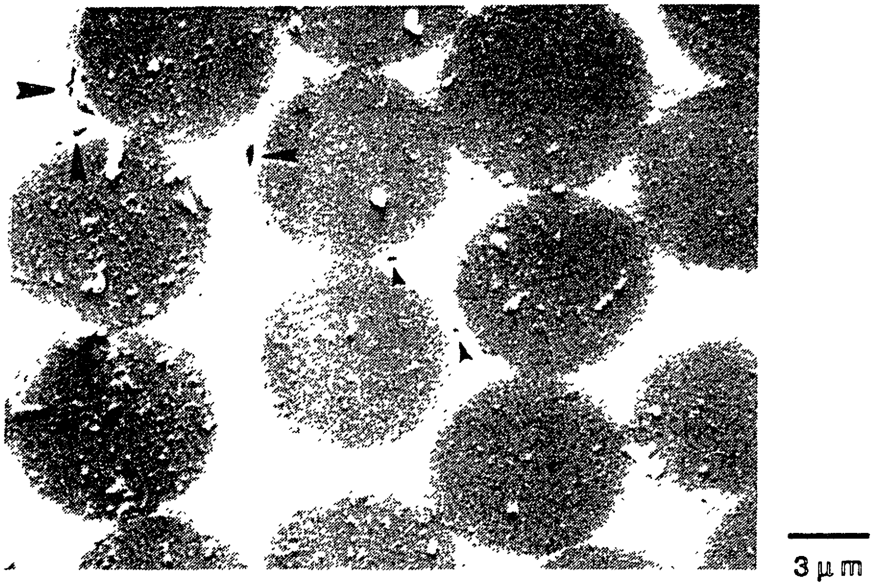

Figure 4.4.7: Secondary electron SEM micrograph of a G/Al-4% Cu MMC (Specimen 16) maintained at 30 mVsce noble to the pitting potential in deaerated 3.15 wt.% NaCl solution of pH~7 for a period of 30 minutes. Arrows denote pit formation between copper-rich segregant and the Al matrix.

4.4.4 G/Al-Zn MMCs

Zn alloy additions of 0.1 and 0.5 wt.% resulted in Ecrit and passive current densities which were quite similar to those determined for G/1100 Al MMCs (see Table 4.4.1). Alloying of Al with Zn above 1wt.% in G/Al-Zn MMCs resulted in a significant reduction in pitting corrosion resistance. These composites pitted spontaneously in the deaerated NaCl solution. Zn additions to the Al matrix were more detrimental to the Ecrit and Eprot values than similar additions of Cu in G/Al-Cu MMCs. The addition of Zn acted to decrease the resistance of the Al film at higher alloying concentrations.

4.5 RESULTS OF CATHODIC POLARIZATION IN AERATED 3.15 Wt.% NaCl SOLUTION

Since Hihara [1989] concluded that the cathodic reduction of oxygen on graphite fibers would be rate limiting for corrosion of G/Al MMCs in aerated solutions, it was decided to test commercial G/Al MMCs by cathodic polarization in aerated 3.15 wt.% NaCl solution. The results in Figures 4.5.1 through 4.5.4, clearly show that in aerated solutions the oxygen diffusion-limited current density was rate limiting for all of the composites studied. The value for the oxygen diffusion-limited current density was approximately 10 $\mu A/cm^2$; however, it should be noted that the standard deviation of the error for the log i values obtained was on the order of ±1 log decade as mentioned in Section 4.2.4.

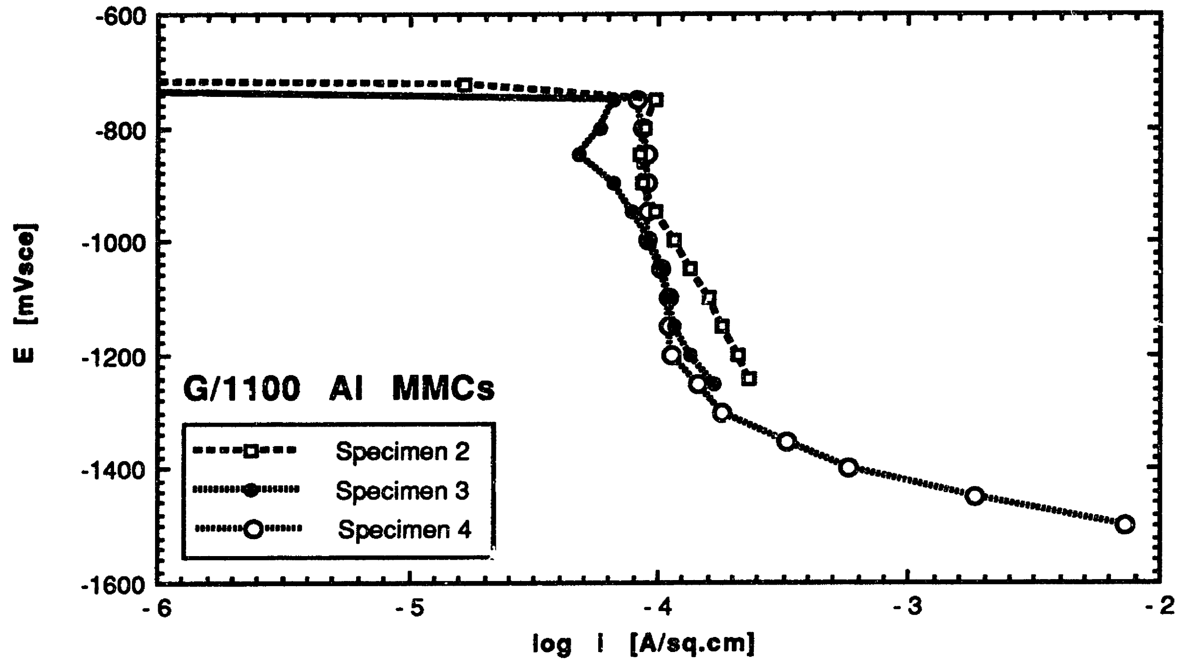

Figure 4.5.1: Cathodic polarization diagram for G/1100 Al MMCs in aerated 3.15 wt.% NaCl solution of pH 7 at 30°C. Scan rate = 0.167 mV/s.

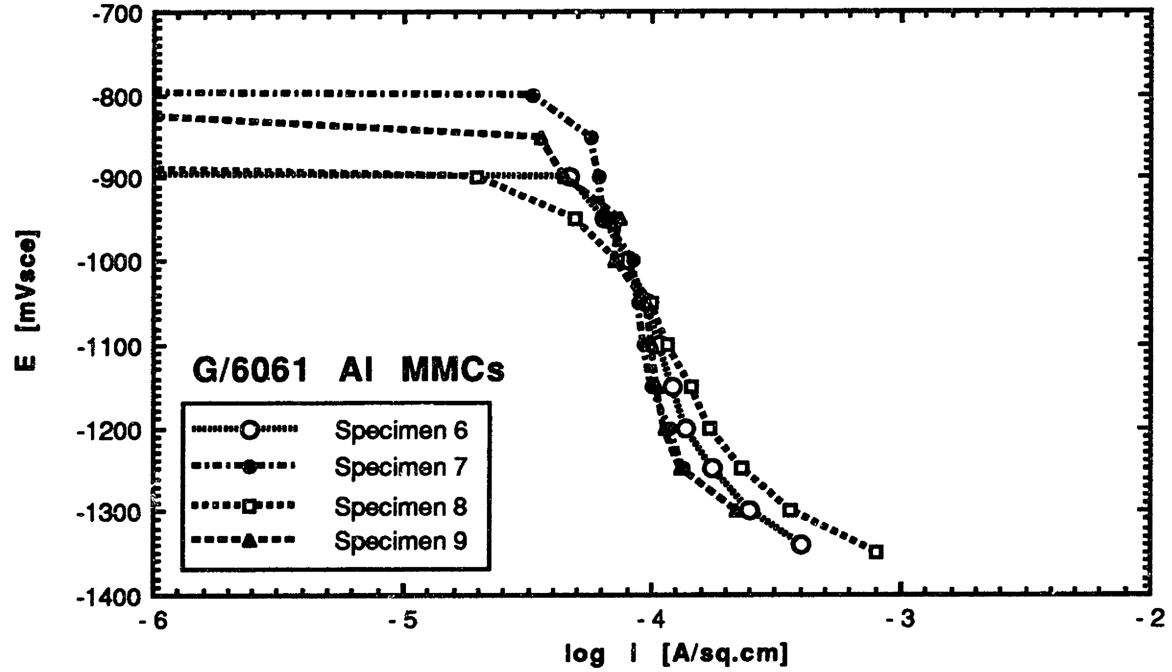

Figure 4.5.2: Cathodic polarization diagram for G/6061 Al MMCs in aerated 3.15 wt.% NaCl solution of pH 7 at 30°C. Scan rate = 0.167 mV/s.

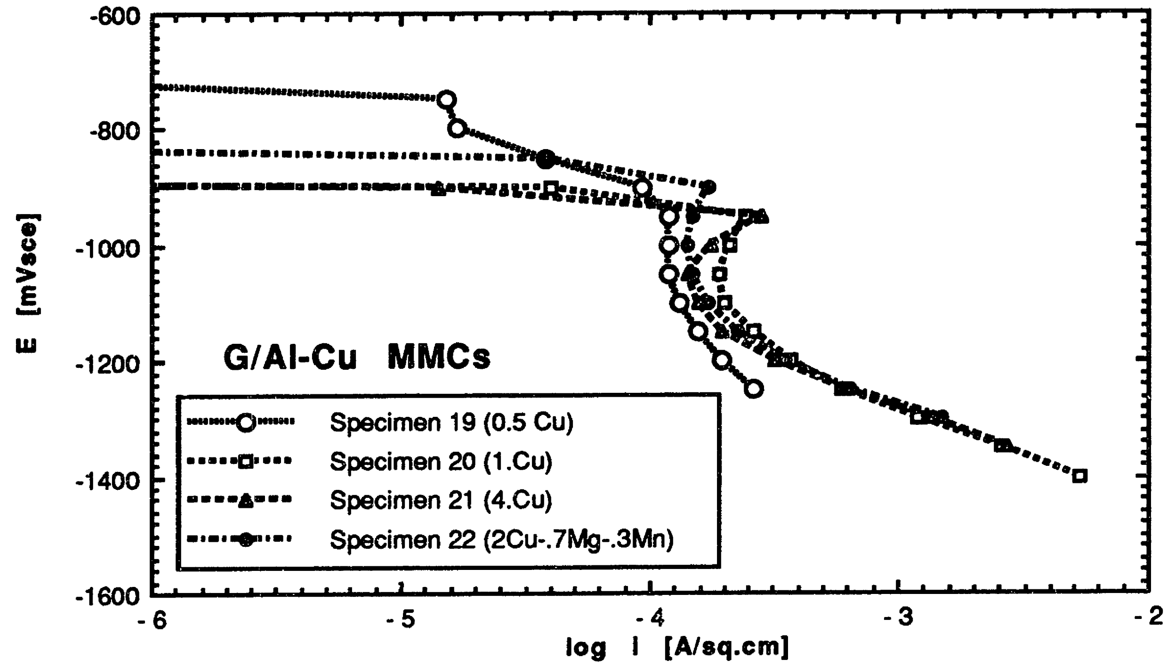

Figure 4.5.3: Cathodic polarization diagram for G/Al-Cu MMCs in aerated 3.15 wt.% NaCl solution of pH 7 at 30°C. Scan rate = 0.167 mV/s.

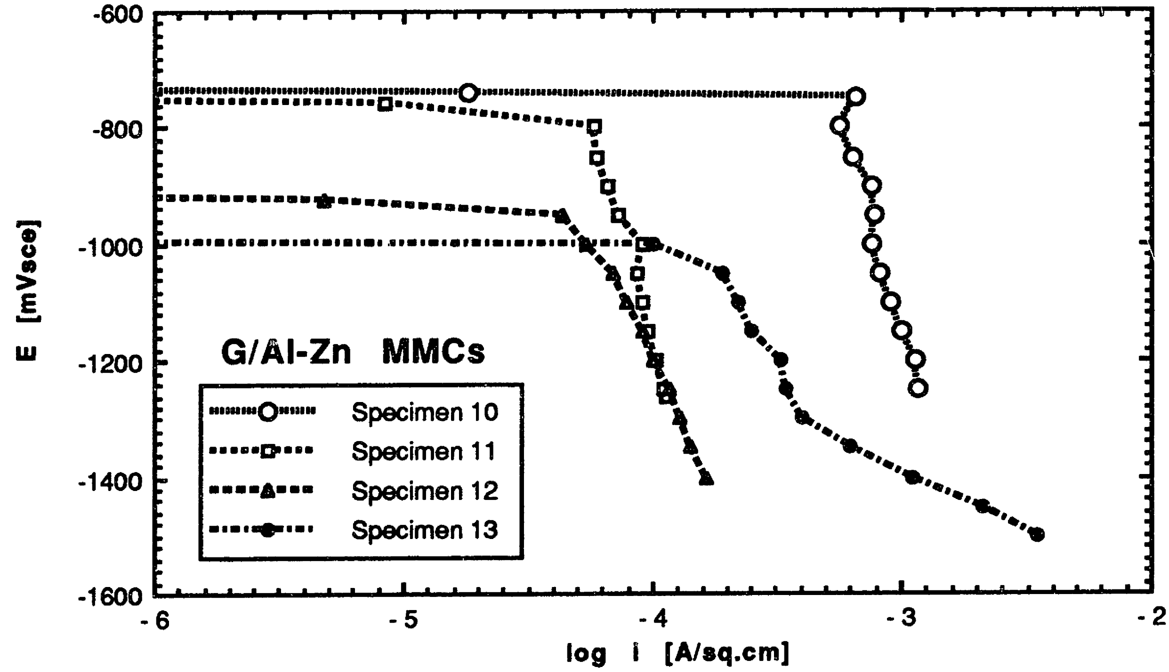

Figure 4.5.4: Cathodic polarization diagram for G/Al-Zn MMCs in aerated 3.15 wt.% NaCl solution of pH 7 at 30°C. Scan rate = 0.167 mV/s.

5. SURFACE ANALYSIS OF CORRODED G/1100 Al AND G/Al-5% Zn MMCs

5.1 INTRODUCTION

A literature search revealed that there were no detailed studies performed to assess oxide and corrosion product formation in G/Al MMCs. Therefore, a two-part study was conducted in order to assess the resultant corrosion products and the distribution of elements on the corroded surface of a G/Al 1100 MMC (Specimen 4) and a G/Al-5% Zn MMC (Specimen 13). Both of these specimens were produced by Aluminium Ranshofen, Ges.m.b.H., Ranshofen, Austria, with the same infiltration process and PAN-based graphite fibers. Details concerning the composites are available in Table 3.2.1. Paramount to this study was the determination of corrosion processes and more specifically, the distribution of matrix alloying elements that were released from the matrix due to corrosion. Therefore, X-ray photoelectron spectroscopy (XPS) was used to determine the composition of corrosion products on the specimen surface. However, since this technique has poor spatial resolution (on the order of 1mm), to locate the elements on specific microstructural features (e.g., the fiber or the matrix) it was necessary to examine the same specimens by Auger Electron Spectroscopy (AES). Together these techniques provide a great deal of information concerning the nature of the corrosion products.

5.2 Experimental Procedure

Both G/Al MMC samples were mounted and polished using the same procedure employed in Section 4.2.1. The samples were placed in separate 500 ml flasks containing 3.15 wt.% NaCl solution. The solution was constantly aerated and maintained at a temperature of 30±0.2°C. The samples were kept in solution for a period of 24 hours, removed and gently rinsed with distilled water to remove the NaCl solution. The samples were then allowed to dry in air and subsequently covered with plastic. The plastic covers were not in contact with the sample surface. The mounted specimens were then mechanically sectioned using a cut-off saw, and the plastic cover was removed. The remaining resin mount was also removed with small pliers. The samples were placed in vacuum no later than two hours after being removed from the solution. The specimens were then examined by XPS, AES and SEM, respectively. The SEM micrographs will be shown first, to portray the corrosion morphology. This will explain why certain areas were chosen for analysis by XPS and AES.

It should be noted that the analyses were not performed *in-situ,* since specimens were exposed to air after they were removed from NaCl solution; moreover, oxidation and growth of films may have occurred in air, while on the other hand, film dehydration may have occurred in ultra-high vacuum (UHV). For this study, the more important aspect was to identify films and other morphological features which developed on G/Al MMCs.

5.2.1 Scanning Electron Microscopy (SEM)

SEM of exposed specimen surfaces was performed subsequent to XPS and AES analysis. Exposure of G/1100 Al MMC (see Figure 5.2.1) to an aerated 3.15 wt.% NaCl solution for one day resulted in the formation of a somewhat discontinuous corrosion product (on the left side). On the right side of Figure 5.2.1, no charging occurred due to the absence of corrosion product. In Figure 5.2.2, the degree of galvanic matrix corrosion is evident. It is apparent that the 1100 Al matrix has uniformly receded in this area.

SEM examination of the G/Al-5% Zn MMC surface exposed to aerated NaCl revealed the presence of an agglomerated corrosion product over a large Al channel (see Figure 5.2.3). This Al channel can be seen more clearly in the metallograph shown earlier for the G/Al-5% Zn MMC (see Figure 3.4.12). Channel formation occurs during pressure infiltration when molten Al pushes fibers aside. At higher magnifications, pitting was also found to occur in narrow Al channels (see Figure 5.2.4).

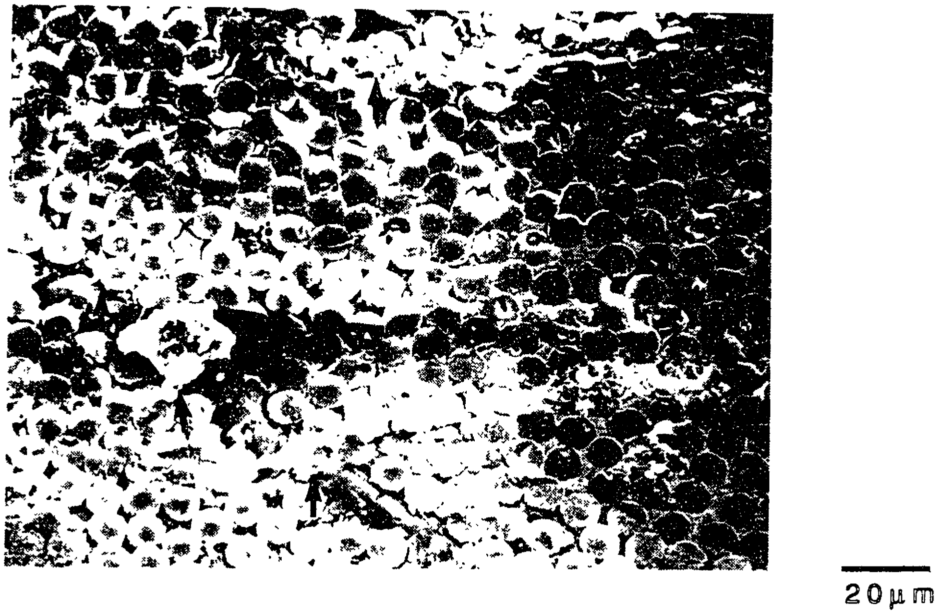

Figure 5.2.1: Secondary electron SEM micrograph for G/1100 Al MMC showing corrosion product formation (left side) after 24 hours in aerated 3.15 wt.% NaCl solution.

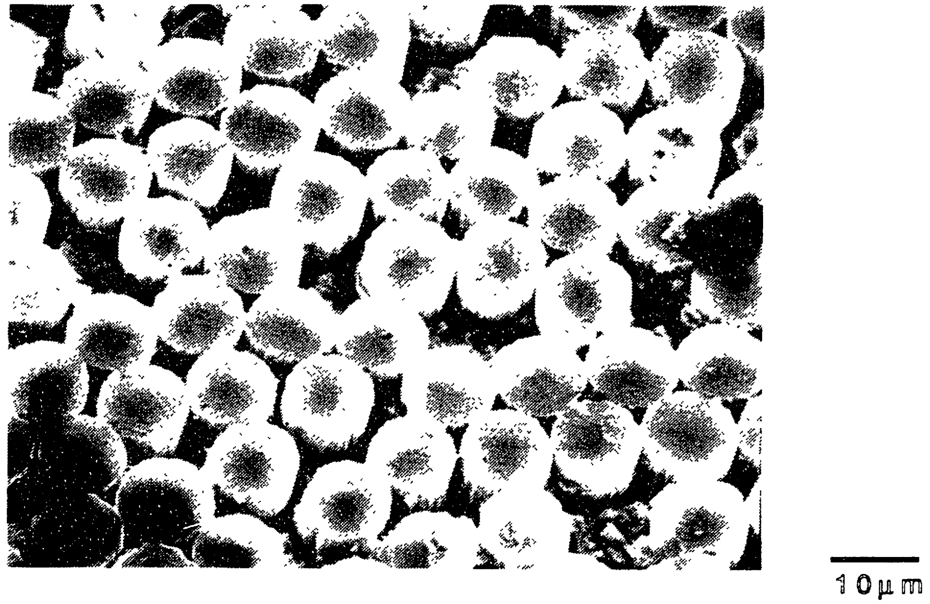

Figure 5.2.2: Secondary electron SEM micrograph for G/1100 Al MMC at a higher magnification showing galvanic corrosion of the Al matrix after 24 hours in aerated 3.15 wt.% NaCl solution.

In Figure 5.2.5, it is clear that a coarser more discontinuous scale had formed on the G/Al-5% Zn MMC. At even higher magnifications (see Figure 5.2.6), the thicker crustier scale is shown (compare Figure 5.2.2). In areas where no thick continuous film was found, galvanic corrosion was observed. For the G/Al-5% Zn MMC, corrosion was more localized, with deeper pits than those found in the matrix of the corroded G/1100 Al MMC.

In general corrosion of the G/Al-5% Zn MMC was more severe with deeper, more localized pitting, than that of the G/1100 Al MMC. Interestingly, it appears that the corrosion product formed much faster on the G/Al-5% Zn MMC, and after 24 hours appeared to be more of a scale rather than a thin film. The corrosion product formation over the large Al channel in the G/Al-5% Zn MMC occurred more rapidly than at other areas on the exposed specimen surface. This phenomenon occurred for other specimens containing Al channels which were examined in this study during anodic polarization.

Figure 5.2.3: Secondary electron SEM micrograph for G/Al-5% Zn MMC showing corrosion product formation over Al channel (left corner) after 24 hours in aerated 3.15 wt.% NaCl solution. Horizontal lines are channels of Al.

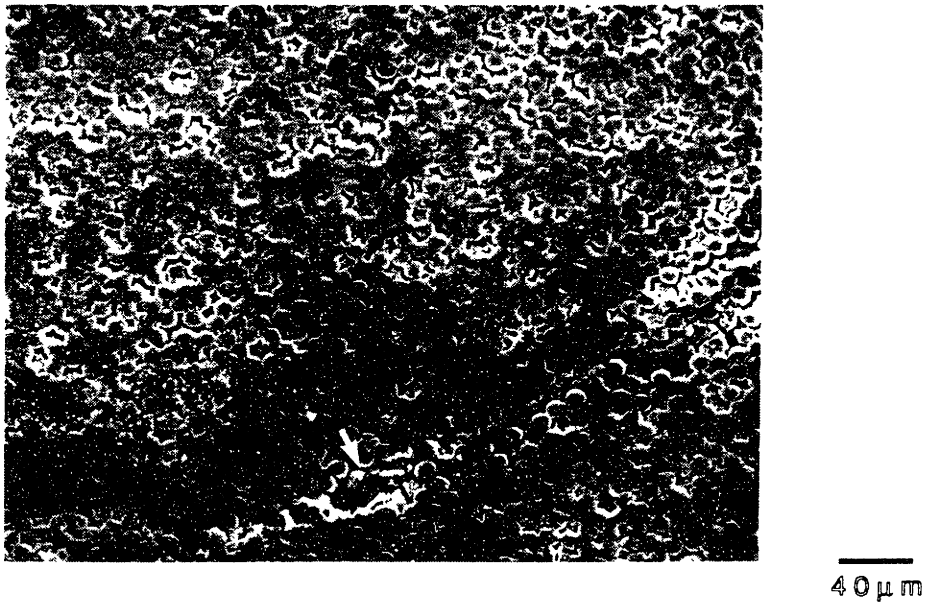

Figure 5.2.4: Secondary electron SEM micrograph for G/Al-5% Zn MMC showing corrosion product formation and pitting (lower center) after 24 hours in aerated 3.15 wt.% NaCl solution.

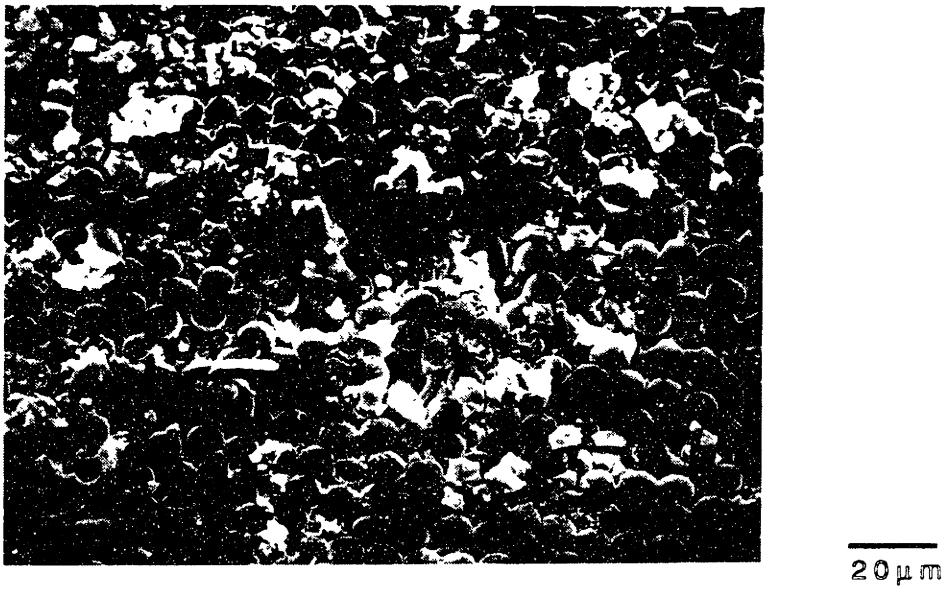

Figure 5.2.5: Secondary electron SEM micrograph for G/Al-5% Zn MMC showing discontinuous corrosion product formation after 24 hours in aerated 3.15 wt.% NaCl solution.

Figure 5.2.6: Secondary electron SEM micrograph for G/Al-5% Zn MMC at high magnification showing discontinuous corrosion product formation after 24 hours in aerated 3.15 wt.% NaCl solution.

5.2.2 X-ray Photoelectron Spectroscopy (XPS)

XPS makes use of Einstein's photon concept, that states the energy of a photon is equal to Planck's constant times the frequency of light. When applied to the photoelectric effect, it is equivalent to

$$h\nu = \phi + K_{max} \tag{5.2.1}$$,

where $h\nu$ is the energy of the photon, ϕ is the work function of the emitting surface or binding energy, and K_{max} represents the maximum energy a photoelectron can have after being ejected from the surface of an impinged material [Briggs and Seah, 1983; Halliday and Resnick, 1981]. In XPS, an X-ray of known energy is impinged on the surface of the material producing photoelectrons, which, when emitted from the top three monolayers of the material, have a specific energy of K_{max}. From equation 5.2.1, it is possible to determine the binding energy of an ejected electron coming from a particular atom. Although the current lateral spatial resolution of XPS is 0.2 mm at best, the technique is powerful since it is sensitive to the oxidation state of chemically bound elements.

The XPS analysis of the corroded surfaces was carried out with a Surface Science Instruments SSX 100 Spectrometer, located at Harvard University, Cambridge, MA. Monochromatic Al K_α (1486.6 eV) radiation was used to probe the core levels. The resolution of the spectrometer was about 0.8 eV for a spot size of 600 μm. A flood gun was used as a source of secondary electrons to prevent charging on films formed on the G/Al MMC's surface. The gun energy was calibrated using a high density polyethylene sample through a hole in a gold foil. Analysis of G/Al MMCs surfaces was also carried-out through a small perforation in a gold foil that covered the rest of the sample. A flood gun energy of ~2.0 eV gave the best full width at half maximum (FWHM) with maximum intensity for the composite specimens surveyed.

In order to determine the atomic percent (a/o) for the elemental regions surveyed by XPS, it was necessary to calculate the number of "corrected counts" from the expression:

$$\text{Corrected Counts} = \frac{\text{Counts}}{S \bullet \sigma_{PE}} \times \frac{E}{1} \qquad (5.2.2),$$

where S is the number of scans over the selected area, σ_{PE} is the photo emission cross section [Briggs and Seah, 1983] (which incorporates the ionizable cross-section of a particular element and the probability that a photoelectron will be emitted for the specific element), and E is the energy range or window span used in collecting specific photoelectrons (for this case the span was 15 eV).

5.3 RESULTS OF XPS SURFACE ANALYSES

Table 5.3.1 shows the atomic percentages (a/o) of elements determined from XPS analysis which incorporated corrected count values (eq. 5.2.2). It is evident that in regions where voluminous corrosion product was found (see lower left corner of Figure 5.2.3), the emission of carbon photoelectrons was reduced. The concentration of Zn decreased for the G/Al-5% Zn MMC in the vicinity of voluminous corrosion product (see Figure 5.2.3), while the percentage of Al increased by a factor of 3 (see Table 5.3.1). Therefore, the corrosion product that grew was primarily composed of Al, but it also contained some Zn. In all analyses taken, the ratio of oxygen to Al was greater than 1.5, the ratio of oxygen to Al in Al_2O_3. The measured ratio of O to Al must have been increased by the presence of other oxidized products on the fiber surface.

Table 5.3.1 Composition of Surface for G/Al MMCs Determined by XPS*

G/Al MMC	Aluminum	Oxygen	Carbon	Zinc
Area with significantly less corrosion product.				
G/1100 Al MMC	9.3	35.93	54.77	N/A
G/Al-5% Zn MMC	7.9	51.41	39.43	1.26
Area of voluminous corrosion product.				
G/1100 Al MMC	19.44	44.35	36.23	N/A
G/Al-5% Zn MMC	22.07	47.49	12.14	0.29

* by a/o

In Figure 5.2.7, the Zn 2p $_{1/2}$ and 2p $_{3/2}$ XPS peaks for the G/Al-5% Zn MMC after exposure to 24 hours of aerated NaCl solution are shown. The Zn 2p $_{1/2}$ and 2p $_{3/2}$ binding energies in Figure 5.2.7a correspond quite convincingly to those attained for the $Zn(OH)_2$ standard (see Figure 5.2.7c). Therefore, it is concluded that $Zn(OH)_2$ was present on the surface at locations with significantly less corrosion product (see the right side of Figure 5.2.3). The region where the large underlying Al channel had existed, i.e. where the large corrosion product had developed, was also probed, and the results can be seen in Figure 5.2.7b. The split energy peaks suggest that Zn in the corrosion product was not only reduced in magnitude, but that the chemical state of the Zn in the area over the Al channel was significantly different. It appears there were two distinct binding energies for Zn, but neither of these split energies have been recorded previously in the literature. Other oxides (in this case a variant of Al_x-O_x) may have interacted in such a way as to incorporate Zn from the corroding matrix. The shift in binding energies did not change the characteristic ΔE (2p $_{1/2}$ and 2p $_{3/2}$) for the pairs of Zn peaks produced (23.06 eV for $Zn(OH)_2$ vs. 22.99 eV for each pair of Zn 2p $_{1/2}$ and 2p $_{3/2}$ peaks in Figure 5.2.7b) [Briggs and Seah, 1983].

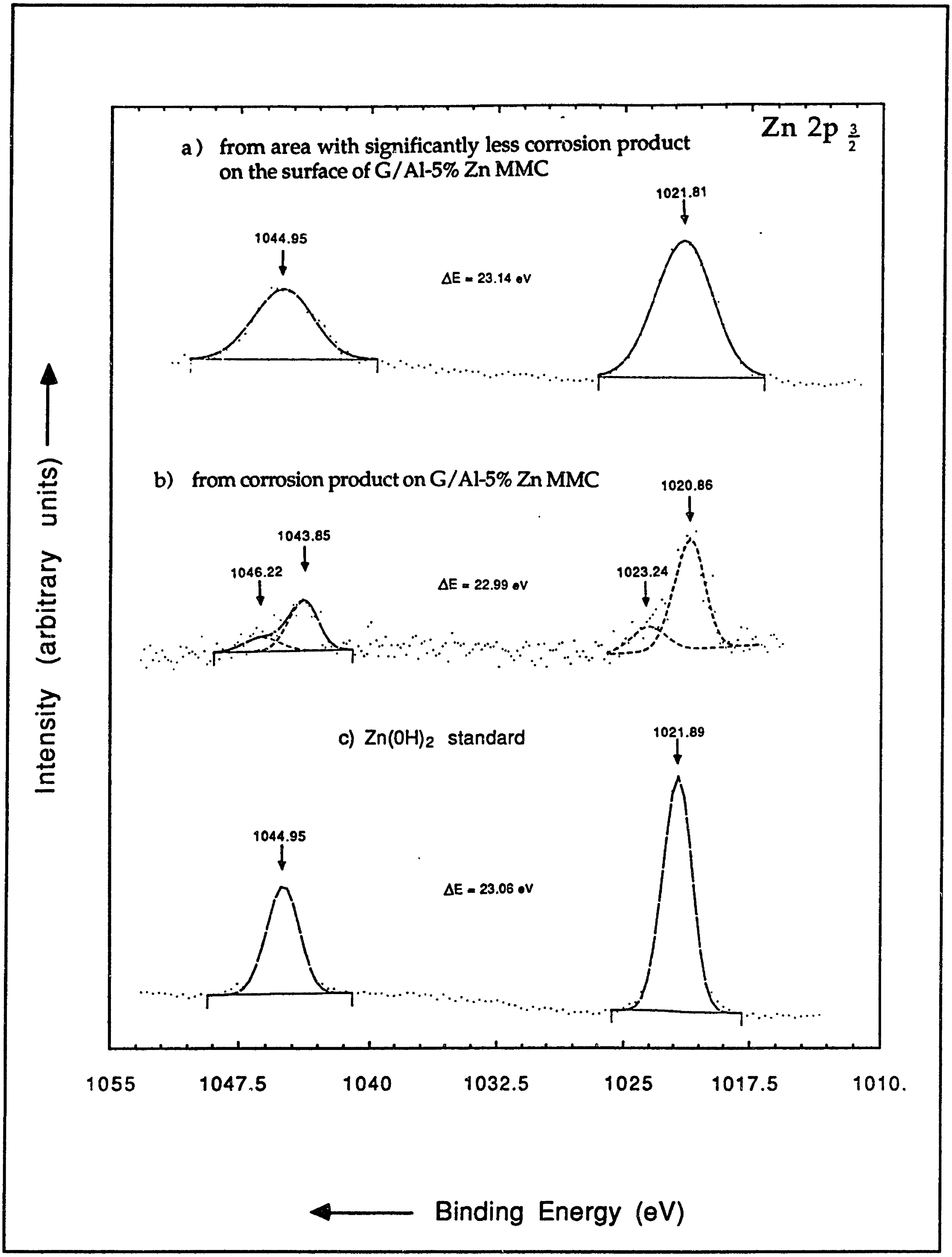

Figure 5.2.7: Zn 2p1/2 and 2p3/2 XPS peaks on G/Al MMC fiber surfaces and on $Zn(OH)_2$ standard.

In Figure 5.2.8, the O 1s peaks on the corroded G/1100 Al MMC are shown. Figure 5.2.9 shows the O 1s peaks for (a) the Al_2O_3 and (b) $Zn(OH)_2$ standards. The Al_2O_3 standard had previously hydrolyzed in air, since the O 1s binding energy was 536.4 eV vs. that in the literature for Al_2O_3, which is 531.5 eV [Briggs and Seah, 1983]. The Al_2O_3 standard itself had not been cleaned and had been left exposed to air and humidity in the laboratory for a long period of time. In Fig 5.2.8a, there are two O 1s peaks, the peak with a binding energy of 533.19 eV corresponds most closely in the literature to $Al(OH)_3$ (533.30 eV), while the peak at 534.68 eV may have been associated with oxygen bound to carbon. Values in the literature for complex carbon-oxygen compounds have binding energies near and above 534 [Wagner, et al., 1979]. In Fig.5.2.8c, an area with significant corrosion product on the G/1100 Al MMC was analyzed; a much stronger O 1s peak from $Al(OH)_3$ was found. The higher energy O 1s peak is most likely associated with oxygen bound to carbon (535.69 eV) and, the emergence of a lower O 1s energy peak corresponds to the binding energy of oxygen in Al_2O_3 (531.07 eV). As expected, the oxygen bound to Zn on the G/Al-5% Zn MMC surface correlated well with those O 1s peaks found for the $Zn(OH)_2$ standard in both regions surveyed (see Figure 5.2.8b and d, and 5.2.9b).

Figure 5.2.10 shows the C 1s peaks determined for both specimens. Most of the C 1s peak values obtained for samples have binding energies above 285 eV. The literature is replete with molecular compounds of carbon with energies above 285 eV. Since we have also found Na in our spectra (a residual element left behind from the NaCl solution), it is possible that Na_2CO_3 could be present: its' C 1s binding energy is 289.1 eV [Wagner, et al., 1979]; however, there are other compounds that may have similar binding energies making identification of carbon peaks at energies above 285 eV difficult at best. In Figure 5.2.10b and 5.2.10d it is apparent that a C 1s peak with a binding energy of 284.1 and 283.98 eV, respectively, can be seen. These C 1s peaks are associated with the carbon bonding in graphite itself (the value reported in the literature for graphite is 284.3 eV [Briggs and Seah, 1983]). This indicates that there were areas with no oxide at all since XPS analysis probes only the top three monolayers of the surface. The discontinuous nature of the oxide film on the G/Al MMC is reflected by the high graphite C 1s signal obtained in Figure 5.2.10d.

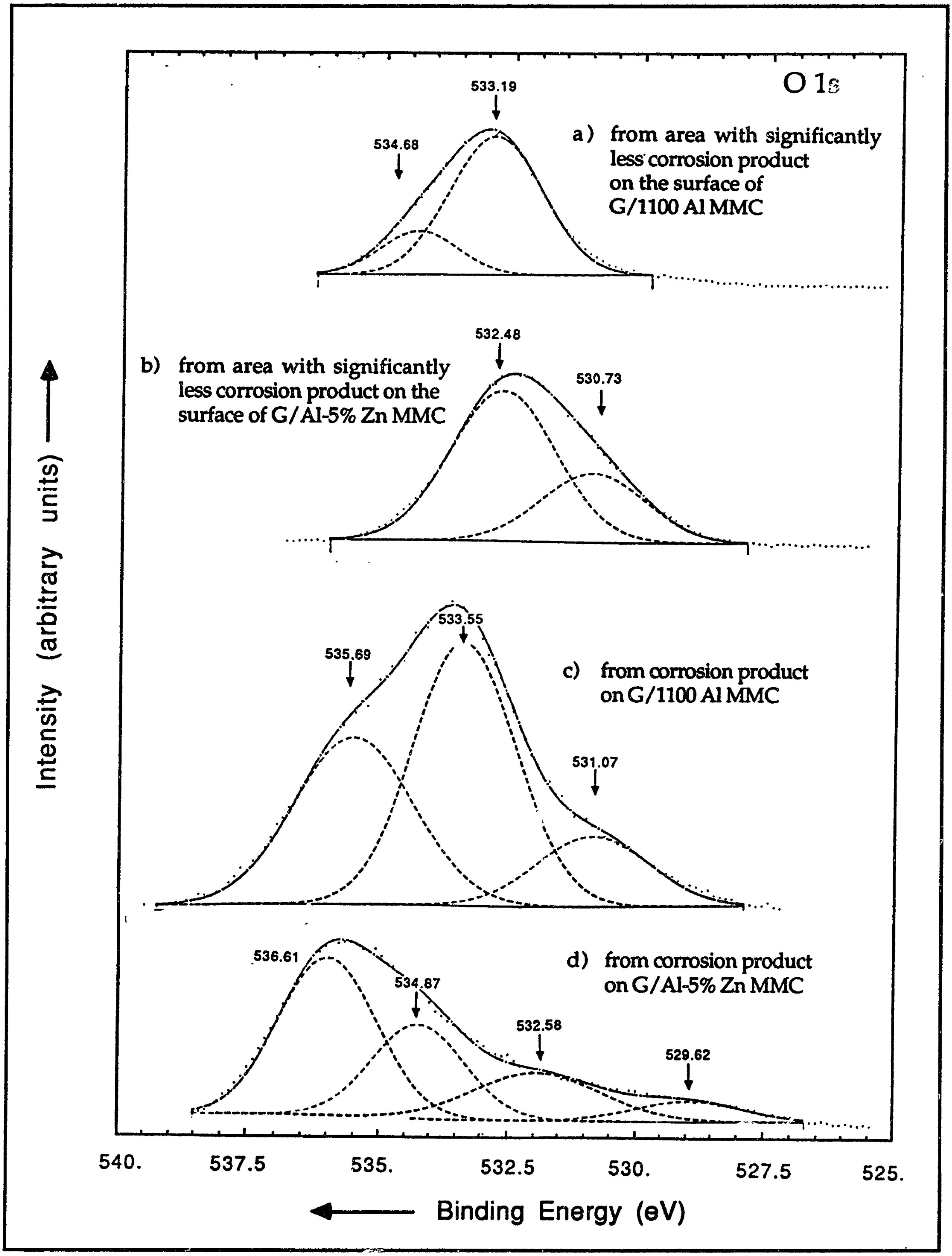

Figure 5.2.8: O 1s XPS peaks on G/Al MMC fiber surfaces.

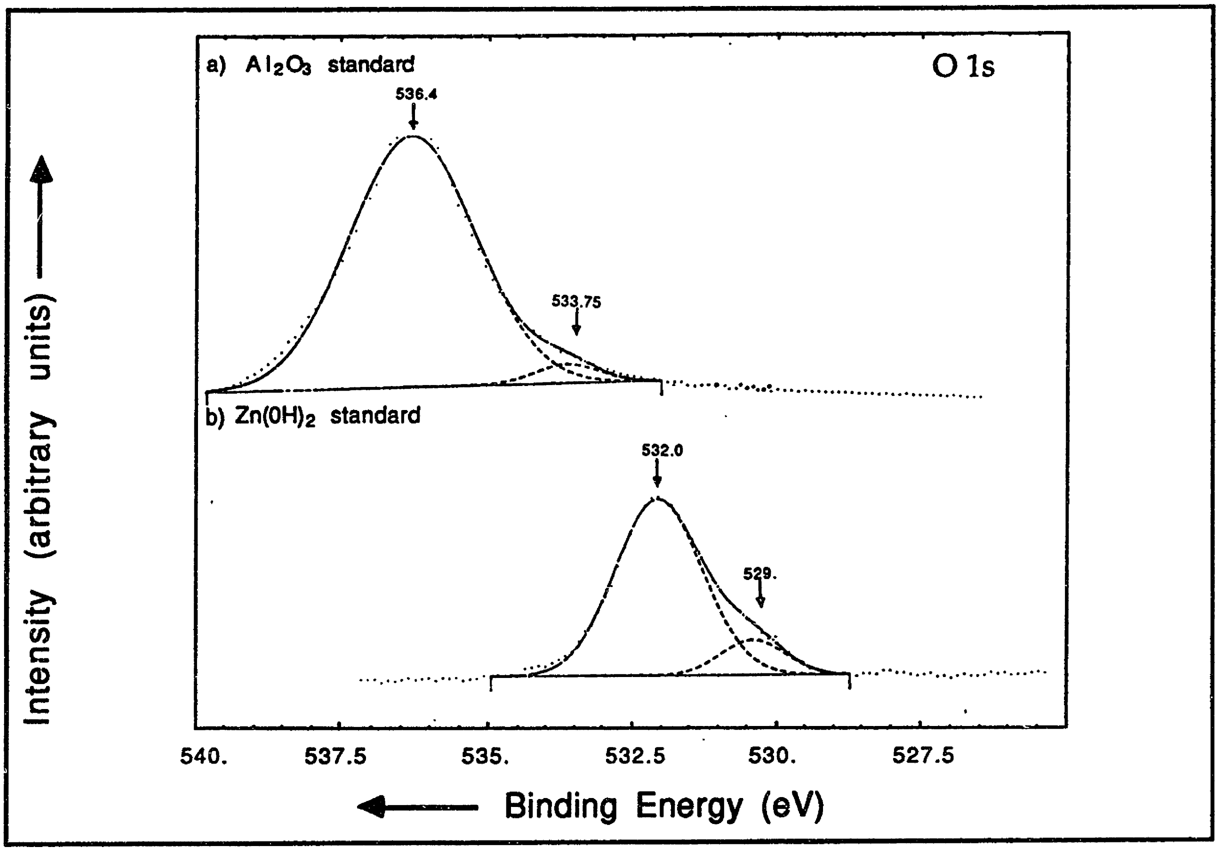

Figure 5.2.9: O 1s XPS peaks on Al_2O_3, and $Zn(OH)_2$ standards.

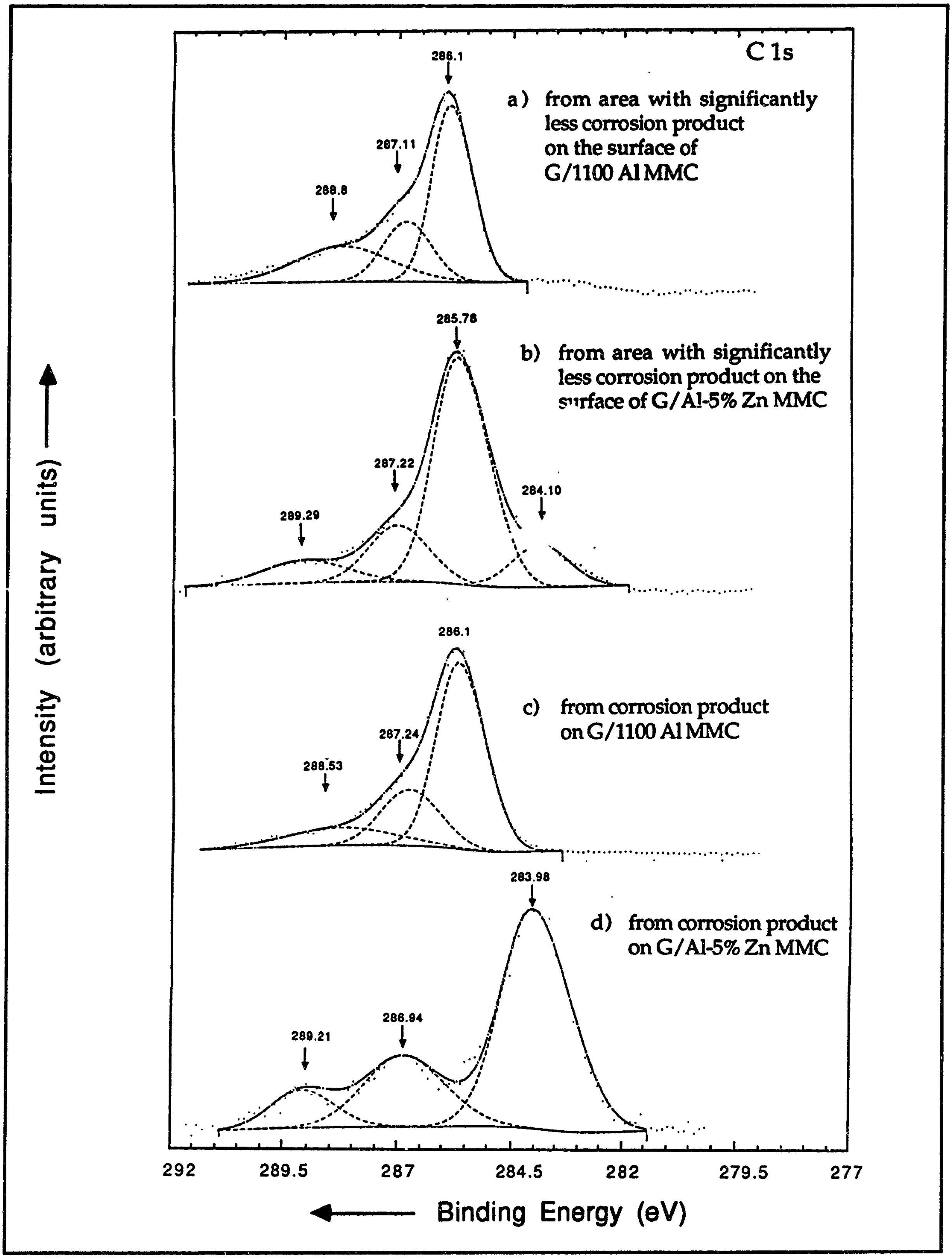

Figure 5.2.10: C 1s XPS peaks on G/Al MMC fiber surfaces.

In Figures 5.2.11 and 5.2.12, the Al 2s and Al 2p energy peaks have been identified, respectively. There are several interesting results that can be derived from the analysis of these peaks. In Figure 5.2.12 it is clear that the Al present on the surface of the fibers in the G/Al-5% Zn MMC was in the form of bayerite $Al(OH)_3$, since the energy value corresponded perfectly to that in the literature (73.9 eV) [Briggs and Seah, 1983]. Therefore, one of the two higher energy peaks in Figure 5.2.5d must be associated with bayerite. Presumably, this is the peak at 118.7 eV, since it was strongest. This would mean that in Figure 5.2.11a and c, bayerite is also present for the G/1100 Al MMC. The literature reports values for Al 2p binding energy for Al_2O_3 at 74.7 eV, and that for bayerite at 73.9 eV. If extrapolation is done, with the assumption that the shift in eVs for the 2s and 2p (ΔE) peaks are nearly the same, one would expect the 2p binding energies to be higher for Al_2O_3 as compared to bayerite, which has been determined to be around 118.7 eV.

In summary, the corrosion product on the surface of the G/1100 Al MMC was composed primarily of Al_2O_3 and some $Al(OH)_3$. The corroded surface of the G/Al-5% Zn MMC, had an oxide containing $Al(OH)_3$ (Compare Figure 5.2.11b and d) in regions containing significant corrosion product (see left side of Figure 5.2.3). Areas with significantly less corrosion product on the surface of the G/Al-5% Zn MMC were covered with a complex Al-Zn oxide. $Zn(OH)_2$ was also determined to be present on the surface of the corroded G/Al-5% Zn MMC in areas with significantly less corrosion product.

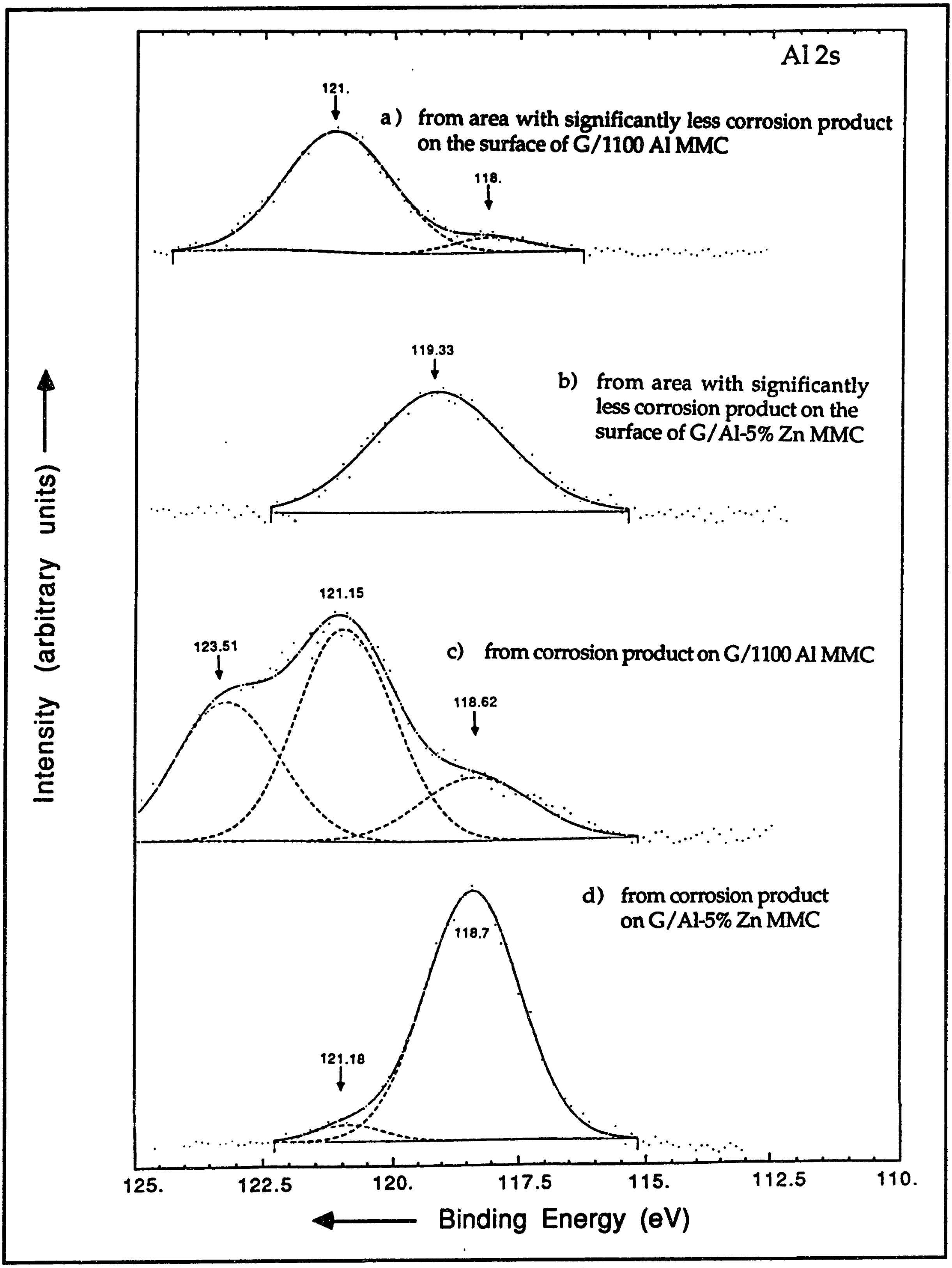

Figure 5.2.11: Al 2s XPS peaks on G/Al MMC fiber surfaces.

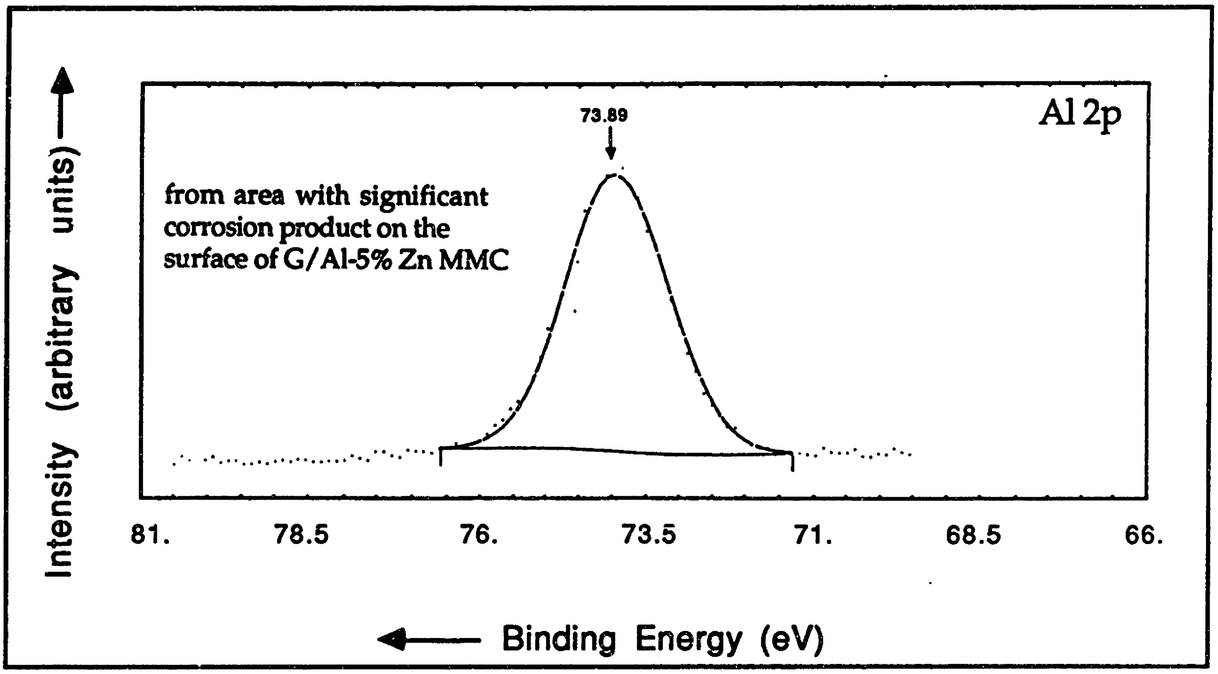

Figure 5.2.12: Al 2p XPS peaks on a G/Al-5% Zn MMC.

5.4 RESULTS OF AES SURFACE ANALYSES

When compared to XPS as a surface analytical technique, AES has the advantage of a much greater lateral spatial resolution, approximately 0.2 µm, while the technique still provides information from the top three monolayers of the material. To accomplish this a 1-10 keV beam is focused on the surface of the sample. Auger electrons created from subsequent electron transitions are ejected from the sample surface. One drawback to AES is that it is not as sensitive to changes in the oxidation state of elements; therefore, although one can locate an element at a more specific location on a sample surface, it is often not possible to establish what chemical state the element is in.

AES analysis was performed on the same specimens previously exposed to XPS analysis in Section 5.2 in order to determine the location of alloying elements after corrosion of the matrix had occurred.

5.4.1 AES Results for the G/1100 Al MMC

The G/1100 Al MMC was examined by AES, after being exposed to aerated NaCl solution for 24 hours. The Auger spectroscope was equipped with SEM imaging. There was very little corrosion product in some areas on the surface. Interestingly, cavern formation due to oxidation of graphite to CO_2 and CO gases occurred on the surface of two graphite fibers in Figure 5.4.1.

AES surveys taken from the area in Figure 5.4.1 on the surface of the graphite fibers, contained no oxygen (see Table 5.4.1a). Other graphite fibers surveyed were apparently covered with a thin oxide film. These regions revealed the presence of carbon and 5 a/o or less oxygen (see Table 5.4.1b). No Al was detected in these regions. Regions that had a visibly thick corrosion product in the SEM had an Al oxide present (see Table 5.4.1c).

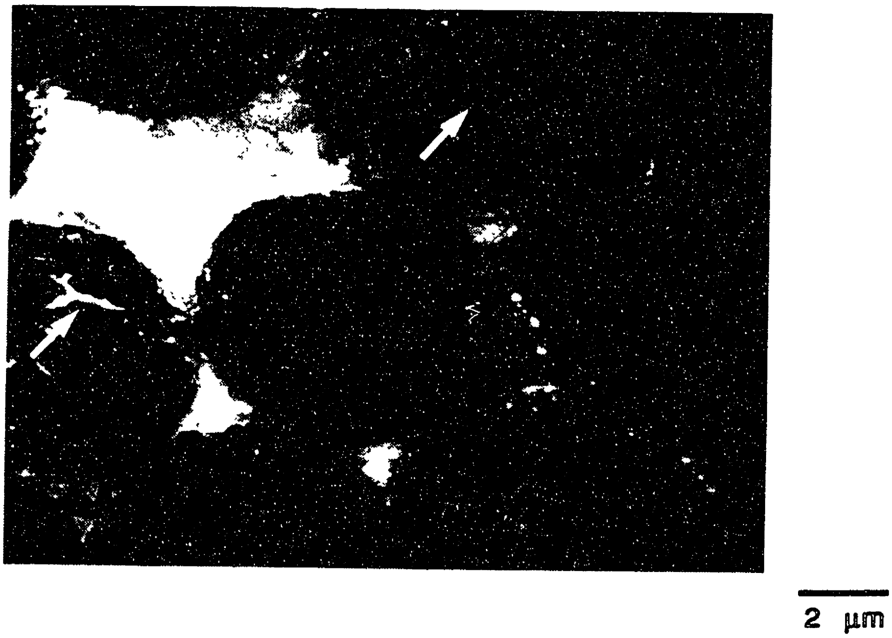

Figure 5.4.1: Secondary electron SEM micrograph for G/1100 Al MMC in a relatively clean area, after 24 hours in aerated 3.15 wt.% NaCl solution. Note cavern formation on graphite fiber surfaces.

Table 5.4.1: Approximate Atomic Concentrations on Fiber Surface Determined by AES for the G/1100 Al MMC

a) on a fiber surface with no visible oxide in SEM,

Element	Peak-to-peak	Sensitivity Factor	Concentration (a/o)
C	200600	0.08	100.00

b) same as in a), and

Element	Peak-to-peak	Sensitivity Factor	Concentration (a/o)
C	191800	0.08	94.36
O	50200	0.35	5.64

c) on a fiber surface with an oxide film visible by SEM.

Element	Peak-to-peak	Sensitivity Factor	Concentration (a/o)
C	110700	0.08	45.94
O	156500	0.35	14.84
Al	82700	0.07	39.22

5.4.2 AES RESULTS FOR THE G/Al-5% Zn MMC

AES analysis was performed on the G/Al-5% Zn MMC to determine the rough compositions of the fiber surfaces. Figure 5.4.2 shows the corroded surface of the G/Al-5% Zn MMC. There are several features on the surface of graphite fibers that warrant attention, noticeably: sharp acicular crystallites on the surface, gray blotchy areas on the graphite fibers, and the surrounding slightly darker matrix. The acicular crystallites where analyzed and found to contain primarily Na, Cl, with traces of Al and O. They are most likely NaCl crystallites formed on the dehydrated fiber surface.

The underlying film was surveyed in several regions to obtain further information. In Figure 5.4.3, a gray blotchy substance (point 1) and a dark oxide-free region (point 2) can be seen. The existence of specific elements at these points and their atomic concentrations were estimated from the AES spectra. It was determined that the gray area (point 1) contained significant amounts of Zn and Al. A rough quantitative analysis was performed using standardless sensitivity factors on surveys taken from the fiber surface. The gray area had a 12. a/o Zn content (see Table 5.4.2a). The dark region (point 2) was primarily carbon, as expected, but, also had a significant concentration of oxygen (see Table 5.4.2b), suggesting that the graphite fiber had formed an oxide.

Table 5.4.2: Approximate Atomic Concentrations on a Fiber Surface in Figure 5.4.3 Determined by AES for the G/Al-5% Zn MMC

a) gray oxide film (point 1),

Element	Peak-to-peak	Sensitivity Factor	Concentration (a/o)
Zn	68800	0.18	12.40
C	65900	0.08	26.72
O	237400	0.35	22.00
Al	83900	0.07	38.88

b) dark black region (point 2),

Element	Peak-to-peak	Sensitivity Factor	Concentration (a/o)
C	112300	0.08	86.30
O	78000	0.35	13.70

c) general fiber (only) surface.

Element	Peak-to-peak	Sensitivity Factor	Concentration (a/o)
Zn	29581	0.18	14.25
C	18697	0.08	20.26
O	87395	0.35	21.65
Al	35395	0.07	43.84

AES elemental maps were acquired over fiber surfaces of the G/Al-5% Zn MMC for Zn, C, O and Al, respectively. To accomplish this, a relatively long acquisition time was employed to acquire a sufficient AES signal from the surface of the specimen (approximately 30 minutes for each element). A Zn AES elemental map (green), corresponding to the SEM image in Figure 5.4.2, is shown in Figure 5.4.4. Zn was found over most of the surface of the graphite fibers, and, produced a bright green signal in areas where the aforementioned gray film (point 1) existed in Figure 5.4.3. When an overall survey was taken for the surface of one fiber (see Table 5.4.2c) the a/o of Zn was found to be 14.25. This was roughly the same as that found for the gray film (compare with Table 5.4.2a). Noticeably, a higher AES signal from Zn was received from around the circumference of the fibers.

Figure 5.4.5 shows the C AES elemental map (red) taken from the the area in Figure 5.4.2. In the absence of Zn, the amount of Auger electrons received from carbon was significant. One is able to see the way in which Zn and carbon complement themselves on the surface of the graphite fibers in Figures 5.4.4 and 5.4.5. In order to better understand the elemental distribution on the surface of the fibers, the Zn and C AES elemental maps (i.e, Figures 5.4.4 and 5.4.5) were superimposed in Figure 5.4.6. In the figure it is clear that Zn is surrounding the perimeter of the fibers (bright green). Further towards the center of the fiber we can see yellow indicating the presence of both Zn and carbon (green and red produce yellow). Regions where bright red exist are primarily carbon. The absence of Zn on the fiber surfaces allowed a stronger carbon signal to be received by AES detector. Note the decrease of the Zn signal in the middle of the recessed Al interstices. Interfacial areas seem to emit Zn Auger electrons, confirming that Zn had segregated preferentially to the G/Al interface. Other elements could be superimposed on this map, however, it becomes more difficult to identify elements if done so.

Figure 5.4.7 shows the O AES elemental map (blue) taken from the the area in Figure 5.4.2. It is apparent that oxygen was greatest near the edge of the fiber, but was also present over nearly the entire surface of the fibers, indicating that graphite oxide had formed with carbon in what appeared as dark black regions in the SEM (see Figure 5.4.3: point 2). The survey for one of the fiber surfaces (see Table 5.4.2c) was found to contain 21.65 a/o oxygen. In areas on the fiber surface where either Al or Zn existed, the oxygen a/o was ~ 21; however, at point 2 in Figure 5.4.3, where no metals were found, the oxygen a/o was nearly half (see Table 5.4.2b) that found on the gray film, point 1. It is apparent from this that the metals present on the surface of the fibers were in the form of metallic oxides. Figure 5.4.8 shows the green Al AES elemental map for the same area. It is dispersed over the surface of the graphite fibers in a similar fashion as that of oxygen. Also, the Al map is noticeably bright from the recessed matrix (see Figure 5.4.2). Absorptivity factors have not been taken into account in the AES elemental maps, therefore, one must be careful not to extrapolate concentration values from the maps. The maps do however, give a compendium of the distribution and location of elements on the corroded samples. Figure 5.4.9 shows the four AES elemental maps for the G/Al-5% Zn MMC in one black and white photograph. In this photograph all of the elements can be compared with just a glance; the photo is also presented for archival purposes.

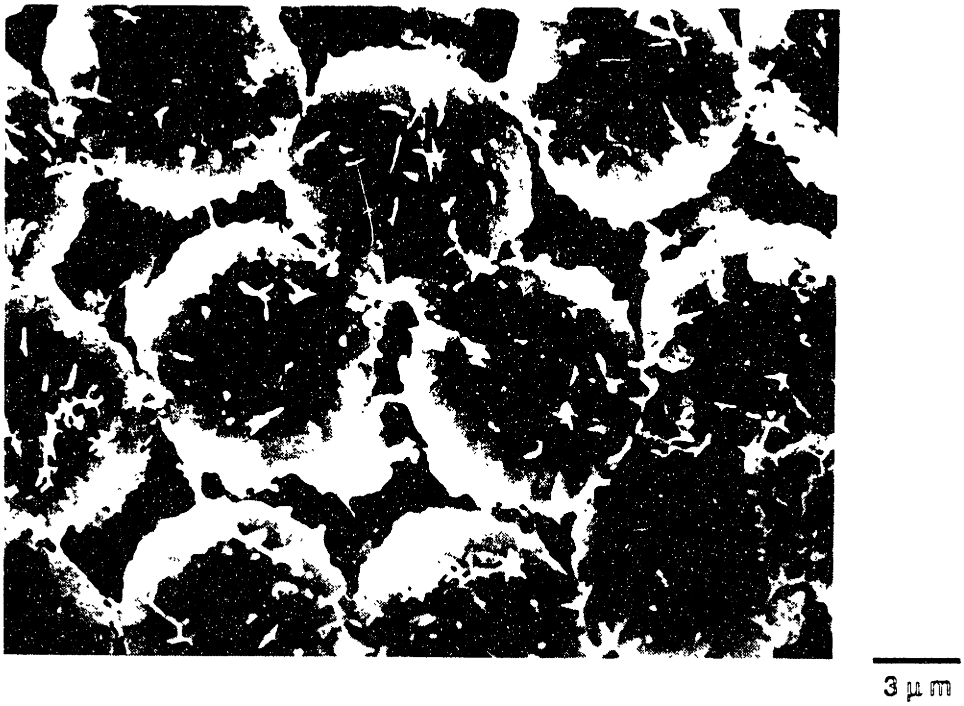

Figure 5.4.2: Secondary electron SEM micrograph for G/Al-5% Zn MMC showing oxide and NaCl crystals after 24 hours in aerated 3.15 wt.% NaCl solution. Horizontal lines are channels of Al resulting from pressure infiltration.

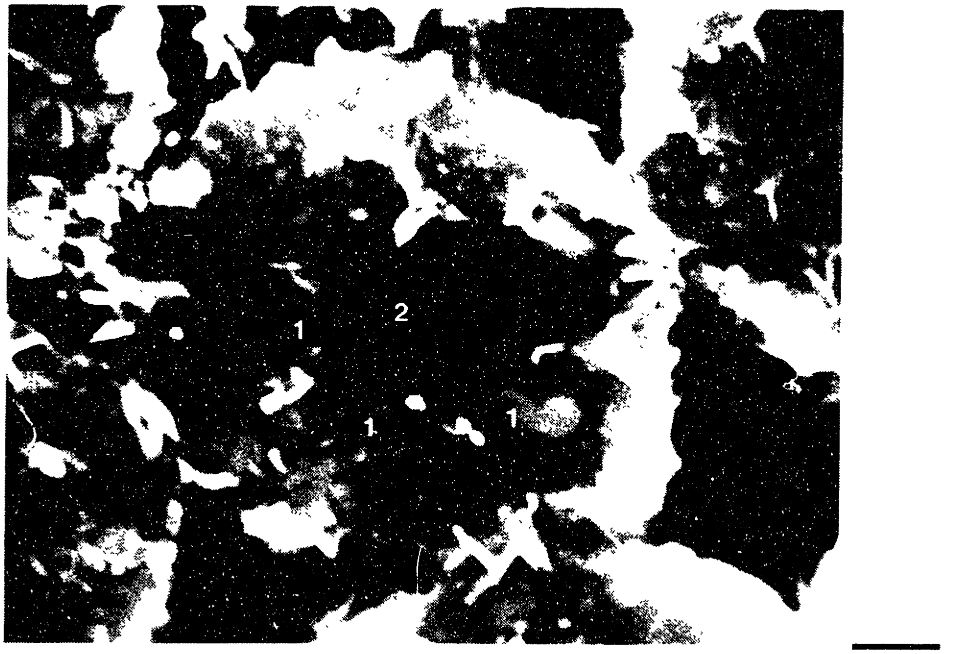

Figure 5.4.3 Secondary electron SEM micrograph of graphite fiber surfaces on a G/Al-5% Zn MMC after 24 hours in aerated 3.15 wt.% NaCl solution, showing: 1) gray film and 2) dark black graphitic region.

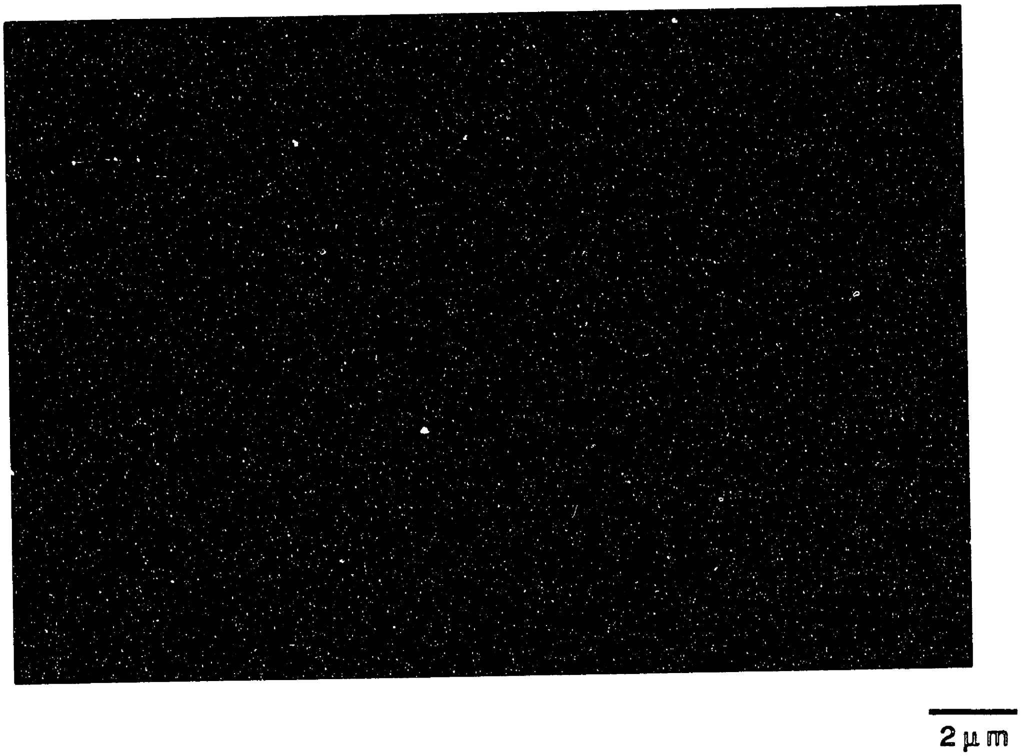

Figure 5.4.4: Zn (in green) AES elemental map on fiber surfaces in Figure 5.4.2 for a G/Al-5% Zn MMC.

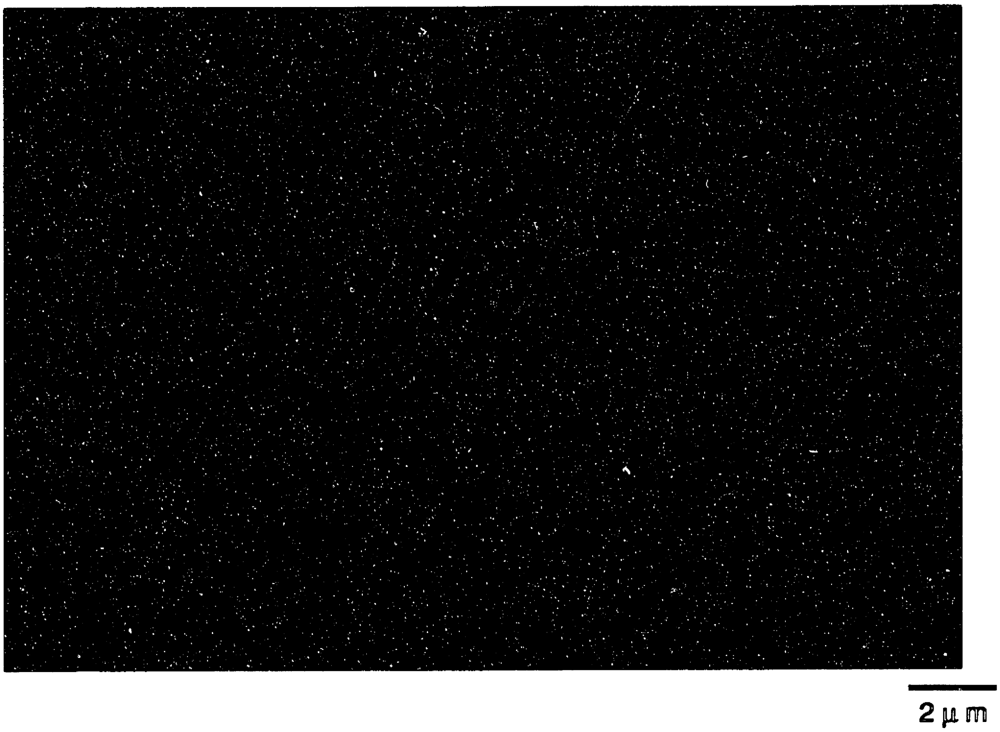

Figure 5.4.5: C (in red) AES elemental map on fiber surfaces in Figure 5.4.2 for a G/Al-5% Zn MMC.

Figure 5.4.6: Zn (in green) and C (in red) superimposed AES elemental maps on fiber surfaces in Figure 5.4.2 for a G/Al-5% Zn MMC. Areas with Zn and C appear as yellow.

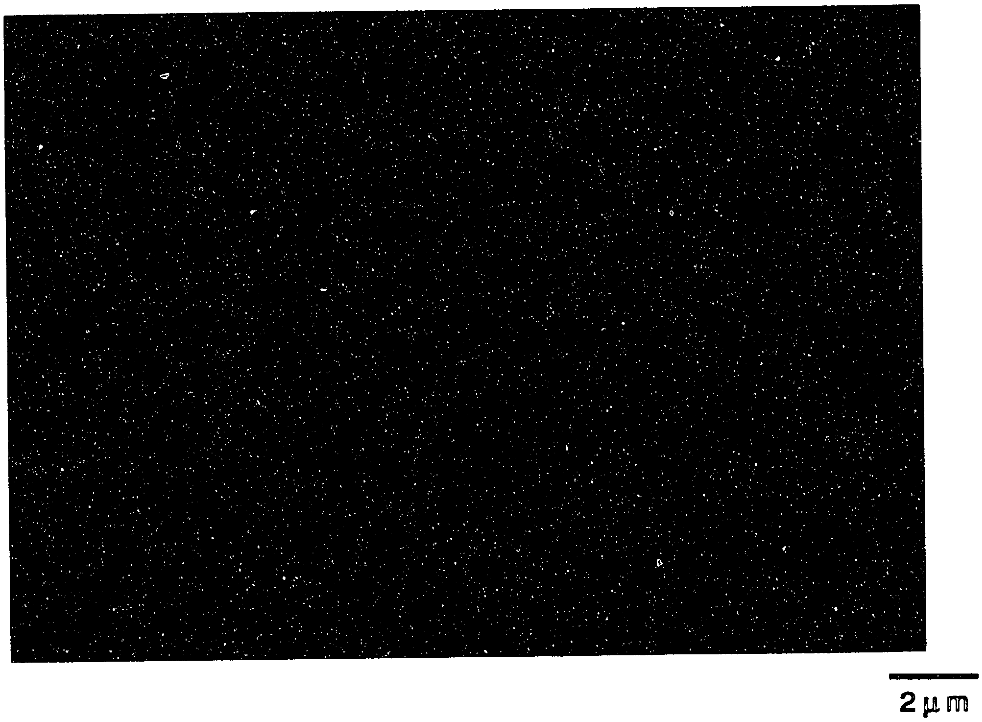

Figure 5.4.7: O (in blue) AES elemental map on fiber surfaces shown in Figure 5.4.2 for the G/Al-5% Zn MMC.

Figure 5.4.8: Al (in green) AES elemental map on fiber surfaces in Figure 5.4.2 for a G/Al-5% Zn MMC.

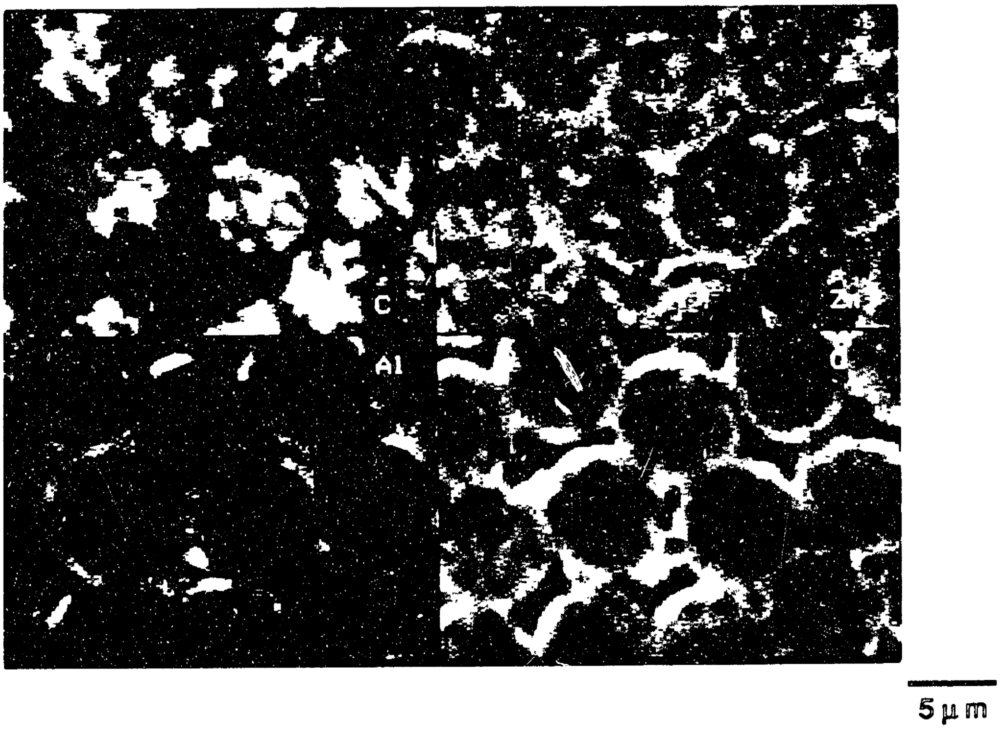

Figure 5.4.9: Archival black and white AES elemental maps showing, from the top left in a clockwise direction, C, Zn, O, and Al maps, respectively, on the fiber surfaces in Figure 5.4.2.

6. SPM TESTING OF MODEL AND COMMERCIAL G/Al MMCS

6.1 INTRODUCTION

SPM testing of model G/Al MMCs was carried out to examine the possibility of reducing corrosion by two different methods: 1) electrical insulation of graphite and 2) cathodic inhibition of oxygen reduction on graphite.

Several commercial MMCs were also tested to determine if the SPM probe could resolve electrochemical phenomena occurring near the surface of the specimens.

Large-scale model G/Al MMCs were made at MIT. These were then examined with the scanning potential microprobe (SPM) at the Marine Biological Laboratory (MBL), Woods Hole, MA. Large-scale model composites were investigated using the scanning vibration electrode technique (SVET) as discussed in Section 2.8. Scheffey and Isaacs have extensively reviewed this technique elsewhere [Scheffey, 1986a, 1986b; Isaacs, 1986, 1988, 1989] and details of the probe electronics used at MBL are also available [Scheffey, 1988]. The fabrication and modifications of the model MMCs are presented in detail.

6.2 EXPERIMENTAL

6.2.1 Fabrication of Model G/Al MMCs

Completely graphitized pitch-based rod, 0.762μm in diameter and 30.5cm in length, was supplied by Micro Mechanics Inc, Ipswitch, MA. To produce model G/Al MMCs, a small furnace was made at the MIT (see Figure 6.2.1). 99.99% pure Al was melted at 680°C in a quartz tube. The quartz tube was coated beforehand with a carbon diffusion barrier [Formkote T50™, EM Corporation, IN] to prevent silicon from entering the melt. A Teflon® [Dupont, DE] cap was inserted after the Al had reached 680°C. The Teflon cap was machined to hold the graphite rod in place during solidification. Although this technique was not performed under hydrostatic pressure, it did facilitate water quenching. This minimized the amount of contact time between the Al and graphite.

Observation of prepared samples with an optical and scanning electron microscope (SEM) showed that the G/Al interface contained no large Al_4C_3 platelets (see Figure 6.2.2).

Quartz tubes with 11mm and 16mm inner diameters were used to compare the SPM results as a function of anodic surface area. Uncoated specimens were polished to 0.3μm with gamma Al_2O_3 powder in pure water (18 MΩ·cm).

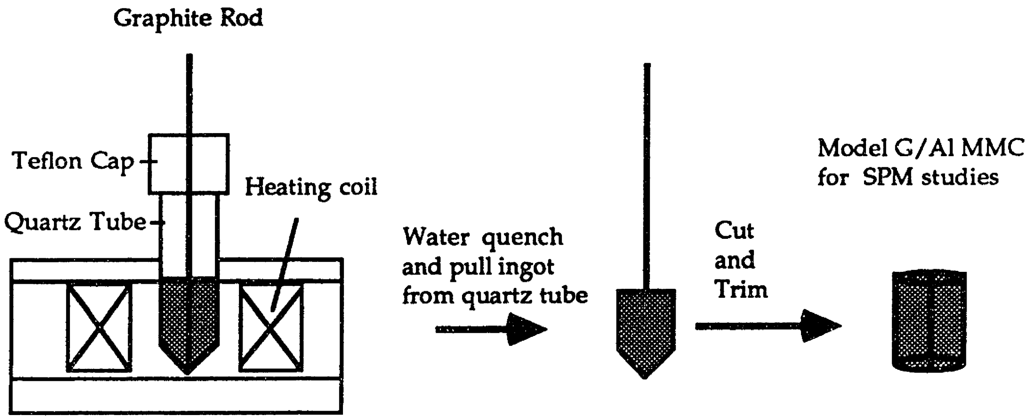

Figure 6.2.1: Schematic for the fabrication of model G/Al MMCs prepared at MIT.

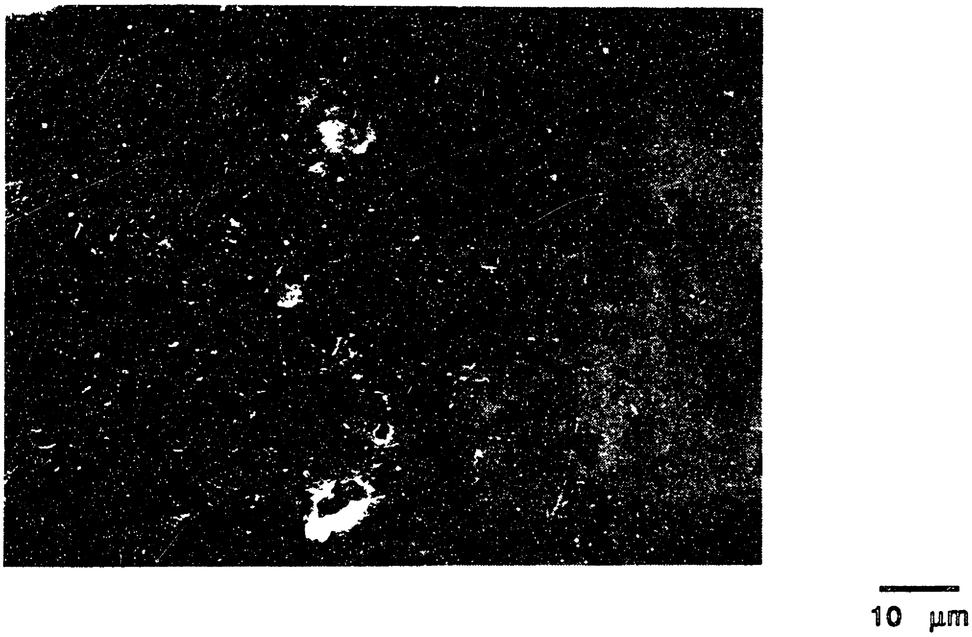

Figure 6.2.2: Representative region of model G/Al MMC interface (graphite on the left). Good interfacial contact was achieved, and no large Al_4C_3 platelets were observable at the interface.

6.2.2 Alumina (Al_2O_3) Coating of Graphite Rod

In order to coat the rod with alumina (Al_2O_3), the alkoxide route was adopted [Katzman, 1987, 1990a]. The technique was successful in producing fine silica coatings on graphite fibers, and it was also reported to work well in forming Al_2O_3 coatings on graphite fibers [Katzman, 1990b]. Graphite rod was baked overnight at 200°C to remove any moisture and contamination. A solution of toluene-based 8-vol.% aluminum isopropoxide ($Al(OC_3H_7)_3$) was ultrasonically mixed for 30 minutes. Thereafter, the baked-rod was placed in solution and ultrasonically bathed for 30 seconds and removed. In order to hydrolyze the coating, the rod was placed above a boiling mixture of pure water (18 MΩ·cm) for 30 seconds. Finally, the rod was placed in a tube furnace containing an argon atmosphere at 500°C for about one minute to vaporize any excess solvent or water and to pyrolyze any unhydrolyzed organometallic compounds. The entire procedure was then repeated to ensure that the coating completely covered the rod.

The rod was viewed by SEM (see Figure 6.2.3). The coating was rough and porous in nature; however, there were no apparent bare spots; the rod was completely coated. Energy dispersive analysis of X-rays (EDAX) revealed only Al, indicating that the film was most probably Al_2O_3. Auger electron spectroscopy (AES) was also used to determine that the coating was Al_2O_3. A known AES spectrum for Al_2O_3 was compared to that obtained from this coating; they were of the same shape and energy. AES was also used to estimate the thickness of the coating. To accomplish this, a 1000Å tantalum oxide/tantalum sample was argon ion-sputtered until the 1000Å oxide was removed. Under the same ion beam conditions, the Al_2O_3-coated graphite rod was sputtered until the AES Al signal from the Al_2O_3 coating disappeared. The rate of oxide removal was assumed to be the same for the tantalum oxide and Al_2O_3 [Katzman, 1987, 1990a]. From these results, the Al_2O_3 coating was determined to be on the order of 4000Å thick. Subsequently, this rod was used for the production of model G/Al MMCs, as outlined in the previous section. All model G/Al MMCs, except those ion-implanted with Zn, were metallurgically polished to 0.3µm with gamma Al_2O_3 powder in pure water (16 MΩ·cm). They were repolished with 0.25µm diamond paste mixed with pure water and then thoroughly rinsed prior to SPM scans at the Marine Biological Laboratory (MBL).

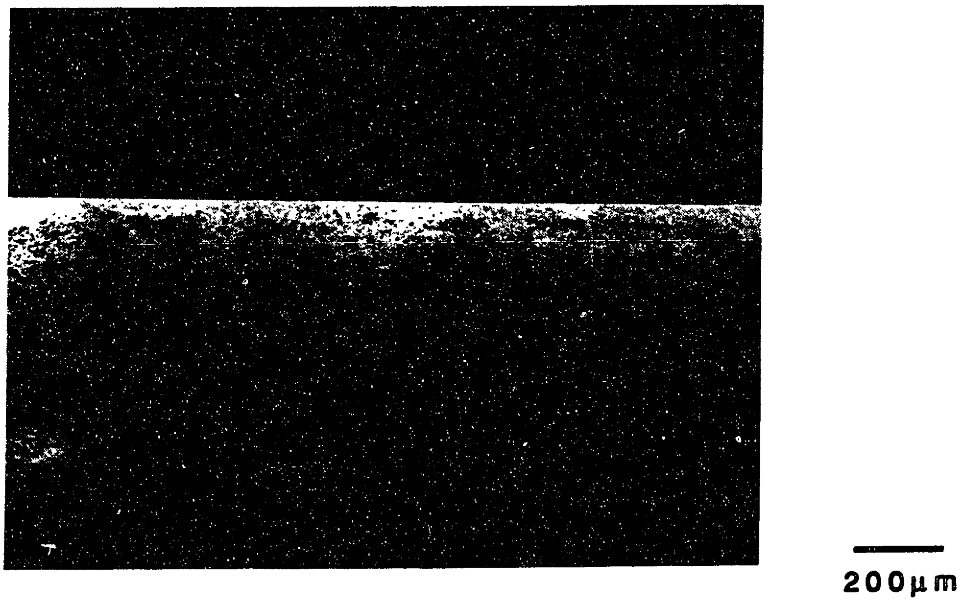

Figure 6.2.3: Secondary electron SEM image of Al_2O_3-coated graphite rod. The rod is completely coated and porous.

6.2.3 Zn Ion Implantation of Model G/Al MMCs

Uniform ion implantation along the circumferential area of the cylindrical graphite rods was not feasible; therefore, the surfaces of the model G/Al MMCs were implanted with Zn^{2+} cations (see Figure 6.2.4). Ion implantation with Zn^{2+} cations was only achievable for implantation depths on the order of 1000Å, and therefore the specimens could not be polished after the implantation or the implanted Zn would be removed. Zn^{2+} cations were implanted at superimposed ion beam energies of 75, 100, 125, 150 and 175 keV to attain a total fluence of 1.2×10^{14} Zn atoms/cm^2 on two model G/Al MMCs of 11mm and 16mm diameter. The various beam energies were employed so that a higher concentration level of Zn would be attained throughout the implanted surface.

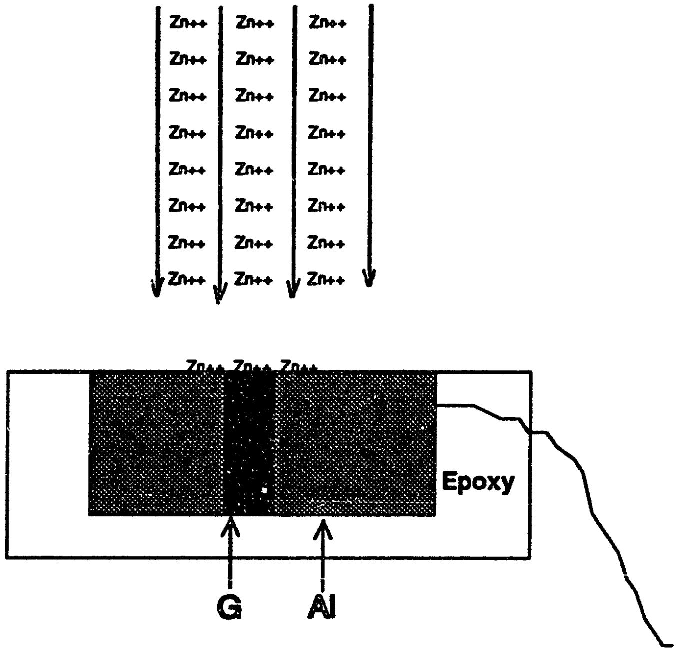

Figure 6.2.4: Schematic showing model MMC geometry during Zn ion implantation.

The rationale behind ion implanting with Zn^{2+} cations was to place Zn atoms in the graphite rod so that they could become solvated as Zn^{2+} cations in solution. Thereafter, the Zn^{2+} cations could migrate and form $Zn(OH)_2$ film on exposed cathodic graphite. This film could then limit the galvanic corrosion process between the graphite and Al by reducing cathodic reduction of oxygen which occurs readily on graphite. Thus, ion-implanted Zn would be acting as a cathodic inhibitor. Addition of as little as 10ppm $ZnCl_2$, a known cathodic inhibitor, to aerated 3.15 wt.% NaCl solutions, resulted in decreased corrosion rates for G/Al galvanic couples by a factor of 10 to 100 [Hihara, 1989] (see Section 2.3).

6.2.4 SPM Testing Procedure †

A schematic of the assembly used at the Marine Biological Laboratory (MBL), Woods Hole, MA is shown in Figure 6.2.5. In the schematic are the probe, model G/Al MMC, optical microscope and assembly to determine the open circuit potential (Ecorr). For each scan point measured, the SPM probe was in vibration for a period of 10 seconds. A probe measurement was taken at 500µm above the surface in order to subtract the background current from the

---

† For additional information concerning SPM analysis refer to Section 2.8

desired surface measurements taken from a height of approximately 27μm above the surface of the sample. Current density vectors measured by the probe were superimposed upon a video image of the investigated specimen. The current density vectors are graphically represented as arrows starting at the position of the observation and with length and direction representing the field measurement. This will be discussed in greater detail in Section 6.3.

In this study Ecorr values for the model G/Al MMCs, with reference to the saturated calomel electrode, were also monitored (see Figure 6.2.5). The results were monitored with a chart recorder for the period of time that the sample was tested by the SVET, approximately 20 minutes. All tests were conducted in 0.01M NaCl exposed to air.

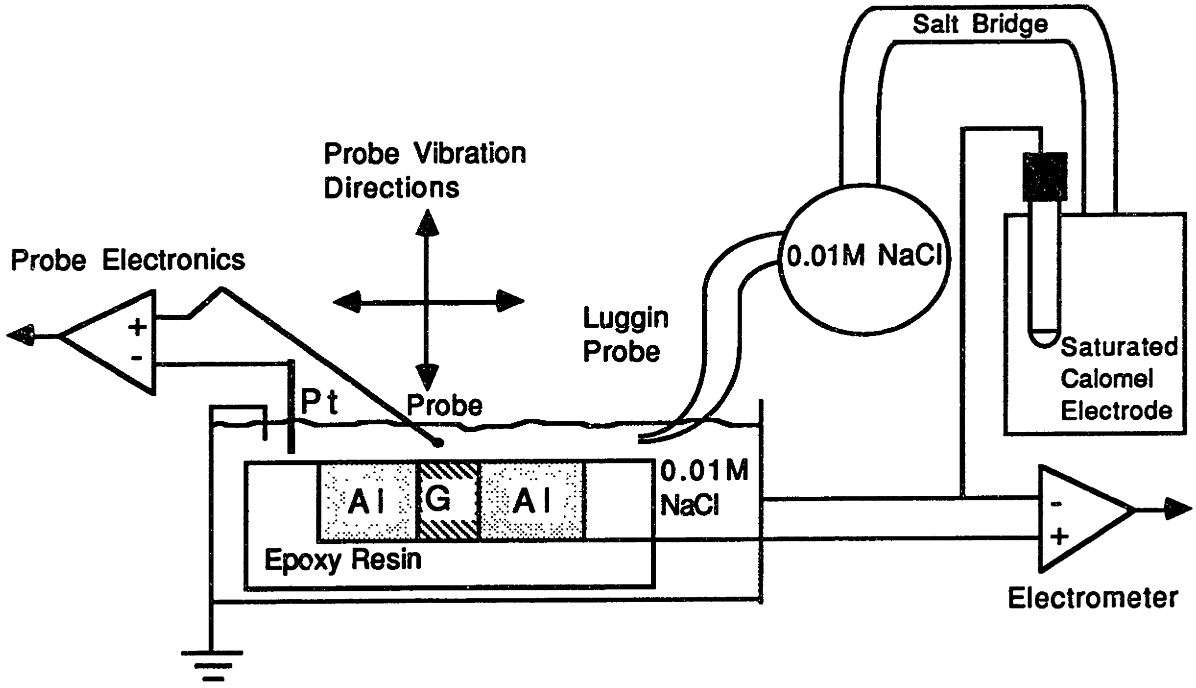

Figure 6.2.5: Schematic of SPM assembly used to study model G/Al MMCs at the Marine Biological Laboratory (MBL), Woods Hole, MA.

6.2.5 Preparation of Commercial G/Al MMCs for SPM Testing

Commercial composites were examined with the SPM in order to see if any features could be discerned with a probe of 7μm in diameter. Table 6.2.1 shows the commercial MMCs examined with the SPM.

Table 6.2.1 Commercial G/6061Al MMCs Studied with the SPM

Spec. #	Matrix	Vol.% Fiber	Fiber Type	Fiber E mod.	Fiber Orientation	Processing Route	Lab. Code
23†	6061 Al	50%	Pitch-Based diam.=10μm.	100 Msi	Continuous	Diffusion Bonding of fiber tows (2000-fibers/tow)	100
24†	6061 Al	42%	"	75 Msi	0-90°	Squeeze Casting	101
25*	6061 Al	51%	"	50 Msi	0-90°	Vapor Deposition/ Diffusion Bonding	102

†DWA Composite Specialties, Inc., Chatsworth, CA 91311.

* CORDEC Corp., Lorton, VA 22079.

Specimen 23 was produced by a process that left behind residual chlorides between fiber tows, which were diffusion-bonded together in the process [Hihara and Latanision, 1990, 1991]. All other commercial MMCs were produced by processes which precluded the use of chlorides.

In the squeeze casting process, sheets of Al-foil are layered between graphite fiber mats held together by an epoxy resin in vacuum. The 0-90° fiber orientation helps to improve the composites anisotropy. At relatively lower temperatures than those used for pressure infiltration, but higher than those used for diffusion bonding processing, the "liquid + solid" melt is 'squeezed' to the desired composite shape. The resultant intermetallic distribution was shown earlier in Figure 2.5.2.

Specimen 25 was processed by first electrically collecting Al on individual graphite fibers and then diffusion bonding the individual fibers between Al-foil, rather than between fiber tows, as was the case for Specimen 23. Therefore, the distribution of fibers in Specimen 25 was more homogeneous.

AES analysis was performed on polished longitudinal cross-sectional areas for Specimens 24 and 25. To accomplish this, known AES spectra [Mortensen, 1986] for pure Al, Al in Al_4C_3, C in Al_4C_3, and C in graphite, were compared with those obtained by analyses. From the spectra obtained, no Al_4C_3 formation could be detected. It is probable that sub-micron Al_4C_3 was present.

To prepare commercial G/Al MMCs for SPM testing, samples of equal transverse cross-sectional areas (Specimens 23 to 25) were painted with two coats of Amercoat® 90 [Ameron Protective Coatings Division], an oxide paint that protects against crevice formation that sometimes occurs between the sides of the specimens and the mounting medium. Thereafter, the specimens were encapsulated in Epon® 828 Resin [Shell Chemical Company, TX] with a slow cure rate (~7 days) to reduce the amount of separation between specimen and mount due to shrinkage. The commercial G/Al MMCs were mechanically polished down to 0.25μm with diamond paste [Buehler Ltd., OH] in 16 MΩ·cm water and rinsed with 16 MΩ·cm water. The specimens were tested with the same parameters as discussed in Section 2.8 and with the same high resistance solution (open to air 0.01M NaCl) as was used for the model G/Al MMCs previously discussed in Section 6.2.4.

6.3 SPM RESULTS FOR MODEL G/Al MMCs

The schematic in Figure 6.3.1 shows how the SPM probe is vibrated in two directions: normal to the surface in the z direction, and parallel to the surface in the x direction. Figure 6.3.1 also shows the two-dimensional representation of x and z directions, which is superimposed on the photo. A negative z component of a current density vector in the photo represents a net cathodic ionic current; a positive z component of a current density vector in the photo indicates a net anodic current. The x and z components of the superimposed current density vector in the photo give the actual directions of the net ionic current in the x and z directions, respectively.

Video images of the model G/Al MMC samples were taken at the beginning of the corrosion study and thereafter every 24 hours after having been left in 0.01M NaCl solution (see Figures 6.3.2 through 6.3.10). The superimposed vectors in the figures give the current density vectors measured by the SVET technique. Regions over graphite were found to be cathodic as opposed to regions over Al which were anodic. Current was found to flow from the Al to the graphite or from anode to cathode, as expected.

For some samples, after 48 hours in solution, a large crevice formed at the G/Al interface (see Figures 6.3.5 and 6.3.7). Regions probed above the crevice were found to be strongly anodic, indicating that dissolution of Al at the crevice was increased.

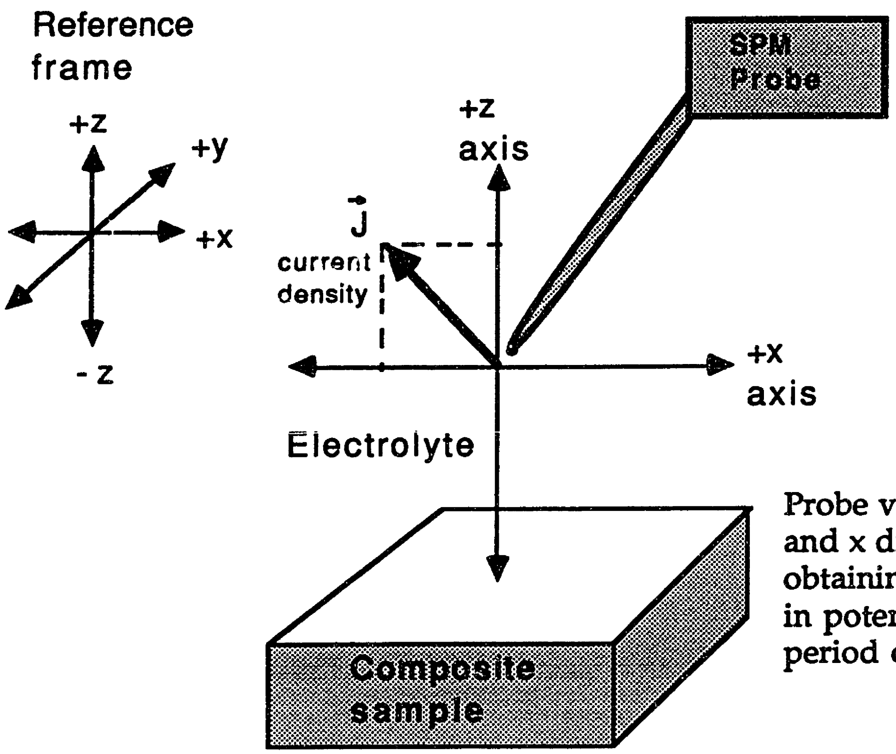

Probe vibrates in the z and x directions obtaining the difference in potential during the period of vibration.

The potential measured during probe vibration is translated to a current density vector.

The two-dimensional representation of x and z current density vectors are superimposed on a photo.

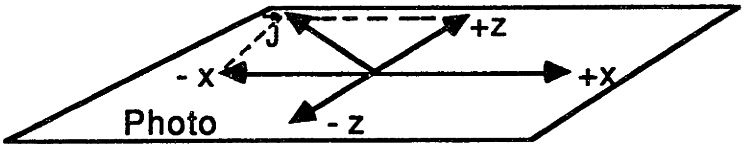

Figure 6.3.1: Schematic representation of current density vectors obtained from SPM analysis.

It was arbitrarily decided to consider the G/Al interface as a reference point; cathodic current densities were measured at a point 90μm from the interface over the embedded graphite rod, while anodic current densities were measured at a distance of approximately 180μm from the interface over the Al. In this way, current density values could be compared over a period of time. Figures 6.3.11 through 6.3.13 show the results of the SPM studies performed on four model G/Al MMCs tested.

In Figure 6.3.11, Ecorr values obtained for the model G/Al MMCs are shown. The Ecorr values were relatively noble (positive), due to the presence of dissolved oxygen; the tests were performed in air. As time elapsed, the Ecorr values moved to more active (negative) values for uncoated and Al_2O_3-coated model G/Al MMCs; this was due to the formation of a crevice at the G/Al interface.

The Al_2O_3-coated graphite did not resist the flow of electrons at the G/Al interface. In fact, the Al_2O_3-coated specimen had the highest corrosion (anodic) current density of all samples tested (see Figure 6.3.13) after 48 hours. The crevice formed can be seen at the G/Al interface in Figure 6.3.5.

The Ecorr values for those specimens which were ion-implanted with Zn became more noble after a period of 24 hours (see Figure 6.3.11). This was corroborated by the magnitude of the cathodic and anodic current density vectors obtained over samples in Figures 6.3.12 and 6.3.13, and will be discussed in Chapter 7.

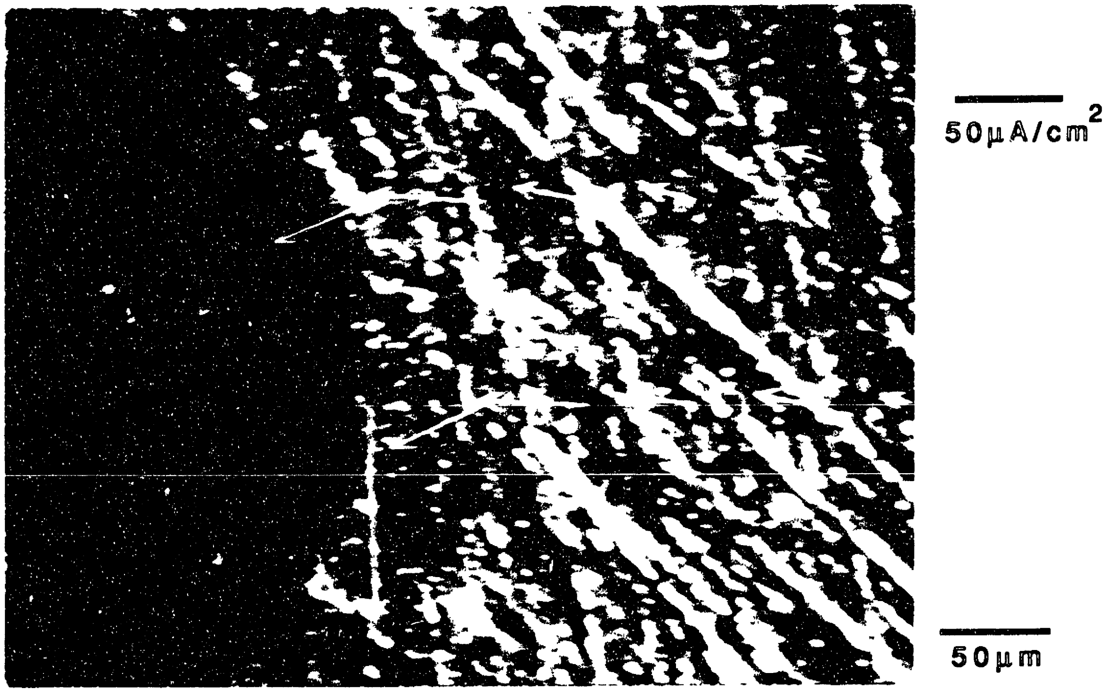

Figure 6.3.2: Video image of an uncoated model G/Al MMC specimen with a 16mm outer Al diameter at time = 0. SPM current density vectors have been superimposed. Solution 0.01 M NaCl open to air. pH~7

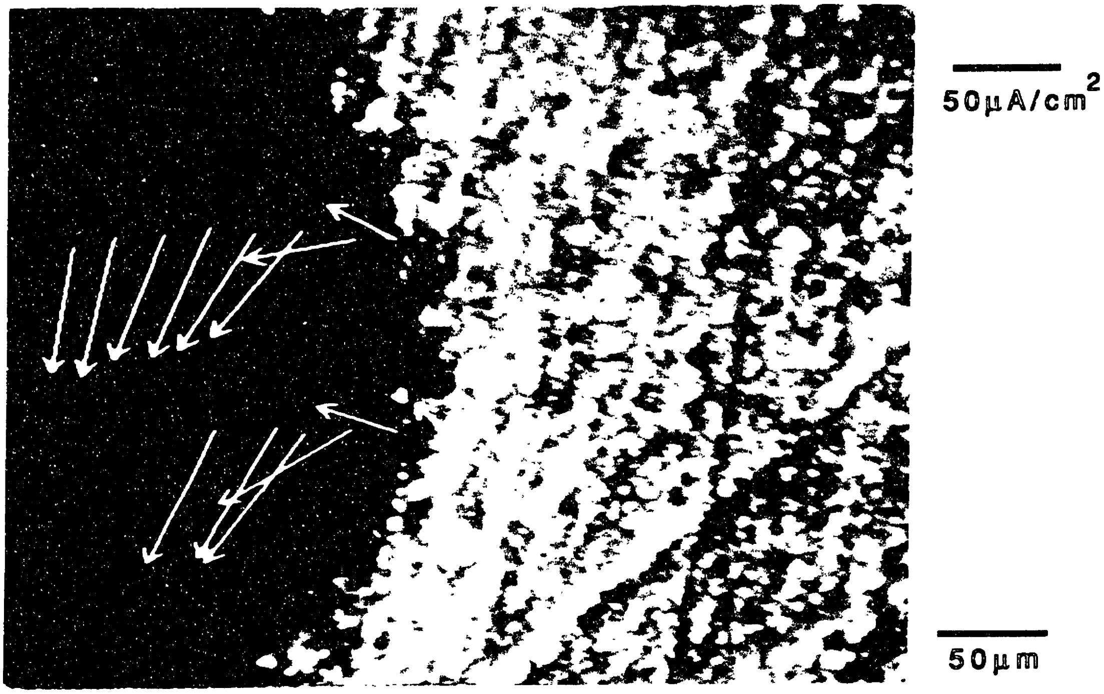

Figure 6.3.3: Video image of an uncoated model G/Al MMC specimen with a 16mm outer Al diameter at time = 48hrs. SPM current density vectors have been superimposed. Solution 0.01 M NaCl open to air. pH~7

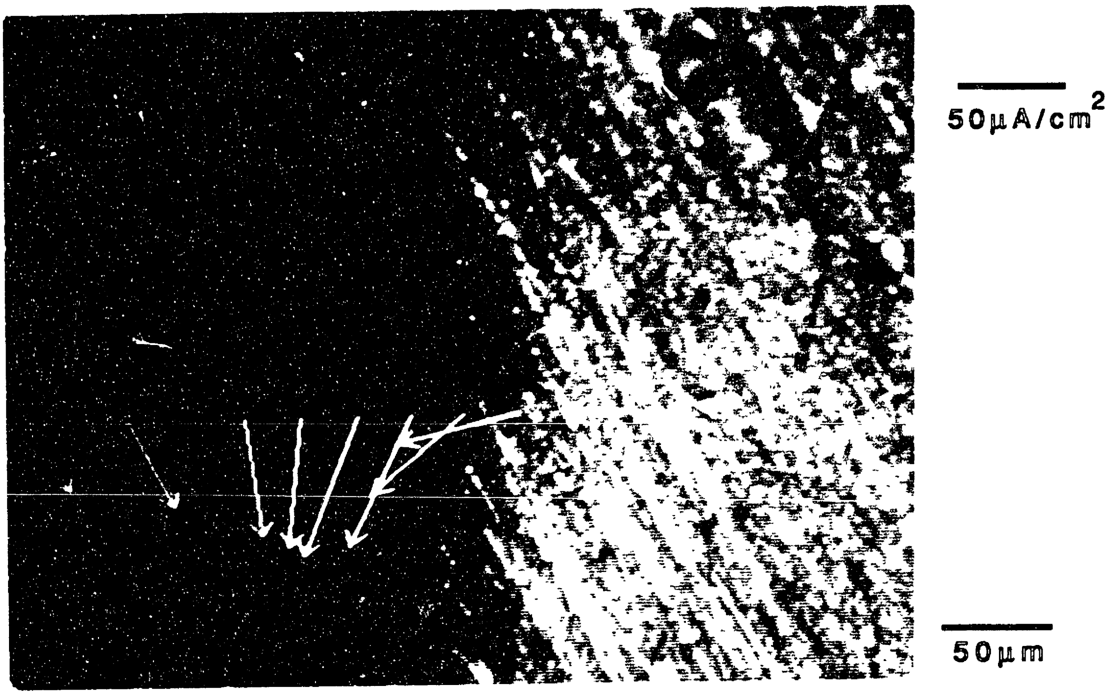

Figure 6.3.4: Video image of an Al_2O_3-coated model G/Al MMC specimen with a 16mm outer Al diameter at time = 0. SPM current density vectors have been superimposed. Solution 0.01 M NaCl open to air. pH~7

Figure 6.3.5: Video image of an Al_2O_3-coated model G/Al MMC specimen with a 16mm outer Al diameter at time = 48hrs. SPM current density vectors have been superimposed. Solution 0.01 M NaCl open to air. pH~7

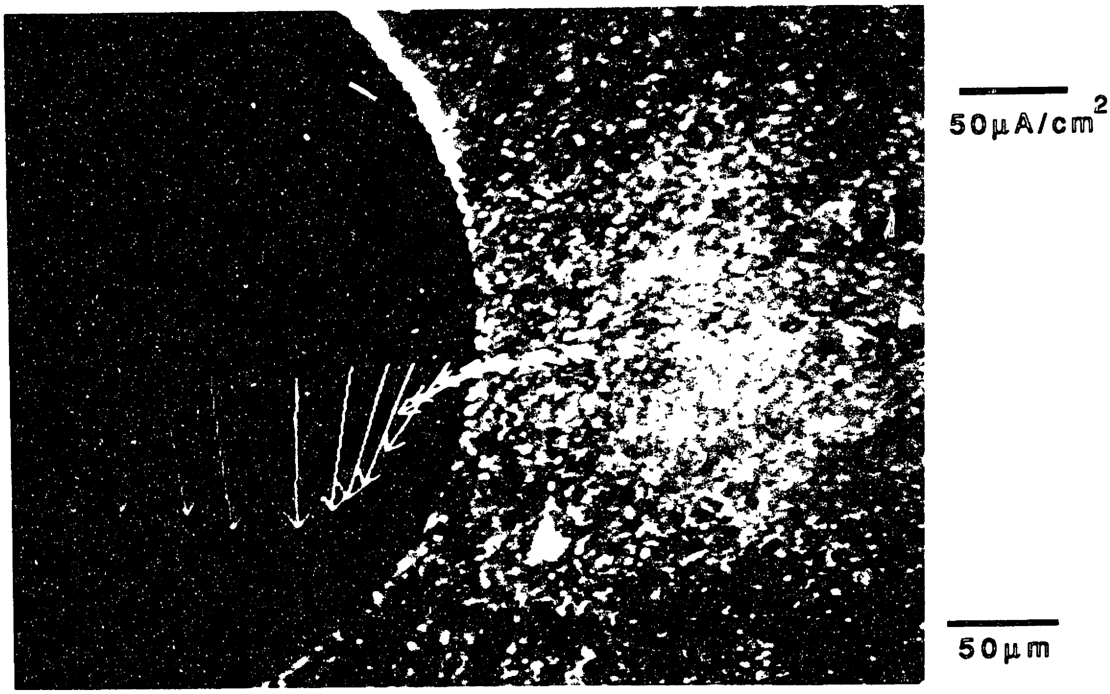

Figure 6.3.6: Video image of an Zn-implanted model G/Al MMC specimen with a 16mm outer Al diameter at time = 0. SPM current density vectors have been superimposed. Solution 0.01 M NaCl open to air. pH~7

Figure 6.3.7: Video image of an Zn-implanted model G/Al MMC specimen with a 16mm outer Al diameter at time = 48hrs. SPM current density vectors have been superimposed. Solution 0.01 M NaCl open to air. pH~7

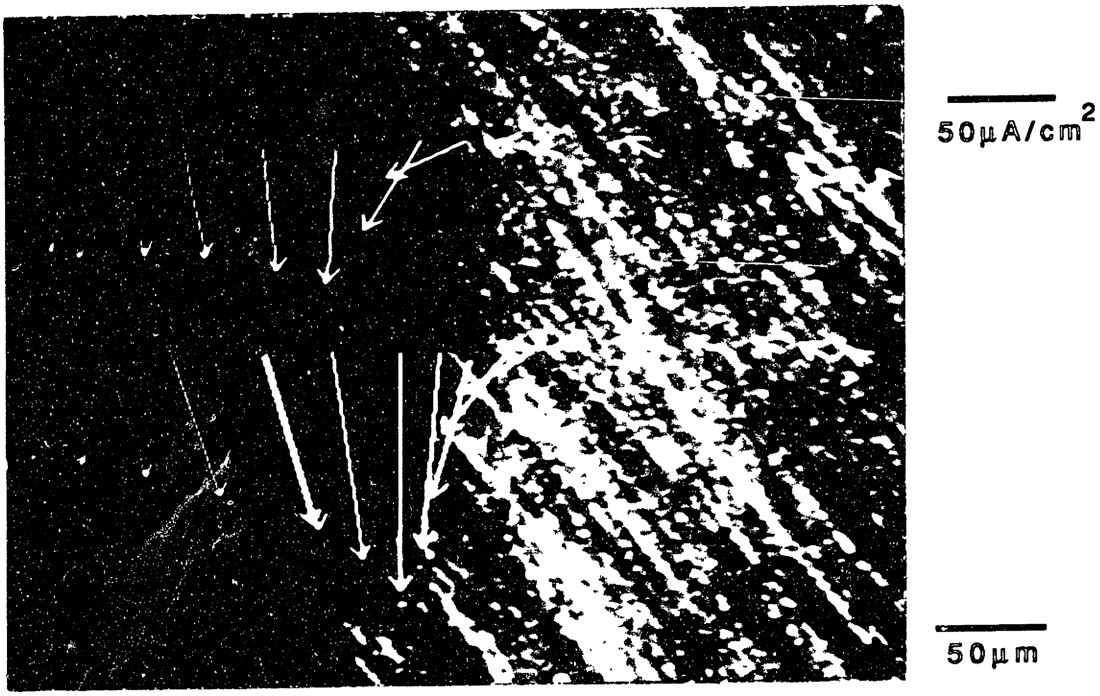

Figure 6.3.8: Video image of an Zn-implanted model G/Al MMC specimen with an 11mm outer Al diameter at time = 0. SPM current density vectors have been superimposed. Solution 0.01 M NaCl open to air. pH~7

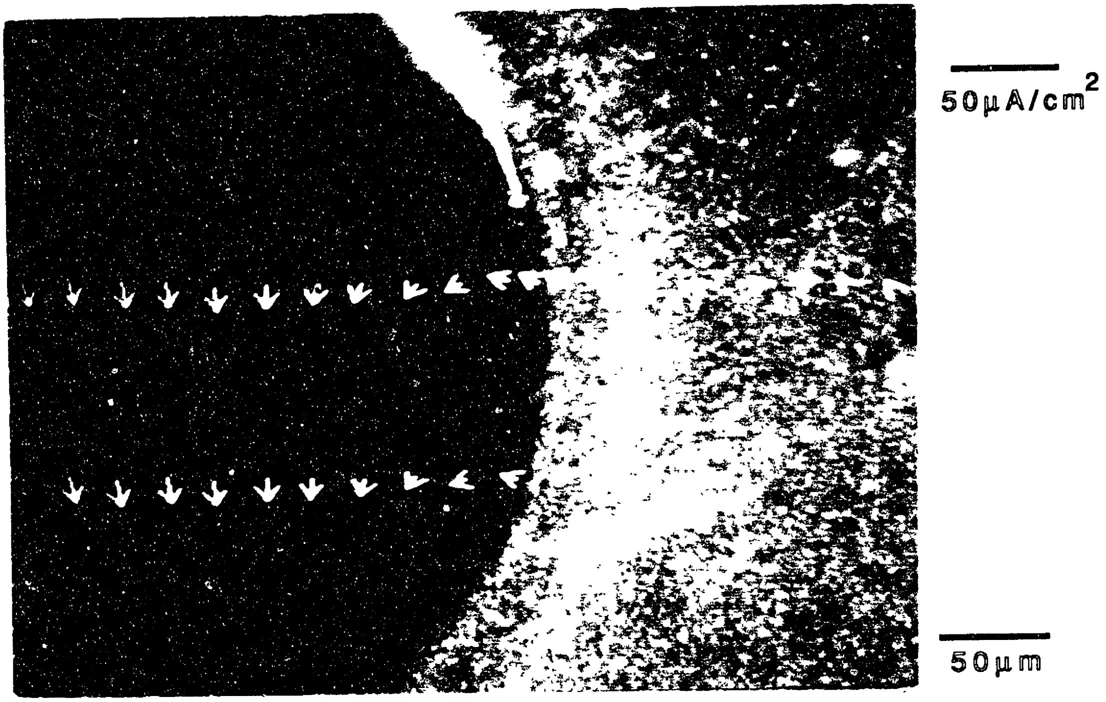

Figure 6.3.9: Video image of an Zn-implanted model G/Al MMC specimen with an 11mm outer Al diameter at time = 24hrs. SPM current density vectors have been superimposed. Solution 0.01 M NaCl open to air. pH~7

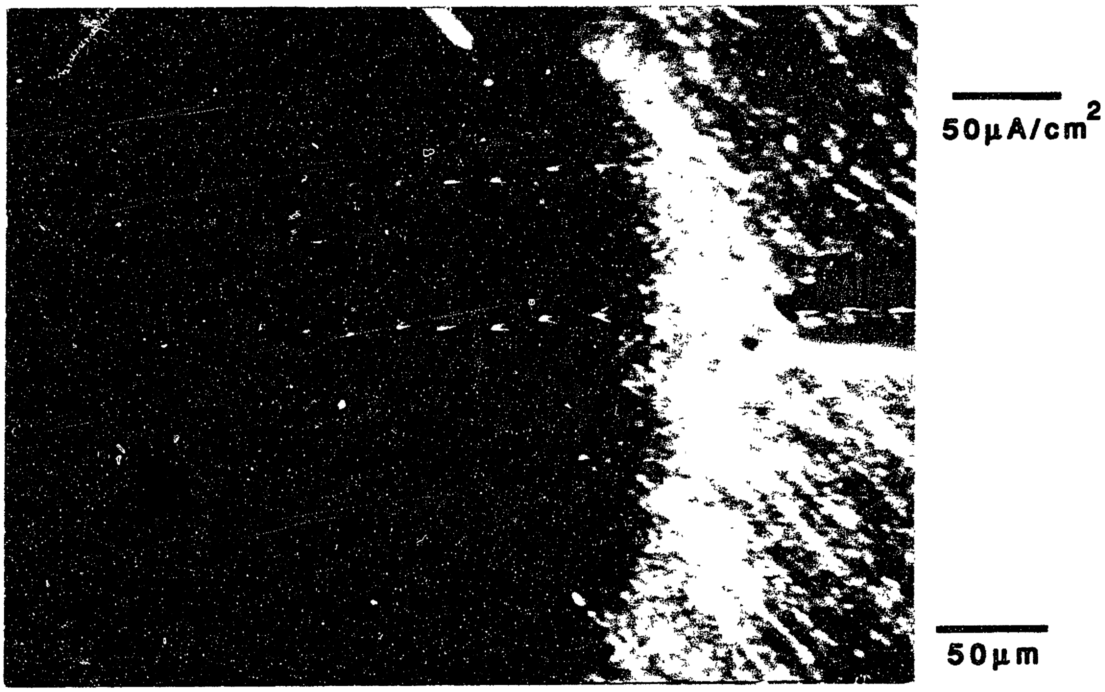

Figure 6.3.10: Video image of an Zn-implanted model G/Al MMC specimen with an 11mm outer Al diameter at time = 48hrs. SPM current density vectors have been superimposed. Solution 0.01 M NaCl open to air. pH~7

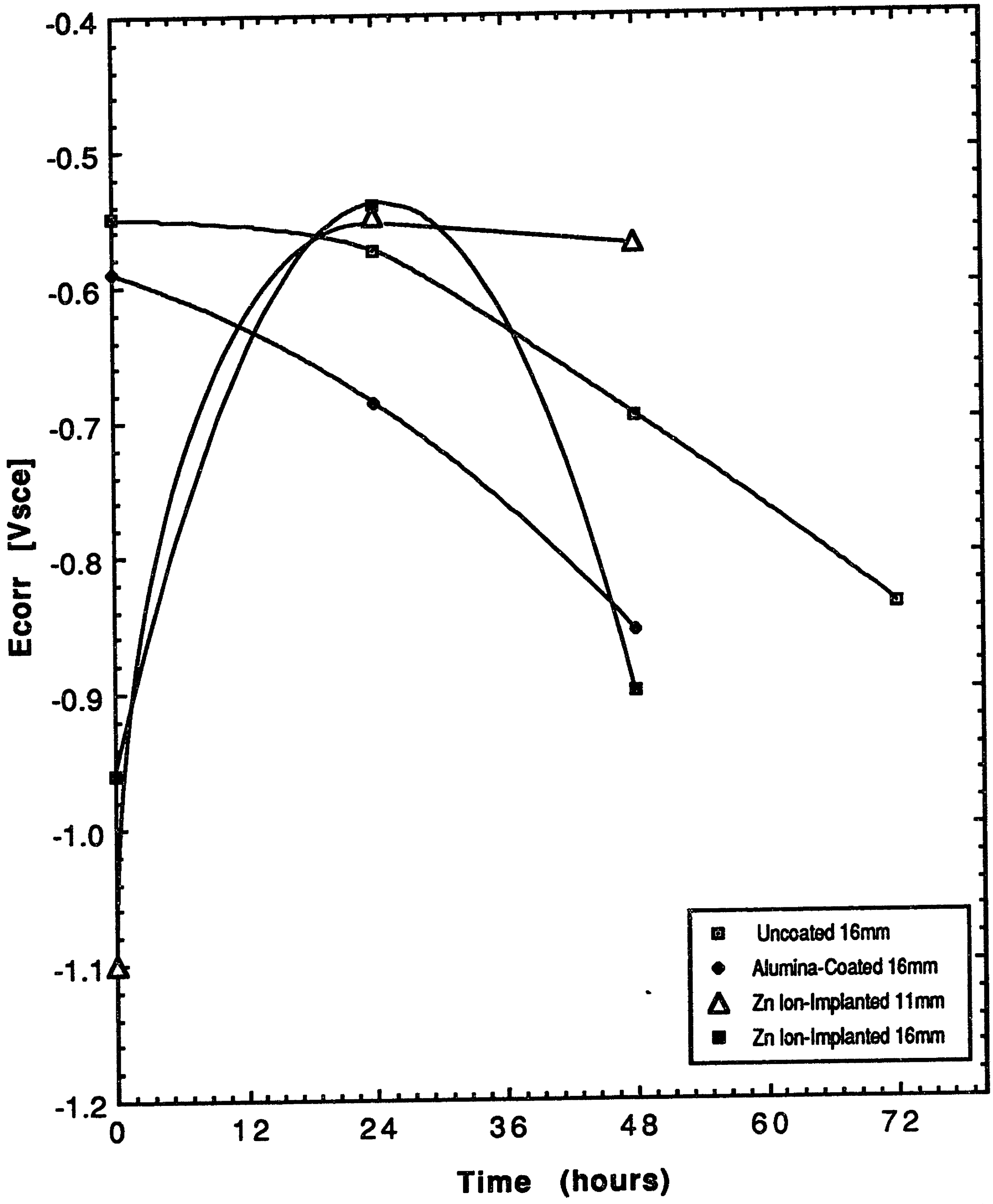

Figure 6.3.11: Graphic representation of the monitored corrosion potential (Ecorr) measured with reference to the saturated calomel electrode vs. time in solution for the model G/Al MMCs studied. Solution 0.01 M NaCl open to air. pH~7

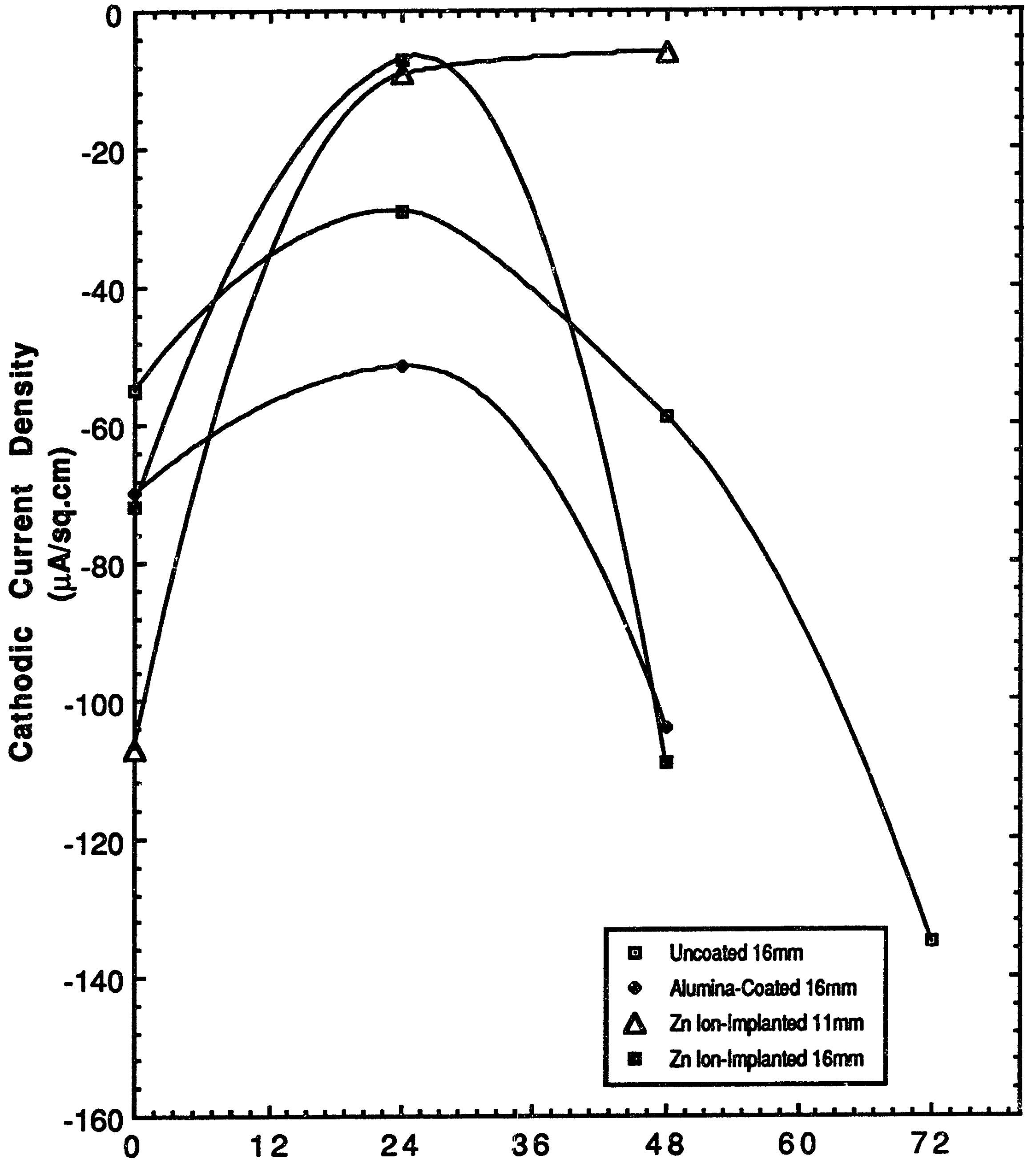

Figure 6.3.12: Graphic representation of SVET cathodic current density measured at 180µm from the G/Al interface over the Al matrix for the model G/Al MMCs studied. Solution 0.01 M NaCl open to air. pH~7

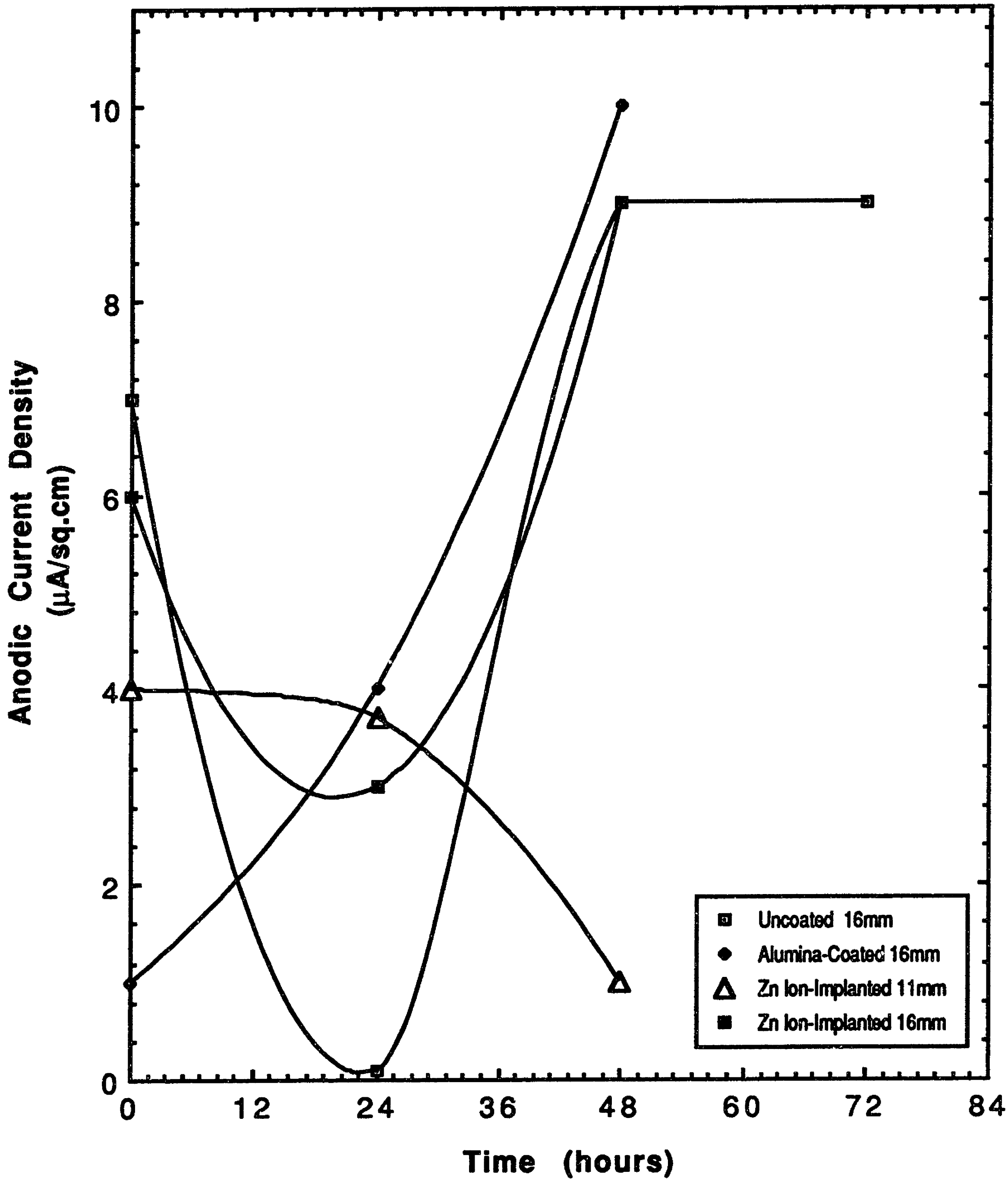

Figure 6.3.13: Graphic representation of SVET anodic current density measured at 180µm from the G/Al interface over the Al matrix for the model G/Al MMCs studied. Solution 0.01 M NaCl open to air. pH~7

6.4 RESULTS FOR COMMERCIAL G/Al MMCS

In Figure 6.4.1, a diffusion-bonded region between two infiltrated tows is centrally located running from north to south in the micrograph. Superimposed are SPM current density vectors. The current density vectors were obtained from probe sampling in only the z direction with respect to the sample surface, i.e., x vibration of the probe was off. Current density vectors have the same meaning as described in Section 6.3.

Apparently, there was a difference in the net ionic current flow between one fiber tow and another for the continuous fiber G/Al MMC (Specimen 23). The fiber tow to the left of the diffusion bond in Figure 6.4.1 seemed to be strongly cathodic (~2.7 $\mu A/cm^2$) at distances further from the diffusion bond, while the fiber tow to the right of the diffusion bond seemed to be strongly anodic (~0.5 $\mu A/cm^2$) at distances further from the diffusion bond. The SPM measurements reveal the macroscopic features of the specimen. This phenomenon is created by the composite design, or more specifically, from the local difference in vol.% fiber. The variation in vol.% fiber from place to place in these samples was more than 5 vol.%. After 30 random point counting measurements, the vol.% fiber finally settles upon an average and is not as greatly affected by further point counting measurements. However, it appears that the local variation does have an effect on surface corrosion phenomena.

Figure 6.4.2 shows an SPM probe measurements taken for a 0-90° interlaminar G/Al MMC (Specimen 24). Regions where large portions of Al are exposed, have cathodic current density vectors superimposed above them. The shift between anodic and cathodic sites occurred at the intersection of interlaminar 0-90° graphite fiber regions, where more Al-foil was used in fabrication.

The magnitude of the current density vectors in 0-90° interlaminar composites (Specimens 24 and 25) was on the average one order of magnitude greater under similar conditions when compared to the continuous fiber G/Al MMC studied (Specimen 23). Ion migration developed on the 'macroscopic' scale between the interlaminar graphite fiber layers. The macroscopic size scale refers to the distance between the interlaminar layers, which is on the order of 100μm as opposed to the 10μm fiber interstice spacing. Macroscopic ionic current deviations changed with the periodicity of the interlaminar layers. Microscopic galvanic cells were not detectable, since the resolution of the narrowest usable probe (7μm) was on the same order as that of the fiber. Smaller probe tips can not be used since they have been shown to create considerable electronic noise [Scheffey, 1986a].

Figure 6.4.3 shows a low magnification micrograph of another SPM probe of a 0-90° interlaminar G/6061 Al MMC (Specimen 25); the anodic and cathodic interlaminar layers can be clearly seen. SPM measurements above fiber-rich layers on the right side of the photo shows that the net ionic reactions are anodic at the location of probing (~30μm above the surface). This would seem to have developed a similar current density map as that in Figure 6.4.2. Figure 6.4.4 shows the results from another SPM test taken above Specimen 25, but with a higher magnification lens. It is unclear at present why some interlaminar regions with fibers transverse to the surface had net anodic ionic current densities while others had net cathodic current densities in Figure 6.4.4. Perhaps the reason is related to the hydrodynamics of ion migration, or because the exposed graphite fiber surfaces for the 0-90° interlaminar composite have very different surface energies due to anisotropy in graphite.

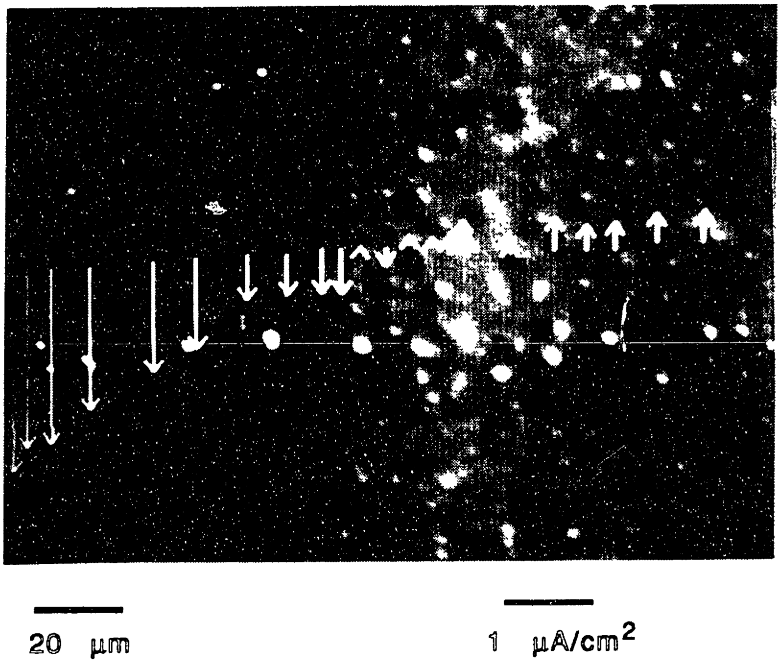

Figure 6.4.1: SPM video image of a continuous fiber G/6061 MMC (Specimen 23), with superimposed current density vectors. A diffusion-bonded region runs from north to south in the center of the photo. Solution 0.01 M NaCl open to air. pH~7

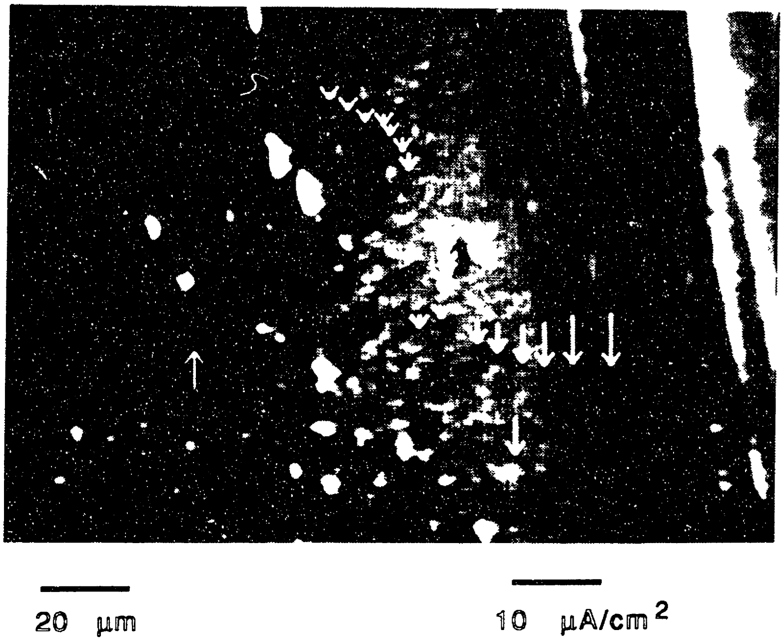

Figure 6.4.2: SPM video image of a continuous fiber G/6061 MMC (Specimen 24) with 0-90° fiber plies; current density vectors are superimposed. Solution 0.01 M NaCl open to air. pH~7

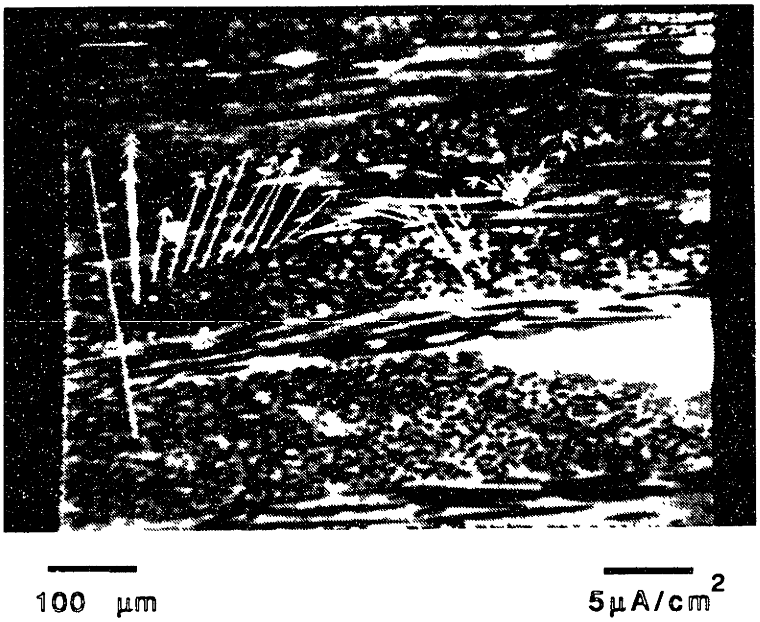

Figure 6.4.3: SPM video image of a G/6061 Al MMC (Specimen 25) with 0-90° fiber plies; current density vectors are superimposed. Solution 0.01 M NaCl open to air. pH~7

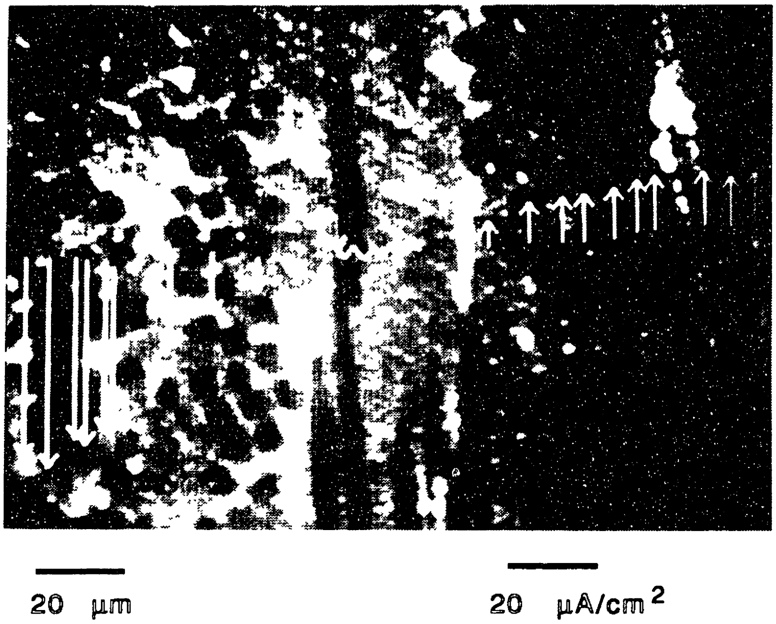

Figure 6.4.4: SPM video image of a G/6061 Al MMC (Specimen 25) with 0-90° fiber plies; current density vectors are superimposed. Solution 0.01 M NaCl open to air. pH~7

7. DISCUSSION

7.1 Anodic Polarization of G/Al MMCs

One of the major goals of the present study was to consider the effect of Al_4C_3 at the fiber-matrix interface on the anodic polarization behavior of the G/Al MMCs during DC potentiodynamic polarization. The following section discusses the effect of Al_4C_3 hydrolysis on the anodic polarization behavior of the G/Al MMCs with Al_4C_3 contents measured by gas chromatography (Section 3.2.2).

7.1.1 Al_4C_3 at the Fiber-Matrix Interface

The difference in Al_4C_3 content for G/1100 Al MMCs Specimen 1 (92 mg/m^2) and Specimen 2 should not have been significant, since they were processed with the same cooling rate (see Figure 4.3.1). However, the difference in the passive current densities after anodic polarization was significant. Furthermore, G/Al 1100 MMCs with differing Al_4C_3 contents (Specimens 3 and 4: 69 mg/m^2 and 40 mg/m^2, respectively) did not show a significant difference in anodic passive current densities (see Figure 4.3.1).

Similar results were found for G/6061 Al MMCs in Figure 4.3.4. Neglecting the sample which had gross Al channels (Specimen 8), and the composite with Torayca PAN-based fibers (Specimen 5), the anodic polarization behavior of the pitch-based G/6061 Al MMCs (Specimens 6, 7, and 9), which had varying Al_4C_3 contents (see Table 3.3.2), were within statistical error of each other.

Therefore, the Al_4C_3 content of a particular G/Al MMC did not correlate with the magnitude of the passive current densities measured by DC potentiodynamic polarization at the scan rate used (0.167 mV/s). If a slower scan rate had been used, it is possible that hydrolysis of Al_4C_3 would have showed a more pronounced effect on the anodic polarization behavior. However, the scan rate employed is accepted as a near equilibrium scan rate [Annual Book of ASTM Standards, 1991b].

7.1.2 Predicted Anodic Polarization Behavior from Mixed-Electrode Theory

The predicted anodic behavior of a 65% pitch-based G/Al MMC and the average anodic polarization behavior measured for the commercial G/Al MMCs tested are shown in Figure 7.1.1. Also shown in the figure is the anodic polarization behavior of a G/1100 Al MMC which had the lowest passive current density (Specimen 2). The curve for the latter specimen attained nearly the same shape and magnitude as that predicted by the mixed-electrode theory. As can be seen in Figure 7.1.1, the diffusion-bonded G/6061 T6-Al MMC studied by Hihara [1989] deviated significantly from mixed-electrode theory. Hihara determined that this was a result of microstructural chlorides in the matrix. The G/6061 Al MMC processed in the absence of microstructural chlorides showed considerably closer resemblance to the predicted anodic behavior; the deviation in passive current density is still considerable, but there is a passivation regime. This deviation was attributable to crevice corrosion observed at the fiber-matrix interface (see Figure 4.3.6).

The average anodic polarization behavior for the G/Al MMCs fabricated with the same PAN-based fiber shown in Figure 7.1.1 and with 4% Cu, 5% Zn, and no alloying elements (G/1100 Al MMCs) in the Al matrix was nearly the same. The tests show that alloy additions and Al_4C_3 content were not as significant in affecting the passive current density as was the type of graphite fiber used in processing the composites. To illustrate this more clearly, and to explain the anomalous behavior of the composites represented in Figures 4.3.4 and 4.3.8 (Specimens 5 and 18), Figure 7.1.2 was constructed.

In Figure 7.1.2 the aforementioned composites that exhibited anomalous anodic polarization behavior are plotted. Although these two specimens had different matrix alloys, their general anodic polarization behavior was nearly the same. The addition of noble Cu to the matrix acts to raise the electrochemical potential of the composite; therefore, the specimen with the Cu alloy addition is shifted ~100 mVsce in the noble (positive) direction.

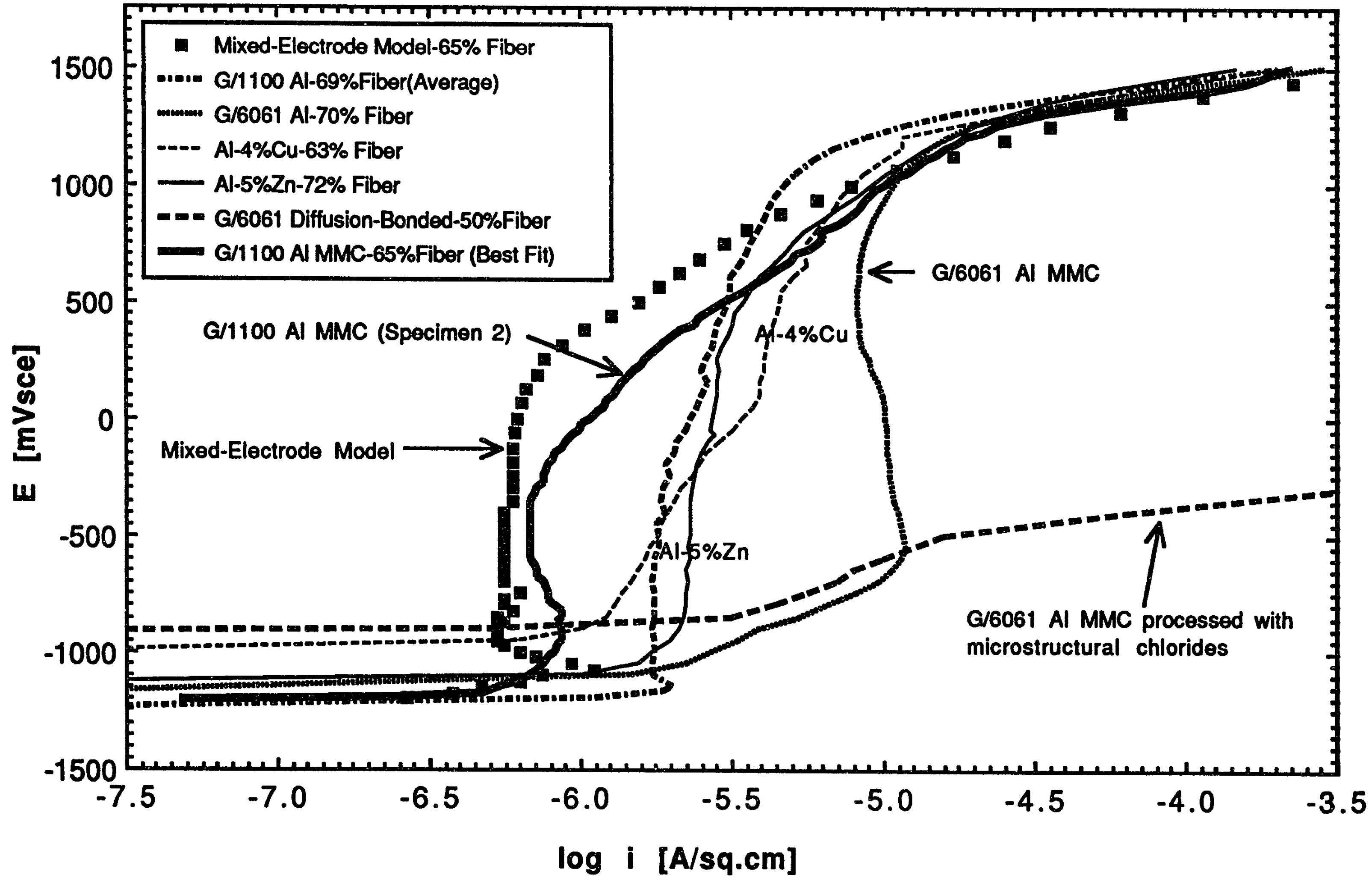

Figure 7.1.1: Predicted anodic polarizatior as a function of fiber vol.% graphite fiber reinforcement plotted against best experimental polarization results from G/Al MMCs with 1100 Al, 6061 Al, Al-4 wt.% Cu, Al-5 wt.% Zn, and 6061-T6 Al (with chlorides present) matrices in deaerated 0.5M Na_2SO_4 of pH 7 at 30°C. Scan rate = 0.167 mV/s.

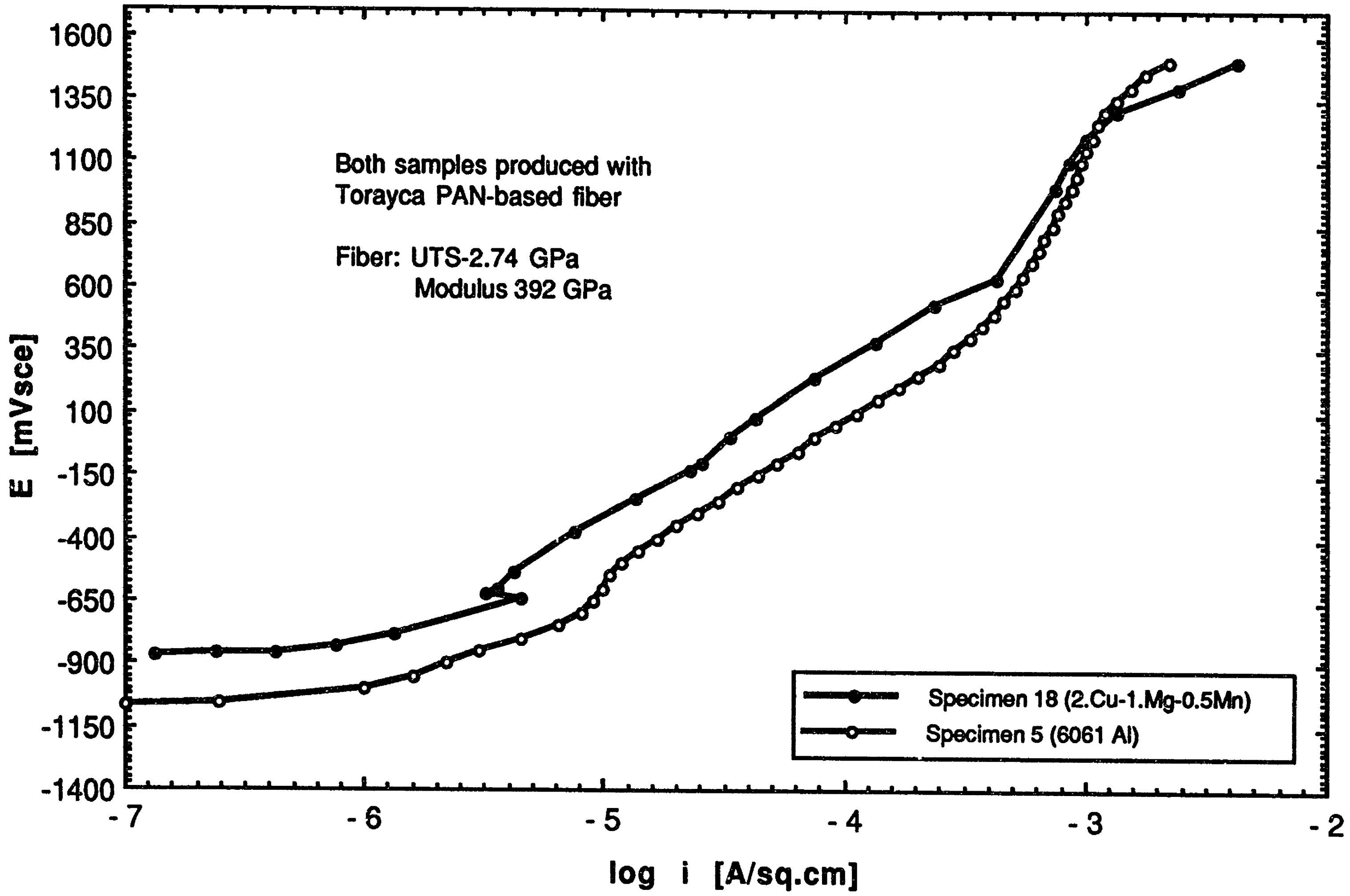

Figure 7.1.2: Comparison of anodic polarization results from G/Al-2% Cu MMC with Mg and Mn additions and a G/6061 Al MMC fabricated with the same graphite fiber in deaerated 0.5M Na_2SO_4 of pH 7 at 30°C. Scan rate = 0.167 mV/s.

After noting that both specimens had PAN-based Torayca M40 3k fibers, a comparison between the pitch-based G/1100 Al MMC (see Figure 4.3.1: Specimen 1) and the G/6061 Al MMCs (see Figure 4.3.4: Specimens 6, 7, and 9) which were fabricated with the same graphite fiber (Thornel P55s) was made; the magnitudes of the anodic passive current densities were also very similar.

G/1100 Al MMCs and G/Al-Cu MMCs which had different matrix compositions but similar PAN-based fiber (see Figure 4.3.1 and 4.3.7: Specimens 2-4 and 19-21), also showed similar anodic polarization behavior. Therefore, in deaerated 0.5M Na_2SO_4 solution, the anodic polarization behavior of the G/Al MMCs was most strongly influenced by differences in commercial fiber type. It is probable that the difference in the commercial fibers internal C-C covalent bonding effected the polarization behavior, since the transverse surfaces of the longitudinal fiber were exposed during anodic polarization testing.

Anodic oxidation of fibers or fiber dissolution, as it has already been pointed out, will occur during anodic polarization, with the principal product being CO_2 gas. Like graphite anodes used for Al reduction in the Hall process [Elliott and Tien, 1981], graphite will have an oxidation efficiency which is dependent on the chemistry and prior process treatment of the graphite. In general, the higher the fiber modulus, the greater the anodic current density will be for the composites at higher anodic overpotentials, as was shown for G/Al-Cu MMCs in Figure 4.3.9. Composites fabricated with high modulus Thornel 55s pitch-based fibers (modulus 400 GPa) had higher passive current densities during anodic polarization than composites fabricated with high modulus Courtaulds PAN-based fibers (modulus 340 GPa), which are reported to have a greater interfacial reactivity toward Al_4C_3 formation than pitch-based graphite fibers.

The more difficult issue is to determine how different fiber types affect the anodic corrosion density measurements. It is only possible to speculate upon which factors may have come into play. In Figure 4.3.9, an increase in the anodic polarization current density occurred at approximately -200 mVsce for almost all G/Al-Cu MMCs. This is the potential where the additional current results from the anodic oxidation of the graphite fibers (see Figure 4.2.4). At potentials noble (positive) to -200 mVsce the difference in anodic polarization current density measurements are associated with the commencement of oxidation of graphite fiber; however, at potentials active (negative) to -200 mVsce, the measured current densities for the G/Al MMCs were often one or two decades greater than that predicted by mixed-electrode theory. This latter result is still unexplained and requires further analysis.

The pre-existence or formation of crevices at potentials active to -200 mVsce will increase measured anodic current densities. Pitch-based G/6061 Al MMCs formed crevices readily during anodic polarization in deaerated 0.5M Na_2SO_4 solution, while G/Al MMCs with Courtaulds PAN-based fibers (compare Figures 4.3.2-3 and 4.3.5-6) did not form crevices in 0.5M Na_2S0_4 solution. For the G/6061 Al MMCs, the deviation in anodic polarization behavior from that predicted by mixed-electrode theory was attributable to the distribution and morphology of the interfacial carbide and associated interfacial segregant which resulted in subsequent crevice corrosion. For the G/1100 (99.99 wt.%) Al MMCs studied, the deviation from mixed-electrode theory (see Figure 7.1.1) at potentials below the equilibrium potential for CO_2 (34 mVsce) or CO (-277 mVsce) gas evolution has not been determined. The increase in measured passive current density may also be due to sub-micron crevice corrosion which was not observable under optical light microscopy.

Exposure to aerated NaCl solution and the etchant which was used for metallography resulted in cavern formation on the surface of the Courtaulds PAN-based graphite fiber (see Figures 3.4.13 and 5.4.1). The degradation of the graphite fibers suggests that in the presence of an Al matrix, graphite fiber is not inert. The susceptibility of individual commercial fibers to cavern formation warrants further investigation. Chemical impurities in graphite may also be related to the observed phenomenon.

For the G/1100 (99.99 wt.%) Al MMCs studied, the anodic behavior of commercial G/Al MMCs compares well with that predicted by the mixed-electrode model (see Figure 7.1.1: Specimen 2). However, if a particular fiber reacts in such a way as to be later prone to crevice corrosion via carbide and segregation interplay at the interface (e.g., pitch-based G/6061 Al MMCs), then the mixed-electrode model is too conservative an estimate, since it assumes that no other phenomenon besides galvanic corrosion will take place when two materials are coupled.

The results show that Courtaulds PAN-based fibers (EHMS 10k 0.7E; Table 3.2.1) are preferable to all other graphite fiber types tested. Results from anodic polarization testing of specimens which were produced with these fibers were in fair agreement with that predicted by mixed-electrode model. One G/Al 1100 MMC (Specimen 2) showed nearly the same anodic polarization behavior as that predicted by the mixed-electrode model (see Figure 7.1.1).

7.2 Anodic Polarization in Deaerated NaCl Solution

Ecrit for G/1100 (99.99 wt.%) Al MMCs was similar to that determined for high purity (99.999 wt.%) Al under similar conditions (see Table 4.4.1); therefore, Ecrit for the Al in the composite was not affected by the presence of graphite fibers.

On the other hand, no true Ecrit for the G/6061 Al MMCs was found during anodic polarization (see Figure 4.4.1). It has been observed that the crevices formed in G/6061 Al MMCs (see Figure 4.4.2). However, no correlation could be found between Al_4C_3 content of the G/6061 Al MMCs and the values obtained for Ecrit values and passive current density's in deaerated 3.15 wt.% NaCl solution. The corrosion current densities measured were not directly proportional to the amount of observable crevice formation, since crevice corrosion is a localized phenomenon. Bruun and Nielsen [1991] have found similar corrosion behavior for continuous alumina fiber/6061 Al MMCs. They claim that Al_8Mg_5 and Mg_2Si provided "tunnel-like" corrosion paths along the fiber-matrix interface. Dull, et al. [1977] found high passive current densities on G/6061 Al MMCs but did not report the formation of crevices at the fiber-matrix interface. Their G/6061 Al MMCs had an Ecrit of -753 mVsce, nearly the same value of Ecrit found by Hihara [1989] for monolithic 6061 T6-Al (see Table 4.4.1). Their squeeze cast G/6061 Al MMCs composites were fabricated with pitch-based (Thornel 50) fibers. This suggests that the results obtained for the G/6061 Al MMCs used in this study may have been related to increased interfacial reaction and segregation resulting from the higher temperatures used during pressure infiltration as opposed to squeeze casting.

Limited concentrations of Cu (0.5 wt.%) or Mg (0.7 wt.%) added to the Al matrix seem to have a beneficial effect on the pitting resistance in G/Al-Cu

MMCs in deaerated NaCl solution. The reason for this is not yet clear. It may be due to fine-scale pitting occurring at sub-micron $CuAl_2$ (θ) eutectic precipitates in fiber interstices (see Figures 3.4.11 and 4.4.6). This fine-scale pitting phenomenon has been observed by Trzaskoma [1991] in particulate reinforced SiC/Al MMCs; the refinement of precipitates in the Al matrix resulted in a more noble Ecrit, presumably by increasing the number of pits which form, and hence, pit growth competition. Jones [1991] has commented on the importance of the cathodic reaction to sustain pitting. He states that pit growth cannot continue without a cathodic reduction reaction to consume the electrons liberated by (i.e., to polarize anodically) the pit anodic reaction. Any pit initiating within the cathodic area of a larger pit is suppressed by cathodic protection. Perhaps finely-dispersed pitting may be sustained since the graphite fibers are available to consume electrons.

7.3 Cathodic Polarization of G/Al MMCs in Aerated NaCl Solution

The large oxygen reduction overpotential on pure (99.99 wt.%) Al matrices affords no advantage in the presence of graphite fibers. G/Al MMCs with pure Al matrices allowed oxygen reduction to occur at the diffusion-limited oxygen reduction current density; therefore, as predicted by Hihara [1989], there was no advantage (from an electrochemical point of view) in using a pure Al matrix as opposed to a 6061 Al, Al-Cu or Al-Zn matrix when composites were exposed to an electrolyte in an aerated environment.

7.4 Surface Analysis of G/Al MMCs Exposed to Aerated NaCl Solution

XPS analysis integrated with SEM micrographs, revealed that the G/Al-5% Zn MMC was oxidized to a greater extent than the G/1100 Al MMC. A thicker more discontinuous corrosion product had formed on the surface of the G/Al-5% Zn MMC, while the matrix had also pitted to a greater extent due to the addition of Zn in the matrix. XPS analysis confirmed the presence of $Zn(OH)_2$ on the surface of the G/Al-5% Zn MMC. Because of the poor spatial resolution of XPS analysis, the location of $Zn(OH)_2$ can only be said to have occurred where no voluminous $Al(OH)_3$ corrosion product was observed.

SEM and AES mapping confirmed that small thin gray areas of a discontinuous Al-Zn oxide film were present on the surfaces of fibers, while

Zn was found by AES elemental mapping to have segregated to the fiber-matrix interface. Evidently, the grey Al-Zn oxide film did not reduce oxygen reduction on the time scale of the test (24 hours), since corrosion proceeded at a greater extent in the G/Al-5% Zn MMC as compared to the G/1100 Al MMC.

Pitting corrosion in Al channels was observed for the G/Al-Zn MMCs exposed to aerated 3.15 wt.% NaCl solution (see Figure 5.2.4). Therefore, Al channels in G/Al MMCs should be avoided from an electrochemical perspective.

7.5 SPM Analysis of Model G/Al MMCs

It has been shown that for model G/Al MMCs, porous Al_2O_3-coated graphite did not reduce the flow of electrons across the G/Al interface (see Figures 6.3.4 and 6.3.5), as predicted by Hihara [1989]. The porous nature of the film was not desirable as an electron resistive barrier. Processing of a more coherent non-porous highly resistive film may be as difficult a problem to solve as the problem of galvanic corrosion itself; therefore, reduction of galvanic corrosion via electrically insulating coatings on graphite fibers is not recommended.

Of the two Zn ion-implanted specimens tested, only the specimen with an 11mm diameter showed a consistent decrease in corrosion current densities after 48 hours (see Figures 6.3.8 through 6.3.10). Both the cathodic and anodic current densities decreased significantly after a period of 24 hours (see Figure 6.3.12 and 6.3.13). For the 11mm diameter Zn ion-implanted specimen, the cathodic current density decreased by a factor of 12 after 24 hours; while after 48 hours, the cathodic current density had dropped by a factor of 20 from the initial cathodic current density. The 16mm diameter Zn ion-implanted specimen showed a similar decrease in corrosion current densities after 24 hours (see Figures 6.3.12 and 6.3.13); however, after 48 hours, both the anodic and cathodic current density values began to increase as a large crevice formed at the G/Al interface (see Figure 6.3.7). One possible explanation for the different behavior is that the anodic area was greater for the 16mm diameter Zn ion-implanted specimen and, hence, the cathodic current density over the graphite rod was greater. Localized crevice corrosion had begun at the G/Al interface after only 24 hours in solution.

Zn ion-implanted specimens were examined by secondary ion mass spectroscopy (SIMS) after removal from solution; however, the presence of $Zn(OH)_2$ was not confirmed, since the concentration of ion-implanted Zn was at the threshold of the detection limit of the instrument. It is probable that in solution Zn solvated. These cations subsequently formed $Zn(OH)_2$ film over graphite, and thus, the cathodic oxygen reduction reaction decreased as observed.

There are at least two possibilities for the breakdown of corrosion inhibition in the 16mm diameter Zn ion-implanted specimen. One possibility is that the local pH of the graphite surface may have become increasingly alkaline for the 16mm diameter Zn ion-implanted specimen with ongoing oxygen reduction. In near neutral solutions, such as 0.01M NaCl, oxygen reduction by the reaction,

$$O_2 + 2H_2O + 4e^- \rightarrow 4(OH)^- \qquad (6.4.1)$$

increases the alkalinity by producing OH^-. Figure 7.5.1 is the Pourbaix (potential-pH) equilibrium diagram. As can be seen, $Zn(OH)_2$ is stable only within a narrow band of pH values. An excessive increase in alkalinity of the solution may lead to the breakdown of the protective $Zn(OH)_2$. Hihara and Latanision [1988a] found that increased alkalinity led to an increase in corrosion during cathodic polarization of a G/6061 T6-Al MMC.

Another possibility is that given the low ion fluence, 1.2×10^{14} atoms/cm^2, and that Zn was not implanted between the fiber-matrix interface, cathodic protection was not effective at the site of the crevice that formed. Higher Zn fluences must be studied to ascertain the level of protection that may be achieved. It seems plausible that had the 11mm Zn ion-implanted specimen been left in solution longer, it may well have begun to corrode at higher corrosion rates as did the 16mm diameter Zn ion-implanted specimen, since a crevice appeared to be forming after 48 hours in solution (see Figure 6.3.10).

Finally, it should be noted that ion implantation of Zn as a cathodic inhibitor was successful in reducing corrosion rates. Therefore, ion implantation of Zn in graphite may be a viable means to reduce the driving force for galvanic corrosion in G/Al MMCs and warrants further investigation.

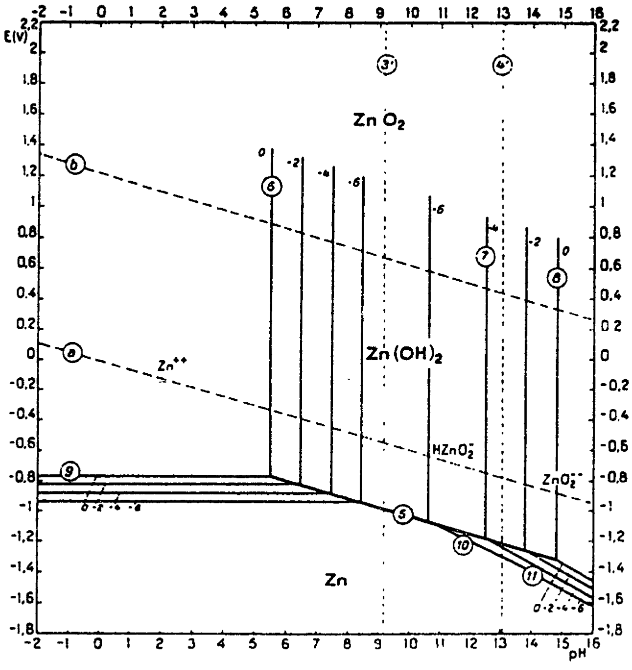

Figure 7.5.1: The pH-potential equilibrium Pourbaix diagram for the system Zn-water at 25°C. [Pourbaix, 1974, p.409]

7.6 SPM Analysis of Commercial G/Al MMCs

In Figure 6.4.1, anodic and cathodic diffusion-bonded tows on alternate sides of the diffusion bond were observed during SPM testing. Evidently, ionic migration at regions above the surface of the diffusion bond were altered due to the local vol.% fiber. This may have been exacerbated by residual microstructural chlorides located at the diffusion-bonded interfaces between fiber tows [Hihara and Latanision, 1988b; Hihara, 1989, 1990].

The results of SPM analysis of analysis of 0-90° interlaminar G/6061 Al MMCs reveal that macroscopic galvanic cells between the interlaminar layers formed (see Figures 6.4.2-6.4.4). The formation of the galvanic cells are most likely influenced by the difference in the surface energy of the exposed graphite fibers, since the internal C-C bond energy of the transverse fibers will be markedly different from the surface energy of the longitudinally exposed fibers; therefore, the rate of oxygen reduction should be different on the graphite fibers in alternate interlaminar regions. However, several SPM analysis showed that the net ionic current density determined above exposed transverse graphite fiber interlaminar regions as compared to exposed longitudinal graphite fiber regions was not always the same. This suggests that system is complicated by the local vol.% fiber and amount of Al matrix (i.e., the net ionic current density is a resultant of the distribution of current sources on the specimen surface).

During the ongoing process of corrosion, greater fiber surface areas will be achieved as a result of matrix corrosion, and as time progresses, the corrosion rates of composites in contact with an electrolyte will not remain constant. Fluctuating cathodic and anodic sites may act to increase corrosion.

Finally, it must be said that the SPM was a valuable tool for studying the corrosion behavior of MMCs, as it was able to conclusively identify cathodic and anodic sites in large scale model G/Al MMCs. It also led to the verification of macroscopic corrosion phenomena in commercial MMCs which had fiber diameters at the resolution of the probe tip. The increased corrosion for 0-90° interlaminar G/6061 Al MMCs was explained by 'macroscopic' electrochemical cells which were created by local differences in graphite fiber: a result of fiber distribution and orientation.

8. CONCLUSIONS

From the experimental results obtained in this present work the following conclusions can be drawn:

8.1 DC ELECTROCHEMICAL STUDIES

1. The commercial fiber type strongly affected the polarization behavior of the G/Al MMCs studied. Anodic oxidation of high modulus and high strength fibers resulted in increased passive current densities and crevice formation at the G/Al interface.

2. Anodic polarization of G/Al MMCs approached that predicted by the mixed-electrode theory. However, the passive current densities attained for G/6061 Al MMCs were well above those predicted by the theory due to crevice corrosion at the G/Al interface. No true pitting potential was found for G/6061 Al MMCs due to crevice corrosion.

3. G/Al-0.5% Cu MMC and G/Al-2% Cu MMC with 0.7% Mg and 0.3% Mn additions showed better pitting resistance than similar fiber type G/1100 Al MMCs and monolithic Al in deaerated 3.15 wt.% NaCl solution.

4. Zn additions above 1wt.% in G/Al MMCs strongly decreased the composites pitting resistance in deaerated 3.15 wt.% NaCl solution.

5. As expected oxygen reduction on G/Al MMCs was easily attainable even for pure Al matrices due to the presence of graphite fibers; therefore, there was no advantage in using a pure Al matrix to deter corrosion in oxygenated conditions.

8.2 SPM STUDIES

1. The cathodic inhibition of oxygen reduction on graphite due to the presence of ion-implanted Zn was confirmed by SPM *in-situ* analysis. For samples with smaller anode to cathode ratios, the protection remained complete after a period of 48 hours.

2. Discontinuous Al_2O_3-coated films were ineffective in reducing the amount of galvanic corrosion that occurred between graphite and the Al matrix. The corrosion rates strongly increased when the Al_2O_3 coating was present - a result of crevice corrosion created by the coating.

3. Corrosion due to macroscopic metallographic features was correlated with the interlaminar composites 0-90° construction and resulted in an order of magnitude increase in current density measurements as compared to that of continuous fiber similar G/Al MMCs.

Suggestions for Future Work

Since ion implantation of Zn was successful in reducing the corrosion rate by a factor of 20 in model G/Al MMCs, it would be useful to explore this phenomenon in commercial G/Al MMCs, paying particular attention to the fluence level of Zn which is necessary to produce a composite that would remain protective for long periods of time. More importantly, it would be useful to invent a process which could produce a similar effect as ion implantation, perhaps a soaking process as Mansfeld [1988, 1990] has shown successful with $CeCl_3$ containing solutions. This could circumvent the problem associated with the cost and difficulty of application to large composite surface areas by the ion implantation process.

Another area that needs further investigation is the effect of commercial fiber type. It has not been concluded as to whether chemical impurities or anisotropic orientation play the most significant role in accelerating the anodic oxidation of the graphite fibers studied. Chemical analyses of several commercial fiber types to determine their associated impurities may prove useful. The orientation of the graphene planes with relation to the fibers longitudinal direction may also be relevant to the rate of graphitic oxidation.

Polarization studies with pyrolytic graphite (with a well-oriented c axis between the graphite basal planes) in various orientations would confirm if the net ionic currents measured with the SPM for 0-90° interlaminar G/6061 Al MMCs could have resulted from the anisotropic surfaces of exposed graphite fiber in alternate layers.

At present, modification of graphite fibers in such a way as to reduce oxygen reduction occurring on their surface remains the most viable means in reducing the corrosion rate in G/Al MMCs.

Bibliography

Agar, J. N. Unpublished results; Summarized by U. R. Evans in "Report on Corrosion Research Work at Cambridge University Interrupted by the Outbreak of War," Journal of Iron and Steel Institute, 141, 1940, p.219.

Akimow, G. W. and Oleschko, A. S., Korrosion Metallschutz, 10, 1934, p.134.

Amateau, M. F. "Progress in the Development of Graphite Aluminum Composite Using Liquid Infiltration Technology," Journal of Composite Materials, 10, 1976, p.1281-1289.

Annual Book of ASTM Standards: Metal-Mechanical Testing; Elevated and Low-Temperature Tests; Metallography, "Volume Fraction by Systematic Manual Point Count Designation," E562-89, 03.01, 1991a, p.589-594.

Annual Book of ASTM Standards: Wear Erosion; Metal Corrosion, "Standard Test Method for Polarization," G5-87, 03.02, 1991b, p.73-79.

Annual Book of ASTM Standards: Wear Erosion; Metal Corrosion, "Standard Test Method for Conducting Cyclic Potentiodynamic Polarization Measurements for Localized Corrosion Susceptibility of Iron-, Nickel-, or Cobalt-Based Alloys," G61-86, 03.02, 1991c, p.223-227.

Aylor, D. M. and Kain, R. M. "Assessing the Corrosion Resistance of Metal Matrix Composite Materials in Marine Environments," Recent Advances in Composites in the United States and Japan, Ed. by J. R. Vinson and M. Taya, ASTM Special Technical Publication, 864, 1983, p.632.

Aylor, D. M. and Moran, P. J. "Effect of Reinforcement on the Pitting Behavior of Aluminum-Base Metal Matrix Composites," Journal of the Electrochemical Society, 132, (6), 1985, p.1277.

Aylor, D. M.; Ferrara, R. J.; Kain, R. M. "Marine Corrosion and Protection for Graphite/Aluminum Metal Matrix Composites," Materials Performance, 23, (7), 1984, p.32-38.

Baker, S. J. and Bonfield, W. "Fracture of Aluminium-Coated Carbon Fibres," Journal of Material Science, 13, 1978, p.1329-1334.

Besenhard, J. O.; Mohwald, H.; Nickl, J. J. "Electrochemical Characterization of Highly Oriented Carbon Fibers," Rev. Chim. Miner., 19, 1982, p.588.

Bhagat, R. B.; Amateau, M. F.; Conway, J. C., Jr; Paulick, J. M.; Chisholm, J. M.; Parnell, J. M.; Seidensticker, D. G. "Squeeze Cast Metal Matrix Composites: Evaluation of Their Strength, Damping Capacity and Corrosion Resistance," Journal of Composite Materials, 23, 1989, p.961-975.

Boffardi, B. P. "Control of Environmental Variables in Water-Recirculating Systems," Corrosion: Vol.13 Metals Handbook Ninth Edition, ASM International, 1987, p.487.

Briggs, D. and Seah, M. P. Practical Surface Analysis by Auger and X-ray Photoelectron Spectroscopy, New York: John Wiley & Sons, Inc., 1983, p.487-513.

Brown, B. K. and Storey, O. W. "Electrochemical Production of Graphitic Oxide," Journal of Trans. Electrochem. Soc., 53, 1928, p.129.

Bruun, N. K. and Nielsen, K. "Corrosion Resistance of Fibre Reinforced Aluminum," Metal Matrix Composites-Processing, Microstructure and Properties, Ed. by Hansen, et al., 12th Risø International Symposium on Materials Science, 1991, p.257-264.

Buonanno, M. A.; Latanision, R. M.; Hihara, L. H.; Chiang, J. F. "Corrosion of Graphite Aluminum Metal Matrix Composites," Environmental Effects on Advanced Materials, Ed. by R. H. Jones and R. E. Ricker, The Mineral, Metals, and Materials Society, 1991, p.267-282.

Chernyshova, T. A. and Kobleva, L. I. "Products of Interaction in the Al-Si Alloy-Carbon Fibre System," Journal of Materials Science, 20, 1985, p.3524-3528.

Clement, J. P.; Rack, H. J.; Wu, K. T.; Spencer, H. G. "Interfacial Modification in Metal Matrix Composites by the Sol-Gel Process," Materials Manufacturing Processes, 5, (1), 1990, p.17-33.

Coleman, S.; McEnaney, B.; Scott, V. "Corrosion Studies on Metal Matrix Composites," Developments in the Science and the Technology of Composite Materials, Fourth European Conference on Composite Materials, Stuttgart, F. R. G., September 25-28, 1990, p.287-292.

Cornie, J. A.; Zhang, G-D.; Li, Q.; Zhang. S-Y; Kowing, B.; Blucher, J. T. "Pressure Infiltration Processing of P-55 (Graphite) Fiber Reinforced Aluminum Alloys," Symposium on Composites-Processing, Microstructures & Properties, 2nd International Ceramic Sceince and Technology Congress of the American Ceramic Society, Orlando, FL, November 13-15, 1990.

CRC Handbook of Chemistry and Physics, 72nd Edition, Ed. by D. R. Lide, Boston: CRC Press, 1991.

Crowe, C. R. "Localized Corrosion Currents from Graphite/Aluminum and Welded SiC/Al Metal Matrix Composites," NRL Memorandum Report 5415, February 18, 1985.

Czyrklis, W. F. "Corrosion Evaluation of Graphite-Aluminum and Graphite-Magnesium Metal Matrix Composites," Corrosion 85, NACE, Paper No. 196, 1985.

Deltombe, E.; Vanleugenhaghe, C.; Pourbaix, M. Atlas of Electrochemical Equilibria in Aqueous Solutions, National Association of Corrosion Engineers, 1974, p.168.

Dresselhaus, M. S.; Dresselhaus, G.; Sugihara, K.; Spain, I. L.; Goldberg, H. A. Graphite Fibers and Filaments, Springer-Verlag, Berlin Heidelberg, 1988.

Dull, D. L.; Harrigan, W. C., Jr.; Amateau, M. F. "Final Report: The Effect of Matrix and Fiber Composition on Mechanical Strength and Corrosion Behavior of Graphite-Aluminum Composites," The Aerospace Corporation, El Segundo, CA, Aerospace Report No. ATR-76 (7564)-1, 1977.

Dull, D. L.; Harrigan, W. C., Jr.; Amateau, M. F. "The Corrosion of 6061 Aluminum Alloy-Thornel 50 Graphite Composite in Distilled Water and NaCl Solution," National Technical Information Service, U.S. Department of Commerce, AD-AO11 761, 1975.

Dunand, D. C. and Mortensen, A. "Thermal Mismatch Dislocations Produced by Large Particles in a Strain-Hardening Matrix," Materials Science and Engineering, A. 132, 1991.

Elliot, J. F. and Tien, J. K., Metallurgical Treatises, USA-China Bilateral Conference (1981: Peking, China) Metallurgical Society of AIME, PA, p.137-157.

Elman, B. S.; Braunstein, G.; Dresselhaus, M. S.; Venkatesan, T. Nucl. Instrum. Methods Phys. Res., B 7/8, 493, IBMM Conference, Cornell University, (July 16-20, 1984), 1985.

Endo, M.; Koyama, T.; Inagaki, M. "Preparation and Electronic Properties of Intercalation Compounds of Graphite Fibers," Synth. Met. 3, 1981, p.177.

England, J. and Hall, I. W. "On the Effect of the Strength of the Matrix in Metal Matrix Composites," Scripta Metallurgica, 20, (5), 1986, p.697-700.

Evans, J. M. and Braddick, D. M. "Corrosion Behavior of Fibre-Reinforced Al Composites," Short Communication, Corrosion Science, 11, 1971, p.611.

Evans, U. R. Metallic Corrosion, Passivity and Protection, London: Arnold, 1937, p.364.

Friend, C.; Naish, C.; O'Brien, T. M.; Sample, G. "The Corrosion Characteristics of a Model C/Al Metal Matrix Composite," Developments in the Science and the Technology of Composite Materials, Fourth European Conference on Composite Materials, Stuttgart, F. R. G., September 25-28, 1990.

Fletcher, R. F. "The Wetting of SiC Particles by Zn-Al Alloys," Master of Science Thesis, MIT, Cambridge, MA, 1989.

Galvele, J. R. "Present State of Understanding of the Breakdown of Passivity and Repassivation," Passivity of Metals, The Electrochemical Society, Inc. 1978, p.285.

Galvele, J. R. and DeMicheli, S. M. "Mechanism of Intergranular Corrosion of Al-Cu Alloys," Corrosion Science, 10, 1970, p.795-807.

Hack, J. E. and Amateau, M. F., eds. Mechanical Behavior of MMCs, Warrendale, PA: Metallurgical Soc. of AIME, 1983, p.335-352.

Halliday, D. and Resnick, R. Fundementals of Physics, Second Edition, New York: John Wiley and Sons, 1981, p.781.

Hansen, M. Constitution of Binary Alloys, 2nd ed., McGraw Hill, 1958, p.348.

Hass, G. "On the Preparation of Hard Oxide Films with Precisely Controlled Thickness of Evaporated Aluminum Mirrors," Journal of the Optical Society of America, 39, (7), 1949, p.532.

Hatch, G. B. "Influence of Inhibitors on Differential Aeration Attack on Steel II - Dichromate and Orthophosphate," Paper presented at Corrosion 64, National Association of Corrosion Engineers, March 1964.

Hihara, L. H. Corrosion of Aluminum Matrix Composites, Ph.D Thesis, MIT, Cambridge, MA, 1989.

Hihara, L. H. and Latanision, R. M. "Cathodic Overprotection of Silicon Carbide/6061-T6 and Graphite/6061-T6 Aluminum Alloy Metal Matrix Composites," Scripta Metallurgica, 22, 1988a, p.413-418.

Hihara, L. H. and Latanision, R. M. "Localized Corrosion of Graphite Fiber/6061-T6 Aluminum Alloy Metal Matrix Composites in Aerated and Deaerated Sodium Sulfate Solutions," Space Age Metals Technology, Ed. by F. H. Froes and R. A. Cull, Covina, CA: SAMPE, 2, 1988b, p.213.

Hihara, L. H. and Latanision, R. M. "Residual Microstructural Chloride in Graphite-Aluminum Metal Matrix Composites," Materials Science and Engineering, A126, 1990, p.231-234.

Hihara, L. H. Private Intercommunication, University of Hawaii at Manoa, Honolulu, HI , January 1990.

Hihara, L. H. and Latanision, R. M. "Localized Corrosion Induced in Graphite/Aluminum Metal-Matrix Composites by Residual Microstructural Chloride," Corrosion, 47, (5), 1991, p.335-341.

Hubner, W. and Wranglen, G. "Studies on the Mechanism of the Pitting Corrosion of Aluminum," Current Corrosion Research in Scandinavia, 1964, p.60.

Isaacs, H. S. "Applications of Current Measurement Over Corroding Metallic Surface," Ionic Currents in Development, Ed. by R. Nuccitelli, New York: A. R. Liss, Inc, 1986, p.37-44.

Isaacs, H. S. "The Measurement of the Galvanic Corrosion of Soldered Copper Using the Scanning Vibrating Electrode Technique," Corrosion Science, 28, (6), 1988, p.547-558.

Isaacs, H. S. "The Localized Breakdown and Repair of Passive Surfaces During Pitting," Corrosion Science, 29, (2/3), 1989, p.313-323.

Isaikin, A. S.; Chubarov, V. M.; Trefilov, B. F.; Silaev, V. A.; Gorelov, Yu. A. "Compatibility of Carbon Filaments with a Carbide Coating and an Aluminum Matrix," Metal Science and Heat Treatment, 22, 1981, p.815-817.

Iseki, T.; Kameda, T.; Maruyama, T. "Some Properties of Sintered Al_4C_3," Journal of Materials Science Letters, 2, 1983, p.675.

Jaffe, L. F. and Nuticelli, R. "An Ultrasensitive Vibrating Probe for Measuring Steady Extracellular Currents" Journal of Cell Biology, 63, 1974, p.614.

Jones, D. A. Principles and Prevention of Corrosion, Macmillan Publishing Company, 1991.

Kackley, N. D. The Scanning Potential Microprobe: Apparatus for the Study if Localized Corrosion, Master of Science Thesis, MIT, Cambridge, MA, 1984.

Katzman, H. A. "Fiber Coatings for the Fabrication of Graphite-Reinforced Magnesium Composites," The Space Division Air Force Systems Command, Los Angeles, CA, Systems Division Report No. SD-TR-86-23, 1986.

Katzman, K. A. "Fibre Coatings for the Graphite-Reinforced Magnesium Composites," Journal of Materials Science, 22, 1987, p.144-148.

Katzman, K. A. "Fiber Coatings for Composite Fabrication," Materials & Manufacturing Processes, 5, (1), 1990a, p.1-15.

Katzman, K. A. Private Intercommunication, The Aerospace Corporation, El Segundo, CA, July 1990b.

Keller, F. and Edwards, J. D. "Formation of the Natural Oxide Film on Aluminum," Metal Progress, 54, (1), July 1948, p.35.

Keller, F.; Hunter, M. S.; Robinson, D. L. "Structural Features of Oxide Coatings on Aluminum," Journal of the Electrochemical Society, 100, (9), 1953, p.411.

Kim, C. T.; Lee, J. K.; Plichta, M. R. "Plastic Relaxation of Thermoelastic Stress in Al/Ceramic Composites," Metal Trans., A.21, 1990, p.673.

Kinoshita, K., Carbon, Electrochemical and Physicochemical Properties, NY: John Wiley & Sons, Inc., 1988, p.316-374.

Kloppers, M. J., Electrochemistry of Iron-Chromium Alloys, Ph.D Thesis, MIT, Cambridge, MA, 1991.

Kohara, S. and Muto, N, "Degradation of Carbon Fibers by Molten Aluminum," Proceedings of International Conference on Composite Materials, Ed. by W. C. Harrigan, Jr.; J. Strife; A. K. Dhingra, San Diego, CA, 1985, p.638-646.

Kokhanov, G. N. and Milova, N. G. Elektrokhimiya, 5, 1969, p.93.

Ksenzhek, O. S. and Chaikovskaya, V. M. "Study of the Anodic Oxidation of Graphite," Journal of Applied Chemistry USSR, 35, 1962, p.1713.

Li, P.; Li, X.; Chung, D. D. L. In Extended Abstracts of the 18th Biennial Conference on Carbon, Worcester, MA, University Park, PA: American Carbon Society, 1987, p.239.

Li, Q.; Megusar, J.; Masur, L. J.; Cornie, J. A. "A High Resolution Transmission Electron Microscopy Study of SiC-Coated Graphite Fiber-Al Composite," Journal of Materials Science and Engineering, A.117, 1989, p.199.

Li, X. G.; Zhang, H. L.; Wu, R. J. "The Effect of Long Period Heat-Treatment on Carbon Fiber Reinforced Aluminum Composite," Proceedings of International Conference on Composite Materials, Ed. by W. C. Harrigan, Jr.; J. Strife; A. K. Dhingra, San Diego, CA, 1985, p.623-629.

Mansfeld, F. and Jeanjaquet, S. L. "The Evaluation of Corrosion Protection Measures for Metal Matrix Composites," Corrosion Science, 26, (9), 1986, p.727-734.

Mansfeld, F.; Lin, S.; Kim, S.; Shih, H. "Corrosion Protection of Al Alloys and Al-based Metal Matrix Composites by Chemical Passivation," Corrosion, 1988, Paper No. 388, p.1-19.

Mansfeld, F.; Lin, S.; Kim, S.; Shih, H. "Chemical Protection of Al Alloys and Al-based Metal Matrix Composites by Chemical Passivation," Corrosion, 1989, 45, (8), p.615-630.

Mansfeld, F.; Lin, S.; Kim, S.; Shih, H. "Pitting and Passivation of Al Alloys and Al-based Metal Matrix Composites," Journal of the Electrochem. Soc., 137, (1), 1990, p.78-82.

Martin, W. H. and Brocklehurst, J. E. "The Thermal Expansion Behavior of Pyrolitic Graphite-Bromine Residue Compounds," Carbon, 1, 1964, p.133.

Meschi, C.; Manceau, J. P.; Flandrois, S.; Delhaes, P.; Ansert, A.; Deschamps, L. "Intercalation of Metal Chlorides in Graphite Fibers," Ann. Phys. Paris, Colloque 2, Suppl. 2, 11, 1986, p.199.

Metals Handbook, American Society for Metals, Metals Park, OH, 1948 ed.

Meyers, M. A. and Chawla, K. K., Mechanical Metallurgy Principles and Applications, Englewood Cliffs, NJ: Prentice-Hall, Inc., 1984, p.438-466.

Mohallem, N. D. S. and Aegerter, M. A. "Multilayer SiO_2 and TiO_2 Coatings on Glasses by the Sol-Gel Process," Journal of Non-Crystalline Solids, 100, 1988, p.526-530.

Mortensen, A. Solidification of Al-4.5 wt.% Cu in the Presence of SiC Fibers, Ph.D Thesis, MIT, Cambridge, MA, 1986, p.128-131.

Mortensen, A. "Interfacial Phenomena in the Solidification Processing of MMCs," Materials Science and Engineering, A135, 1991, p.1-11.

Mortensen, A.; Cornie, J. A.; Flemings, M. C., "Solidification Processing of Metal-Matrix Composites," Journal of Metals, (F) 1988a, p.12-19.

Mortensen, A.; Cornie, J. A.; Flemings, M. C., "Columnar Dendritic Solidification in a Metal-Matrix Composite," Metallurgical Transactions A, (19A), March 1988b, p.709-721.

Mortensen, A. and Iljoon, J, "Solidification Processing of Metal-Matrix Composites," International Materials Review, (F) 1992a, in print

Mortensen, A. Private Intercommunication, Cambridge, MA, March, 1992b.

Moshier, W. C.; Davis, G. D.; Ahearn, J. S. "The Corrosion and Passivity of Aluminum Exposed to Dilute Sodium Sulfate Solutions," Corrosion Science, 27, (8), 1987, p.785.

Motoki, K. and Okura, A. "Formation of Intermetallic Compound in Composite Materials," Progress in Science and Engineering of Composites, Ed. by T. Hayashi; K. Kawata; Umekawa, ICCM-IV, Tokyo, 1982, p.1281-1287.

Natishan, P. M.; McCafferty, E.; Hubler, G. K. "Passivity Mechanisms of Surfaces Produced by Ion Beam Mixing and Ion Plantation," Annual Report, October 1988-November 1989, Office of Naval Research, NRL Publication No. 167-6320, May 1990.

Paciej, R. C. and Agarwala, V. S. "Influence of Processing Variables on the Corrosion Susceptibility of Metal-Matrix Composites," Journal of Science and Engineering Corrosion, 44, 1988, p.680-684.

Payer, J. H. and Sullivan, P. G. "Corrosion Protection Methods for Graphite Fiber Reinforced Aluminum Alloys," Bicentennial of Materials, 8th National Sample Technical Conference, Vol.8, Society for the Advancement of Material and Process Engineering, Seattle, WA, October 12-14, 1976.

Petzow, G, Metallographic Etching, American Society for Metals, Metals Park, OH, 1976, p.41.

Portnoi, K. I.; Zabolotskii, A. A.; Timofeeva, N. I. "Effect of Matrix Composition on the Reactions of the Components of C-Al Composite Materials,"Metal Science and Heat Treatment, 22, 1981, p.813-815.

Pourbaix, M, Atlas of Electrochemical Equilibria in Aqueous Solutions, National Association of Corrosion Engineers, 1974. p.172

Pryor, M. J. and Keir, D. S. "The Nature of Aluminum as a Cathode," Journal of the Electrochemical Society," 102, (10), 1955, p.605.

Rkee, S. K. "Wetting of Ceramics by Liquid Aluminum," Journal of the American Ceramics Society, 53, (7), 1970, p.251

Salamanca-Riba, L.; Braunstein, G.; Dresselhaus, M. S.; Gibson, J. M.; Endo, M.: Nucl. Instrum. Methods Phys. Res., IBMM Conference, Cornell University, (July 16-20, 1984), B 7/8, 1985, p.487.

Saxena, M.; Modi, O. P.; Yegneswaren, A. H.; Rohatgi, P. K. "Corrosion Characteristics of Cast Aluminum Alloy-3 wt.% Graphite Particulate Composites in Different Environments," Corrosion Science, 27, (3), 1987, p.249-256.

Scheffey, C. "Electric Fields and the Vibrating Probe, for the Uninitiated," Ionic Currents in Development, Proceedings of a Satellite Meeting to the Tenth International Congress of the International Society of Developmental Biologists, University of California, Los Angeles, CA, (August 2-4, 1985), Ed. by R. Nuccitelli, New York: A. R. Liss, Inc., 1986a, pg. xxv-xxvii.

Scheffey, C. "Pitfalls of the Vibrating Probe Technique," Ionic Currents in Development, Proceedings of a Satellite Meeting to the Tenth International Congress of the International Society of Developmental Biologists, University of California, Los Angeles, CA, (August 2-4, 1985) Ed. by R. Nuccitelli, New York: A. R. Liss, Inc, 1986b, p.3-12.

Scheffey, C. " Two Approaches to Construction of Vibrating Probes For Electric Current Measurement in Solution," Rev. Sci. Instrum., American Institute of Physics, 59, (5), 1988, p.787-792.

Schmitt, T, Private Intercommunication, Aluminium Ranshofen, Ges.m.b.H., Ranshofen Austria, July, 1991.

Simensen, C. J. "Comments on the Solubility of Carbon in Molten Aluminum," Metallurigical Transactions A, A. 20, January 1989, p.191.

Taya, M. and Arsenault, R. J., Metal Matrix Composites Thermomechanical Behavior, Elmsford, NY: Pergamon Press, 1989, p.5-8.

Taya, M. and Mori, T. "Dislocations Punched-Out Around a Short Fiber in a Short Fiber Metal Matrix Composite Subjected to Uniform Temperature Change," Acta Metal., 35, 1987, p.155.

Taylor, C. S. and Edwards, J. D. "Some Reflection and Radiation Characteristics of Al," Heating, Piping, and Air Conditioning, 11, 1939, p.59.

Towata, S; Yamada, S; Ohwaki, T. "Strength and Interfacial Reaction of High Modulus Carbon Fiber-Reinforced Aluminum Alloys," Transactions of the Japan Institute of Metals, 26, (8), 1985, p.563-570.

Trzaskoma, P. P. "Localized Corrosion of Metal Matrix Composites," Environmental Effects on Advanced Materials, Ed. by R. H. Jones and R. E. Ricker, The Minerals, Metals and Materials Society, 1991, p.249-265.

Trzaskoma, P. P. "Pit morphology of Aluminum Alloy and Silicon Carbide/Aluminum Alloy Metal Matrix Composites," Corrosion, 46, (5), 1990, p.402-409.

Trzaskoma, P. P ; McCafferty, E.; Crowe, C. R. "Corrosion Behavior of SiC/Al Metal Matrix Composites," Journal of the Electrochemical Society, 130, (9), 1983, p.1804.

Trzaskoma, P. P. and McCafferty, E. "The Effect of Anodic Coatings on the Pitting of Silicon Carbide/Aluminum Metal Matrix Composites," Proceedings of the Symposium on Aluminum Surface Treatment, Ed. by R. S. Alwitt and B. E. Thompson, The Electrochemical Society, NJ, 1986, p.171-180.

Turnbull, A. "Review of Corrosion Studies on Aluminum Metal Matrix Composites," NPL Report DMM (A) 15, November 1990.

Uhlig, H. H. and Revie, R. W. Corrosion and Corrosion Control, 3rd ed., New York: John Wiley & Sons, Inc., 1985, p.226.

Van Muylder, J. and Pourbaix, M. "Carbon," Atlas of Electrochemical Equilibria in Aqueous Solutions, Ed. by M. Pourbaix, National Association of Corrosion Engineers, 1974, p.449.

Vassilaros, M. G.; Davis, D. A.; Steckel, G. L.; Gudas, J. P. "Marine Corrosion of Graphite/Aluminum Composites," Mechanical Behavior of Metal-Matrix Composites, Ed. by J. E. Hack, and M. F. Amateau, The Metallurgical Society of the AIME, 1983, p.335.

Wagner, C. D., Riggs, W. M., Davis, L. E., Moulder, J. F., Muilenberg, G. E. Handbook of X-ray Photoelectron Spectroscopy, MN: Perkin - Elmer Corporation, 1979.

Walkenhoerst, W. Naturwiss., 34, 1947, p.373.

Wood, G. C.; Sutton, W. H.; Richardson, J. A.; Riley, T. N. K.; Malherbe, A. G. "The Mechanism of Pitting of Aluminum and its Alloys," Localized Corrosion, National Association of Corrosion Engineers, 1974, p.526.

Wu, R. "Interfacial Behaviors and Its Influence on the Mechanical Properties of Carbon Fiber Reinforced Aluminum Composites," Interfaces in Polymer, Ceramic, and Metal Matrix Composites, Ed. by H. Ishida, Elsevier Science Publishing Co., Inc., 1988, p.43-55.

Xiu-Qin, C and Geng-Xiang, H. "A TEM Investigation of the Interfaces of Carbon-Fiber Reinforced Aluminium Composites," Interfaces in Polymer, Ceramic, and Metal Matrix Composites, Ed. by H. Ishida, Elsevier Science Publishing Co., Inc., 1988, p.381-387.

APPENDICES

Appendix A: The pH-potential Equilibrium Pourbaix Diagram for Al

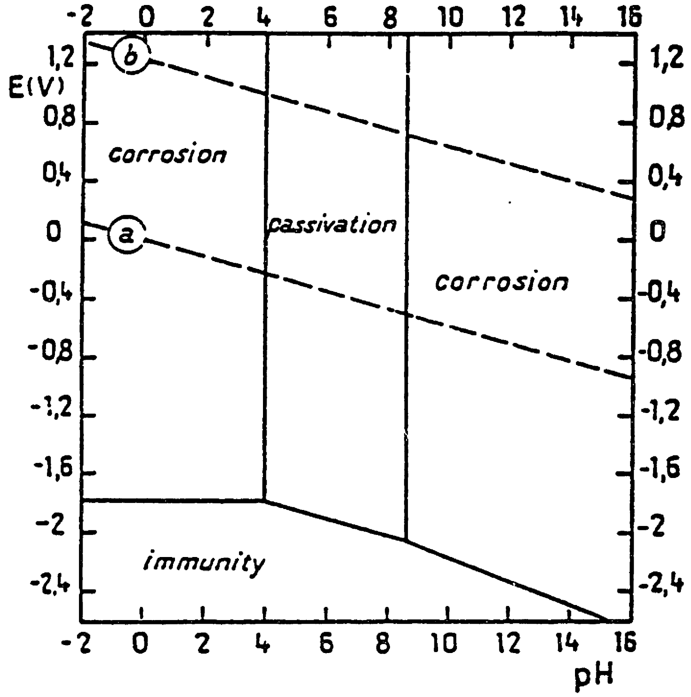

(a) Passivation by a film of hydrargillite $Al_2O_3.3H_2O$.

Pourbaix diagram of Al at 25°C for unit activities with hydrargillite as the stable oxide. [Pourbaix, 1974, p.172]

Appendix B: Al-rich Magnesium-Silicide Phase Diagram

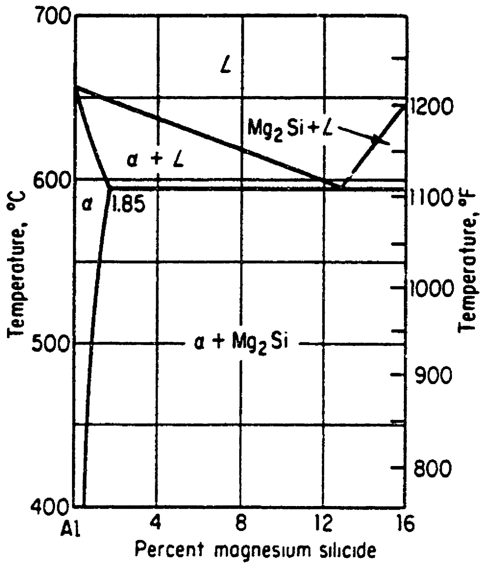

Aluminum-rich portion of the aluminum-magnesium silicide system.

[Metals Handbook, 1948, p.1246]

Appendix C: Al-Zn Phase Diagram

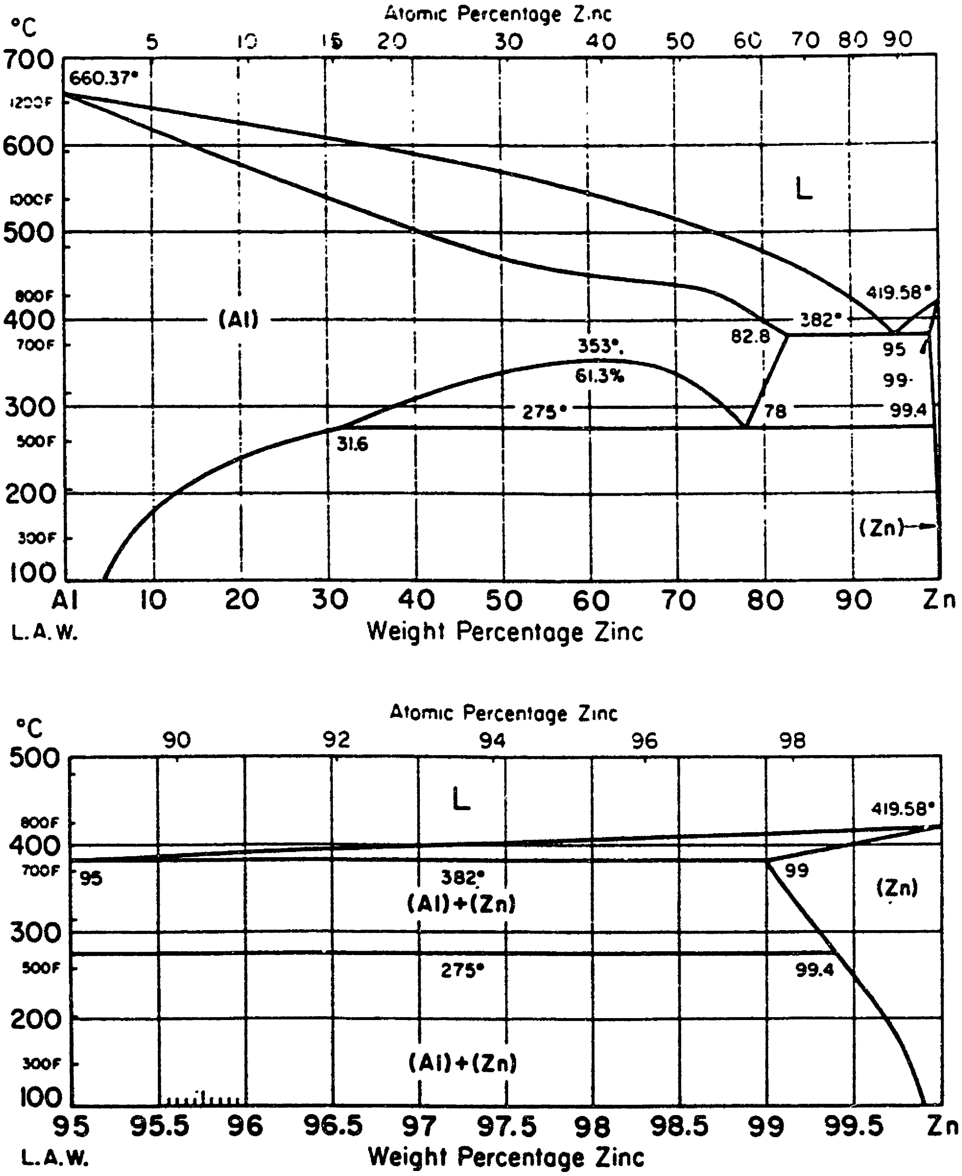

The Al-Zn binary phase diagram.

[Metals Handbook, 1948, p.1250]

Appendix D: Mechanical Three-Point Bend Testing of G/Al MMCs

In order to assess the role of Al_4C_3 during electrochemistry the Al_4C_3 contents of G/Al MMCs were measured by gas chromatography in Chapter 3. Measured Al_4C_3 contents were shown to correlate with mechanical three-point bend testing. The results are presented below.

Tables D-1 and Table D-2 reveal the results of Al_4C_3 analysis and three-point bend testing on G/6061 Al, 1100 Al and Al-Zn MMCs. Table D-1 reveals that the weakest G/6061 Al MMCs (Specimens 7a and b) had the greatest Al_4C_3 content of the composites studied. Correspondingly, The strongest G/6061 Al MMC (Specimens 9a and b), had the lowest average Al_4C_3 content (~8 mg/m^2).

In Table D-2 the moduli for G/1100 Al and Al-Zn MMCs were approximately 20% higher than the moduli for the G/6061 Al MMCs which were fabricated with a higher modulus pitch-based graphite fiber (see Tables 3.2.1 and 4.2.1).

Since, other researchers have found that PAN-based fibers have a higher propensity to react than do pitch-based fibers (see section 2.5.5), it is clear that the lower moduli and poor strength of the G/6061 MMCs must have been a result of degradation of graphite fiber related to the alloy additions to the matrix (i.e., Si and Mg), which were found surrounding the fiber-matrix (see Figures 3.4.5 and 3.4.6). In this study many trends were uncovered after having normalized the stress with respect to the volume fraction, and the pull-out length with respect to the diameter of fiber. Also, in order to do any mechanical or electrochemical testing, one must remove this outer skin and measure the volume fraction of the remaining composite by point counting or by image analysis techniques.

Figure D-1 shows a graphical representation of the effect of the Al_4C_3 content on the normalized fracture stress of the G/1100 Al MMCs. The stress was corrected for the volume fraction of graphite fiber and normalized with respect to the strongest composite of all composites studied. In this figure the increase in Al_4C_3 resulted in a strong decrease in UFS at around 60 mg/m^2 of Al_4C_3. The fiber pull-out ratio seems to have decreased with an increase in Al_4C_3 content; a planar brittle fracture was observed by SEM for the sample with the highest Al_4C_3 content. The slight rise and then steep decrease in UFS would correlate with an increase in interfacial strength from the growth of Al_4C_3 at the interface.

Table D-1: Mechanical Properties of G/6061 MMCs

Spec.#	Lab Code	vol%C	Al_4C_3 $\frac{mg}{m^2}$	σ_{max} N/mm^2	E Modulus GPa
6a	255 I	69.3	54.5	481.3	183.7
6b	255 II	69.4	47.2	511.2	194.1
7a	256 I	65.0	260.4	428.9	191
7b	256 II	66.0	172	461	221.2
8a	257 I	61.4	60.9	676.5	197.3
8b	257 II	61.8	16.3	824.9	198.4
9a	258 I	73.9	10.8	801.3	215.4
9b	258 II	73.9	5.2	883.5	192.9

Table D-2: Mechanical Properties of G/1100 and G/Zn-Al MMCs

Spec.#	Lab Code	vol%C	Al_4C_3 $\frac{mg}{m^2}$	σ_{max} N/mm^2	E Modulus GPa
2	G/1100 Al 130	64.0	76.66	800	230
3	G/1100 Al 181	65.8	56.27	920	225.5
4	G/1100 Al 182	68.8	30.11	950	222
10	247 -0.1wt.% Zn	68.3	29.37	971	195.3
11	248 -0.5wt.% Zn	67.8	58.36	885.1	219.5
12	249 -1.0wt.% Zn	69.5	44.25	841.1	220
13	250 -5.0wt.% Zn	71.6	49.61	859.4	202.8

The decrease in UFS would be a result of too much Al_4C_3 at the interface which reduced the defect-to-defect distance along the fiber, allowing Al_4C_3 platelets to act as crack initiation sites.

Figure D-2 shows a similar representation for G/6061 Al MMCs. In this figure we can again see that the strength of the composite went through a maximum. At higher Al_4C_3 contents, the normalized fracture stress sharply decreased. This is complemented by a decrease in fiber pull-out ratio, similar to that shown in Figure D-1.

In Figure D-3, no clear correlation between the Zn concentration and the Al_4C_3 content was found. However, the fiber pull-out ratio was generally proportional to the fracture stress for the G/Al-Zn MMCs.

Figure D-4 shows that for the G/Al-Zn MMCs, an increase in Zn concentration resulted in a decrease in the normalized fracture stress. The decrease in UFS occurred rapidly from 0.1 to 1.0 wt.%Zn additions to the Al matrix. Anomalous behavior of a G/Al-0.1 wt.%Zn MMC resulted in the normalized UFS comparable to a rapidly-cooled G/1100 Al MMC (see Table D-2). The small addition of Zn resulted in decreased Al_4C_3 contents which were generally only attainable with rapid cooling schemes for G/1100 Al MMCs. This latter result may be of commercial significance.

Figure D-5 shows the fiber pull-out ratio vs. the Al_4C_3 content for the composites studied. It is clear that there exists an inverse relationship between the Al_4C_3 content and the fiber pull-out ratio. Also, it appears as though the relative fiber pull-out ratios for all the samples studied were on the same scale for a given Al_4C_3 content. Fiber pull-out was measured at the tensile fracture surface of the fractured bar to eliminate the effects of shear stress in the center of the fractured specimen. The problem with measuring fiber pull-out data is that some fibers may fracture at points away from the principal crack, reducing the shear stress on the cracked fiber. Such a fiber would have a new shear stress distribution from zero stress at the point of the new crack, increasing linearly to a maximum at the plane of the principal propagating crack [Mortensen, 1992b]. Therefore, strictly speaking, the fiber pull-out length, and strength is a function of the defect-to-defect distribution along the length of fibers, and fibers fracturing away from the principal plane

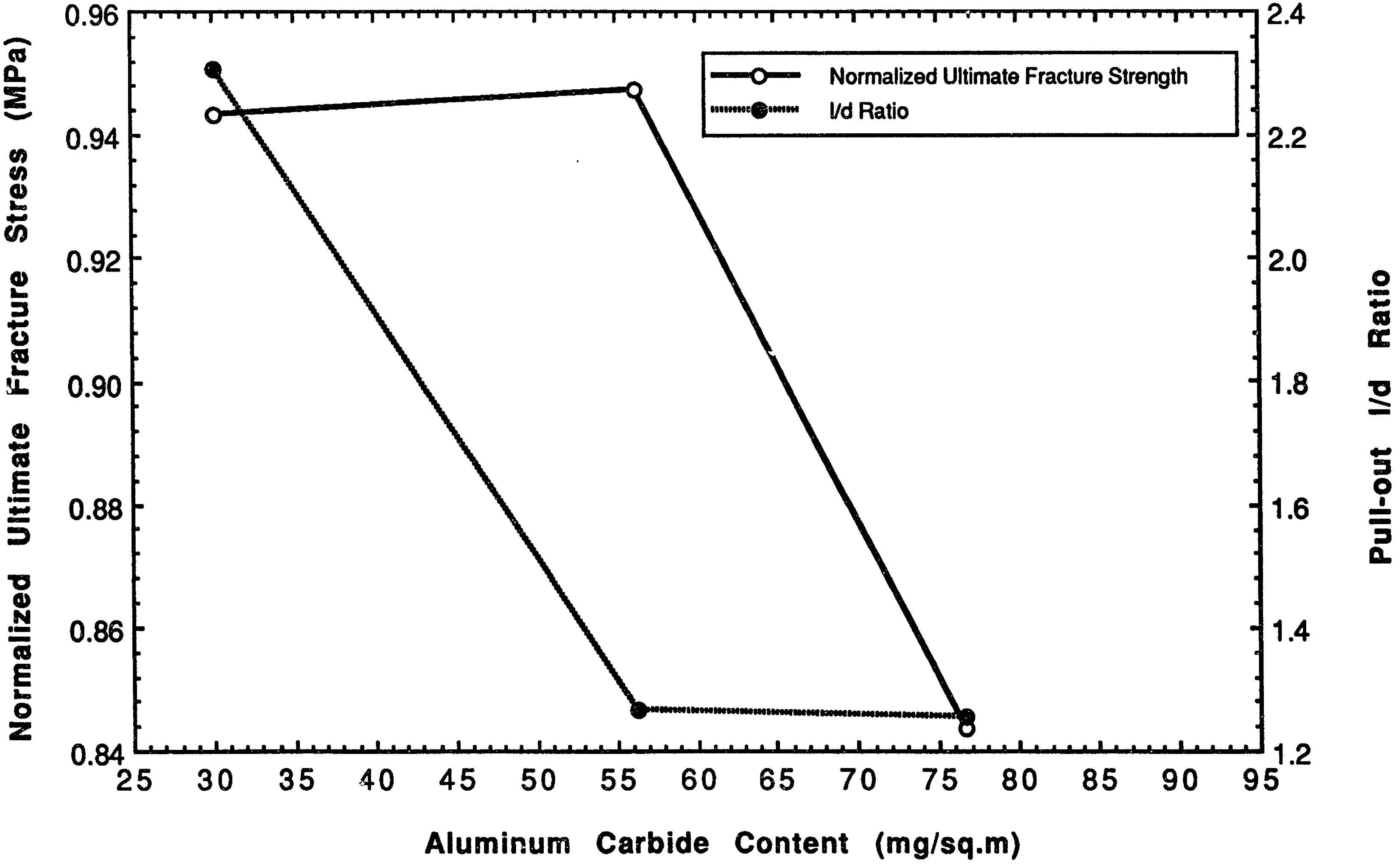

Figure D-1: Representation of carbide content versus the normalized fracture strength and fiber pull-out ratio for the G/1100 Al MMCs studied.

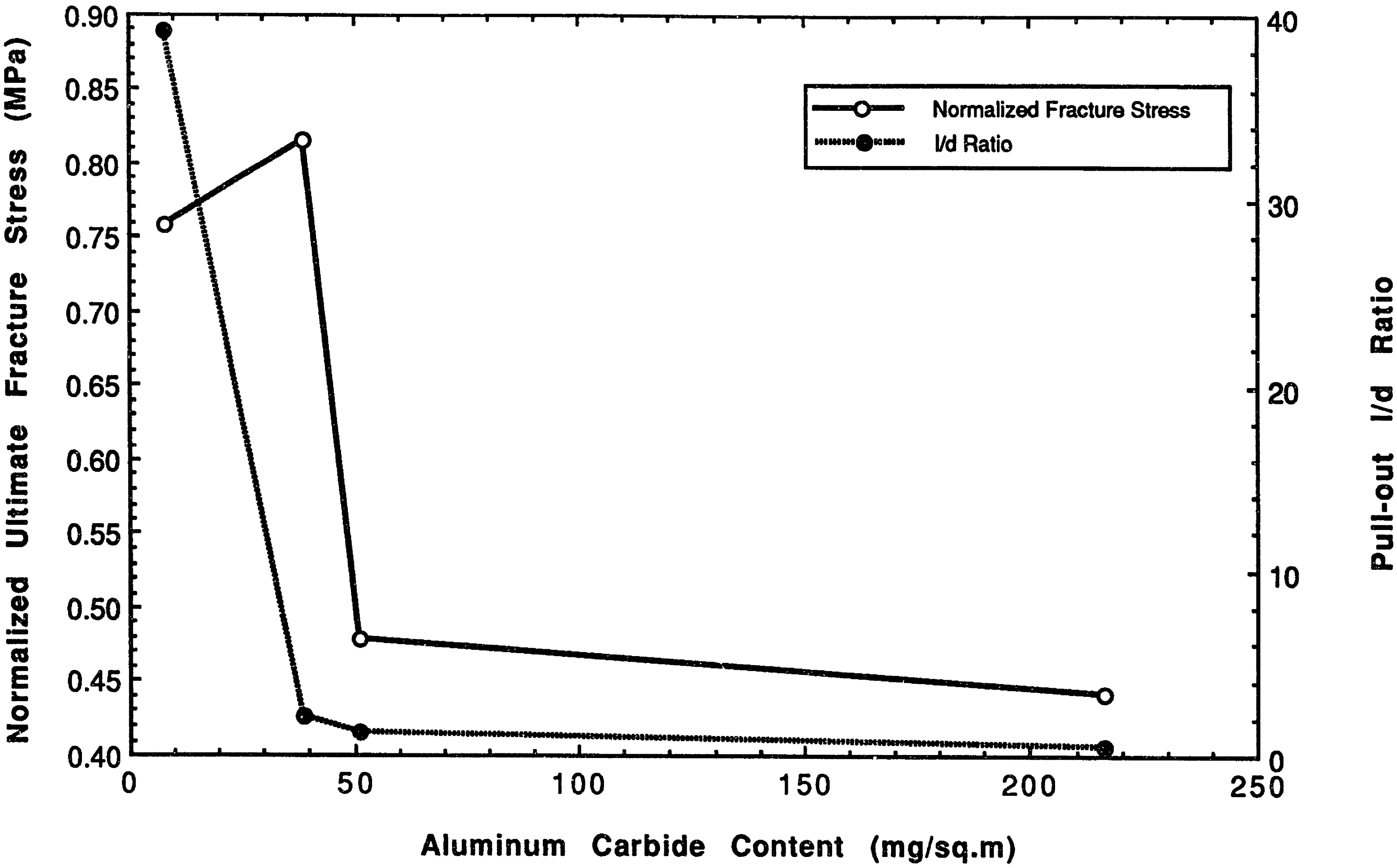

Figure D-2: Representation of carbide content versus the normalized fracture strength and fiber pull-out ratio for the G/6061 Al MMCs studied.

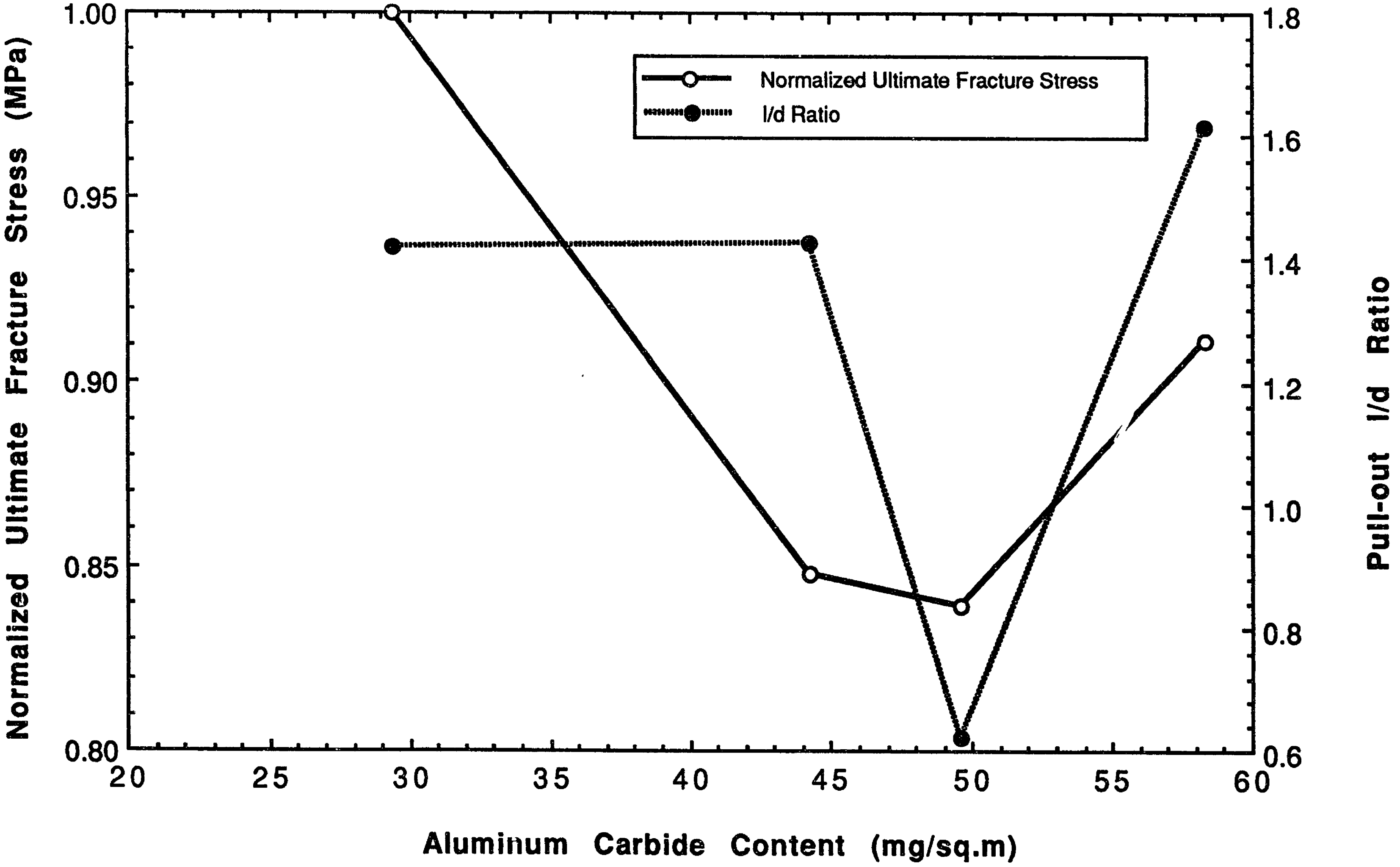

Figure D-3: Representation of carbide content versus the normalized ultimate fracture strength and fiber pull-out ratio for the G/Zn-Al MMCs studied

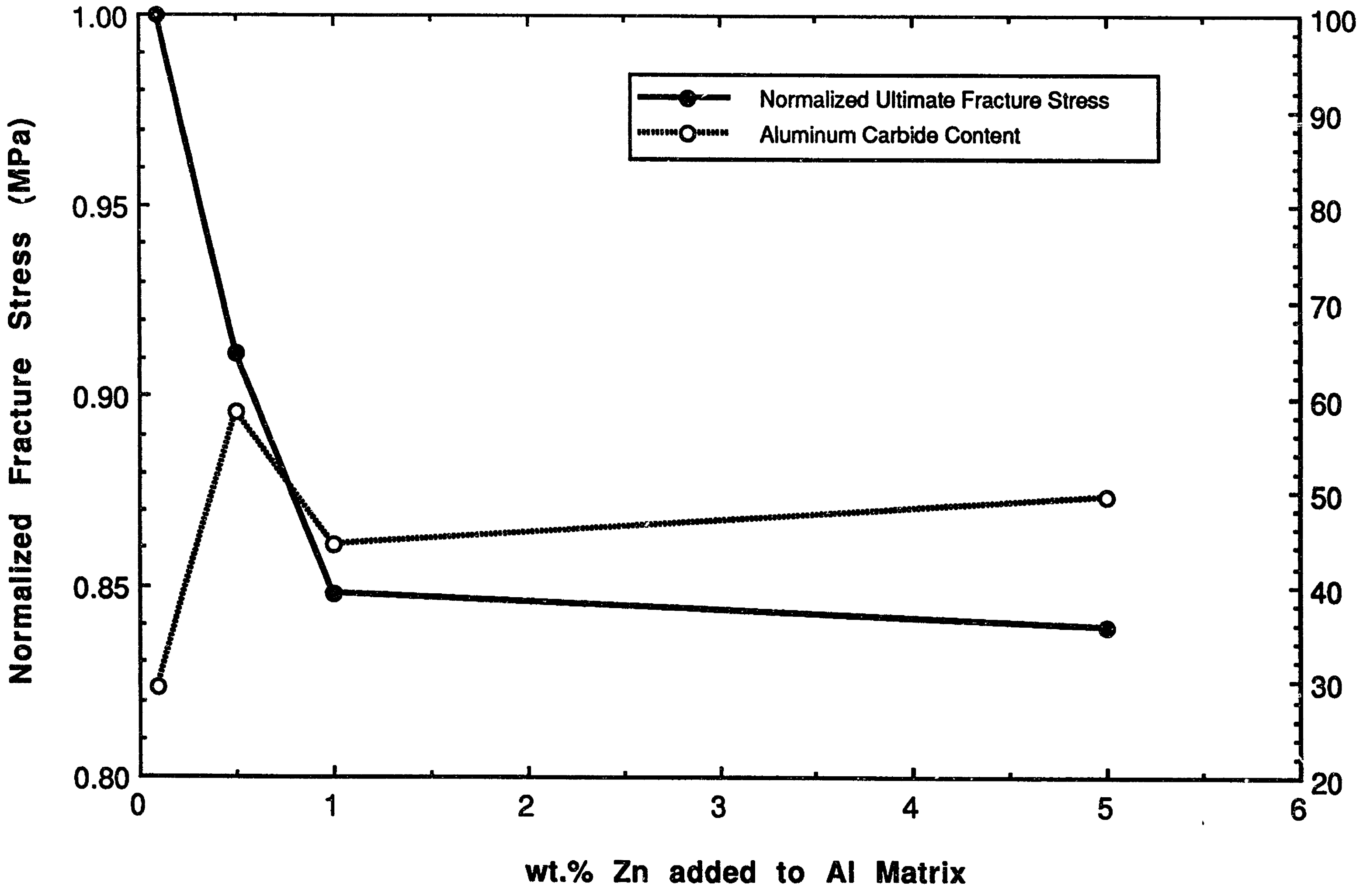

Figure D-4: Representation of carbide content versus the normalized fracture strength and fiber pull-out ratio for the G/Zn-Al MMCs studied.

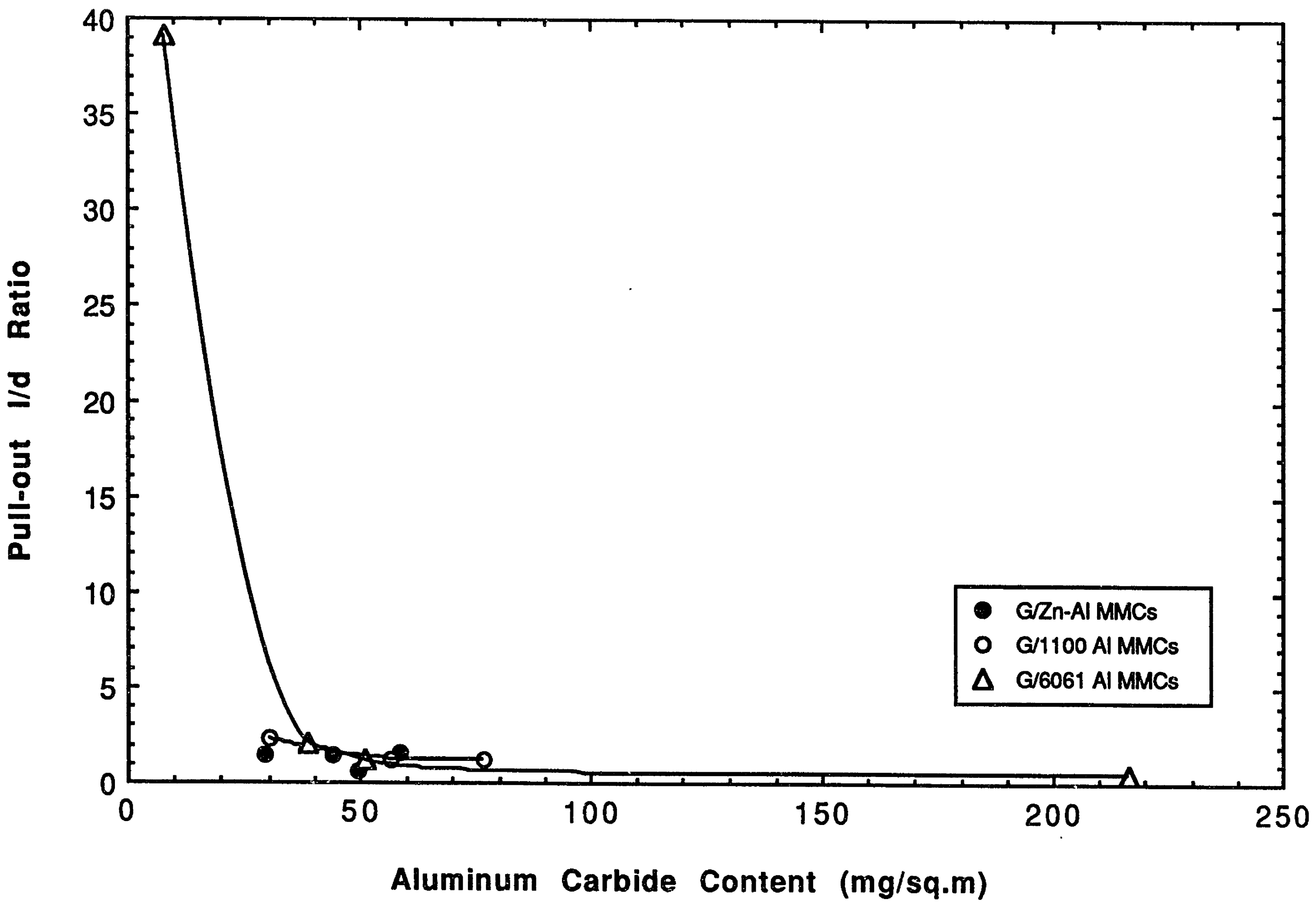

Figure D-5: Representation of carbide content versus the fiber pull-out ratio for the G/Al MMCs studied.

of crack growth may not be pulled out at all during three-point bending. Measurement of the fiber pull-out ratio is not as reliable as mechanical data and is better considered qualitative than quantitative.

Figure D-6 reveals the side-by-side comparison of the Al_4C_3 vs. normalized UFS for G/1100 Al, 6061 Al, and Al-Zn MMCs. While it is apparent that a maximum strength was observed for G/1100 and 6061 Al MMCs, a similar relationship was not found for the Zn containing composites, which contained varying amounts of Zn. It should be mentioned that we attempted to control the amount of Al_4C_3 that formed in the Zn containing samples by using, as close as possible, the same cooling rate for specimens (See Table 3.2.2).

From the results of gas chromatography, it has been shown that the cooling rate is inversely proportional to the amount of Al_4C_3 formed. Our results are in agreement with those of Baker and Bonfield [1978], Chernysyshova and Kobeleva [1985], and Towata, et al. [1985]. Interfacial strength will increase with the formation of Al_4C_3. As time proceeds at temperature, the amount of platelet Al_4C_3 becomes large enough to negatively affect the UFS of the of the G/Al MMC by creating an excessively strong interfacial bond. It is necessary to solidify the composite at the optimal cooling rate in order to achieve the best Al_4C_3 to fiber ratio. The results indicate that for the G/1100 Al MMCs studied the maximum normalized strength was attained between the values of 56.27 and 30.1 mg/m^2 Al_4C_3 (see Figure D-1 and Table D-2). Thereafter, these values were converted to 18.1 and 9.6 mg Al_4C_3/gm fiber, respectively; the mean of these two values is 13.85 mg/gm fiber. This agrees with the result of Chernysyshova and Kobeleva [1985], but their Al_4C_3 content was reported for a composite matrix of Al with 12 wt.%Si (see Table D-3). For G/6061 Al MMCs the maximum strength during three-point bending was attained at 7.8 mg Al_4C_3/gm fiber, a slightly lower value than for the G/1100 Al MMCs. If we assume that the experimental error in the Al_4C_3 calculation was ±8 mg/m^2 for Al_4C_3, this would correspond to an error of ~±1.5 mg Al_4C_3/gm fiber. Therefore the difference in the Al_4C_3 content for the two composite systems can be considered significant. Portnoi, et al. [1981], have shown that the addition of 12 wt.%Si to Al resulted in a narrowing of the

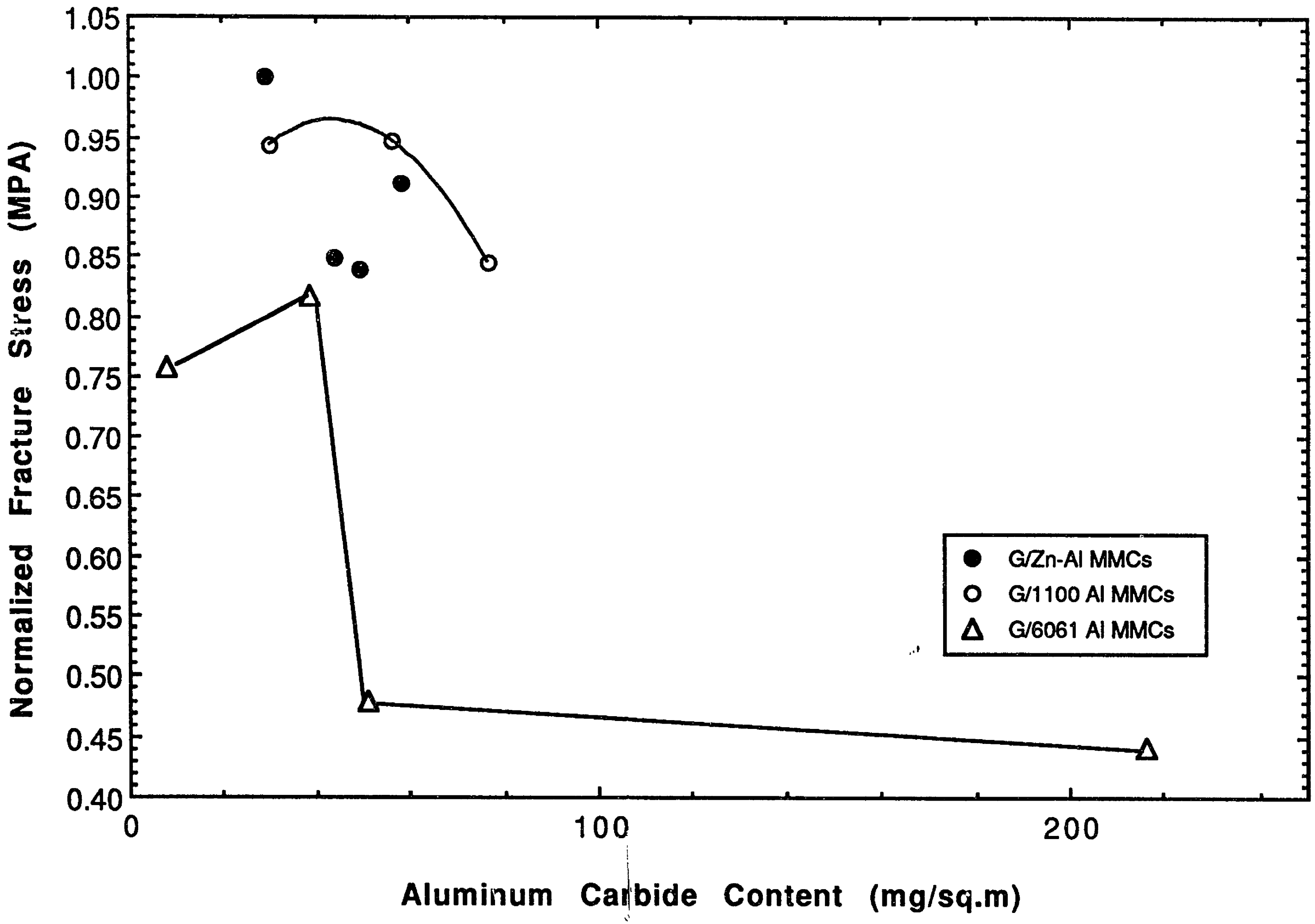

Figure D-6: Representation of carbide content versus the normalized fracture strength for the G/Al MMCs studied.

optimal Al_4C_3 content, which was shifted to a lower tolerable Al_4C_3 content for maximum fracture strength.

Table D-3: Optimal Al_4C_3 Values Determined by Gas Chromatography

Researcher	Matrix		
	Al-12%Si	1100 Al	6061 Al
Portnoi, et al.	9.6	35	N/A
Chernysyshova and Kobeleva	13.8	N/A	N/A
Buonanno	N/A	13.8	7.8

N/A = not available
*all values in mg Al_4C_3 /gm of fiber

Comparison of this data leads the author to believe that indeed, the addition of Si and Mg to the Al matrix resulted in a quicker decrease in UFS for the G/6061 Al MMCs than that found for G/1100 Al MMCs.

Portnoi, et al. [1981], convincingly argue that a Si rich eutectic Si-Al phase formed at the interface of their G/Al-12 wt.%Si MMCs. They produce convincing micrographs of the as-etched fibers with and without Si-Al precipitates on their surfaces. They claim that this Si-Al eutectic phase reduced the amount of Al_4C_3 formed by increasing the bond strength between the Si-Al phase and graphite fibers - much the same way Al_4C_3 does. While, on the other hand, Chernysyshova and Kobeleva [1985] claim that SiC is forming at the interface and causing the reduction in Al_4C_3 by the same phenomenon.

The possibility that both SiC and a segregated eutectic (Si-Al rich or Mg_2Si in the case of an 6061 Al matrix) may have formed simultaneously at the interface exists. Moreover, the main point is that, additions of Si and Mg to Al tend to segregate to the fiber-matrix interface, degrading the mechanical strength of the system more rapidly than that found for other alloy additions (e.g., Ti).

As for the role of Mg, besides forming intermetallic magnesium silicide in the Al matrix, Towata, et al. [1985], have shown that Mg is a strong oxide former, and as such, reacts with oxygen on preheated fibers during processing. Carbon was shown to be able to diffuse better through these oxides reacting to a greater extent with the matrix and increasing the shear strength significantly through exacerbated Al_4C_3 formation. This may add to the decrease in strength found for G/6061 MMCs (see Figure D-6), since 6061 Al contains only 0.6 wt.%Si.

An important point determined in this study, was that the degradation of the normalized UFS occurred with the addition of Zn to the Al matrix (see Figure D-4). It is most likely due to a Zn rich eutectic phase which formed at the interface during non-equilibrium solidification (see Figure 5.4.4).

Mortensen, et al. [1988b], have shown that for G/Al-4.5 wt.%Cu MMC with a graphite fiber interstice spacing radius of 5 x 10^{-6}m requires approximately 100 seconds for complete homogenization during solidification, since the presence of fibers affects secondary dendrite coarsening. However, this refers to homogenization of solute in the matrix and not for solute at the fiber-matrix interface. Interfacial reactions with carbon and oxygen, may alter further homogenization of solute in the matrix and create irreversible interfacial products. Backscattered electron imaging in the SEM indicates that homogenization of the matrix for the most part was accomplished for G/6061 Al and G/Al-Zn MMCs; however, there was still considerable solute enrichment at the interface.

SEM fractography of G/Al-5%Zn MMCs exposed fiber surfaces after fracture revealed little degradation of the fiber surface, suggesting that the bond between the interface was weak. Processed G/Al MMCs have been shown to have a chemical bond at the interface [Mortensen, 1986, 1988, 1992]. This chemical bond makes G/Al MMCs strong in tension and even stronger in shear [Towata, et al., 1985]. Fletcher [1989] has shown that the bonding in short fiber SiC/Zn MMCs is principally physical in nature. No chemical bond is known to form between C and Zn [Hansen, 1958]. This would suggest that a weak interfacial bond at the fiber-matrix interface results in a decrease in the UFS observed for the G/Al-Zn MMCs studied (see Figure D-4), since only a physical bond could form between Zn and graphite fibers.

Appendix E: Al-Cu Phase Diagram

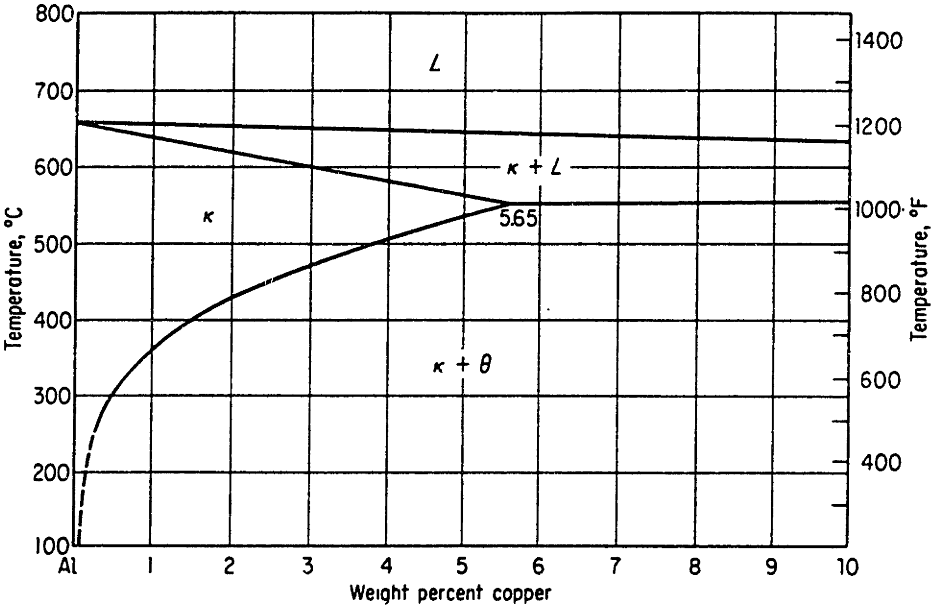

Aluminum-rich portion of the copper-aluminum alloy system. [Metals Handbook, 1948, p.1160]

Appendix F: Individual Polarization Tests Performed on G/Al MMCs in Deaerated 0.5M Na_2SO_4 solution.

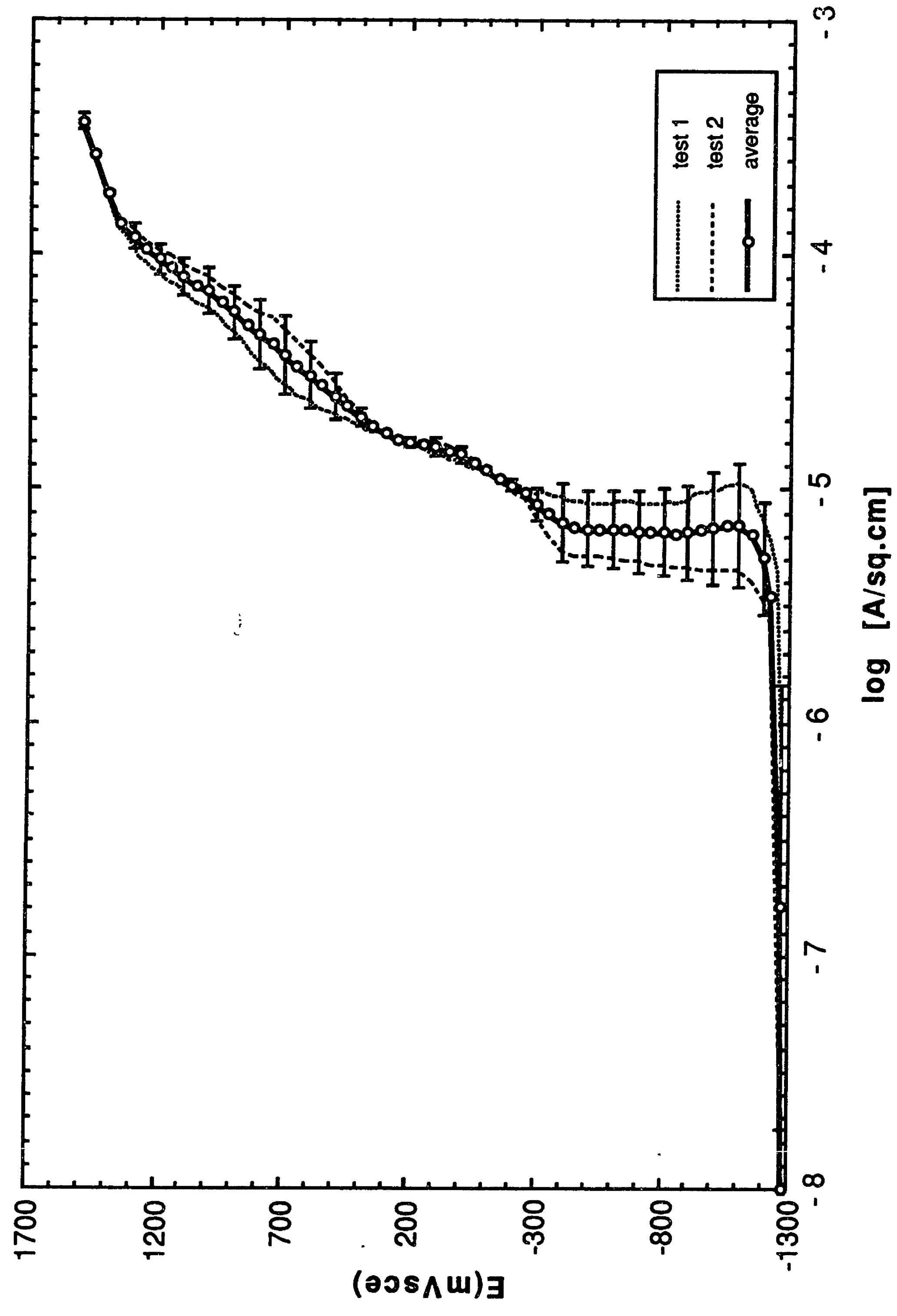

Appendix F-1: Anodic polarization diagram of Specimen 1, a G/1100 Al MMC in deaerated 0.5M Na_2SO_4 solution of pH~7 at 30°C. Scan rate = 0.167 mV/s; Ecorr = -1278 mVsce, SD = 8.5 mVsce.

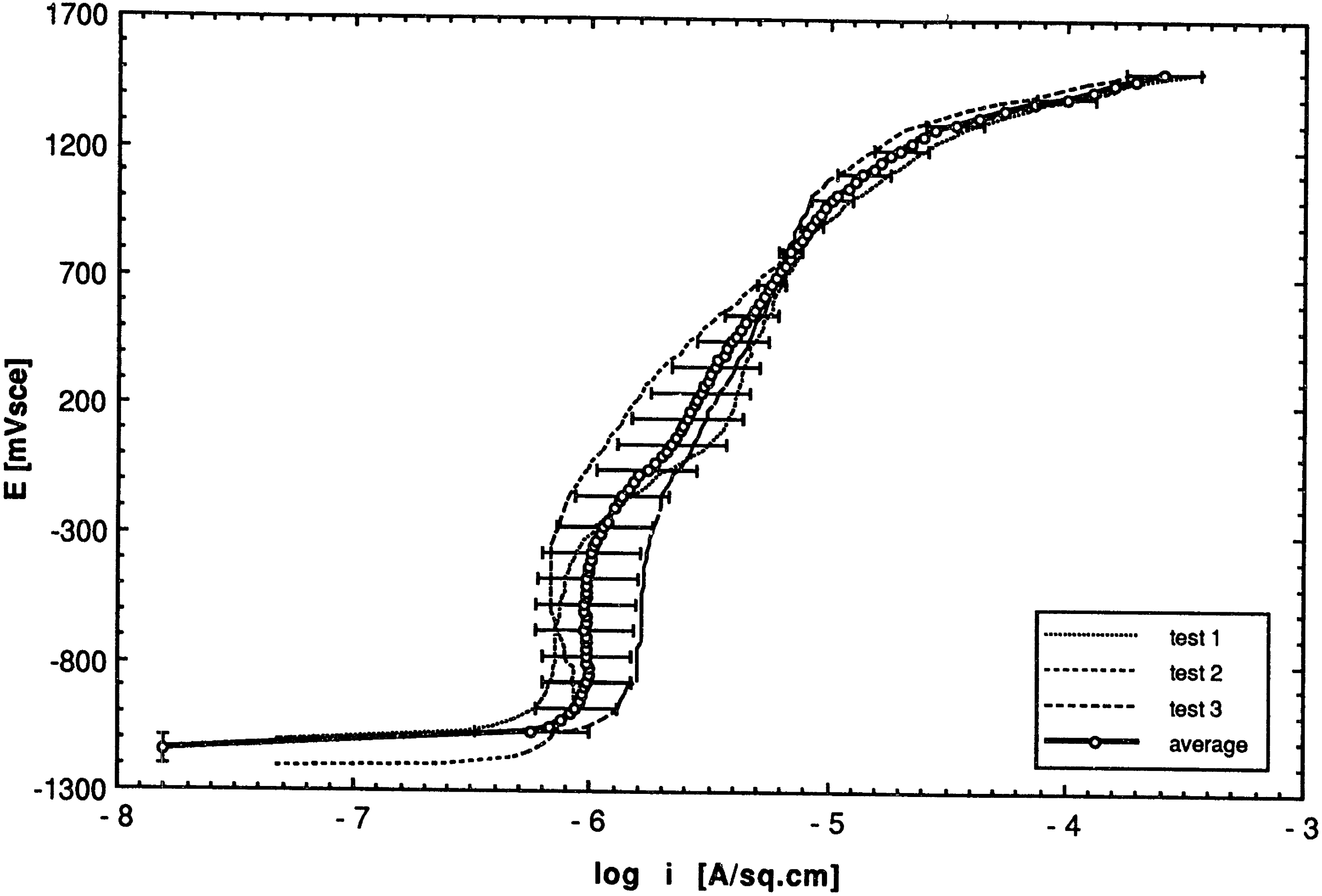

Appendix F-2: Anodic polarization diagram of Specimen 2, a G/1100 Al MMC in deaerated 0.5M Na_2SO_4 solution of pH~7 at 30°C. Scan rate = 0.167 mV/s; Ecorr = -1143 mVsce, SD = 58 mVsce.

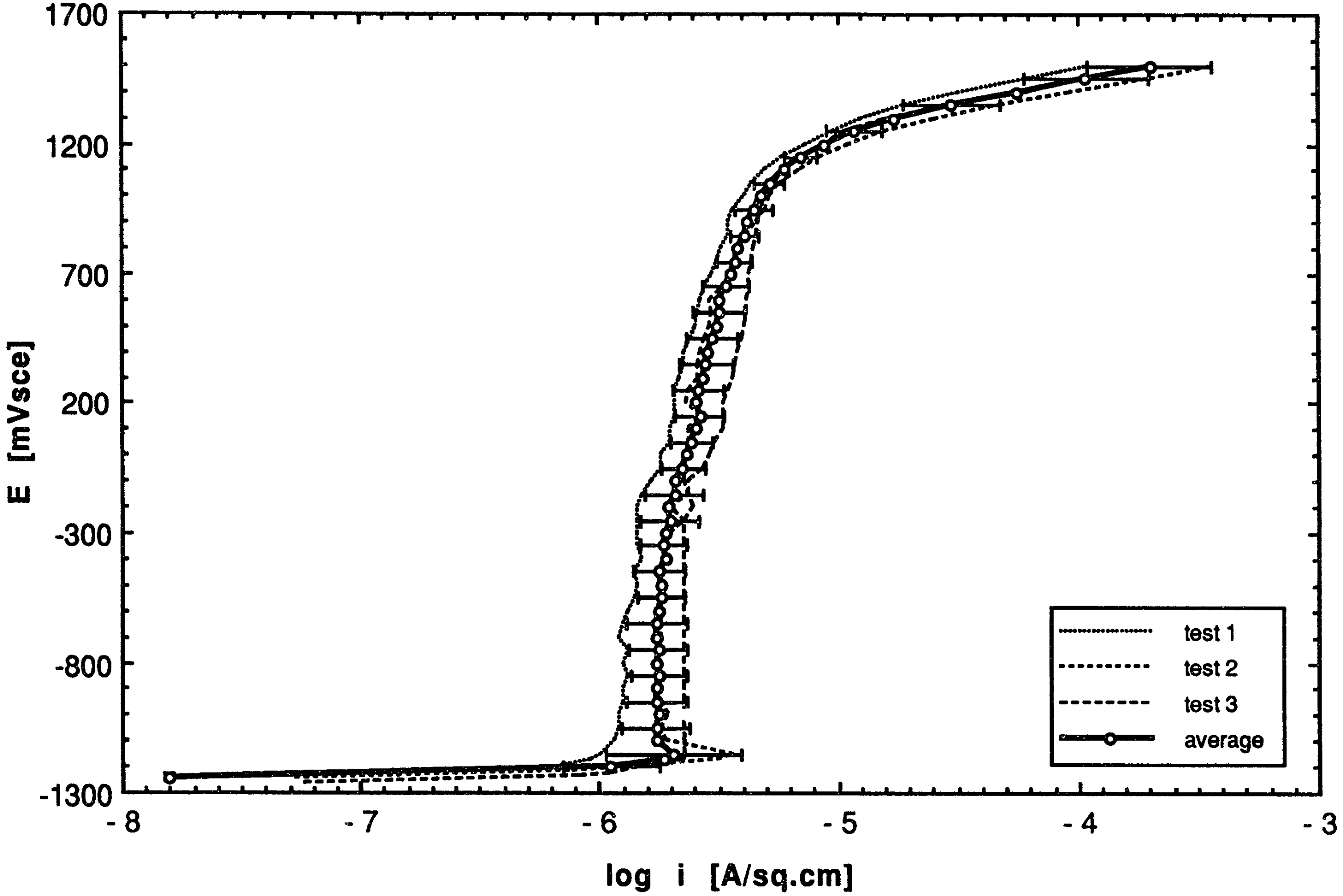

Appendix F-3: Anodic polarization diagram of Specimen 3, a G/1100 Al MMC in deaerated 0.5M Na_2SO_4 solution of pH~7 at 30°C. Scan rate = 0.167 mV/s; Ecorr = -1242 mVsce, SD = 16.5 mVsce.

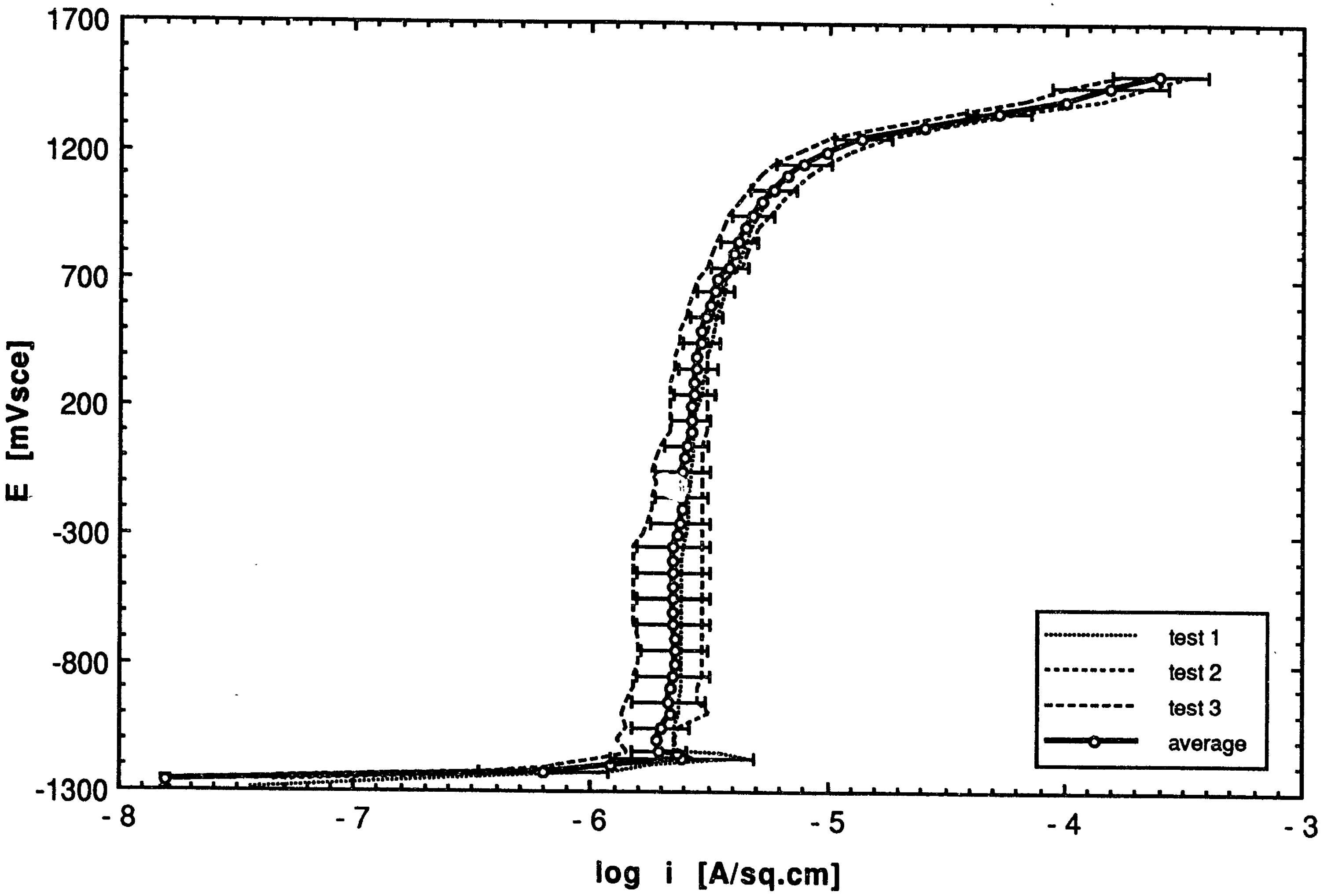

Appendix F-4: Anodic polarization diagram of Specimen 4, a G/1100 Al MMC in deaerated 0.5M Na_2SO_4 solution of pH~7 at 30°C. Scan rate = 0.167 mV/s; Ecorr = -1264 mVsce, SD = 22.48 mVsce.

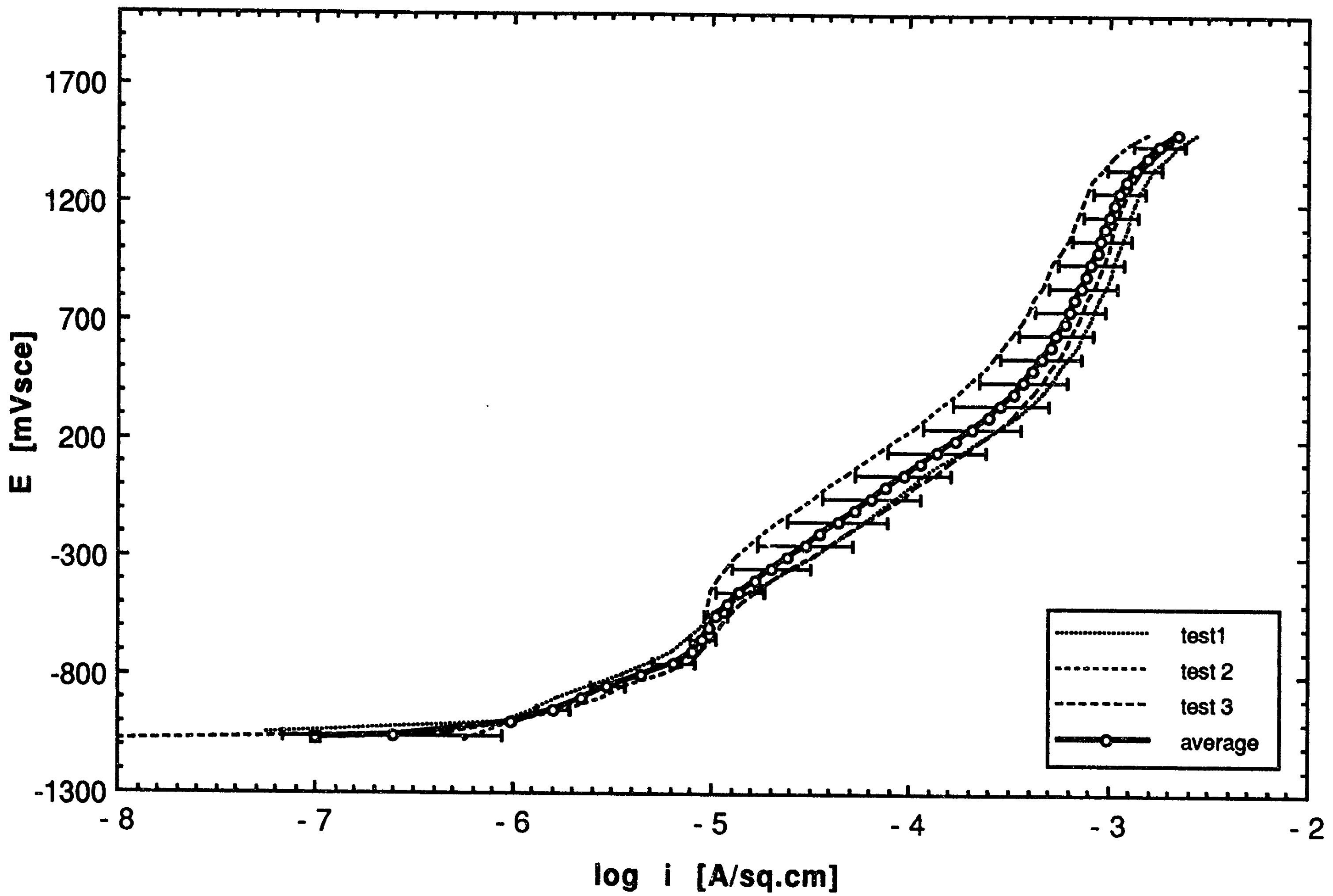

Appendix F-5: Anodic polarization diagram of Specimen 5, a G/6061 Al MMC in deaerated 0.5M Na_2SO_4 solution of pH~7 at 30°C. Scan rate = 0.167 mV/s; Ecorr = -1071 mVsce, SD = 18 mVsce.

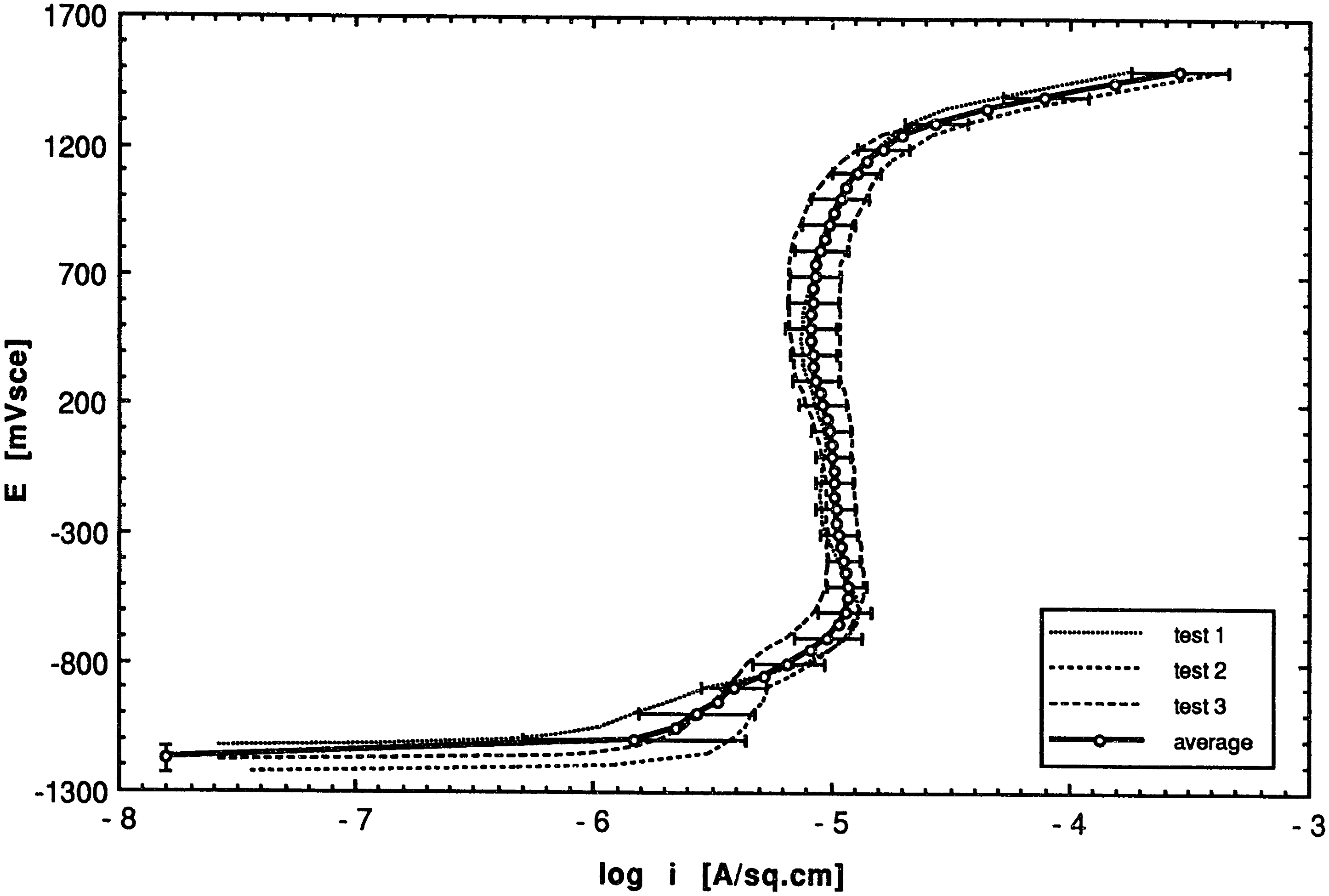

Appendix F-6: Anodic polarization diagram of Specimen 6, a G/6061 Al MMC in deaerated 0.5M Na_2SO_4 solution of pH~7 at 30°C. Scan rate = 0.167 mV/s; Ecorr = -1176 mVsce, SD = 48 mVsce.

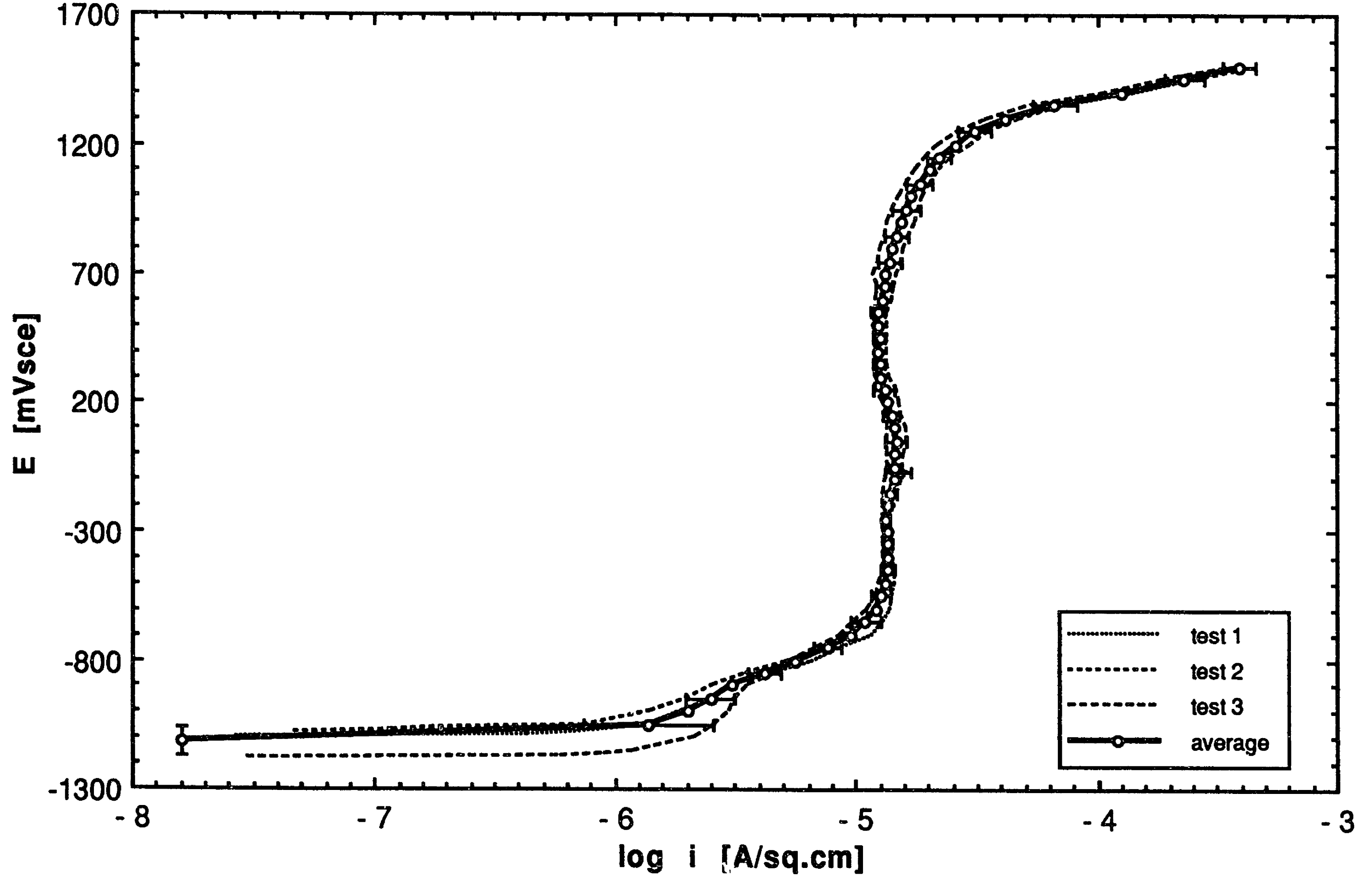

Appendix F-7: Anodic polarization diagram of Specimen 7, a G/6061 Al MMC in deaerated 0.5M Na_2SO_4 solution of pH~7 at 30°C. Scan rate = 0.167 mV/s; Ecorr = -1120 mVsce, SD = 55 mVsce.

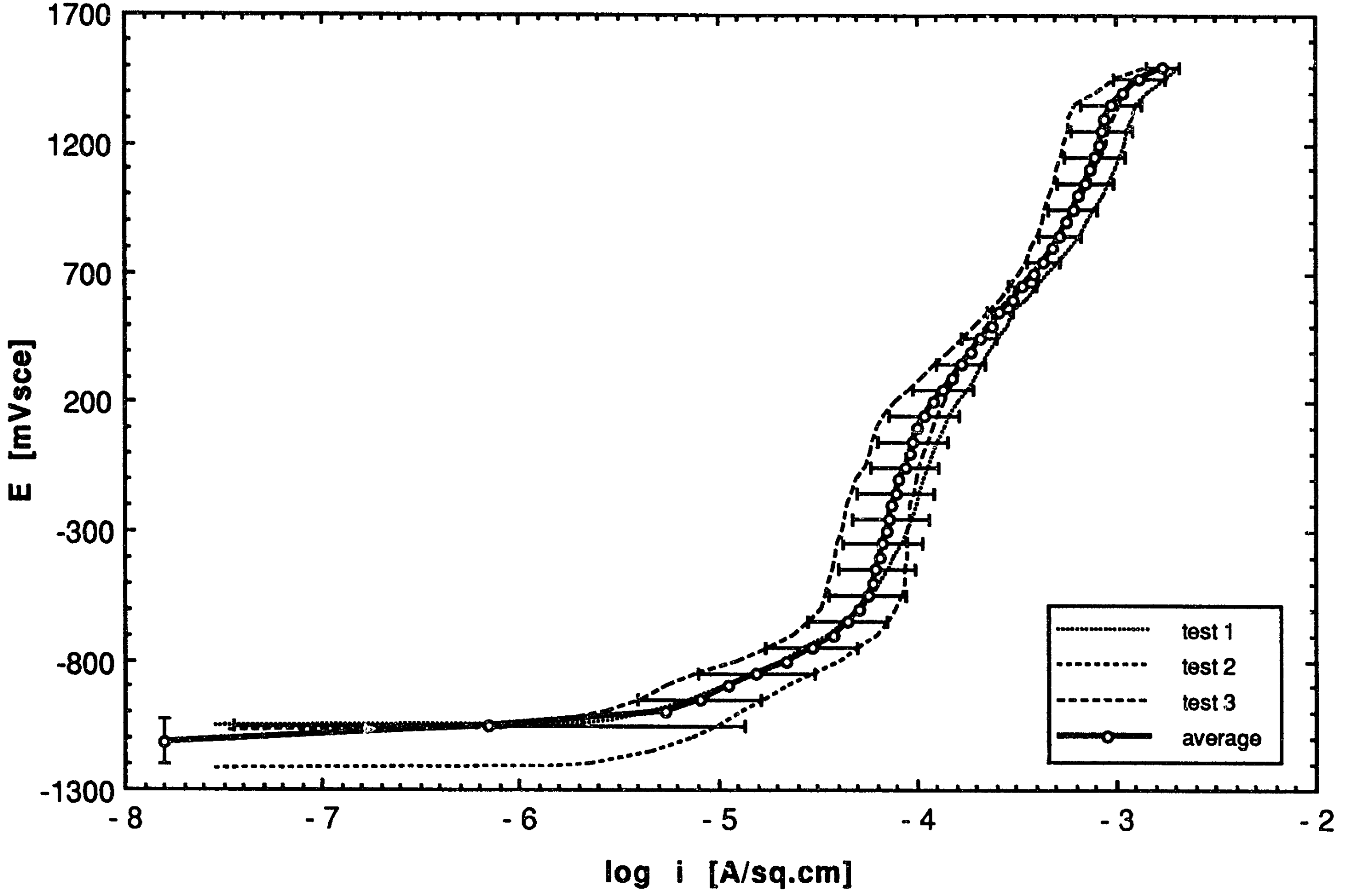

Appendix F-8: Anodic polarization diagram of Specimen 8, a G/6061 Al MMC in deaerated 0.5M Na_2SO_4 solution of pH~7 at 30°C. Scan rate = 0.167 mV/s; Ecorr = -1113 mVsce, SD = 87 mVsce.

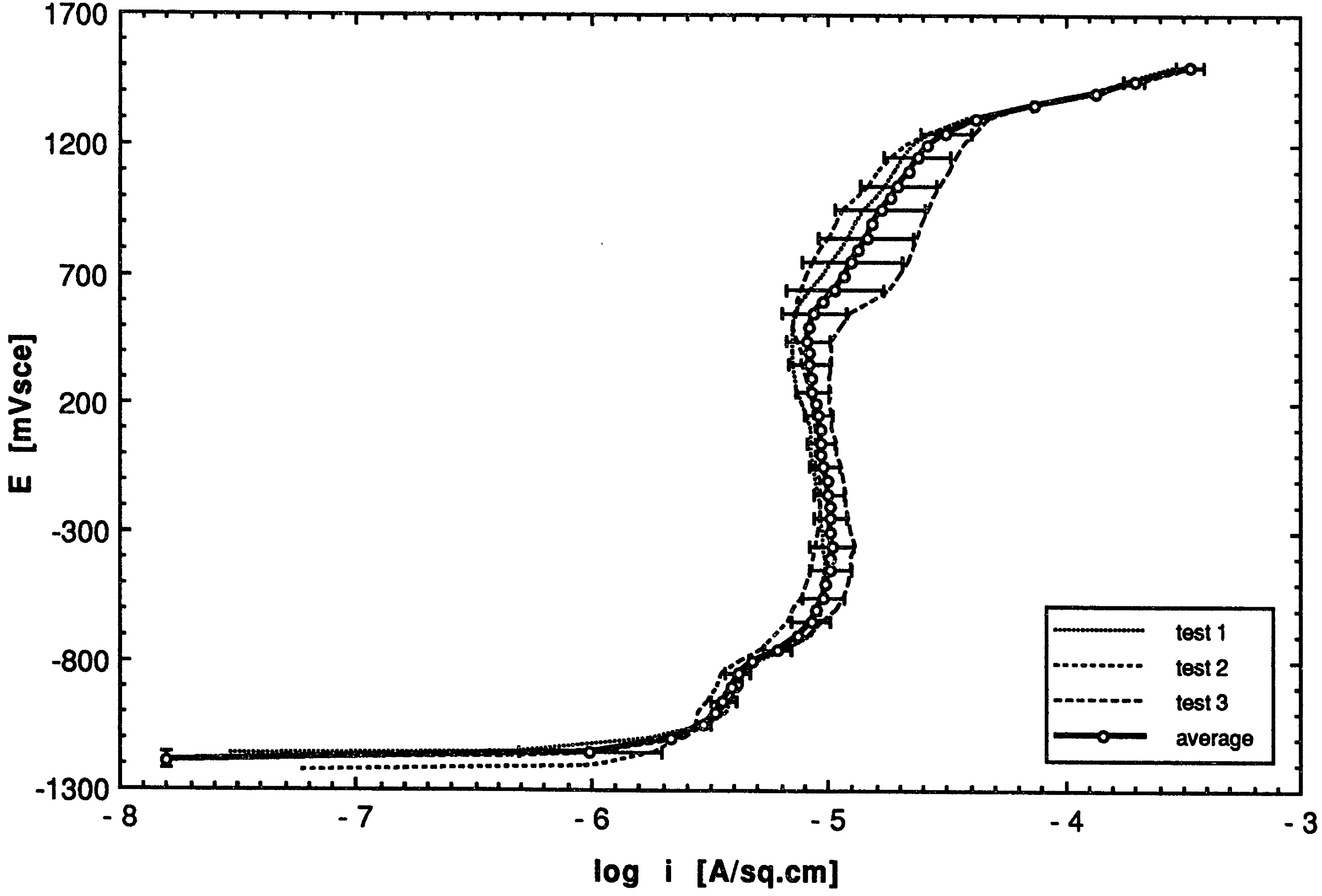

Appendix F-9: Anodic polarization diagram of Specimen 9, a G/6061 Al MMC in deaerated 0.5M Na_2SO_4 solution of pH~7 at 30°C. Scan rate = 0.167 mV/s; Ecorr = -1188 mVsce, SD = 39 mVsce.

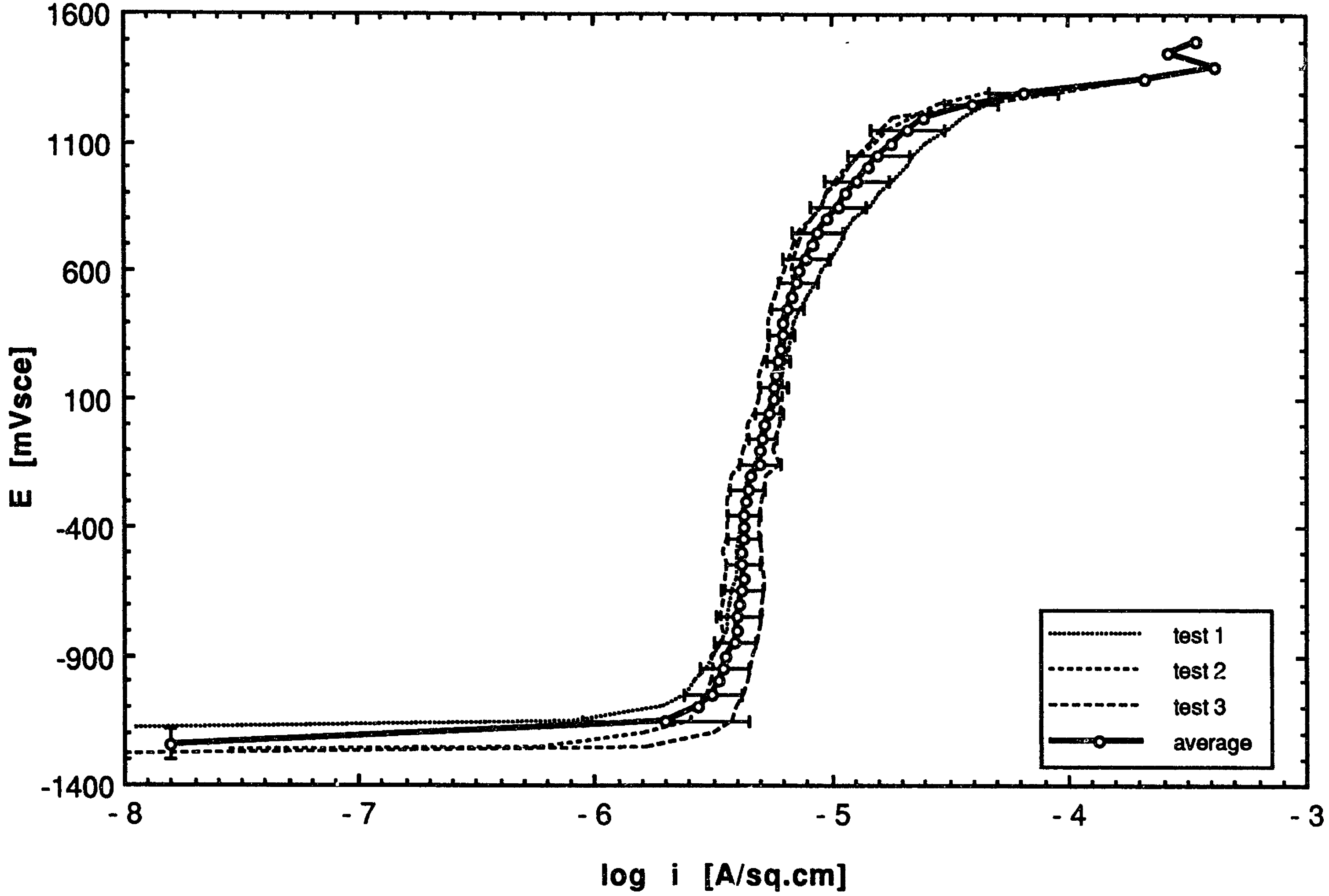

Appendix F-10: Anodic polarization diagram of Specimen 10, a G/Al-0.1%Zn MMC in deaerated 0.5M Na_2SO_4 solution of pH~7 at 30°C. Scan rate = 0.167 mV/s; Ecorr = -1240 mVsce, SD = 56 mVsce.

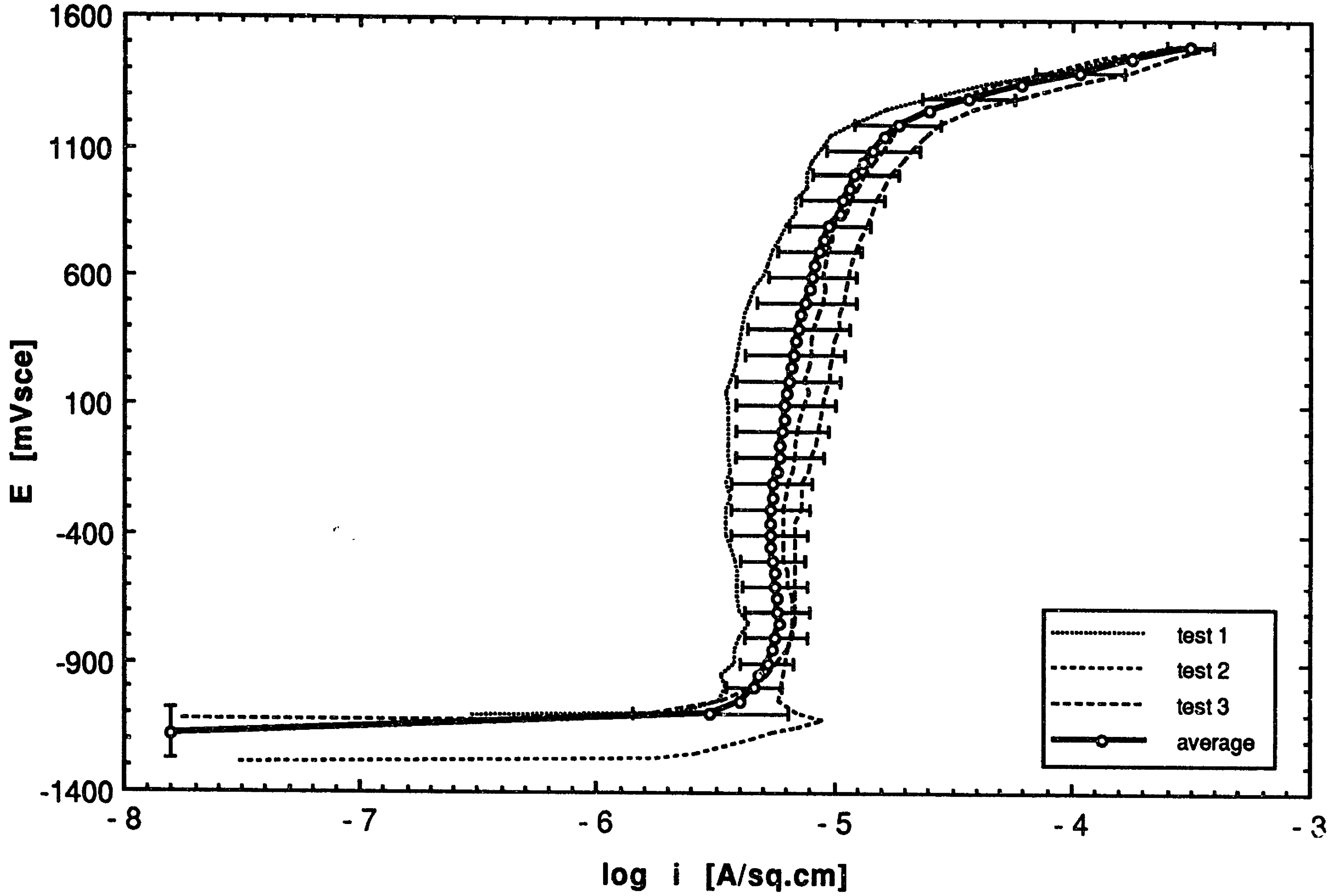

Appendix F-11: Anodic polarization diagram of Specimen 11, a G/Al-0.5%Zn MMC in deaerated 0.5M Na_2SO_4 solution of pH~7 at 30°C. Scan rate = 0.167 mV/s; Ecorr = -1176 mVsce, SD = 98 mVsce.

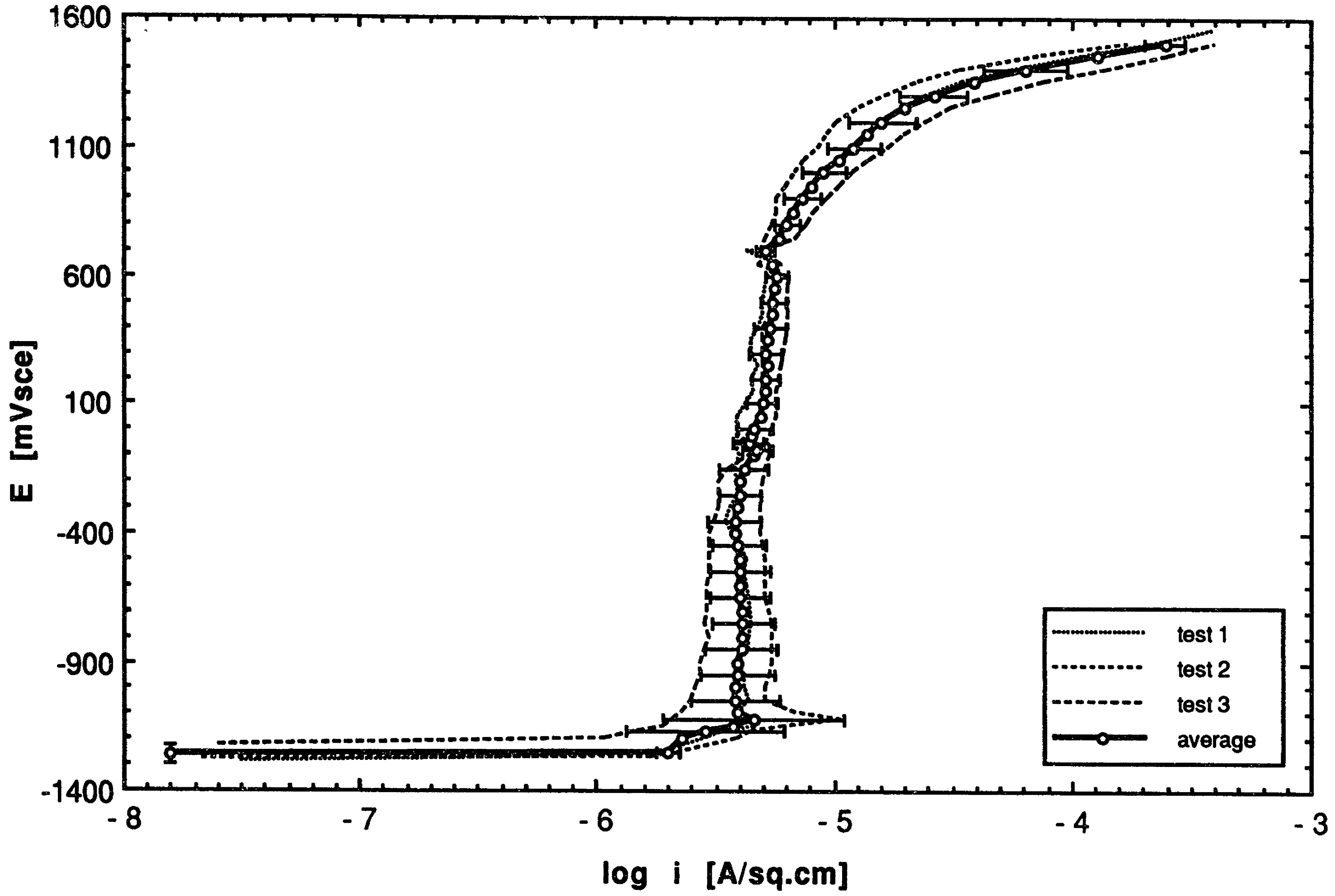

Appendix F-12: Anodic polarization diagram of Specimen 12, a G/Al-1%Zn MMC in deaerated 0.5M Na_2SO_4 solution of pH~7 at 30°C. Scan rate = 0.167 mV/s; Ecorr = -1265 mVsce, SD = 37 mVsce.

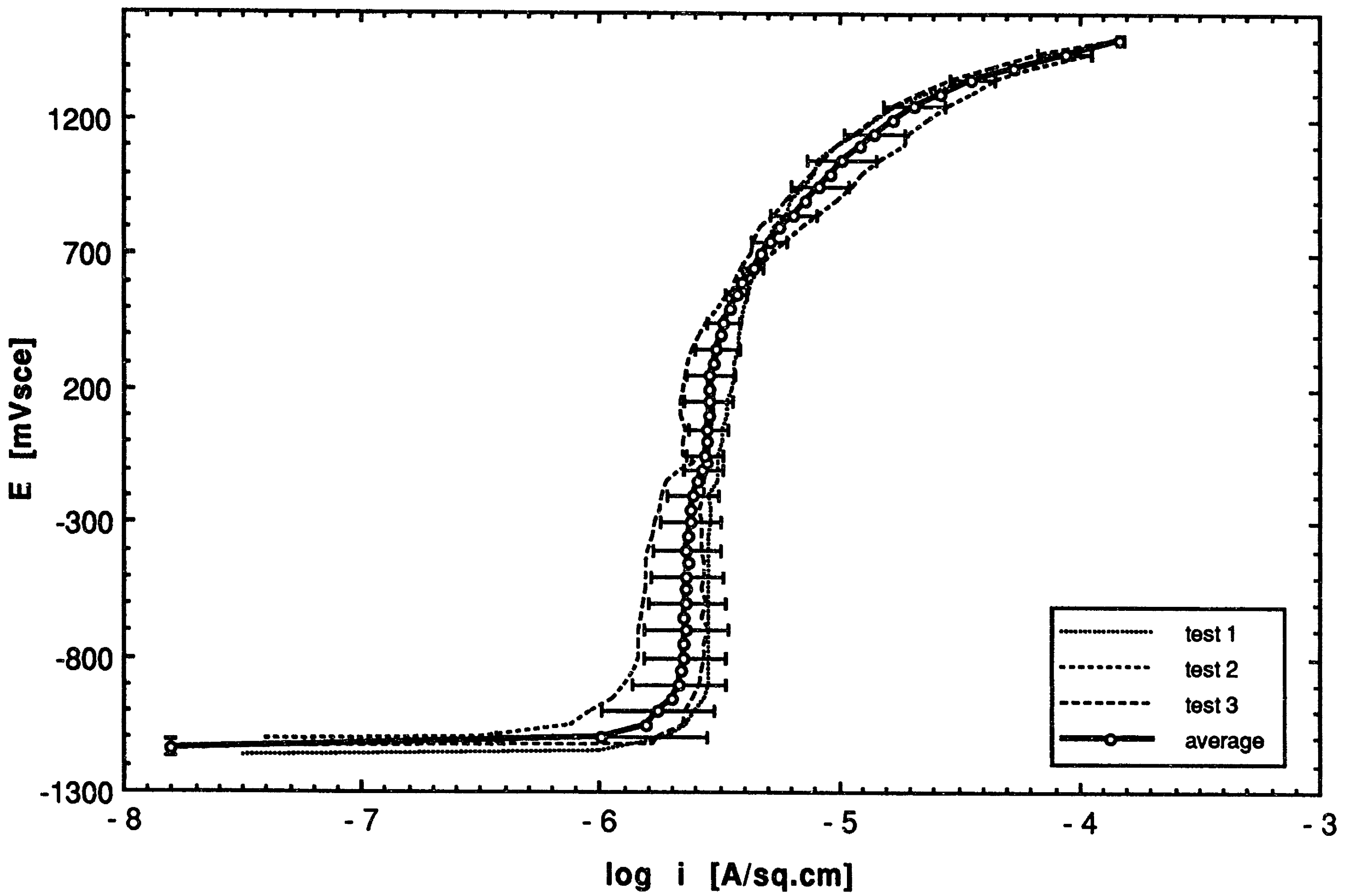

Appendix F-13: Anodic polarization diagram of Specimen 13, a G/Al-5%Zn MMCin deaerated 0.5M Na_2SO_4 solution of pH~7 at 30°C. Scan rate = 0.167 mV/s; Ecorr = -1136 mVsce, SD = 31 mVsce.

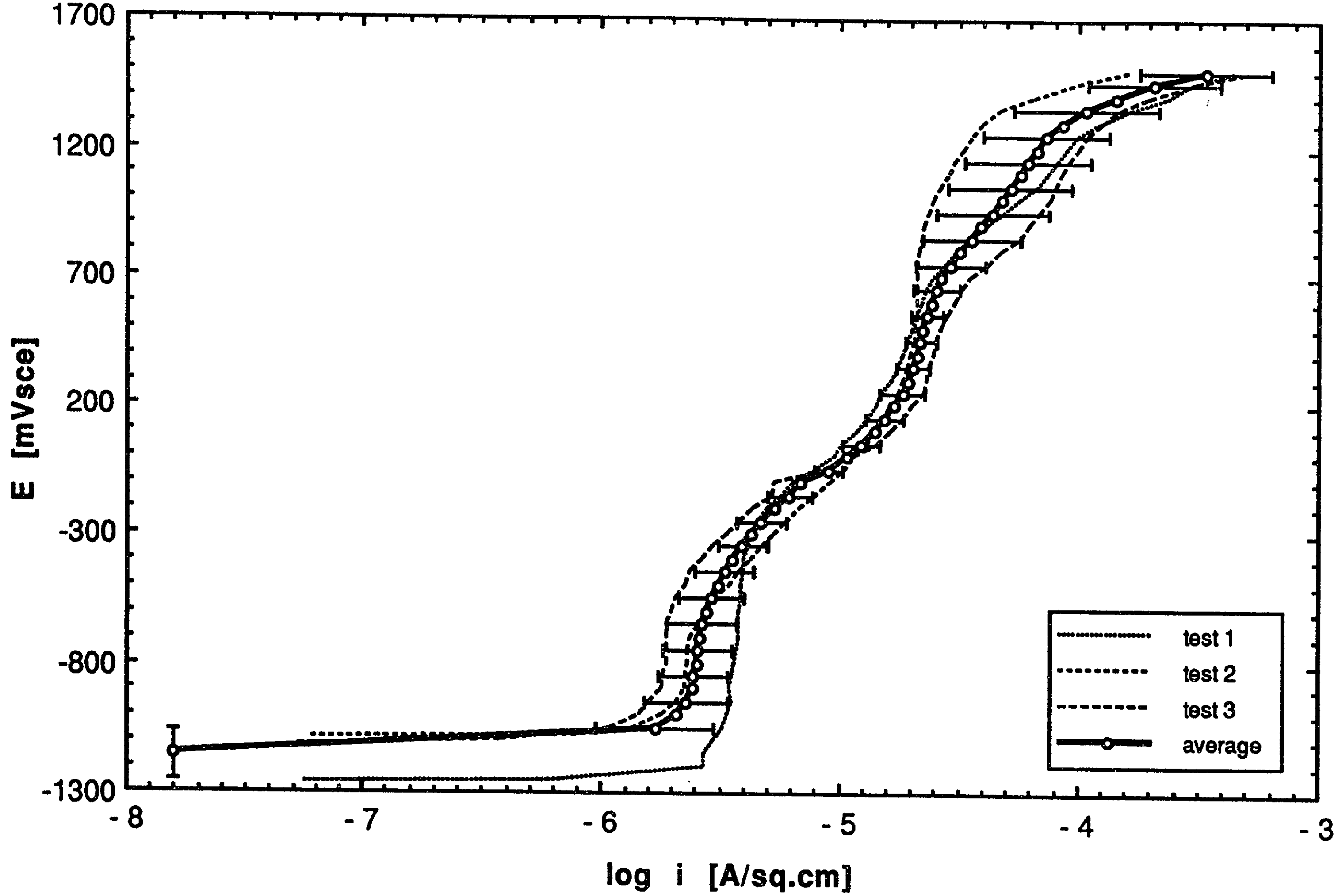

Appendix F-14: Anodic polarization diagram of Specimen 14, a G/Al-0.5%Cu MMC in deaerated 0.5M Na_2SO_4 solution of pH~7 at 30°C. Scan rate = 0.167 mV/s; Ecorr = -1156 mVsce, SD = 95 mVsce.

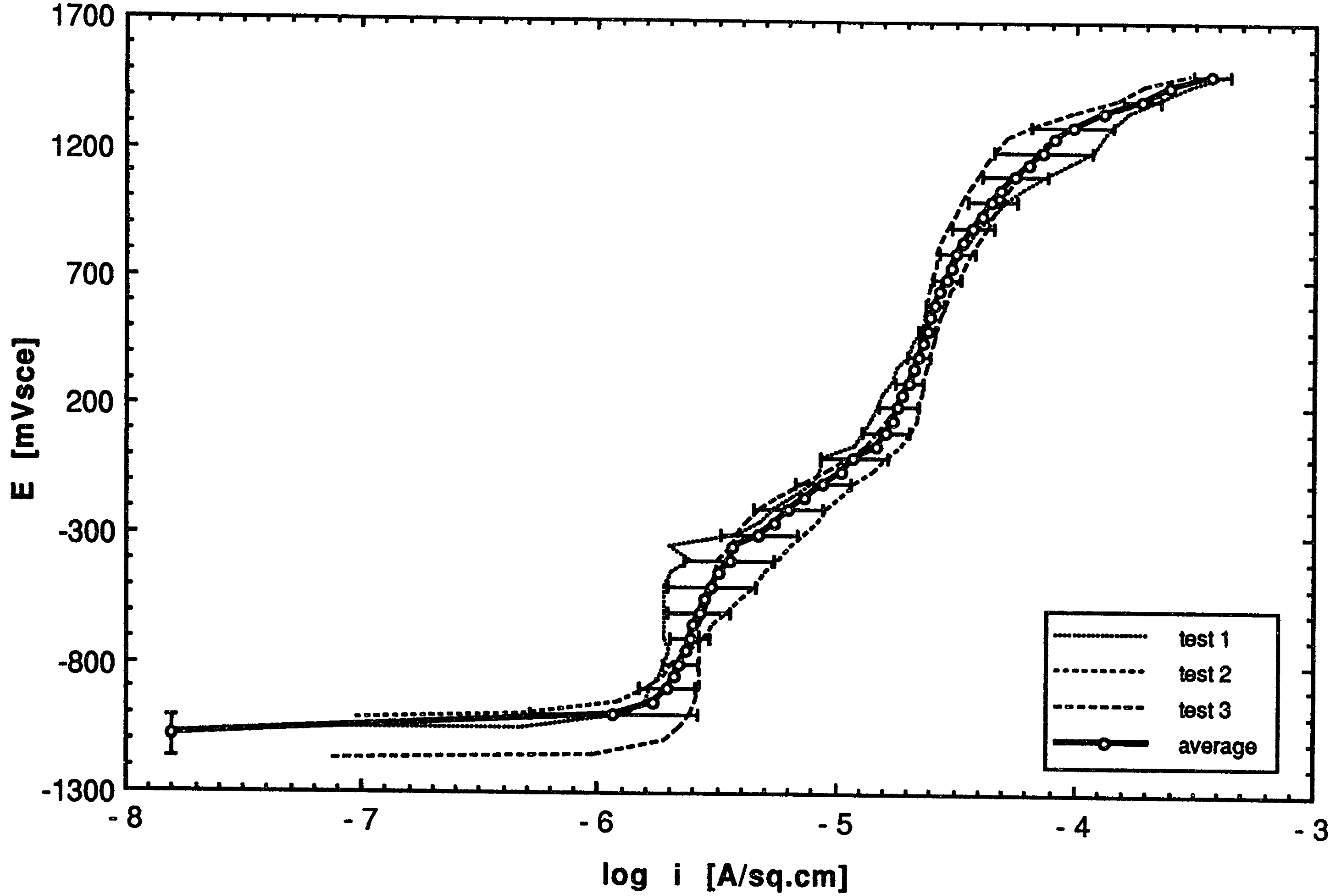

Appendix F-15: Anodic polarization diagram of Specimen 14, a G/Al-1.0%Cu MMC in deaerated 0.5M Na_2SO_4 of pH 7 at 30°C. Scan rate = 0.167 mV/s; Ecorr = -1081 mVsce, SD = 79 mVsce.

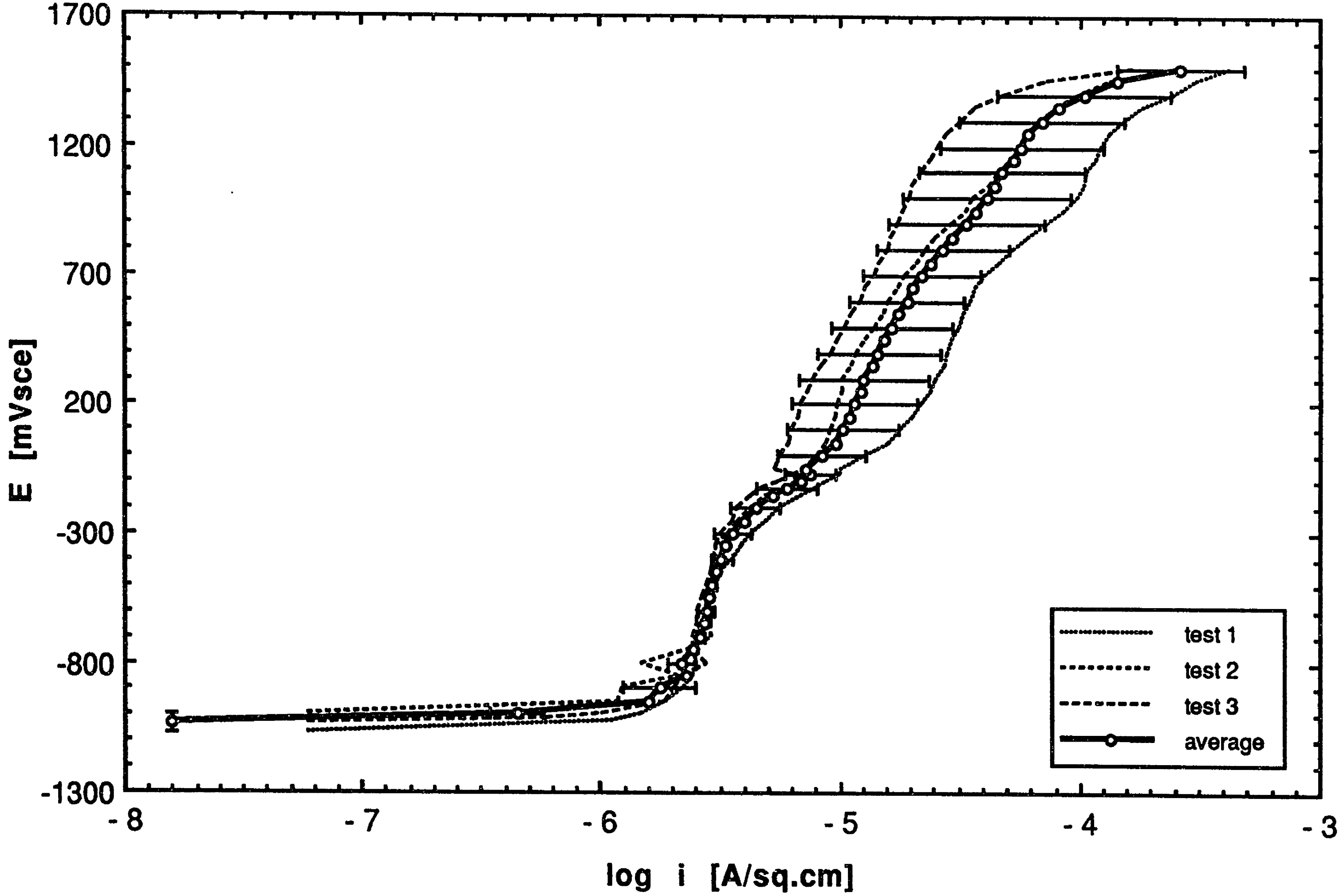

Appendix F-16: Anodic polarization diagram of Specimen 16, a G/Al-4%Cu MMC in deaerated 0.5M Na_2SO_4 solution of pH~7 at 30°C. Scan rate = 0.167 mV/s; Ecorr = -1033 mVsce, SD = 35 mVsce.

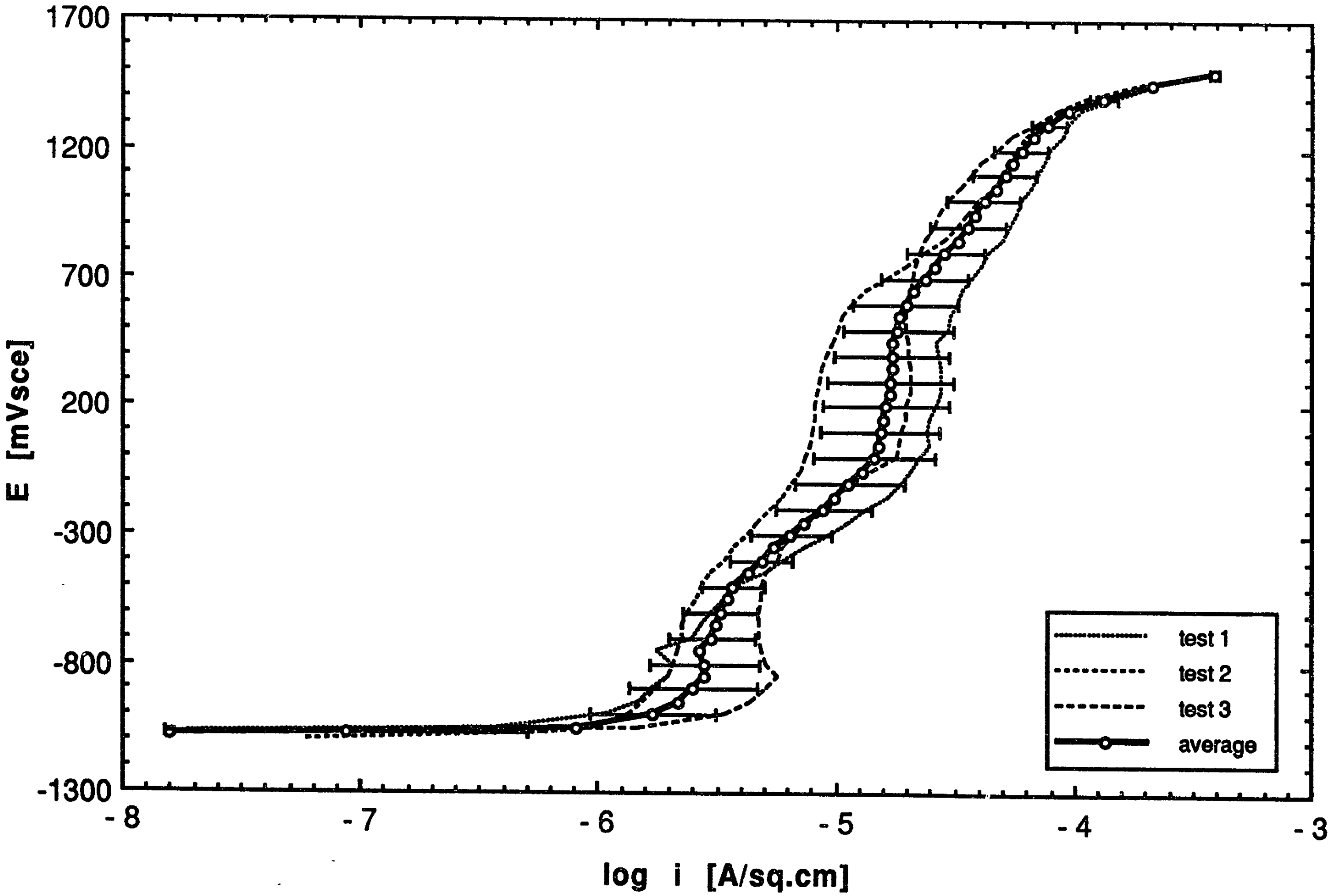

Appendix F-17: Anodic polarization diagram of Specimen 17, a G/Al-2%Cu MMC in deaerated 0.5M Na_2SO_4 solution of pH~7 at 30°C. Scan rate = 0.167 mV/s; Ecorr = -1078 mVsce, SD = 14 mVsce.

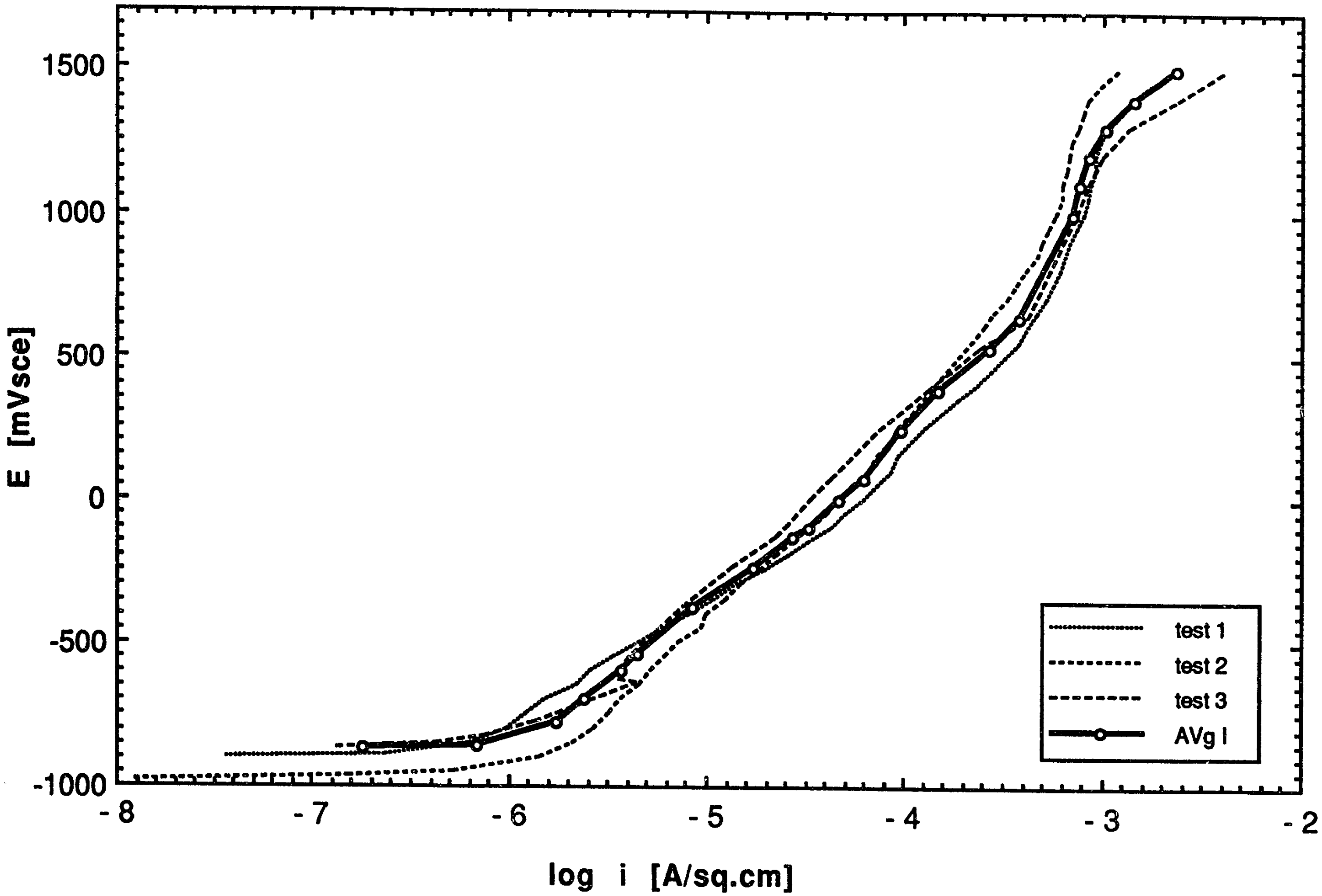

Appendix F-18: Anodic polarization diagram of Specimen 18, a G/Al-2%Cu MMC in deaerated 0.5M Na_2SO_4 solution of pH~7 at 30°C. Scan rate = 0.167 mV/s; Ecorr = -1078 mVsce, SD = 14 mVsce.

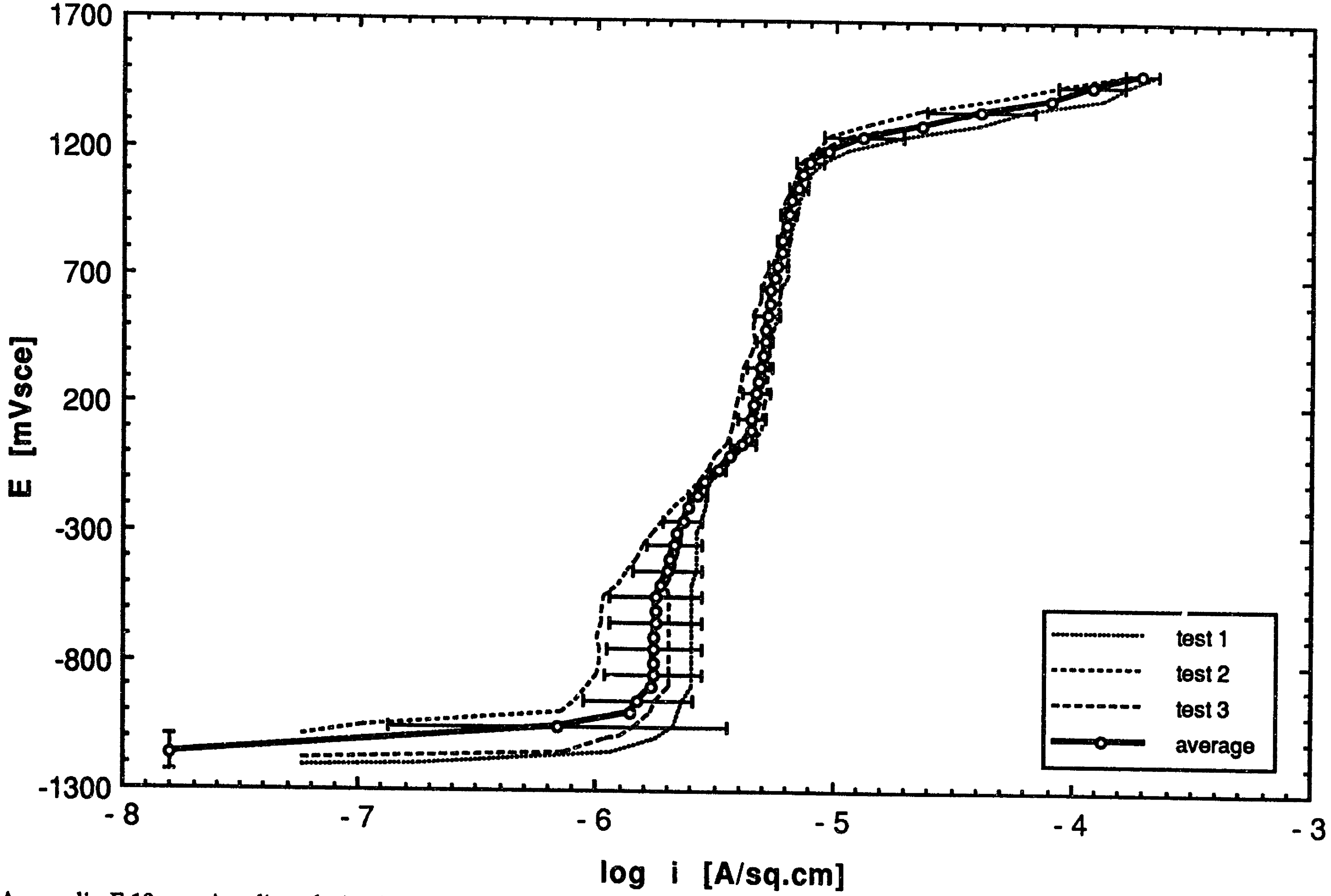

Appendix F-19: Anodic polarization diagram of Specimen 19, a G/Al-0.5 %Cu MMC in deaerated 0.5M Na_2SO_4 of pH 7 at 30°C. Scan rate = 0.167 mV/s; Ecorr = -1158 mVsce, SD = 65 mVsce.

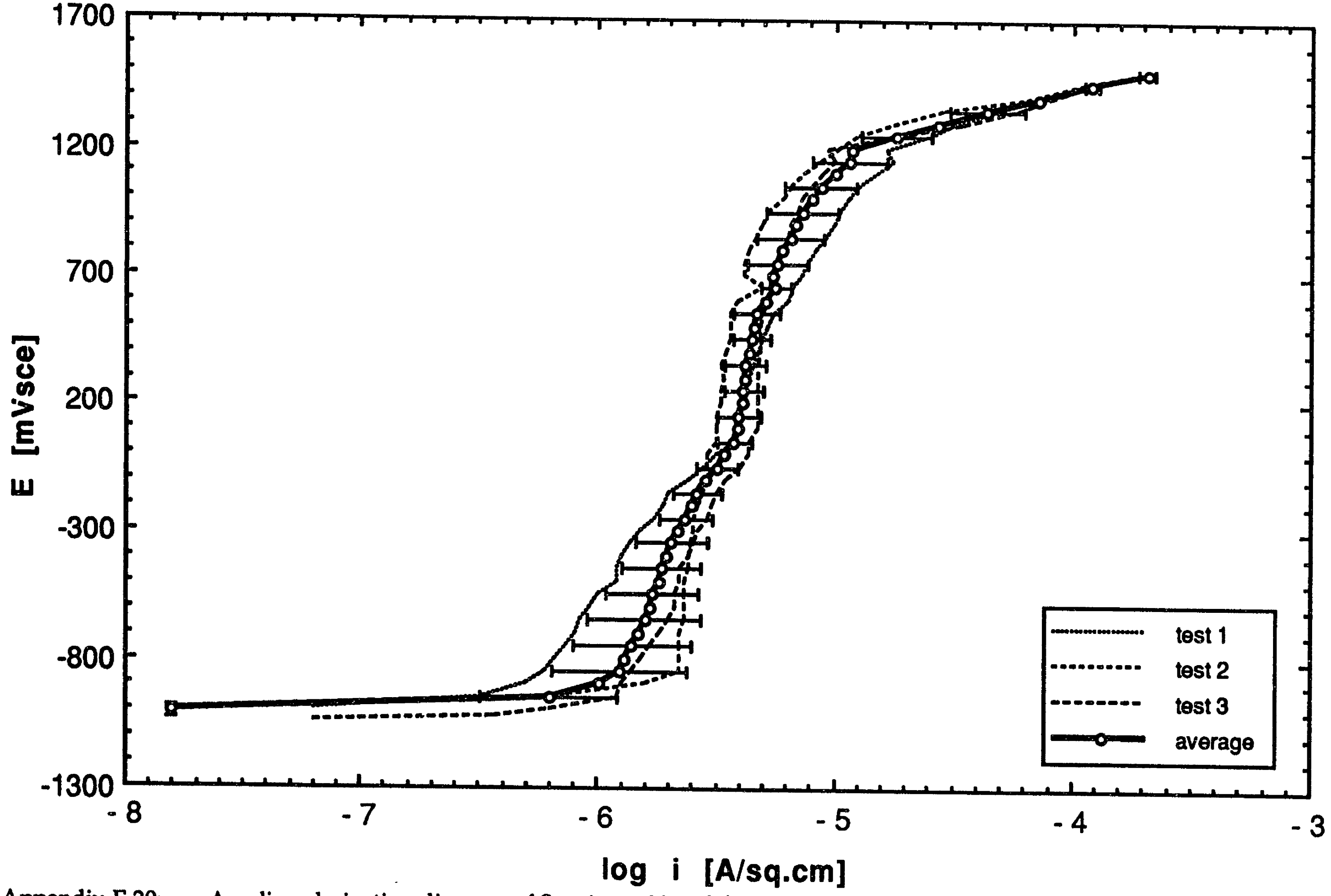

Appendix F-20: Anodic polarization diagram of Specimen 20, a G/Al-1%Cu MMC in deaerated 0.5M Na_2SO_4 solution of pH~7 at 30°C. Scan rate = 0.167 mV/s; Ecorr = -1010 mVsce, SD = 27 mVsce.

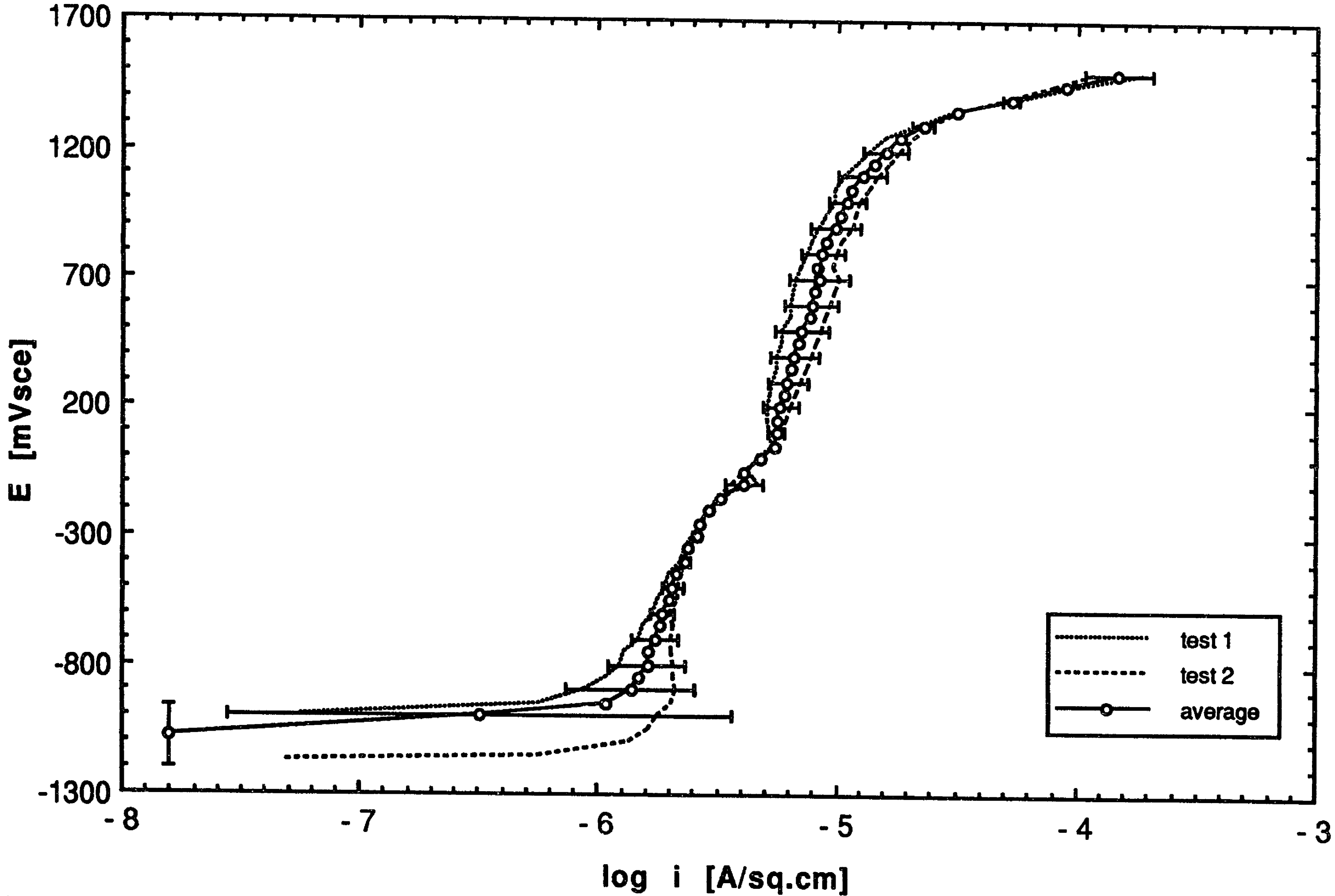

Appendix F-21: Anodic polarization diagram of Specimen 21, a G/Al-4%Cu MMC in deaerated 0.5M Na_2SO_4 solution of pH~7 at 30°C. Scan rate = 0.167 mV/s; Ecorr = -1084 mVsce, SD = 118 mVsce.

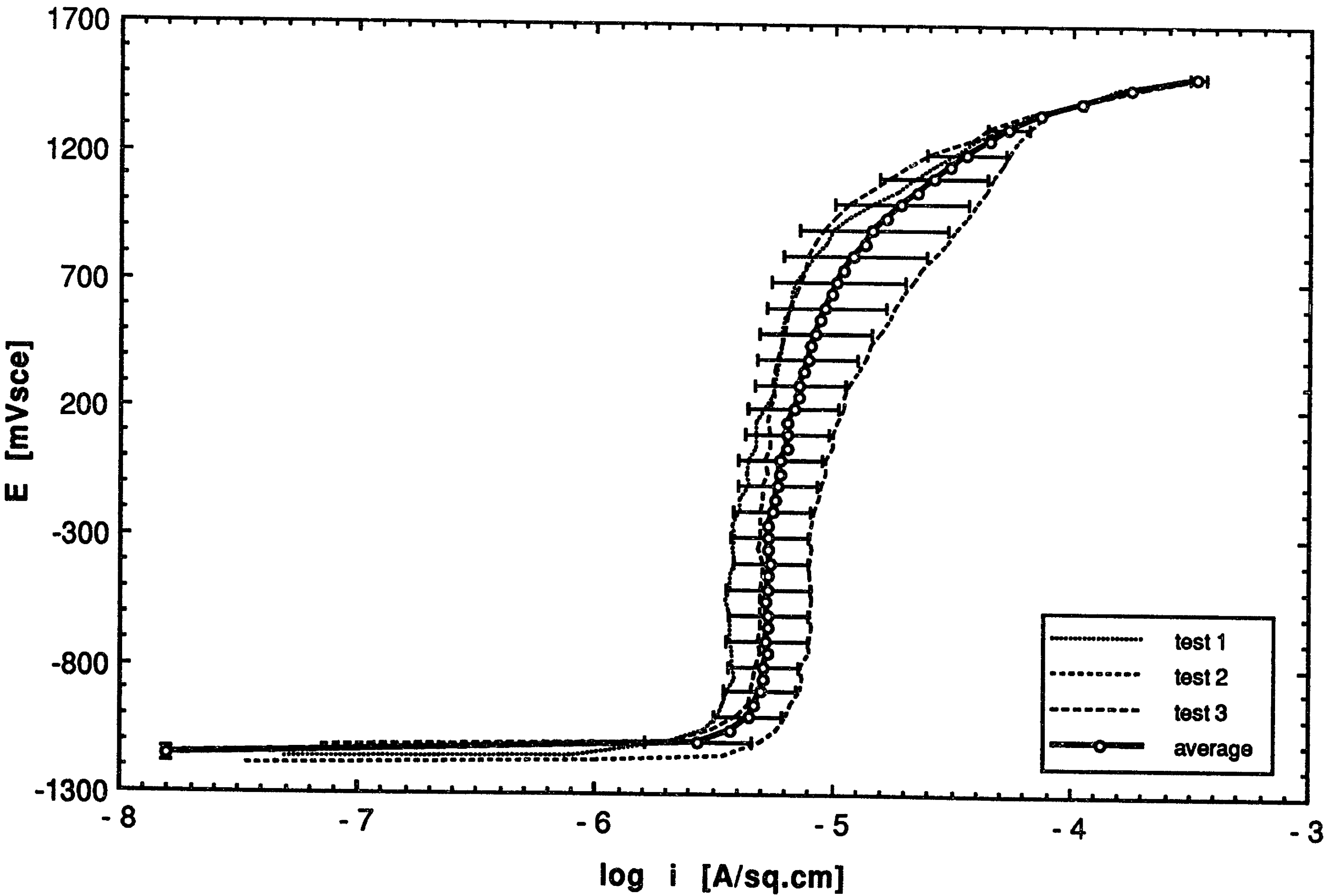

Appendix F-22: Anodic polarization diagram of Specimen 22, a G/Al-2%Cu MMC in deaerated 0.5M Na_2SO_4 solution of pH~7 at 30°C. Scan rate = 0.167 mV/s; Ecorr = -1153 mVsce, SD = 37 mVsce.

Biographical Note

The author was born to Anthony and Roberta Buonanno, in New York. After completing four years at Xaverian High School, a Jesuit, all-boys, academic preparatory school in Brooklyn, NY, he entered Polytechnic Institute of New York. There he began his studies in the field of metallurgy and materials science. While spending his junior summer working at United Technologies Carrier Corporation, Research Division, Syracuse, NY, he decided to further his studies at graduate school. Working under Professor L. S. Castleman, a fine scientist and alumnus of MIT, at 'Polytech,' the author applied and was accepted for graduate studies at MIT.

At MIT, he began his studies in the field of metallurgy with Professor M. Cohen and Dr. G. B. Olson and received the degree of Master of Science in Metallurgy. After a brief period of indecisiveness, the author returned to MIT to begin his Ph.D. and immediately passed the written portion of the general exam at MIT. Working as a teaching assistant, and thereafter, in high temperature mechanical behavior of titanium aluminide, the author was invited to study Scanning Reflection Electron Microscopy by NTT, Tokyo, Japan. After thoroughly enjoying 3 months of research in Tokyo, the author returned to the U.S. and joined the H. H. Uhlig Corrosion Laboratory, passing the oral portion of the general exam.

Subsequently, the author became interested in Japanese culture, business and politics and minored in Japanese while at MIT. The author married Nobuko Terakawa of Nara City, Japan, at Longfellow's Wayside Inn, Sudbury, MA. The author worked at Aluminum Ranshofen, Ranshofen, Austria, in the summer of 1991 through his affiliation with Dr. Helmut Kaufmann of Austria, for period of 3 months, preparing and studying composites related to his dissertation. In the fall of 1991, the author accepted the Boston Chapter NACE H. H. Uhlig Corrosion Award. Upon completion of the present work in May of 1992, the author began working for the General Technology Division of IBM, East Fishkill, NY, in thin film metallurgy.